Title
Sympathetically-cooled quantum chemical dynamics and progress towards a technique for internal state readout of a molecular ion

Author
Puri, Prateek

Publication Date
2019

Peer reviewed|Thesis/dissertation

UNIVERSITY OF CALIFORNIA

Los Angeles

Sympathetically-cooled quantum chemical dynamics and progress towards a technique for internal state readout of a molecular ion

A dissertation submitted in partial satisfaction
of the requirements for the degree
Doctor of Philosophy in Physics

by

Prateek Puri

2019

ABSTRACT OF THE DISSERTATION

Sympathetically-cooled quantum chemical dynamics and progress towards a technique for internal state readout of a molecular ion

by

Prateek Puri
Doctor of Philosophy in Physics
University of California, Los Angeles, 2019
Professor Eric R. Hudson, Chair

This dissertation focuses on observing and controlling cold atom-ion collisions. Such collisions have numerous applications ranging from providing insight into the formation of the interstellar medium to presenting a potential platform for developing quantum information architectures. The experimental apparatus at the center of this work is a hybrid atom-ion trapping system in which laser-cooled Ca atoms held within a magneto-optical trap are spatially overlapped with ions localized within an ion trap. The ions studied in this work are both laser-cooled atomic ions as well as sympathetically cooled molecular ions. As detailed in the remainder of this thesis, by employing tools such as optical pumping, collision energy control, and mass spectrometry, reactions between these species can not only be studied with high precision but can also be controlled, leading to expanded tools for reaction engineering as well as the creation of exotic chemical species. Finally, this work also includes efforts to use inelastic collisions between room temperature $BaCl^+$ molecular ions and cold Ca atoms to create ro-vibrational ground state molecules, a precursor for developing a high-fidelity qubit based on rotational levels in polar molecules.

The dissertation of Prateek Puri is approved.

Karoyl Holzcer

Paul Hamilton

Wesley C. Campbell

Eric R. Hudson, Committee Chair

University of California, Los Angeles

2019

To my parents

Table of Contents

List of Figures

List of Tables

Acknowledgments

When I was studying physics as an undergraduate, I usually operated as a lone wolf. In general, I enjoyed being around other students, but somehow, when it came to academics, I preferred to forgo study groups and review sessions in favor of quietly brooding over textbooks in my apartment. As I entered graduate school, I found out quickly that this formula for success no longer applied, especially within the field of experimental atomic, molecular, and optical (AMO) physics. Often times, it takes an entire village to make things happen in the lab, and thankfully, the UCLA AMO department, a collection of incredibly talented scientists studying a diverse set of research problems, provided the perfect collaborative environment.

Working with so many other driven, intelligent people has been one of the most enjoyable aspects of graduate school for me. Approaching a difficult problem alone can often be intimidating, but through combining the diverse skillsets of the various individuals within UCLA AMO together, we've been able to create a collective problem-solving machine that can tackle even the most daunting lab obstacles. Whether it's by putting dormant optics up for donation or by fibering laser light to down-the-hallway neighbors, we are constantly helping one another move forward with our projects. Even outside of the lab, through events like hosting casual journal club meetings or organizing focus group sessions to test-drive our conference presentations, I always felt like I was in a welcoming environment where I could give and receive constructive feedback. Instead of trying to conceal my lack of understanding with aggressive head nodding when learning about a new topic, I felt comfortable asking what seemed like my deepest, darkest stupid questions - a practice I found often expedited genuine learning.

I was molded into the physicist I am today through experiences with several outstanding researchers/friends over the years. Alexander Dunning and Steven Schowalter were the first two people I started working with seriously after I joined the lab as an undergraduate and started slowly transitioning to graduate school. For better or worse, when I was first studying physics, my perception of what scientists were like was shaped by Big Bang Theory

Hollywood archetypes, and my first few interactions with physicists did little to change this perception. In addition to teaching me countless lessons about basic experimental physics, Alex and Steven were really some of the first people to show me that it was possible to be a great scientist while also still being a cool dude, and our weekly Thursday night escapes to Barney's Beanery after long data runs in the lab were emblematic of this. Steven, a.k.a. Dr. Schowtime, in particular played a central role in guiding my transition from an impressionable undergraduate into an independent researcher and really served as an academic, as well as a personal, role model for me during my early days at UCLA.

After Alex and Steven moved on to greener pastures, I worked side-by-side Michael Mills for the next several years. Like any good buddy comedy, our success was largely a function of our contrasting styles. Mike's more methodical approach was a perfect complement to my 'guns blazing' mentality, and we blended our two techniques together to perform some really exciting and unique experiments. As I progressed through graduate school, I began to appreciate how important effective communication is to success in science, and Mike is someone I've always felt incredibly comfortable talking with, whether our conversation centered on micromotion compensation or Game of Thrones fan theories. Although I may have learned more about Michigan sports along the way than I would have liked, over the last few years we did some great science together and, equally importantly, also had a great times outside the lab (select highlights include nightclub poster sessions in Barcelona and competitive mechanical bull riding).

Christian Schneider has also been one of the most consistent fixtures of my graduate school experience. He's probably the closest thing to a human AMO Google that I've ever seen. Whether talking about a niche data analysis technique or dissecting an electronics issue, he has helpful comments to offer on almost any lab-related problem. The man who mastered the art of telling dad jokes long before becoming a father also mastered the art of being an enthusiastically helpful team player. While I don't think I ever developed the ground-loop-prevention skills he would have liked, he gave me countless lessons on how to become a good scientist, and beyond that, I'll always look forward to our next animated conversation on Westwood bike lane policy.

Justin Jeet joined the Hudson lab at roughly the same time as I did, and he's always been one of the people I felt like I could relate to most easily in the group. In addition to serving as a co-conspirator for lunchtime getaways to Westwood, he was also willing to drop whatever he's doing at a moment's notice to lend a helping hand in the lab. More than anything, he's probably the person who has taught me the most about the value of hard work and hustle. Academically, he's been both my TA and my co-worker at times, but through it all, he's always been a great friend. Whenever I was struggling through the ups and downs of an experiment, our light-hearted conversations about Marvel films or random pop-culture events provided much needed personal decompression.

Rounding out the group, I would like to thank Anthony Ransford, Justin Christensen, David Hucul, and Elizabeth West, as well as the rest of UCLA AMO. As a group, we seem to understand how to balance hard work with cutting loose, as evidenced by the incredible research our groups have produced over the last few years amidst a steady stream of happy hours, self-proclaimed intramural basketball championships, and DAMOP 'networking events'. In particular, whenever I needed a break from the world of chemical reactions, Anthony, Justin, and Dave were there to teach me about the latest and greatest from the quantum information field, and I'm a much more complete scientist because of it. Aside from just talking shop, I've always felt incredibly comfortable having conversations with these three about life outside the lab, and I personally learned a lot from our meandering, Lagunitas-induced conversations about personal worldviews, ethics, and most importantly, whether or not it's possible to construct a brown laser. In addition, while my first instinct when facing a problem in the lab is to resort to the 'quick-and-dirty' approach, Elizabeth taught me the benefit of doing things the right way, and her general lab knowledge, as well as her brave editing abilities, have become essential additions to the group. To all future UCLA AMO members, Grant Mitts in particular (shoutout MOTion project 3.0), I hope you enjoy your experience as much as I did and that there continues to be journal club meetings, 'still-cheaper' group philosophies, creative ICE'ing, and an overall thriving community of basement dwellers at UCLA for years to come.

I also have to thank the man, the myth, the legend - Eric Hudson. From White House

visits to co-founding a center for quantum science, it's truly remarkable what he has been able to accomplish since coming on the UCLA scene a few years ago. He has a tireless work ethic and a genuinely inspiring optimism that gives you hope even when buried in the deepest depths of experimental failure. I first knew him as a undergraduate student who attended more office hours than I'm sure he would have liked, but even back then, I remember being thoroughly impressed by his ability to decompose complex ideas into simple, easily-understandable components, all while maintaining the relaxed aura of someone who had just come back from the beach (which probably was often the case). I could have taken many different routes after finishing my undergraduate degree, but one of the main reasons I came back to UCLA for graduate school was because I was genuinely excited about the idea of throwing on a pair of laser goggles and continuing to work with Eric.

Lastly, this section would feel incomplete if I didn't include the amazing set of friends and family that have supported me over the years. It was a lot easier to endure endless nights in the lab knowing that I had a group of incredible people to spend time with afterwards. To the Mag Seven (Exclusive), my UCLA undergrad family, the Rhode Island delegation, and to my parents and sisters, thank you all so much for playing such a large role in my life (and for putting up with my unpredictable drooling); you all have shaped me into the person I am today.

To finish up, when I first started graduate school, I found myself constantly asking the question - 'Is this the best path for me?'. It was a frustrating question to think about since trying to determine what's 'best' for your life is quite difficult, opportunity costs being as hard to evaluate as they are. I honestly still can't answer that question today, and I may never be able to answer it confidently. But I don't think it's a question I'm going to think about much in the future because I've accomplished some things and met some people during my graduate school experience that have honestly made my time at UCLA feel very valuable and rewarding.

Vita

2011-2014	Undergraduate student researcher under Professor Eric R. Hudson (UCLA), Atomic Molecular and Optical Physics
2014	B.Sc. (Physics), UCLA, *Summa Cum Laude*
2014	*E. Lee. Kinsey Prize for Most Outstanding Graduating Senior (UCLA)*
2015	M.Sc. (Physics), UCLA
2015-2015	Teaching Assistant, Department of Physics and Astronomy (UCLA)
2014-present	Graduate student researcher under Professor Eric R. Hudson (UCLA), Atomic, Molecular and Optical Physics
2015-2016	*Leo P. Delsasso Fellowship (UCLA)*
2015-2018	*National Science Foundation Graduate Student Researcher Fellowship (UCLA)*

Publications

P. Puri, M. Mills, I. Simbotin, J. A. Montgomery, R. Côté, C. Schneider, A. Suits, and E. Hudson, "Reaction blockading in a reaction between an excited atom and a charged molecule at low collision energy", *Nat. Chem.* (2019).

M. Mills, P. Puri, M. Li., S. Schowalter, A. Dunning, C. Schneider, S. Kotochigova, and

E. Hudson, "Engineering excited-state interactions at ultracold temperatures", *Phys. Rev. Lett.* (2019).

M. Li, M. Mills, P. Puri, S. Kotochigova, and E. Hudson, "Excitation-assisted nonadiabatic charge-transfer reaction in a mixed atom-ion system", *Phys. Rev. A.* (2019).

P. Puri, M. Mills, E. P. West, and E. Hudson. "High-resolution collision energy control through ion position modulation in atom-ion hybrid systems", *Rev. Sci. Instrum.* **89**, 083112 (2018).

P. Puri, M. Mills, I. Simbotin, J. A. Montgomery, R. Côté, C. Schneider, A. Suits, and E. Hudson, "Synthesis of a mixed-hypermetallic oxide from a ultracold reagents in an atom-ion hybrid system", *Science* **357**, 1370-1375 (2017).

M. Mills, P. Puri, Y. Yu, A. Derevianko, and E. Hudson, "Efficient repumping of a Ca magneto-optical trap", *Phys. Rev. A.* **96**, 033402 (2017).

S. Schowalter, A. Dunning, K. Chen, P. Puri, S. Kotochigova, C. Schneider, and E. Hudson, "Blue-sky bifurcation of ion energies and the limits of neutral-gas sympathetic cooling of trapped ions", *Nat. Comm.* **7**, 12448 (2016).

A. Dunning, S. Schowalter, P. Puri, S. Kotochigova, A. Petrov, and E. Hudson, "Photodissociation spectroscopy of the dysprosium monochloride molecular ion", *J. Chem. Phys.* **143**, 124309 (2015).

P. Puri, S. Schowalter, S. Kotochigova, A. Petrov, and E. Hudson, "Action spectroscopy of $SrCl^+$ using an integrated ion trap time-of-flight mass spectrometer", *J. Chem. Phys.* **131**, 014309 (2014).

CHAPTER 1

Introduction

This dissertation encapsulates the last several years of research I performed as a member of Professor Eric Hudson's lab at UCLA. We are an atomic, molecular, and optical (AMO) physics group, and in general, our field is interested in studying the underlying properties of atoms, molecules, and light, as well as interactions between these species. A discipline that is as challenging as it is diverse, AMO physics requires a unique blend of engineering, experimental design, and theoretical modeling. This variety not only encourages you to approach lab problems from multiple perspectives but also helps ensure that if you are sick of banging your head against the wall trying to solve one difficult problem, there are several different ones you can rotate your attention to.

While there are many systems one may choose to study at a quantum level within AMO physics, our project is primarily concerned with studying interactions between charged species and neutrals and low temperatures. Ultracold atoms and ions are systems that have both been investigated extensively for applications ranging from quantum computation to metrology. In our hybrid trapping apparatus, we pair the strengths of both species together by spatially overlapping a cold atom magneto-optical trap (MOT) with a four rod linear quadrupole ion trap (LQT), enabling interactions between the two to be studied at temperatures near absolute zero. By observing, and controlling, collisions between the two species, we can investigate a diverse range of physical processes - including but not limited to cold chemistry, quantum information encoding, and non-equilibrium thermodynamics.

Of all these applications, perhaps the primary goal of the project is to utilize inelastic collisions between cold atoms and molecular ions to produce internally ground state molecules and to thereafter obtain complete internal state control over the species. Once this control

has been established, it can be exploited for a host of applications such as state-to-state chemistry and high fidelity quantum logic.

However, pairing atoms and ions within an hybrid trapping apparatus also presents a series of challenges. Namely reactions between the two, as well as problematic thermodynamics, can serve as limiting mechanisms to the efficiency of the sympathetic cooling for ground state molecule preparation. Indeed, some of the work in this thesis was initially geared towards understanding the reaction-related limitations of atom-ion sympathetic cooling. However, while our foray into chemistry may have begun as a means to address an unintended nuisance, it quickly blossomed into an accidental romance, as we realized what an ideal platform hybrid traps, equipped with orthogonal optical and mass-spectrometry detection techniques, provide for studying chemical reactions. Through adapting many of the techniques of ultracold physics towards the study of chemical reactions, we have been able to produce exotic chemical species and unlock new tools for reaction engineering, paving the way to transition from merely observing chemistry to actually controlling it with high precision. In the future, we hope others build on this work, perhaps allowing these reaction control techniques, which include the ability to start and stop reactions as well as to select product outcomes, to be extended to more complex systems of interest to the broader biological and chemistry communities.

1.1 Dissertation outline

A brief summary of each chapter included in this dissertation is presented in this section.

Chapter 2: Molecular structure

A general overview of molecular structure is discussed, including a description of molecular energy levels and angular momenta couplings. The Born-Oppenheimer approximation is reviewed, and methods for calculating both elastic and inelastic cross-sections are presented. Finally, classical long-range capture theory is discussed as a tool for fast-and-loose calcula-

tions of atom-ion inelastic collision rates.

Chapter 3: Ion trapping theory

The fundamentals of ion trapping theory are reviewed. The equations of motion of an ion held within a four-rod radiofrequency trap are derived, and the properties of the corresponding Mathieu equation solutions are discussed. Apart from providing spatial confinement for ionic species, the utility of ion traps for both mass filtering and energy-tuning are also mentioned.

Chapter 4: Interaction of light with matter

This chapter provides a review of basic light-matter interactions. First, Rabi flopping equations are derived by considering a simple two-level system in the presence of a classical EM field. Later, a casual treatment of the density matrix formalism is presented and the corresponding optical Bloch equations are developed. As a comparison to these coherent treatments, an Einstein rate equation method for analyzing atomic electronic populations in the presence of resonant radiation is also presented.

Finally, the applications of these light-matter interactions are discussed. In particular, standard laser cooling theory is reviewed as well as magneto-optical trapping fundamentals.

Chapter 5: Electronic structure calculations

A simple overview of basic electronic structure methods used to numerically solve for various properties of molecular systems is presented. In particular, the Hartree-Fock method is discussed as a formalism to numerically treat the many-body molecular Hamiltonian, and post-Hartree-Fock methods that can better account for electron correlation energy are also discussed. As much of the experimental work presented in this thesis is cross-confirmed

through computational chemistry calculations, a cursory understanding of these methods is beneficial.

Chapter 6: Experimental implementations

For future MOTion project scientists, this chapter will likely be the most useful as it covers the nuts and bolts behind a majority of the measurement techniques and experimental hardware in the lab. First, an overview of the MOTion drive electronics used to control the ion trap and the time-of-flight mass spectrometer (ToF-MS) is presented, as well optimization procedures for tuning the performance of these systems. Next, the structure of the specific molecules and atoms studied in this thesis is reviewed, and their loading mechanisms into the hybrid trapping apparatus are discussed.

ToF-MS and imaging detection methods are described next. In particular, the capability of the ToF-MS for providing ion number and mass information on ions held within the LQT is discussed, and the ways in which fluorescence images can provide similar information is also described. The operating principles of the leak valve system utilized for introducing controlled amounts of gaseous reagents into our vacuum system are also reviewed.

The Ca MOT hardware and imaging system is described, and a step-by-step procedure for measuring MOT temperature, density, and lifetime is provided. An analogous description of the magnetic trap also present in our system is given as well. Lastly, after discussing how to calculate the geometric overlap of the atom and ion species, a description of all laser systems present in the lab, as well as their locking mechanisms, is presented.

Chapter 7: Ca electronic structure and laser-cooling pathways

This chapter chronicles our foray into Ca atom spectroscopy. In particular, it details a series of novel single-laser Ca laser-cooling repumping schemes that were discovered and found to provide superior performance when compared to the standard 672 nm pathway.

The lifetime and maximum MOT density achieved with each repump is presented, with the 453 nm line providing efficiency approaching the limit of what is possible in any single-color configuration. In addition to greatly enhancing the quality of Ca laser-cooling, this work also demonstrates how MOT's can be used for atomic metastable state spectroscopy.

Chapter 8: High resolution atom-ion collision energy control

This chapter describes a series of experiments and simulations that were performed in order to develop an improved method for controlling atom-ion collision energy. This parameter is of critical importance for controlling reaction outcomes, and further, may be used to identify theory-sensitive scattering resonance features. The discussed method relies on controlled modulation of ion position through careful manipulation of the ion trapping potential and can afford order-of-magnitude improvements in energy resolution as compared to micromotion-based methods over a collision energy range of 0.01-120 K.

Chapter 9: Synthesis of a mixed hypermetallic oxide

In this chapter, an experiment to characterize the $BaOCH_3^+ + Ca \rightarrow CaBaO^+ + CH_3$ reaction is discussed. Firstly, the reaction products, as well as the reaction rate, was determined through a series of ToF-MS measurements. Then the pathway of the reaction was discovered by manipulating Ca laser cooling parameters to alter atomic electronic state populations, eventually allowing us to locate which Ca electronic level was responsible for the reaction. A series of electronic structure and long-range capture theory calculations were performed, with the results supporting the experimental findings. In summary, this experiment resulted in the production of the first ever observed mixed hypermetallic oxide from a spin-assisted production pathway, and further, demonstrated how the tools of ultracold physics could be applied towards studying and controlling polyatomic chemistry.

Chapter 10: Low temperature reactions between $BaCl^+$ and Ca^*

Inelastic collisions between the $BaCl^+$ and Ca species have been proposed as method to produce ground state molecules. However, if chemical reactions were to occur between the pair, the effectiveness of the method could be severely compromised. While ground-state reactions between the two species are energetically precluded, excited state reactions can, in principle, occur. In this work, we discuss the conditions under which such excited state reactions can be neglected, and in turn, experimentally demonstrate a reaction blockading phenomena general to nearly all atom-ion excited state reaction processes. Essentially by considering the interplay between spontaneous emission and collision trajectories, we discover that at low collision energies, excited state atom-ion reactions are severely inhibited. In addition to analyzing the relationship between collision energy and reaction rate, we also employ a statistical phase space model to explain observed product branching ratios and perform advanced electronic structure and long-range capture theory calculations to better understand the system, with the results in good agreement with experiment.

Chapter 11: Optical control of radiatively suppressed charge exchange collisions

The reaction blockading effect discussed in the previous chapter, which is thought to be general to all ion-excited-state-atom systems, is experimentally demonstrated in the $Yb^+ + Ca$ system. Further, a method to optically control this process is experimentally presented and is further confirmed through theoretical calculations. The method, which relies on the introduction of a so-called 'catalyst laser', allows for excited state chemistry to be observed at cold temperatures and opens new avenues in low-temperature reaction engineering.

Chapter 12: Rotational-state readout and future outlook

While several hurdles to molecular internal state control have previously been overcome,

such as problematic reactions and thermodynamics, developing a method for rotational state readout is the current limitation for further coherent studies with molecules in the MOTion project. In this final chapter, our recent efforts towards developing such a method for state readout are summarized. In particular, a two-photon photodissociation scheme is presented that relies on driving a rotational-state-selective dissociation transition in order to measure molecular populations. Progress developing this method is presented and remaining challenges are summarized, with the latter mainly boiling down to lack of precise molecular spectroscopy.

CHAPTER 2

Molecular Structure

At first glance understanding the structure of a diatomic molecule may seem like a trivial extension to understanding that of a single atom, but in fact, the act of increasing the number of atoms in the system by one yields an extraordinary amount of additional complexity. For example, in comparison to atoms, molecules have many more modes in which to store energy. As with atoms, they may possess translational kinetic energy, and electrons within the molecule may be promoted to various excited states. However, unlike atoms, they may also rotate and vibrate, providing different energy scales for the system and also introducing an additional angular momentum that can couple to other momenta in the molecule.

As is true for many quantum systems, one can gain intuition by first considering the Hamiltonian. In general, the simplified molecular Hamiltonian [BC03] looks like the following:

$$\hat{H} = \hat{H}_e + \hat{H}_{vib} + \hat{H}_{rot} + \hat{H}_{SO} + \hat{H}_{SR} + \hat{H}_{HFS} + \hat{H}_{\Lambda d} \tag{2.1}$$

where the terms from left to right correspond to the electronic, vibrational, rotational, spin-orbit, spin-rotational, hyperfine, and Λ-doubling terms. Here, the terms in the Hamiltonian are approximated as being uncoupled from one another, but in the most rigorous treatments, coupling between various components of the molecular wavefunction prevents these energy terms from being treated independently. However, under the Born-Oppenheimer approximation (see Sec. 2.3), the electronic, vibrational, and rotational terms are assumed to be uncoupled, and the remaining terms can generally be treated as perturbative additions.

The different terms in Eqn. 2.1 create a hierarchy of energy scales within the system. For example, splittings between different electronic states are generally the most energetic

and typically assume values on the ~ 100 THz level, which can generally be accessed using commercial laser technology.

Vibrational splittings are generally the next largest, with vibrational separations typically in the ~ 1 THz regime. The vibrational energy, corresponding to $\hat{H}_{vib}$, arises from oscillations in the internuclear spacing, which can often be treated as a harmonic-oscillator interaction. Vibrational transition energies typically exist within a laser diode "hole" and thus are typically only addressable using state-of-the-art MidIR laser technology or two-photon Raman excitation schemes.

Lastly, the nuclei may also rotate around one another ($\hat{H}_{rot}$), and these rotational energy splittings tend to be in the ~ 10 GHz regime, which is typically very convenient to address using commercial microwave technology. The small energy separation of these states, amongst other useful properties [DeM02], make them an attractive candidate for quantum information studies [HC18], as will be discussed later in this text.

2.1 Electronic structure

The structure of molecules parallels atomic structure in many ways. Atomic states are generally defined by the different types of angular momentum they possess. In these systems, the electronic angular momentum is carried solely by the valence electrons, since the total angular momentum of the paired inner-shell electrons sums to zero. The electronic angular momentum is stored as spin ($\mathbf{S}$) and orbital angular momentum ($\mathbf{L}$), while the nucleus may also possess nuclear spin ($\mathbf{I}$). Further, atomic electronic quantum states are also characterized by a principal quantum number n which labels which radial solution to the Schrödinger equation describes a particular electron's wavefunction (i.e. $1s$, $2s$, $3s$). To first order, n determines an electron's energy; however, higher-order interactions within the atom generally ensure that electrons that share the same n are not energetically degenerate.

Molecules are similar to atoms in many of these regards but offer additional complexity due to their more sophisticated structure. With regards to angular momenta, diatomics have an additional degree of freedom in the form of nuclear rotational angular momentum ($\mathbf{N}$).

	Atomic property		Molecular property		
Angular momentum	Symbol	Values	Symbol	Projection	Values
Electronic spin	$\mathbf{S}$	0,$\frac{1}{2}$,1,...	$\mathbf{S}$	Σ	0,$\frac{1}{2}$,1,...
Electronic orbital angular momentum	$\mathbf{L}$	s,p,d,...	$\mathbf{L}$	Λ	Σ, Π, Δ,...
Nuclear rotational angular momentum			$\mathbf{N}$		0,1,2,...
Nuclear spin	$\mathbf{I}$	0,$\frac{1}{2}$,1,...	$\mathbf{I}$		0,$\frac{1}{2}$,1,...
Total angular momentum (minus $\mathbf{I}$)	$\mathbf{J}$	0,$\frac{1}{2}$,1,...	$\mathbf{J}$	Ω	0,$\pm\frac{1}{2}$,$\pm$1,...

Table 2.1: Table take from Ref. [Ham10] describing the various angular momenta atoms and molecules may possess. While the $\mathbf{S}, \mathbf{L}, \mathbf{J}$, angular momentum vectors are well defined quantities in atomic systems due to their spherical symmetry, in molecules, the "good" quantum numbers depend on how the various angular momenta couple together, with the couplings generally able to be described by one of the limiting Hund's cases.

Table 2.1 gives an overview of the various types of angular momentum present in molecules and atoms.

While atoms possess spherical symmetry, diatomic molecules possess cylindrical symmetry. Due to the spherical symmetry in atoms, the conserved quantities are the electronic spin $\mathbf{S}$, the orbital angular momentum, $\mathbf{L}$, and the overall total electronic angular momentum, $\mathbf{J} = \mathbf{S} + \mathbf{L}$.

In diatomics, the total angular momentum of the molecule $\mathbf{J}$ is the vector sum of the various angular momenta in the system, as $\mathbf{J} = \mathbf{L} + \mathbf{S} + \mathbf{N}$, where the $\mathbf{L}$ and $\mathbf{S}$ vectors are defined as in the atomic case. $\mathbf{J}$ is always conserved (neglecting hyperfine for the moment); however, in general, due to the cylindrical symmetry of the system, the various components of $\mathbf{J}$ may precess about the internuclear axis. Since these angular momentum vectors rotate in time, the individual vectors themselves are often not conserved quantities; instead, the ways in which the various angular momenta couple to one another will determine what the conserved quantities are.

Examples of "good" quantum numbers in diatomic molecules, assuming for example

Hund's case (a) coupling (see Sec. 2.1.2), are Σ and Λ, the projections of $\mathbf{S}$ and $\mathbf{L}$ onto the internuclear axis, respectively. Similarly, $\Omega = \Sigma + \Lambda$, the $\mathbf{J}$ projection, is also conserved and is given as the vector sum of the orbital and spin projections.

However, while the above projections are assumed to be well-defined quantities in Hund's case (a), different types of angular momenta coupling within the molecule can lead to other types of Hund's cases where these quantities are not conserved, just as is the case in atomic systems with strong-field and weak-field Zeeman splittings, for example.

Further, similar to atomic spectroscopic notation, molecular angular momenta quantum numbers can be condensed into a molecular term symbol for state-labeling as

$$^{2\Sigma+1}\Lambda^{+/-}_{\mathbf{\Omega},(\mathbf{g/u})} \tag{2.2}$$

where the $(+/-)$ refers to (even/odd) reflection symmetry of the electronic state along an arbitrary plane containing the internuclear axis and (g/u) refers to (even/odd) parity inversion symmetry about the center of mass position of diatomic. For example in $BaCl^+$, the two lowest lying molecular states are the $X^1\Sigma^+$ and $A^1\Pi$ states. Here the X and A letters are used to designate the energetic ordering of electronic states with the same spin multiplicity. The X symbol is reserved for the ground state, while A,B,C... symbols specify states of increasing energy. Similarly, for excited states with different multiplicities than the ground state, the letters a,b,c... are used to denote such ordering. However, this notation does vary from resource to resource and further can be altered if a new state is found in a physical system that is lower in energy than previously discovered states; thus state labeling should be cross-confirmed through other means when browsing the literature.

In general, the $\mathbf{L}$ projections are allowed to be negative since the electrons can either rotate clockwise or counterclockwise about the internuclear axis; however, unless considering higher order angular momentum couplings (see Sec. 2.1.1), these different rotations are energetically degenerate. Therefore, in the molecular term symbols, Λ typically refers to the absolute value of orbital angular momentum projection, but we can introduce another number $|M_L|$ to describe the signed value of the $\mathbf{L}$ projection. For example, given a total angular momentum magnitude L, $M_L \in \{-L, -L+1, ...L-1, L\}$, where M_L is the projection of the

orbital angular momentum onto the internuclear axis, with $\Lambda = |M_L|$.

In general, the number of Λ states that are accessible in a given diatomic molecule can be determined by considering the **L** values of the individual atomic constituents. For example, if considering the number of Λ states that exist in a molecule composed of two atoms that each have a P-state valence electron, first consider the different angular momentum projections of each atom. Since L=1 for each atom, $M_{L_1} \in \{-1, 0, 1\}$ and $M_{L_2} \in \{-1, 0, 1\}$, for the valence electron in the first and second atom, respectively. Combining these projections in all nine possible ways ($|M_{L_1} + M_{L_2}|$) produces 3 distinct Σ ($\Lambda = 0$) states, 4 Π ($\Lambda = 1$) states, and 2 Δ ($\Lambda = 2$) states. For this molecule then, $M_L \in \{-2, -1, 0, 1, 2\}$.

Lastly, the above discussion mostly focused on angular momenta in molecules; however, molecular states are also characterized by a radial solution to the Schrödinger equation. Each electron in a molecule can be thought of as residing in a 'molecular orbital', typically labeled as σ, that is described by a solution to the electronic Hamiltonian, as discussed in Chapter 5. Similar to atomic orbitals, these molecular orbitals will have different energies and the molecular principle quantum number, similar to the atomic n, is used to characterize which orbital an electron is occupying (1σ, 2σ, etc.), with orbitals generally increasing in energy as a function of this principal quantum number.

2.1.1 Energy splittings and angular momentum couplings

It is worth reiterating that for molecules in which $|\Lambda| \geq 1$, a two-fold degeneracy exists, essentially because there are two directions in which the electrons can rotate, counterclockwise and clockwise with respect to the internuclear axis. While both of these rotations are nominally energetically degenerate, interactions with the nuclear rotation and other angular momenta can lift this degeneracy, yielding so-called Λ-doublets.

Further, for situations in which both Σ and Λ are greater than zero, the orbiting electrons create a magnetic field that interacts with spin of the electrons, creating an energy splitting in a similar manner to traditional spin-orbit coupling in atoms. This energy splitting is typically given a

$$\hat{H}_{SO} = A\vec{L} \cdot \vec{S} \tag{2.3}$$

where A is the spin-orbit coupling constant. This results in a further splitting of degenerate Ω states into $|2\Omega + 1|$ distinct energy levels, with the splitting roughly approximated, under a coupling such as Hund's case (a), as $\Delta E_{SO} = AM_L M_S$ (M_S is defined similarly to M_L above).

In addition to these electronic quantum numbers, one or both of the nuclei may possess nuclear spin, leading to a nuclear spin angular momentum vector **I**. Once again, how the various **J**, **L**, **S**, **I**, and **N** couple together, and thus what the 'good' quantum numbers are, depend on the system of interest. This is qualitatively similar to determining what the 'good' quantum numbers are in an atomic system simultaneously undergoing spin-orbit coupling and Zeeman shifts - ultimately how large these perturbations are in relation to the base Coulomb interaction will determine the conserved quantities.

2.1.2 Hund's case (a)

In general,the angular momentum coupling in most diatomic systems will fall under one of the limiting cases presented in Hund's cases. As an example, we will consider a Hund's case (a) molecule, whose angular momentum couplings are presented graphically in Fig. 2.3.

In Hund's case (a), we consider the Coulombic interaction to be the dominant term in our Hamiltonian, which is much larger than the spin-orbit interaction, which in turn is much larger than the rotational energy of the diatom. In this situation, **L** cannot be independently conserved since the system lacks spherical symmetry. Instead it precesses about the internuclear axis, leading to a well defined projection Λ. The orbital motion of the electrons produces a magnetic field that defines the quantization axis for **S** and causes it to precess about the internuclear axis due to the spin-orbit interaction. **S**, unlike **L**, does not need a spherically symmetric potential to be conserved, and in this case, we can consider both **S** and its projection, Σ, to be well-defined. Therefore, $\Omega = \Sigma + \Lambda$ is also well-defined, as is the total angular momentum J since the total angular momentum is always conserved.

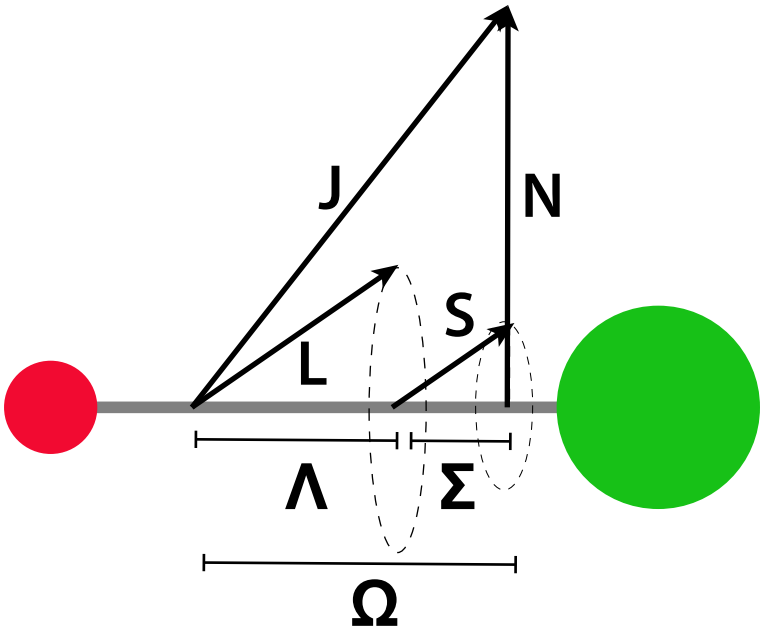

Figure 2.1: Illustration of Hund's case (a)

The eigenstates of the system are characterized by the quantum numbers $|J, \Omega, \Sigma, \Lambda, S\rangle$. In this regime, the spin-orbit coupling is considered to be large in comparison to the nuclear rotation.

This gives a set of mutually commuting operators $\{\hat{J}, \hat{J}_z, \hat{S}, \hat{S}_z, \hat{L}_z\}$ and their associated eigenvalues characterize our quantum state, $|J, \Omega, S, \Sigma, \Lambda\rangle$. Here, $\mathbf{N}$ is not considered a good quantum number and is instead defined as $\mathbf{N} = \mathbf{J} - \mathbf{\Omega}$. Evaluating $\langle J, \Omega, S, \Sigma, \Lambda | \hat{N}^2 | J, \Omega, S, \Sigma, \Lambda \rangle$ will yield the rotational splittings that will define the rotational energy levels of the molecule. Further, since Ω and Λ are well-defined, Eqn. 2.3 can be used to calculate ΔE_{SO}. In other Hund's cases, the conserved quantities change, and thus the expressions for the spin-orbit and rotational energy terms will change as well. In general, it is not always easy to tell *a priori* what type of coupling case a molecular state will fall into; rather, in these cases, observed spectra can be used to infer what type of coupling is dominant in the molecule, providing additional insight into its structure [BJP03].

2.2 Ro-vibrational structure

We can now turn our attention to the rotational and vibrational energy level structure of a diatomic molecule. As a first-order approximation, we can consider the rotational and vibrational terms of Eqn. 2.1 to be independent of the other terms in the Hamiltonian and then employ a simple semi-classical treatment to obtain the rotational and vibrational energy levels of the molecule. This approach may seem *ad-hoc* at the moment but will become formalized later through application of the Born-Oppenheimer approximation.

2.2.1 Vibrational structure

We can approximate the relative motion of the nuclei in a diatom [Dem06] as that of a harmonic oscillator with characteristic frequency ω_0, yielding states with energies of

$$E_{vib} = \hbar\omega_0(v + 1/2) \tag{2.4}$$

where v is the vibrational quantum number. While this model is accurate for low lying vibrational levels, as higher vibrational states are sampled, the potential becomes more anharmonic. In this regime, the Morse potential $V(r) = D_E[1 - e^{-a(r-r_e)}]$ is a better approximation for the radial potential, where D_E is the dissociation energy of the molecule, r_e is the equilibrium internuclear separtion distance, and a is a free parameter fit to a particular molecular system. Solving the radial Schrödinger equation with Morse potential, the energy eigenvalues can be given as [Dem06]

$$\begin{aligned} E_{vib} &= \hbar\omega_0(v + 1/2) - \frac{\hbar^2\omega_0^2}{4D_E}(v + 1/2)^2 \\ \rightarrow E_{vib}/hc &= \omega_e(v + 1/2) - \omega_e\chi_e(v + 1/2)^2 \end{aligned} \tag{2.5}$$

where ω_e and $\omega_e\chi_e$ are the commonly used term symbols quoted in literature (units of cm^{-1}).

2.2.2 Rigid rotor model of diatomic molecules

To asses the nuclear rotational energy of a diatom, one can model the system as a rigid-rotor [Dem06]. Under this model, rotations of the molecule through any axis that contains the center-of-mass yield a rotational kinetic energy of

$$E_{rot} = \frac{1}{2} I\omega^2 = \frac{J^2}{2I} \tag{2.6}$$

where ω is the angular velocity of the molecule, I is the moment of inertia, given as $I = m_a r_a^2 + m_b r_b^2$, where m_i and r_i describe the mass and distance from the rotational axis of the i^{th} atom in the diatomic molecule, and $|J| = I\omega$ is the quantized rotational angular momentum. The eigenvalues of the $\hat{J}^2$ operator lead to energy eigenvalues of

$$\begin{aligned} E_{rot} &= \frac{J(J+1)\hbar^2}{2\mu r_e 2} \\ \rightarrow E_{rot}/hc &= B_e J(J+1) \end{aligned} \tag{2.7}$$

where μ is the reduced mass of the system and r_e is the equilibrium internuclear separation of the molecule. B_e is the rotational spectroscopic constant that is typically quoted in literature (units cm^{-1}).

A higher-order approximation to this rotational model considers the non-rigidity of the molecule. Instead of being completely rigid, the molecule can be approximated as oscillating as a spring with a spring constant k about its equilibrium distance. A rotating body will experience a centrifugal force that will displace the spring from its equilibrium position, leading to the equality

$$\mu\omega^2 r = \mu \left(\frac{J}{I}\right)^2 r = \frac{J(J+1)\hbar^2}{\mu r^3} = k(r - r_e). \tag{2.8}$$

Solving for r, we find the new equilibrium internuclear separation distance of the molecule is defined by the equation $r_c = r_e + \frac{J(J+1)\hbar^2}{k\mu r_c^3}$. To proceed further, the following approximation

can be made by finding r_c to first order in small displacements from r_e:

$$r_c \approx r_e \left(1 + \frac{J(J+1)\hbar^2}{\mu k r_e^4}\right) = r_e(1+\delta). \tag{2.9}$$

Now, we can further approximate Eqn. 2.7 through a Taylor expansion

$$\begin{aligned} E_{rot} &= \frac{J(J+1)\hbar^2}{2\mu r_c^2} \\ &\approx \frac{J(J+1)\hbar^2}{2\mu} \frac{1}{r_e^2(1+\delta)^2} \\ &\approx \frac{J(J+1)\hbar^2}{2\mu r_e^2}(1-2\delta) = \frac{J(J+1)\hbar^2}{2\mu r_e^2}\left(1 - \frac{2J(J+1)\hbar^2}{\mu k r_e^4}\right) \end{aligned} \tag{2.10}$$

which leads to

$$E_{rot} \approx \frac{J(J+1)\hbar^2}{2\mu r_e} - \frac{J^2(J+1)^2\hbar^4}{\mu^2 k r_e^6} \tag{2.11}$$

As can be seen above, one of the effects of centrifugal distortion is to shift the equilibrium distance of the molecule to larger values. At a fixed J, this serves to reduce the angular velocity, and thus the angular kinetic energy, resulting in the negative energy correction term.

Another effect, however, is a positive energy correction term associated with displacement of the spring. This can be calculated as

$$\Delta E_{rot} = \frac{1}{2}k(r_c - r_e)^2 \approx \frac{1}{2}k\delta^2 = \frac{J^2(J+1)^2\hbar^4}{2\mu^2 k r_e^6} \tag{2.12}$$

As can be seen, the above correction term is positive as the string is stretched from its equilibrium distance, increasing the calculated potential energy of the system.

Combining both effects we see

$$\begin{aligned} E_{rot} &\approx \frac{J(J+1)\hbar^2}{2\mu r_e} - \frac{J^2(J+1)^2\hbar^4}{2\mu^2 k r_e^6} \\ \rightarrow E_{rot}/hc &= B_e J(J+1) - D_e J^2(J+1) \end{aligned} \tag{2.13}$$

where D_e is the centrifugal distortion constant typically quoted in literature.

Combing both rotational and vibrational energy terms, the ro-vibrational energies, E_{vJ}, can finally be approximated as

$$E_{vJ}/hc = \omega_e(v+1/2) - \omega_e\chi_e(v+1/2)^2 + B_eJ(J+1) - D_eJ^2(J+1) \tag{2.14}$$

2.3 The Born-Oppenheimer approximation

We will now give a more formal treatment of the first three terms in Eqn. 2.1, which consist of terms associated with both electronic and nuclear energy. The generic non-relativistic Hamiltonian for a diatomic molecule is given as

$$\begin{aligned}\hat{H} =& -\sum_{I=1}^{N}\frac{\hbar^2}{2M_I}\nabla_{R_I}^2 - \sum_{i=1}^{n}\frac{\hbar^2}{2m_e}\nabla_{r_i}^2 + \frac{1}{2}\sum_{\substack{I,J=1\\I\neq J}}^{N}\frac{1}{4\pi\epsilon_0}\frac{Z_IZ_Je^2}{|\mathbf{R}_I-\mathbf{R}_J|} \\ &+ \frac{1}{2}\sum_{\substack{i,j=1\\i\neq j}}^{n}\frac{1}{4\pi\epsilon_0}\frac{e^2}{|\mathbf{r}_i-\mathbf{r}_j|} - \sum_{I,i=1}^{I=N,i=n}\frac{1}{4\pi\epsilon_0}\frac{Z_Ie^2}{|\mathbf{R}_I-\mathbf{r}_i|} \\ =& \hat{T}_N + \hat{T}_e + \hat{V}_{NN} + \hat{V}_{ee} + \hat{V}_{Ne}\end{aligned} \tag{2.15}$$

where M_I refers to the mass of the I^{th} nucleus; $\hbar$ is the reduced Planck's constant; $\nabla_{R_I}^2$ is the Laplacian operator with respect to the I^{th} nucleus's spatial coordinates, R_I; m_e is the mass of the electron; $\nabla_{r_i}^2$ is the Laplacian operator with respect to the i^{th} electron's spatial coordinates, r_i; ϵ_0 is the vacuum permittivity of free space; Z_I is the nuclear charge of the I^{th} nucleus; $\mathbf{R_I}$ is the vector representing the position of the I^{th} nucleus; $\mathbf{r}_i$ is the vector representing the position of the i^{th} electron; and N and n are the total number of nuclei and electrons, respectively.

From left to right, the terms in the equation represent the kinetic energy of the nucleus ($\hat{T}_N$), the kinetic energy of the electrons ($\hat{T}_e$), the nucleus-nucleus repulsion terms ($\hat{V}_{NN}$), the electron-electron repulsion terms($\hat{V}_{ee}$), and lastly, the electron-nucleus attraction terms ($\hat{V}_{Ne}$). In general, the above Hamiltonian is analytically unsolvable, and in order to treat these types of many-body systems theoretically, approximation methods must be employed.

One of the most popular approximation techniques for treating the molecular Hamiltonian is the Born-Oppenheimer approximation. When looking at Eqn. 2.15, one of the most problematic aspects is $\hat{V}_{Ne}$, which mixes both electronic and nuclear coordinates. Without this term, the Hamiltonian would be separable into terms that depend exclusively nuclear or electronic coordinates, implying that the solution to the Schrödinger equation would also be separable as

$$\Psi(\mathbf{r}, \mathbf{R}) = \psi_p(\mathbf{r})\chi_{v,J}(\mathbf{R}) \tag{2.16}$$

where $\Psi(\mathbf{r}, \mathbf{R})$ is the total wavefunction of the system, dependent on both nuclear ($\mathbf{R}$) and electronic coordinates ($\mathbf{r}$), where $\mathbf{r}$ denotes a vector of all $\mathbf{r_i}$ coordinates in the problem and $\mathbf{R}$ denotes a vector of all $\mathbf{R_i}$ coordinates in the problem. $\psi_p(\mathbf{r})$ describes the p^{th} electronic wavefunction of the system, and $\chi_{v,J}(\mathbf{R})$ describes the nuclear wavefunction of the system, indexed by the (v, J) vibrational and rotational quantum numbers (to be discussed in more detail below).

Most conveniently, we would like to be able to neglect all terms in Eqn. 2.15 that mix nuclear and electronic coordinates so we could obtain the above separable solution; however, there really isn't any justification for this since many of the mixing terms are of the same order as the non-mixing terms in the Hamiltonian.

However, we can note that $M_A >> m_e$ ($M_A/m_e \approx 1800$), which implies that electronic motion will have very little effect on the position of the nuclei, whereas the electrons should respond nearly instantaneously to changes in nuclear motion. Therefore, we can rewrite Eqn. 2.16 as

$$\Psi(\mathbf{r}, \mathbf{R}) = \psi_p(\mathbf{r}, \mathbf{R})\chi^p_{v,J}(\mathbf{R}) \tag{2.17}$$

which implies that the nuclear wavefunction is independent of electronic coordinates [BO27] and that the electronic wavefunction depends only parametrically on nuclear coordinates. The nuclear wavefunction is now also indexed by p since, as we will see shortly, the electrostatic potential included in the nuclear Schrödinger equation will also depend on the

electronic state of the molecule.

Inserting Eqn. 2.17 into Eqn. 2.15, we see for the $\hat{T}_N$ term

$$\begin{aligned}\hat{T_N}\psi_p(\mathbf{r},\mathbf{R})\chi^p_{v,J}(\mathbf{R}) &= -\frac{\hbar^2}{2}\sum_{I=1}^{N}\frac{1}{M_I}[\psi_p(\mathbf{r},\mathbf{R})\nabla^2_{R_I}\chi^p_{v,J}(\mathbf{R}) \\ &\quad + \chi^p_{v,J}(\mathbf{R})\nabla^2_{R_I}\psi_p(\mathbf{r},\mathbf{R}) + 2\nabla_{R_I}\psi_p(\mathbf{r},\mathbf{R})\cdot\nabla_{R_I}\chi^p_{v,J}(\mathbf{R})] \\ &\approx -\frac{\hbar^2}{2}\sum_{I=1}^{N}\frac{1}{M_I}\psi_p(\mathbf{r},\mathbf{R})\nabla^2_{R_I}\chi^p_{v,J}(\mathbf{R})\end{aligned} \tag{2.18}$$

The latter approximation can be made since the $\nabla_{R_I}\chi^p_{v,J}(\mathbf{R}) \gg \nabla_{R_I}\psi_p(\mathbf{r},\mathbf{R})$. In a classical sense, this is intuitive [BO27] since the nucleus is heavy and well-localized to a pointlike distribution, meaning its wavefunction changes drastically as a function of the nuclear coordinate, allowing the nuclear gradient term to dominate over the electronic terms. After incorporating the rest of the terms from Eqn. 2.15 into the Schrodinger equation $H\Psi = E\Psi$, we see

$$\frac{[\hat{T}_e + \hat{V}_{ee} + \hat{V}_{Ne}]\psi_p(\mathbf{r},\mathbf{R})}{\psi_p(\mathbf{r},\mathbf{R})} = E - \frac{[\hat{T}_N + \hat{V}_{NN}(\mathbf{R})]\chi^p_{v,J}(\mathbf{R})}{\chi^p_{v,J}(\mathbf{R})} \tag{2.19}$$

Since the RHS of the above equation is a function of $\mathbf{R}$ alone, the left side must be as well, leading to

$$[\hat{T}_e + \hat{V}_{ee} + \hat{V}_{Ne}]\psi_p(\mathbf{r},\mathbf{R}) = \phi_p(\mathbf{R})\psi_p(\mathbf{r},\mathbf{R}) \tag{2.20}$$

The above equation is known as the electronic eigenvalue equation [BO27] and can be used to solve for the electronic eigenvalues $\phi_p(\mathbf{R})$ as well as the electronic wavefunctions, $\psi_p(\mathbf{r},\mathbf{R})$. While the above equation is by no means simple to solve, we have effectively transformed the analytically-impossible molecular Hamiltonian problem into a slightly less complex electronic Hamiltonian problem that can be attacked using state-of-the-art computational chemistry techniques. The key difficulty in solving the above equation is the electron-electron repulsion terms, which mix the coordinates of all the electrons in the system. While this indeed poses

a challenge, a suite of computational techniques has been developed to address this issue, which will be discussed in detail in Chapter 5.

After solving for the appropriate electronic eigenvalues and eigenfunctions, there will be a corresponding reduced nuclear Hamiltonian from Eqn. 2.19 that can be solved as well, given as

$$[\hat{T_N} + V_{NN}(\mathbf{R}) + \phi_p(\mathbf{R})]\chi^p_{v,J}(\mathbf{R}) = E\chi^p_{v,J}(\mathbf{R}) \tag{2.21}$$

where $\phi_p(\mathbf{R})$ is the electronic eigenvalue associated with the p^{th} electronic eigenstate.

For the case of diatomic molecules of interest in this work, the corresponding nuclear wavefunction, $\chi^p_{v,J}(\mathbf{R})$, may be further separated into functions that depend solely on the radial ($S^p_v(R)$) and angular ($Y_J(\theta,\alpha)$) variables of the system as

$$\chi^p_{v,J}(R,\theta,\alpha) = S^p_v(R)Y_J(\theta,\alpha) \tag{2.22}$$

where θ and α are the polar and azimuthal variables, respectively. Inserting this solution into Eqn. 2.21, we can perform another separation of variables to isolate the nuclear Schrödinger equation into its rotational and vibrational components.

Since the molecular potential curve ($\phi_p(R)$) depends only on the internuclear separation distance, the radial form of the Schrödinger equation resembles that of a hydrogen atom [Gri05] and is given as

$$\Big[\frac{1}{R^2}\frac{d}{dR}\left(R^2\frac{dS^p_v(R)}{dR}\right) + \frac{2\mu}{\hbar^2}(E-\phi_p(R)) - \frac{J(J+1)\hbar^2}{2\mu R^2}\Big]S^p_v(R) = 0 \tag{2.23}$$

where we have absorbed the nuclear repulsion term, $\hat{V}_{NN}$ into $\phi_p(R)$ for notational simplicity. Similarly, $Y_J(\theta,\alpha)$ is determined by solving the following equation:

$$\frac{1}{\sin\theta}\frac{\partial}{\partial\theta}\left(\sin\theta\frac{\partial Y_J(\theta,\alpha)}{\partial\theta}\right) + \frac{1}{\sin^2\theta}\frac{\partial^2 Y_J(\theta,\alpha)}{\partial\alpha^2} + J(J+1)Y_J(\theta,\alpha) = 0 \tag{2.24}$$

Once the above electronic, vibrational, and rotational wavefunctions have been obtained, we can say that a general wavefunction of the system is given as

$$\Psi(\mathbf{r},\mathbf{R}) = \sum_{v,J,p} C_{v,J,p}\chi^{p}_{v,J}(\mathbf{R})\psi_p(\mathbf{r},\mathbf{R}) \tag{2.25}$$

where $C_{v,J,p}$ are expansion coefficients.

After the total molecular wavefunction has been determined, many other quantities of interest for the molecule, such as transition rates, photo-dissociation rates, etc., can be calculated [Jec14, PST07, DS09].

2.3.1 Transition rates

One of the most relevant quantities of interest to calculate in molecular physics experiments are rates of transitions between ro-vibrational levels, driven by external electric fields. Within the Born-Oppenheimer approximation, a generalized transition rate, Γ_T, can be estimated via Fermi's Golden Rule by considering the transition dipole matrix element. The electric dipole energy is proportional to $E\hat{\epsilon}\cdot\mathbf{p}$, where E is the electric field amplitude, $\hat{\epsilon}$ is the unit vector pointing in the direction of the incident electric field, and $\mathbf{p}$ is the dipole function [Dem06] given as

$$\mathbf{p} = -e\sum_i \mathbf{r_i} + e\sum_i \mathbf{R_i} = \mathbf{p_e} + \mathbf{p_N} \tag{2.26}$$

where the $\mathbf{p_e}$ ($\mathbf{p_N}$) term corresponds to the electronic (nuclear) dipole moment contribution. Typically only the outermost valence electron is involved in the transition but we will leave the summation general for the moment.

Using Fermi's Golden Rule in a diatomic system, Γ_T is proportional to

$$\begin{aligned}
\Gamma_T &\propto E^2 |\left\langle Y_{J'}(\theta,\alpha)S^{p'}_{v'}(R)\psi_{p'}(\mathbf{r},R)|\hat{\epsilon}\cdot\mathbf{p}|\psi_p(\mathbf{r},R)S^{p}_{v}(R)Y_J(\theta,\alpha)\right\rangle|^2 \\
&\propto E^2 |\left\langle Y_{J'}(\theta,\alpha)S^{p'}_{v'}(R)\right|\left\langle\psi_{p'}(\mathbf{r},R)|\hat{\epsilon}\cdot\mathbf{p_e}|\psi_p(\mathbf{r},R)\right\rangle|S^{p}_{v}(R)Y_J(\theta,\alpha)\rangle \\
&+ \left\langle Y_{J'}(\theta,\alpha)S^{p'}_{v'}(R)\psi_{p'}(\mathbf{r},R)|\hat{\epsilon}\cdot\mathbf{p_N}|\psi_p(\mathbf{r},R)S^{p}_{v}(R)Y_J(\theta,\alpha)\right\rangle|^2 \\
&\propto E^2 |\left\langle Y_{J'}(\theta,\alpha)S^{p'}_{v'}(R)|d_{p,p'}(R,\theta,\alpha)|S^{p}_{v}(R)Y_J(\theta,\alpha)\right\rangle \\
&+ \left\langle Y_{J'}(\theta,\alpha)S^{p'}_{v'}(R)\right|\left(\left\langle\psi_{p'}(\mathbf{r},R)|\psi_p(\mathbf{r},R)\right\rangle\right)\hat{\epsilon}\cdot\mathbf{p_N}|S^{p}_{v}(R)Y_J(\theta,\alpha)\rangle|^2
\end{aligned} \tag{2.27}$$

where $d_{p,p'}(R,\theta,\alpha)$ is the transition dipole moment function (obtained from evaluating $\hat{E}\epsilon \cdot \mathbf{p}$ over the electronic states in the system). We can analyze the above equation for two particular cases.

In the first case, we can consider overtone transitions within the same electronic state ($\psi_{p'}(\mathbf{r},R) = \psi_p(\mathbf{r},R)$). The first term in Eqn. 2.27 will be 0 since $\mathbf{p_e}$ is a symmetric function, meaning $d_{p,p'}(R,\theta,\alpha)$ will evaluate to 0. Therefore, overtone transitions only arise from the second term in Eqn. 2.27, which represents the nuclear dipole energy contribution. For homonuclear molecules, however, $\mathbf{p_N} = 0$, and thus overtone transitions are electric dipole forbidden in these systems and thus are much more easily driven in heteronuclear systems [AP10].

In the second case, we can consider transitions between different electronic states ($\psi_{p'}(\mathbf{r},R) \neq \psi_p(\mathbf{r},R)$). Now the second term is zero since the electronic functions are orthonormal, meaning only the first term contributes [Dem06]. The first term in general is a complicated integral over both electronic and nuclear coordinates; however, a common approximation [Dem06] is to assume $d_{p,p'}(R,\theta,\alpha) = d_{p,p'}$, a constant. Using this approximation

$$\begin{aligned} \Gamma_T &\propto d_{p,p'}^2 \left\langle S_{v'}^{p'}(R) | S_v^p(R) \right\rangle^2 \mathrm{H_{J,J'}} \\ &\propto d_{p,p'}^2 FCF(p',v',p,v) \mathrm{H_{J,J'}} \end{aligned} \tag{2.28}$$

where $FCF(p',v',p,v)$ is known as the Franck-Condon Factor and describes the vibrational wavefunction overlap and $\mathrm{H_{J,J'}}$ is known as the Hönl-London factor. The Hönl-London factors are the molecular equivalent of Clebsch-Gordon coefficients and are responsible for rotational selection rules. The rotational selections rules mirror those in atoms, primarily because the rotational components of the wavefunction are essentially spherical harmonics, matching their atomic counterparts. Namely, for molecular transitions, $\Delta J = -1, 0, 1$, with $\Delta J = 0$ implying $\Delta\Lambda = \pm 1$ to conserve angular momentum (J=0→J'=0 is forbidden). The $\Delta J = -1, 0, 1$ transitions are known as the P, Q, and R branch transitions respectively. In additional to these rotational selection rules, the FCF acts as a sort of 'weak vibrational selection rule' by suppressing transitions with poor vibrational wavefunction overlap. Finally, $d_{p,p'}$ encodes the electronic state selection rules, which follow those similarly found in atoms

in which $\Delta S = 0$, $\Delta\Sigma = 0$, $\Delta\Lambda = 0, \pm 1$, and $\Delta\Omega = 0, \pm 1$. For more detailed information on these selection rules, the reader is referred to Refs. [BC03, HH79].

2.3.2 Born-Oppenheimer breakdown

The Born-Oppenheimer approximation is also referred to as the adiabatic approximation. The approximation inherently assumes that if the electrons are initialized in state $\psi_n(\mathbf{r}, \mathbf{R}(\mathbf{t} = \mathbf{0}))$, they will remain in the same eigenstate as they adiabatically evolve to changes in the internuclear separation distance as $\psi_n(\mathbf{r}, \mathbf{R}(\mathbf{t}))$. That is to say, as the nuclei slowly approach one another, the electronic wavefunction evolves adiabatically to remain in the the same eigenstate, albeit one whose energy is changing with internuclear separation distance. This is analogous to a ground state particle in a box whose boundaries are slowly widening in time. As long as the expansion of the box is slow enough, the particle will remain in the ground state even as the energy of that ground state, which depends on the boundaries of the box, changes.

However, this need not always be the case, and there may be situations in which adiabaticity is broken as the electrons are unable to respond quickly enough to sudden changes in internuclear separation distance. In our particle-in-a-box analog, this resembles a case where the box is suddenly yanked to a new distance, which suddenly causes the 'pre-yank' wavefunction to be re-expressed in the basis set of the 'post-yank' box, potentially leading to non-ground state components in the wavefunction. While a full treatment of Born-Oppenheimer breakdown is provided elsewhere [Mar05], a casual analysis will be provided here.

To estimate when non-Born Oppenheimer effects become important to first order, we can consider the neglected terms in Eqn. 2.18, and apply first order perturbation theory using the Born-Oppenheimer electronic and nuclear wavefunctions, as

$$V_{n,v,J} = \sum_{v',J',n'} \frac{|\left\langle \chi^{n'}_{v',J'}(\mathbf{R})\psi_{n'}(\mathbf{r},\mathbf{R})|\hat{V}|\psi_n(\mathbf{r},\mathbf{R})\chi^{n}_{v,J}(\mathbf{R})\right\rangle|^2}{E_{n,v,J} - E_{n',v',J'}} \tag{2.29}$$

where $\hat{V}$ is the operator associated with neglected terms in Eqn. 2.18 [Voo15].

Qualitatively, we can see that the non-Born-Oppenheimer terms become more significant when the energy spacing between Born-Oppenheimer surfaces $E_{n,v,J} - E_{n',v',J'}$ is small, as occurs at so-called "avoided crossings", as shown in Fig. 2.2. In theory, the non-adiabatic terms, even when BO states are spaced closely in energy, may still be small if the matrix elements in Eqn. are near-zero; however, evaluating such matrix elements is a more difficult enterprise and not considered here.

Typically when $E_{n,v,J} - E_{n',v',J'}$ is small, the individual Born-Oppenheimer electronic surfaces, $\phi_n(R)$, are no longer accurate, and couplings can occur from one Born-Oppenheimer surface to the other. Here, the 'true' electronic wavefunctions, and thus the electronic potential energy surfaces the nuclei experience, will be a linear combination of Born-Oppenheimer terms. Therefore, if a system begins in a particular Born-Oppenheimer eigenstate, as the internuclear separation distance changes and an avoided crossing is approached, the state can be re-projected into another Born-Oppenheimer state, if energy conservation permits such an event given the collision energy of the system.

To first order, the probability of transfer can be approximated by Landau-Zener theory [BD80, Hal13] as

$$P_{a\to b} = \exp(-2\pi\omega_{ab}\tau) \tag{2.30}$$

where ω_{ab} is the effective Rabi frequency between the states, which is set by other parameters related to their coupling strength, and τ is a measure of the interaction time, classically thought of as how long it takes the nuclei to pass through the avoided crossing. However, a set of more sophisticated techniques is often used for more accurate predictions of transfer probabilities [ZD88, HB76].

The two surfaces that are coupled together may have observably distinct properties, such as which atom within the two body system contains a majority of the system charge, and thus these nonadiabatic transitions can leading to physically observable phenomena such as charge-exchange collisions and chemical reactions.

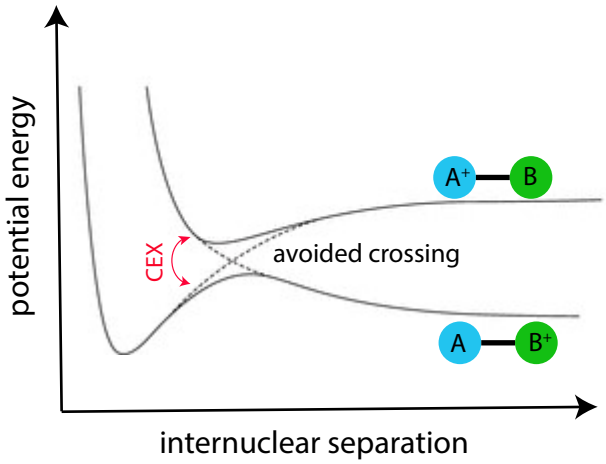

Figure 2.2: Born-Oppenheimer Breakdown

When the energy spacing between Born-Oppenheimer surfaces is small, non-adibatic components of the molecular Hamiltonian can mix the eigenstates together, leading to observable phenomena such the two-body charge-exchange reaction in this example where $A^+ + B \rightarrow A + B^+$. Here the potentials with the dotted lines are the diabatic BO potentials (assumed to be of different symmetries) while the solid lines show adiabatic potentials in which this degeneracy has been lifted due to non-adiabatic perturbations.

2.4 Collision cross-sections

Observing collisions between atoms and ions is the cornerstone of much of the work contained in this thesis, and thus, accurate calculations of collisional cross-sections are paramount to interpreting experimental results. In the range of temperatures explored here, there are a host of methods that may be employed for this purpose, ranging from highly sophisticated electronic structure calculations to simple classical models. Often, there is a compromise between accuracy and computational effort, and consequently, the approach taken will depend on the constraints of the problem of interest. Here, we will focus on a series of classical and semiclassical models that can be employed to estimate these cross-sections.

2.4.1 Elastic collisions

In general, an elastic collision is defined as a collision where total kinetic energy is conserved. Such collisions are crucial in processes such as atom-ion translational sympathetic cooling and low-temperature evaporative cooling. Semiclassical models may be used to understand the collisional cross sections of such events.

For a given atom-ion system, the potential between the two nuclei is derived from a central force, and thus angular momentum is conserved, according to Noether's thereom. This means that the scattering wavefunction can be expanded in eigenfunctions of the total nuclear orbital angular momentum operator, known as partial waves.

Recalling the radial Schrödinger equation for a two-body system in Eqn. 2.23, the long-range asymptotic behavior of $S_v^p(R)$ can be approximated [SN11] as

$$u_\ell(R) \sim \sin(kR - \frac{\ell\pi}{2} + \eta_\ell(k)) \tag{2.31}$$

where $S_v^p(R) = u_\ell(R)/R$, k sets the incoming kinetic energy as $E = \frac{\hbar^2 k^2}{2\mu}$, and $\eta_l(k)$ is the phase shift of the ℓ^{th} partial wave.

Using the partial wave expansion, the total elastic cross section, σ_{el}, of a scattering event is given as [SN11]

$$\sigma_{el} = \frac{4\pi}{k^2} \sum_{l=0}^{\infty} (2\ell + 1) \sin^2 \eta_\ell(k) \tag{2.32}$$

Thus, the problem of determining the elastic cross section is equivalent to the problem of determining the phase shifts for different partial waves by solving the radial Schrödinger equation. For the systems in this work, we can assume the scattering potential to be dominated by the standard C_4 atom-ion interaction (see Sec. 2.4.3).

There are a variety of approximation techniques for calculating the required phase shifts. In the regime of most interest in this work, several partial waves are accessible. The typical approach is to approximate the elastic cross section by splitting our partial wave contributions into two general regimes and making different approximations for the phase shifts in each.

The first general regime is for partial waves with $\ell < \ell_{max}$ where ℓ_{max} is defined as the maximum angular momentum the colliding pair can have and still reach short range. ℓ_{max} is set by the collision frame energy and the corresponding centrifugal barrier height and is given as (see Sec. 2.4.3)

$$\ell_{max} = \frac{(8\mu^2 C_4 E)^{1/4}}{\hbar} \tag{2.33}$$

For partial waves with $ell < \ell_{max}$ the colliding pair will reach short range, and thus the corresponding phase shift will be sensitive to details of the short range intermolecular potential. In general, these features are difficult to calculate accurately, thus it is standard to set $\sin(\eta_l)^2 \approx 1/2$ in this range [CD00].

On the other hand, for $\ell > \ell_{max}$, the partial waves cannot scale the centrifugal barrier and are assumed to be insensitive to the short-range features of the molecular potential. Therefore, phase shifts in this regime are assumed to be solely dependent on the long-range form of the atom-ion interaction. The WKB approximation can be employed [CD00,DMW58] to estimate these phase shifts as

$$\eta_\ell^{WKB} \approx -\frac{\mu}{\hbar^2}\int_{R_0}^{\infty} \frac{V(R)}{\sqrt{k^2 - (\ell+1/2)^2/R^2}} \tag{2.34}$$

where R_0 is the classical turning point of the incoming particle.

For the standard C_4 potential used in this work, the above integral can be evaluated exactly; however, an estimate for the classical turning point must be made. Utilizing the approximation presented in Ref. [CD00], we obtain

$$\eta_\ell^{WKB} \approx \frac{\pi\mu^2 C_4}{4\hbar^4}\frac{E}{\ell^3} \tag{2.35}$$

Further, for $\ell > \ell_s$, we will assume $\sin(\eta_\ell) \approx \eta_\ell$ [CD00].

Using these results the total inelastic cross section can be estimated by splitting the sum in Eqn. 2.32 into two regions. For $\ell \approx \ell_{max}$, the above treatment for either regime is really not appropriate, so for now, we will leave the angular momentum value at which we choose

to split our sum flexible and define this quantity as ℓ_s. This will give us some wiggle room to account for errors in our treatment by varying ℓ_s.

The total elastic cross section can now be expressed as

$$\begin{aligned}
\sigma_{el} &= \frac{4\pi}{k^2}\sum_{\ell=0}^{\infty}(2\ell+1)\sin^2\eta_\ell(k) \\
&= \frac{4\pi}{k^2}\sum_{\ell=0}^{\ell_s-1}(2\ell+1)\sin^2\eta_\ell(k) + \frac{4\pi}{k^2}\sum_{\ell_s}^{\infty}(2\ell+1)\sin^2\eta_\ell(k) \\
&\approx \frac{4\pi}{k^2}\left(\sum_{\ell=0}^{\ell_s-1}(2\ell+1)\frac{1}{2} + \int_{\ell_s}^{\infty} 2\ell(\eta_\ell^{WKB})^2 d\ell\right) \\
&= \frac{4\pi}{k^2}\left(\frac{\ell_s^2}{2} + \frac{1}{2}\frac{\pi^2\mu^2C_4^2E^2}{16\hbar^8}\frac{1}{\ell_s^4}\right) \\
&= \frac{2\pi}{k^2}\ell_s^2(1+(\eta_{\ell=\ell_s}^{WKB})^2)
\end{aligned} \tag{2.36}$$

Quantum mechanical calculations [CD00] have demonstrated that a reasonable value of ℓ_s is one such that $\eta_{\ell_s}^{WKB} = \pi/4$, which yields $\ell_s = ((\mu^2C_4E)/\hbar^4)^{1/3}$.

Finally, the total elastic cross section can be obtained as

$$\sigma_{el} \approx \left(\frac{\pi^3\mu C_4^2}{\hbar^2}\right)^{1/3}\left(1+\frac{\pi^2}{16}\right)E^{-1/3} \tag{2.37}$$

2.4.2 Inelastic scattering

Many of the phenomena of interest studied in this work, such as internal molecular sympathetic cooling, charge exchange, etc., are inelastic processes where the kinetic energy of the collision complex is not conserved. Instead a portion of this energy is either released or absorbed into an inelastic process, such as internal state conversion or charge-exchange.

Estimates of the cross-section of these inelastic events can be performed most accurately by solving the radial Schrödinger equation numerically as is done with the close-coupling method [FSL91]. However, a far simpler semiclassical treatment can also be used as a rough estimate, similar to that presented in the Sec. 2.4.1.

In order for an inelastic events to occur, the collision complex must clear the angular momentum barrier and reach short range. For a fixed collision complex energy E and assuming a C_4 potential, the maximum angular momentum than can be possessed (see Sec. 2.4.3) is

$$\ell_{max} = \frac{(8\mu^2 C_4 E)^{1/4}}{\hbar} \tag{2.38}$$

We can make the same approximation as for the elastic cross-section that for $\ell < \ell_{max}$, $\sin(\eta_\ell)^2 \approx 1/2$; however, diverging from our elastic treatment, we will assume that higher partial waves do not contribute to the cross-section whatsoever and additionally we will modify our cross-section formula by a constant factor [BV12]. Then, the total inelastic cross-section can be estimated as

$$\begin{aligned} \sigma_{ie} &= \frac{2\pi}{k^2} \sum_{\ell=0}^{\ell_{max}-1} (2\ell+1)\sin(\eta_\ell)^2 \approx \frac{\pi}{k^2}\ell_{max}^2 \\ &= \pi \left(\frac{2C_4}{E}\right)^{1/2} \end{aligned} \tag{2.39}$$

for the standard C_4 collision. Of course, if a non-C_4 interaction is present in the system, such as a C_3 interaction, ℓ_{max} may be recalculated, as discussed in the next section, and then the above summation may be appropriately updated.

2.4.3 Capture theory models

For the above calculations, the calculation of ℓ_{max} will depend on the particular interaction between the atom and ion in the system. Such interactions can become complicated if electronic excitations are involved that create non-spherically symmetric electron distributions that give rise to higher order electrostatic interactions.

Capture theory models are a convenient tool to estimate the rates at which such collisions occur. These models assume that the long-range form of molecular potentials govern whether a collision will occur or not, and further, that the probability of an inelastic process occurring once a short-range collision occurs is unity. In reality, short-range features

of a molecular potential (coupling strengths between Born-Oppenheimer surfaces, etc.) can produce a probability less than unity (see Sec. 2.3.2 and Ref. [BV12]), but capture models provide a convenient upper bound on the rate at which such processes can occur.

Long-range potentials are typically described using a power-low expansion

$$V(R) = \sum_n \frac{-C_N}{R^N} \tag{2.40}$$

where the C_N coefficients are determined by the nature of the atom-ion interaction responsible for the potential term. For example, the C_4 interaction, known as the Langevin interaction, is caused by an approaching monopole polarizing the neutral atom of interest, thereby creating a induce dipole-monopole attractive interaction.

The induced dipole moment of a neutral atom placed within the field of a singly charged monopole is determined from an atom's polarizability as

$$\begin{aligned} \vec{p} &= \alpha \vec{E} \\ &= \frac{e}{4\pi\epsilon_0}\frac{\alpha}{R^2}\hat{r} \end{aligned} \tag{2.41}$$

where $\vec{p}$ is the atomic dipole moment and α is the atomic polarizability. This leads to a separation distance dependent atom-ion potential energy of

$$\begin{aligned} V(R) &= -\int_0^R E(\vec{R}') \cdot dp(\vec{R}') \\ &= -\int_0^{E(R)} E(R')\left[\alpha dE(R')\right] \\ &= -\frac{1}{2}\alpha[E(R)]^2 \\ &= -\frac{1}{2}\frac{e^2}{(4\pi\epsilon_0)^2}\frac{\alpha}{R^4} \\ &= -\frac{C_4}{R^4} \end{aligned} \tag{2.42}$$

where R is the atom-ion internuclear separation distance at which the potential is to be calculated and $C_4 = \frac{\alpha}{2}\frac{e^2}{(4\pi\epsilon_0)^2}$. For most cases, it is only necessary to consider the first one or two leading terms in Eqn. 2.40, as high order terms will generally have a minimal effect.

Once the appropriate long-range potential has been derived, capture theory can be applied to derive collision cross sections. In the capture theory model, the collision complex can be assumed to reach short range and collide if it is able to clear any potential energy barriers (Fig. 2.3).

Where do these barriers come from? In addition to the long-range atom-ion interaction, centrifugal barriers in the collision complex exist that depend on the orbital angular momentum of the system, ℓ, where $\hbar\ell = \mu v b$, where μ is the reduced mass of the complex, v is the collision velocity, and b is the collision impact parameter. As we will see below, we can place restrictions on these parameters of the system to ensure the complex reaches short-range.

Considering both the centrifugal barrier and atom-ion attractive potential, the total effective potential [CD00] is given as

$$V_{eff}(R) = \frac{\hbar^2 \ell^2}{2\mu R^2} - \frac{C_N}{R^N} \tag{2.43}$$

A short-range event will occur, at a given collision energy, if the incoming particles approach each other under a critical angular momentum $\hbar\ell_{max} = \pi v b_{max}$, where b_{max} is the critical impact parameter associated with ℓ_{max}. Assuming hard-sphere collisions, b_{max} can be used to calculate an energy-dependent cross section $\sigma(E) = \pi b_{max}^2(E)$, which can be averaged over the collision energy distribution of the sample to yield collision rates. The procedure for determining the cross-section will go as follows: **(1)** Determine $\ell_{max}(E)$, **(2)** Determine $b_{max}(E)$ from (1), **(3)** calculate the cross-section as $\pi b_{max}^2(E)$.

The first step in determining $\ell_{max}(E)$ is determining the height of the energetic barrier. The separation distance at which the barrier maximum occurs, R_{max}, can be found by setting the derivative of Eqn. 2.43 to 0, resulting in

$$R_{max} = \left(\frac{N C_N \mu}{\hbar^2 \ell^2}\right)^{\frac{1}{N-2}} \tag{2.44}$$

which can be used to find the height of the potential barrier, $V_{max}(R_{max})$, as

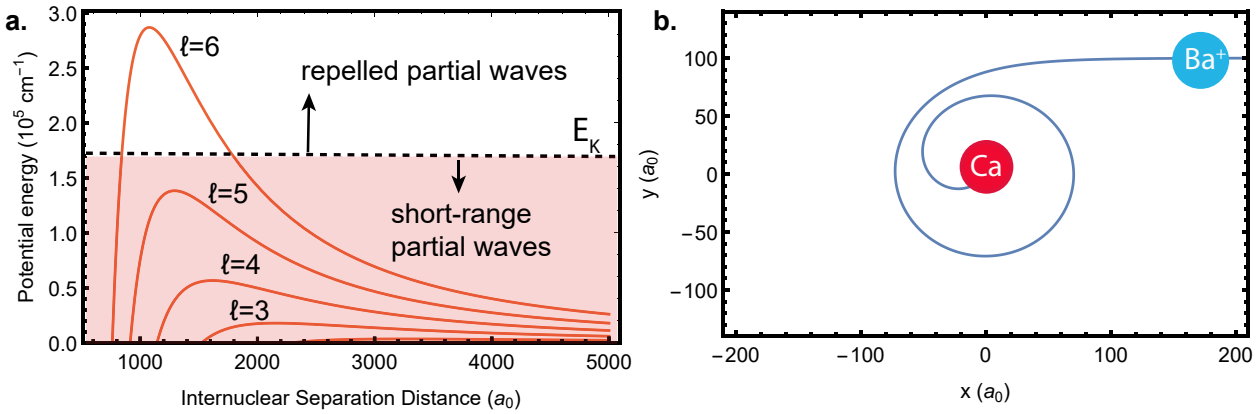

Figure 2.3: Capture theory models

(a) Molecular potentials at various ℓ values for a prototypical C_4 potential. For $\ell > 6$, the incoming kinetic energy, E_k is no longer large enough to scale the centrifugal barrier, and thus only partial waves with angular momenta below this value will reach short range. **(b)** Calculated trajectory for a prototypical collision event in which $\ell < \ell_{max}$. As can be seen in the plot, the collision pair spiral inwards towards each other until a collision occurs.

$$V_{max} = \left(\frac{\hbar^2 \ell^2}{\mu}\right)^{\frac{N}{N-2}} (NC_N)^{-\frac{2}{N-2}} \left(\frac{1}{2} - \frac{1}{N}\right) \tag{2.45}$$

When the incoming kinetic energy of the complex, $E \geq V_{max}$ the collision pair will reach short range. Therefore, at a given collision energy, ℓ_{max} can be calculated by setting $E = V_{max}$ and inverting the subsequent equation as

$$\begin{aligned} E &= \left(\frac{\hbar^2 \ell_{max}^2}{\mu}\right)^{\frac{N}{N-2}} (NC_N)^{-\frac{2}{N-2}} \left(\frac{1}{2} - \frac{1}{N}\right) \\ \rightarrow \ell_{max} &= \frac{1}{\hbar} \left(\frac{2E}{N-2}\right)^{\frac{N-2}{2N}} (C_N)^{\frac{1}{N}} (\mu N)^{1/2} \end{aligned} \tag{2.46}$$

With this in hand, we can use $\ell_{max} = \mu v b_{max}$ and $E = \mu v^2/2$ to calculate $\sigma(E)$ as

$$\begin{aligned} \sigma(E) &= \pi [b_{max}(E)]^2 \\ &= \pi N \left(\frac{1}{N-2}\right)^{\frac{N-2}{N}} \left(\frac{C_N}{2E}\right)^{\frac{2}{N}} \end{aligned} \tag{2.47}$$

Lastly, the collision rate, $k(E)$, which is separate quantity from the cross-section, is given as $k(E) = \sigma(E)v\rho$ where ρ is the scattering center density [Swi62] (taken to be the number density of the atom cloud in this work).

Experimentally, $k(E)$ is an common quantity to consider since both the collision rate and the collision energy are convenient experimental parameters to measure/tune in the lab [Ebe16, PMW18]. As seen from Eqn. 2.47, the functional form of $k(E)$ can be used to backtrack N, the power of the dominant long-range potential in the complex, yielding valuable insight into the physical system.

Physically, the scaling of $k(E)$ depends primarily on two competing factors. Firstly, $k(E) \propto \sigma(E)$, and in general, the cross-section is a monotonically decreasing function of E. The larger kinetic energy of the collision complex, the smaller the impact parameter of the collision must be in order for the attractive atom-ion force to be able to induce an inwardly spiraling collision, as shown in Eqn. 2.47. However, at the same time $k(E) \propto v \propto E^{1/2}$. Essentially, the larger E is the larger v is, and thus, the more scattering centers a particular particle will pass through in a given unit of time.

These two effects cancel out exactly for the C_4 interaction, leading to an energy-independent collision rate. However, for inverse power law potentials with $N < 4$, $\sigma(E)$ decreases abruptly enough as a function of energy to dominate over the collision velocity enhancement factor ($v = (2E/\mu)^{1/2}$), causing $k(E)$ to decrease with increasing collision energy. On the other hand, for $N > 4$, the collision velocity factor dominates over $\sigma(E)$, which has reduced energetic sensitivity in this regime, resulting in cross-sections that increase with increasing collision energy.

Further, we can average $k(E)$ over the energy distribution of the sample to get a better sense of a rate that would be measured experimentally. The simplest case to consider is a collision energy set by a standard Maxwell-Boltzmann distribution at a temperature, T, as

$$k_T = \int_0^\infty P(E)\sigma(E)dE \tag{2.48}$$

where $P(E)$ is the normalized Maxwell-Boltzmann probability energy distribution, given as

$$P(E) = 2\sqrt{\frac{E}{\pi}}\left(\frac{1}{k_B T}\right)^{3/2} e^{-\frac{E}{k_B T}} \tag{2.49}$$

However, in the atom-ion systems considered in this thesis, a Maxwell-Boltzmann energy distribution is often too simplistic and in general one needs to consider energy distributions that include effects such as micromotion interruption [CSH14, RW17] and ion-ion heating [CSR13, SDC16] for the most accurate collision-rate calculations. Lastly, while we have only considered attractive potentials thus far, the sign of the C_N coefficients can also lead to repulsive potentials in certain situations, precluding short-range collisions from occurring.

CHAPTER 3

Ion trapping theory

In order to perform high precision optical manipulations on charged species, these particles must first be sufficiently spatially localized. The standard protocol for achieving such localization is through a technique known as ion trapping. Ion trapping theory is well-documented in the literature [BMB98], and only a brief conceptual overview will be presented in this work.

3.1 Motion within an ion trap

3.1.1 Time dependent trapping potentials

Within ion traps, electromagnetic fields are utilized to create a confining potential that guides charged species to an effective potential minimum. The most natural potential to consider that could match such conditions is a three-dimensional harmonic oscillator who potential is given as

$$V(x, y, z) = \alpha x^2 + \beta y^2 + \gamma z^2 \tag{3.1}$$

For a typical trapping potential, the coefficients of the quadratic terms would all need to be positive. However, as echoed in Earnshaw's theorem [Ear48], the electrostatic arrangement of particles needed to create such a potential would also need to satisfy Laplace's equation as

$$\nabla^2 V(x, y, z) = 2(\alpha + \beta + \gamma) = 0 \tag{3.2}$$

which implies that α, β, and γ cannot all have positive values, and by extension, trapping potentials cannot exist in all three dimensions simultaneously when using static fields.

However, we can 'cheat' by using time-varying fields to overcome this hurdle and provide

a three-dimensional restoring force, under certain conditions. However, before dabbling in time-dependent potentials, the appropriate electrode geometry for the ion trap must be selected. Electrodes arranged in a hyperbolic geometry are capable of producing a potential that strongly resembles that presented in Eqn. 3.1, and thus are of considerable practical interest within the ion trap community. Electrode geometries that resemble the idealized hyperbolic configuration but permit a larger degree of optical access, such as the four-rod linear quadrupole trap (LQT) utilized in this work, can also produce similar potentials while offering other experimental conveniences, and therefore the remainder of this discussion will assume a LQT geometry.

The electrostatic potential produced from electrodes arranged in the hyperbolic geometry is given as

$$\Phi(r,z) = \frac{\Phi_0}{r_0^2}(r^2 - z^2) \tag{3.3}$$

where Φ_0 is a scale-factor constant.

If a sinusoidally-varying voltage is placed on one pair of rods while a constant voltage is placed on the other pair, the potential then becomes

$$\Phi(x,y,t) = \frac{V_{rf}\cos(\Omega t) + U_{DC}}{2r_0^2}(x^2 - y^2) \tag{3.4}$$

where V_{rf} is the amplitude of the time-varying radiofrequency (rf) voltage, Ω is the rf oscillation frequency, U_{DC} is the DC voltage, and r_0 is the distance between the rods and the trap center. Trapping in the z-dimension will be performed using purely static fields and will be discussed later, with the proceeding section focusing on the time-dependent trapping present in the x and y dimensions.

Newton's law can be used to solve for the equations of motion of an ion placed within this potential as

$$\vec{\mathbf{F}} = m\ddot{\mathbf{r}} = Q\nabla\Phi(\mathbf{r},t) \tag{3.5}$$

where $Q(m)$ is the charge (mass) of the ion.

For the x-dimension this leads to

$$\ddot{x} = \frac{Q}{mr_0^2}(V_{rf}\cos(\Omega t) + U_{DC})x \tag{3.6}$$

and correspondingly for the y-dimension

$$\ddot{y} = -\frac{Q}{mr_0^2}(V_{rf}\cos(\Omega t) + U_{DC})y \tag{3.7}$$

These equations can be simplified by making the following substitutions: $a_x = -a_y = \frac{4qU_{DC}}{mr_0^2\Omega^2}$, $q_x = -q_y = \frac{2qV_{rf}}{mr_0^2\Omega^2}$, and $\tau = (t\Omega)/2$, yielding the following Mathieu differential equation

$$\ddot{u_i} + (a_i - 2q_i\cos(2\tau))u_i = 0 \tag{3.8}$$

where the u_x and u_y dimensions are defined by the pair of orthogonal unit vectors that point from the center of one rod to the center of its diagonally opposed counterpart (Fig. 1B in Ref. [BMB98]).

Only certain values of a and q will produce stable trajectories, resulting in the LQT stability regions presented in Fig. 3.2. Since the underlying Mathieu a and q-parameters depend on the ion mass, V_{rf}, and Ω, the stability regions will depend on these parameters as well, meaning these parameters can be varied to control which species are stable within the trap, thereby allowing the LQT to serve as a mass filter.

The resulting trajectory for an ion within an ion trap in both one and two dimensions is shown in Fig. 3.1 for particular trap parameters. In general, ion motion can be decomposed into oscillations of two kinds - a slow oscillation at the secular frequency of the trap (secular motion) and a faster oscillation at the driving frequency of the trap (micromotion).

As seen in the stability diagrams in Fig. 3.2, for low q-values (assuming $U_{DC} = 0$), ion motion is generally stable, and in this regime, the trajectories more closely resemble that of a harmonic oscillator. However, at high q-values, the effects of micromotion become more apparent, with trajectories generally becoming unstable when $q \gtrsim 0.908$.

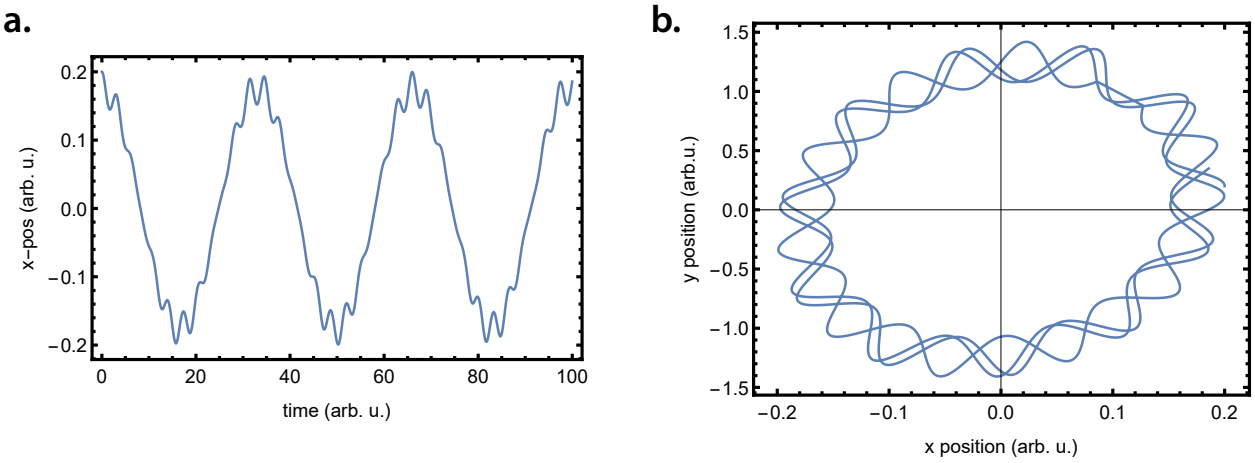

Figure 3.1: Paul trap trajectories

(a) Radial dimension trajectory for an ion held within a 3D Paul trap under standard stable ion trapping parameters. The ion's motion can be decomposed into oscillations of two types - a slower secular oscillation and a faster micromotion at the trap drive frequency.**(b)** A parametric plot of the x-y motion of a trapped ion under standard trapping conditions.

3.1.2 Low q limit solution

A approximate analytical solution to Eqn. 3.5 can derived [LL82] when in the low-q limit where $q \ll 1$. In this regime, we can consider the total ion motion as the sum of the respective micromotion ($u_m(t)$) and secular motion ($u_s(t)$) components as $u(t) = u_s(t) + u_m(t)$. In this regime, the amplitude of secular motion dominates over the micromotion amplitude (meaning $u(t) = u_s(t) + u_m(t) \approx u_s(t)$); whereas, the acceleration of the fast time-scale micromotion dominates over the secular acceleration (meaning $\ddot{u}(t) = \ddot{u}_s(t) + \ddot{u}_m(t) \approx \ddot{u}_m(t)$). Using these approximations, the ion equation of motion presented in Eqn. 3.6 ($U_{DC} = 0$) can be solved as

$$\begin{aligned} \ddot{u}_s(t) + \ddot{u}_m(t) &= \frac{Q}{mr_0^2} V_{rf} \cos(\Omega t)(u_s(t) + u_m(t)) \\ \ddot{u}_m(t) &\approx \frac{Q}{mr_0^2} V_{rf} \cos(\Omega t) u_s(t) \\ \rightarrow u_m(t) &= -\frac{QV_{rf}}{mr_0^2\Omega^2} \cos(\Omega t) u_s(t) \end{aligned} \tag{3.9}$$

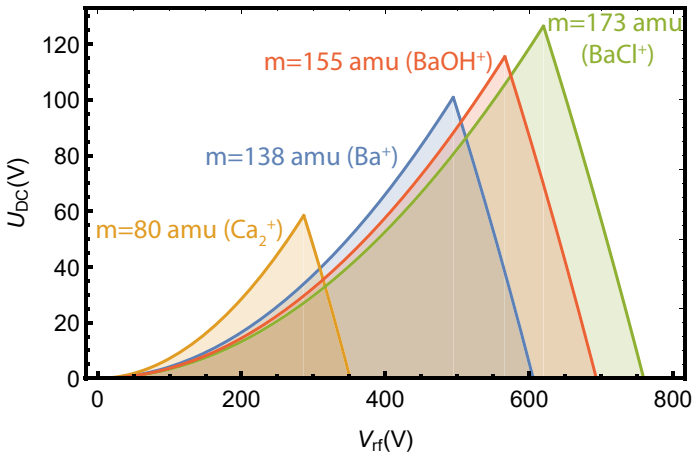

Figure 3.2: Ion trap stability diagrams

Regions of stability as a function of V_{rf} and Ω for various ions studied in this thesis. When the Matheui-q paramter is greater than ≈ 0.908, the trajectories of all ions are unstable.

where the last equality was obtained by assuming the secular motion was slowly varying over a micromotion oscillation period.

With this expression for micromotion in hand, one can then back substitute into the ion equation of motion and average over one micromotion oscillation period to obtain an expression for the secular motion as

$$\begin{aligned} \ddot{u}(t) &\approx \frac{Q}{mr_0^2} V_{rf}\cos(\Omega t)(1 - \frac{Q}{mr_0^2\Omega^2} V_{rf}\cos(\Omega t))u_s(t) \\ &\rightarrow \langle \ddot{u}(t)\rangle_{1/\Omega} \approx \langle \ddot{u}_s(t)\rangle_{1/\Omega} = -\frac{Q^2V_{rf}^2}{2m^2r_0^4\Omega^2}u_s(t) \\ &= -\omega_s^2 u_s(t) \end{aligned} \tag{3.10}$$

which implies the secular motion is simply harmonic motion at the pseudopotential oscillation frequency $\omega_s = q\Omega/(2\sqrt{2})$. Putting our approximate expressions for micromotion and secular motion together, we see that

$$u(t) = u_m(t) + u_s(t) = A\cos(\omega_s t)(1 - \frac{q}{2}\cos(\Omega t)) \tag{3.11}$$

here A is a constant that specifies the initial displacement of the ion from the trap null.

A few general observations can be made from this approximation. Firstly, the amplitude of micromotion scales with the amplitude of secular motion, i.e. at the outermost points of secular trajectory, at the secular potential turning points, the amplitude of micromotion is greatest.

The average kinetic energy of the ion can be approximated [BMB98] in the low-q limit as

$$\langle E_{kin} \rangle = \frac{1}{2} m \langle \dot{u}(t) \rangle^2 \approx \frac{1}{4} A^2 (\omega_s^2 + \frac{1}{8} q_i^2 \Omega^2) \tag{3.12}$$

with the first (second) term corresponding to the energy of the secular motion (micromotion) (these terms are approximately equal in this regime).

Correspondingly, the average energy of the ion can be tuned by controlling the secular amplitude, and thus also the micromotion energy, of the ion, either by creating an ion sample with a tunable radial spread or by introducing a stray electric field into the system that offsets the ion sample from the trap null. Such considerations are important to hybrid trapping experiments where ion energy is tuned as a means to scan the collision energy of atom-ion interactions, as to be discussed later in this thesis.

Also of note, the secular frequency is mass-dependent and correspondingly, oscillating electric fields can be introduced into the trap in order to secularly excite certain masses, pumping energy into these species until they are ejected from the LQT. This is yet another feature that permits the quadrupole trap to function secondarily as a mass filter, which will be of use for several experiments studied in this work.

3.1.3 General solution

Outside of the low-q regime, more general solutions can be found to that Mathieu equation that possess more frequency components than the simple secular model described above. These solutions are given generally [LBM03] as

$$u_j(t) = A_j c_j(a_j, q_j, \tau) + B_j s_j(a_j, q_j, \tau) \tag{3.13}$$

where A_j and B_j are amplitude coefficients and $c_j(a_j, q_j, \tau)$ and $s_j(a_j, q_j, \tau)$ are the even and odd Mathieu functions, respectively. The Mathieu functions themselves are periodic functions, and thus, their sum can also be expanded in a Fourier series, for example [CSH14] as

$$u_j(a_j, q_j, \tau) = \sum_{n=-\infty}^{\infty} C_{2n} \left(b_n e^{i(\beta_j + 2n)\tau} + c_n e^{-i(\beta_j + 2n)\tau} \right) \tag{3.14}$$

where C_{2n}, b_n, and c_n are expansion coefficients. The $n = 0$ term corresponds to the harmonic-oscillator-like, secular motion trajectory discussed earlier, and the higher order terms collectively give rise to the micromotion component. In general, the motion will be a linear combination of oscillations at frequencies $\omega_{j,n} = (\beta_j + 2n)\Omega/2$. β_j in general is a complicated function of both a and q, but approximations of these frequencies can be derived to various degrees of accuracy. Generally speaking, in the j^{th} dimension [cTR06]

$$\beta_j \approx \sqrt{a_j - \frac{q_j^2(a_j - 1)}{a_j(a_j - 1)^2 - q_j^2} - \frac{q_j^4(5a_j - 7)}{32(a_j - 1)^3(a_j - 4)}} \tag{3.15}$$

although a more convenient, albeit less accurate, approximation is given as $\beta_j \approx \frac{1}{2}\Omega\sqrt{a_j^2 + q_j^2/2}$ [BMB98].

The trap depth, or the maximum amount energy an ion can obtain and still remain in the trap, can be approximated by calculating the secular energy in each dimension at the position of the trap electrodes (R_i), given as

$$D_i = \frac{1}{2} m \omega_{i,0}^2 R_i^2 \tag{3.16}$$

As considered thus far, the axial and radial ion motions are uncoupled; however, if the ion is subject to elastic collisions that mix the radial and axial energies, at an ion energy of $D_{min} = min\{D_x, D_y, D_z\}$, the particle will possess enough energy to clear its secular potential and be expelled from the trap.

3.1.4 Excess micromotion

If a stray DC electric field, $E_{DC,i}$, is present in the trap in the i^{th} dimension, the equilibrium position of the ion can be shifted off the trap null, leading to a new equilibrium position of

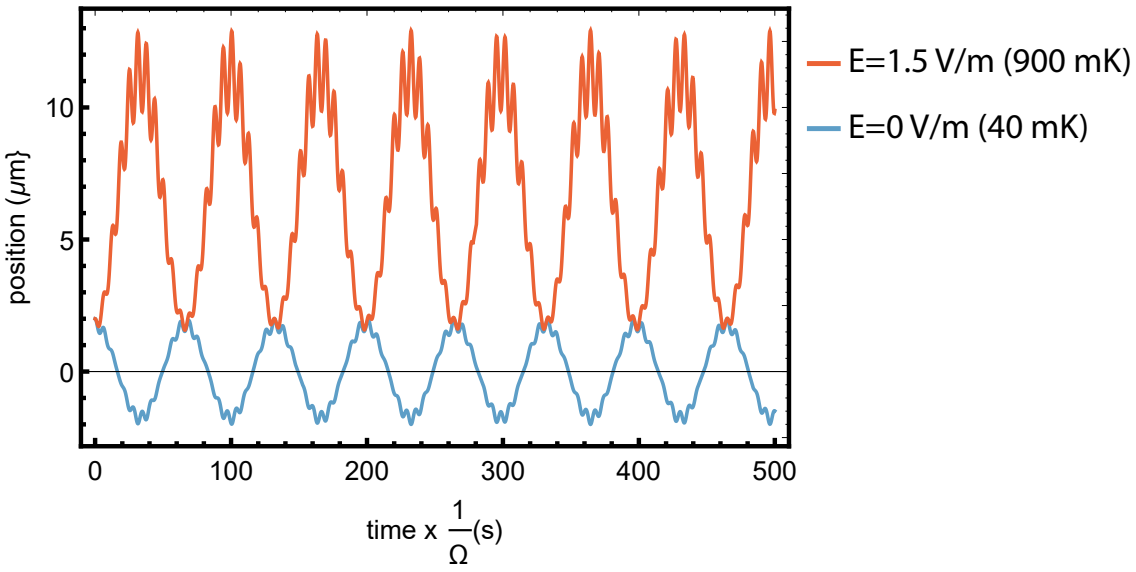

Figure 3.3: Excess micromotion trajectories

Radial dimension ion trap trajectories for cases in which both no offset electric field is applied and when a 1.5 V/m field is applied. When the offset electric field is present, the average kinetic energy of the ion increaes from 40 mK to 900 mK and the average ion position is shifted off the null of the trap

$$r_{0,i} = \frac{QE_{DC,i}}{m\omega_i^2} \tag{3.17}$$

To first approximation, this modifies the equation of motion of the ion as

$$r_i(t) = (r_{0,i} + A\cos(\omega_s t))(1 - \frac{q}{2}\cos(\Omega t)) \tag{3.18}$$

leading to a modified kinetic energy [BMB98] of

$$E_{KE} \approx \frac{1}{4}A^2(\omega_s^2 + \frac{1}{8}q_i^2\Omega^2) + \frac{1}{2}m(\frac{q\Omega}{2\sqrt{2}})^2 r_{0,i}^2 \tag{3.19}$$

The energy included in the last term is known as excess micromotion energy and posses a challenge to hyrbid-trapping experiments seeking to reach the ultracold regime ($\lesssim 1$ mK) [CGc12]. Technically, if the ion were a point-particle placed exactly on the trap null, there would be no excess micromotion energy. However, the non-zero spatial spread of the ion wavefunction

means some component of the ion will always reside off-axis, meaning some degree of excess micromotion energy is inevitable [CLC13]. While this minimized amount of excess micromotion energy is negligible for the experiments in this thesis, a much more problematic concern is electric fields that can force the ion to reside $\approx 10 - 100$ μm off the trap null, leading to excess micromotion energies on the order of ~ 10 K.

However, excess micromotion can be reduced by minimizing $r_{0,i}$ by superimposing DC voltages onto the trap electrodes that compensate for stray electric fields in the system. Fig. 3.3 displays trajectories for ions placed under identical trapping conditions except for an added offset electric field. As described above, the effect of the offset field is to displace the ion from the trap null, where it executes higher energy orbits.

However, another source of excess micromotion energy is phase mismatches between the rf voltage applied to different rods, due to differing cable lengths for example, which serve to effectively add an oscillating stray electric field that cannot be compensated for through DC shimming. This phase mismatching effect, along with imperfect DC compensation, typically provide the dominant sources of micromotion in most ion trap systems.

3.1.5 Axial localization

Thus far, our discussion has focused on radial confinement. In order to produce axial confinement, endcap electrodes are placed along the trap axis and are held at a constant DC voltage. When superimposed on the existing rf potential, a total trap potential is obtained as follows

$$\Phi(x,y,z) = \frac{V_{rf}\cos(\Omega t) + U_{DC}}{2r_0^2}(x^2 - y^2) - \frac{\kappa U_{ec}}{z_0^2}(z^2 - \frac{1}{2}(x^2 + y^2)) \tag{3.20}$$

In this model, the z-dimension contains a purely static trap at secular frequency $\omega_z = \sqrt{\frac{\kappa U_{ec}}{m z_0^2}}$. In addition to axial trapping, placing voltages on the endcap electrodes gives rise to additional anti-trapping radial terms, as seen in Eqn. 3.20. These terms give rise to a radial defocusing effect on the ion sample that downshifts the radial secular frequencies of the trap and thereby changes the spatial radial distribution of the ion cloud. Further, in certain

electrode geometries, projections of the rf trapping field may exist along the z dimension, meaning that axial micromotion will also exist [TRL12], although such effects are generally not considered to be significant at the ion energies studied in this work.

3.2 Ion crystal equilibrium positions

In general the equilibrium position of ions within the LQT can be solved for by minimizing the overall potential energy of the multi-ion system, which includes terms from the ion trap potential as well as ion-ion repulsion. For the simplest case of a 1D ion chain placed along the radial trap null, we can restrict ourselves to only considering the secular energy associated with the axial dimension. The total system potential energy for the N ions is given as

$$V(z_1, z_2, ...z_n) = \sum_{i}^{N} \frac{1}{2} m\omega_z^2 z_i^2 + \frac{Q^2}{8\pi\epsilon_0} \sum_{i,j,i\neq j}^{N} \frac{1}{|z_i - z_j|} \tag{3.21}$$

After enforcing the multivariate minimization condition $\frac{\partial d}{\partial z_i} V(z_1, z_2, ...z_n) = 0$, we are left with a set of coupled equations that can be solved to yield the equilibrium position of each ion. These equations are only analytically solvable for one or two ion systems; however numerical studies have concluded, for larger systems, that the separation between adjacent ions at the center of the chain scales approximately as $N^{-0.559}$ [Jam98]. Further, the above analysis can be extended to include more dimensions for situations in which two and three dimensional structures are studied where ion positions deviate from the trap null.

CHAPTER 4

Interaction of light with matter

4.1 Two level system

Much of the work completed in thesis involves coupling light with matter to achieve various objectives, whether that be laser-cooling, studying the reactivity of excited electronic quantum states, or other purposes. The simplest interaction one can imagine is light interacting with a two level system. For our purposes, the two level system can most relevantly be taken to represent different electronic states within an atom or molecule. Using a semiclassical analysis, the light source can be taken to be a plane wave that creates an electric field

$$\vec{E}(\vec{r},t) = \vec{E}_0 \cos(\omega t - \vec{k}\cdot\vec{r}) \tag{4.1}$$

where $\vec{E}_0$ is the electric field amplitude vector, ω_0 is the frequency of the electric field, and $\vec{k}$ is the field k-vector. The atomic energy levels can be said to be $E_2 = \hbar\omega_0$ and $E_1 = 0$, respectively.

In general we may say the total wavefunction, $|\Psi(t)\rangle$, of such a system can be expressed as

$$|\Psi(t)\rangle = c_1(t)e^{-iE_1t/\hbar}|\phi_1\rangle + c_2(t)e^{-iE_2t/\hbar}|\phi_2\rangle \tag{4.2}$$

where $|\phi_i\rangle$ are the stationary states of the system and $c_i(t)$ are the time-dependent state coefficients.

Now, we can solve Schrödinger's equation for the system

$$\hat{H}\left|\Psi(t)\right\rangle = i\hbar\frac{d}{dt}\left|\Psi(t)\right\rangle \tag{4.3}$$

where $\hat{H}$ is the Hamiltonian of the system. The Hamiltonian consists of two terms, a stationary component, $\hat{H}_0$, that gives rise to the static natural energy levels of the system and a time-dependent component related to the electric-dipole interaction

$$\hat{H}_I = -\vec{\mu}\cdot\vec{E}(\vec{r},t) \tag{4.4}$$

where $\vec{\mu} = e\vec{r}$ is the electric dipole moment operator for our system. At this point, we can make the assumption that the wavelength of our light source is much larger than the spatial dimension of the atomic wavefunction (certainly true for the 400-1000 nm radiation typically used in this thesis). Thus, making what is known as the electric dipole approximation, we can remove the spatial dependence of our electric field and only consider the time-dependent component as

$$\vec{E}(\vec{r},t) \approx \vec{E}(t) = \vec{E}_0\cos(\omega t - \phi_E) \tag{4.5}$$

where we can choose an initial time for the interaction such that $\phi_E = 0$. Further if we assume $\vec{E_0} = E_0\hat{x}$, then $-\vec{\mu}\cdot\vec{E}(t) = -exE_0\cos(\omega t)$

Equipped with this simplification, we can now express our Hamiltonian in matrix notation

$$i\hbar\frac{d}{dt}\begin{pmatrix} c_1(t)e^{-iE_1t/\hbar} \\ c_2(t)e^{-iE_2t/\hbar}\end{pmatrix} = \left(\begin{pmatrix} 0 & 0 \\ 0 & \hbar\omega_0\end{pmatrix} - E_0\cos(\omega t)\begin{pmatrix} V_{11} & V_{21} \\ V_{12} & V_{22}\end{pmatrix}\right)\begin{pmatrix} c_1(t)e^{-iE_1t/\hbar} \\ c_2(t)e^{-iE_2t/\hbar}\end{pmatrix} \tag{4.6}$$

where $V_{ij} = \langle\phi_i|ex|\phi_j\rangle$. Since x is an odd function and the stationary states are parity eigenstates, $V_{11} = V_{22} = 0$ and $V_{12} = V_{21}^*$, by symmetry.

The time derivatives in the above equations can be evaluated as

$$\begin{aligned}\frac{d}{dt}c_1(t)e^{-iE_1t/\hbar} &= \dot{c}_1(t) \\ \frac{d}{dt}c_2(t)e^{-iE_2t/\hbar} &= \left(\dot{c}_2(t) - \frac{iE_2}{\hbar}c_2(t)\right)e^{-iE_2t/\hbar}\end{aligned} \tag{4.7}$$

since $E_1 = 0$.

This allows us to reduce the Schrödinger equation to the following set of coupled differential equations

$$\begin{aligned} i\hbar\dot{c}_1(t) &= -E_0\cos(\omega t)V_{21}c_2(t)e^{-i\omega_0 t} \\ i\hbar\dot{c}_2(t)e^{-i\omega_0 t} &= -E_0\cos(\omega t)V_{12}c_1(t) \end{aligned} \tag{4.8}$$

Now we can substitute $\cos(\omega t) = \frac{e^{i\omega t}+e^{-i\omega t}}{2}$, leading to

$$\begin{aligned} i\dot{c}_1(t) &= -\frac{\Omega_{21}}{2}(e^{-i(\omega+\omega_0)t} + e^{i(\omega-\omega_0)t})c_2(t) \\ i\dot{c}_2(t) &= -\frac{\Omega_{12}}{2}(e^{i(\omega+\omega_0)t} + e^{-i(\omega-\omega_0)t})c_1(t) \end{aligned} \tag{4.9}$$

where we define the Rabi frequency $\Omega_{ij} = \frac{E_0}{2\hbar}\langle\phi_i|ex|\phi_j\rangle$. It is generally most convenient to solve the above equations under certain approximations. Namely, let us drop the terms rotating at $\omega+\omega_0$. In most cases of interest, we will be considering optical radiation sources at the $\sim$THz level under near resonant conditions ($\omega_0 \approx \omega$), so the $\omega-\omega_0$ terms will be relatively slowly rotating and thus more important for the dynamics we are considering (additionally, later we will see that the amplitude of higher frequency terms also is suppressed).

Using this so called rotating wave approximation (RWA), our differential equations become

$$\begin{aligned} \dot{c}_1(t) &= \frac{i\Omega_{21}}{2}(e^{i\Delta t})c_2(t) \\ \dot{c}_2(t) &= \frac{i\Omega_{12}}{2}(e^{-i\Delta t})c_1(t) \end{aligned} \tag{4.10}$$

where $\Delta = \omega - \omega_0$.

The first equation above can be substituted into the differentiated version of the second equation, leading to the following formula

$$\frac{d^2}{dt^2}c_2(t) + i\Delta\frac{d}{dt}c_2(t) + \frac{|\Omega|^2}{4}c_2(t) = 0 \tag{4.11}$$

Then using the Ansatz $c_2(t) = Ae^{-rt}$,this can be converted into the eigenvalue problem

$$\lambda^2 + i\Delta\lambda + \frac{|\Omega|^2}{4} = 0 \tag{4.12}$$

where the subscripts on the Rabi frequency are no longer needed as the magnitude of the quantity is now taken. This eigenvalue equation can be solved to yield the following solution

$$\lambda_\pm = i(-\Delta/2 \pm \sqrt{\Delta^2 + \Omega^2}) \tag{4.13}$$

yielding the general solution

$$c_2(t) = A(e^{\lambda_+ t} - e^{\lambda_- t}) \tag{4.14}$$

after enforcing the initial condition $c_2(0) = 0$. This solution can be plugged into Eqn. 4.10 to solve for $c_1(t)$ and combined with the initial condition $c_1(0) = 1$ to yield the final probability amplitude solutions

$$\begin{aligned} |c_2(t)|^2 &= \frac{|\Omega|^2}{|\Omega|^2 + \Delta^2}\left[\sin\left(\frac{\sqrt{|\Omega|^2 + \Delta^2}}{2}t\right)\right]^2 \\ |c_1(t)|^2 &= \frac{1}{|\Omega|^2 + \Delta^2}\left(|\Omega|^2\left[\cos\left(\frac{\sqrt{|\Omega|^2 + \Delta^2}}{2}t\right)\right]^2 + \Delta^2\right) \end{aligned} \tag{4.15}$$

The results for the excited state population are displayed in Fig. 4.1. As can be seen from the figure, the population oscillates between the ground and excited states at a frequency known as the generalized Rabi frequency $\Omega'(\Delta) = \sqrt{|\Omega|^2 + \Delta^2}/2$ in a process is known as Rabi-flopping. When exposed to radiation for $t_\pi = \pi/(2\Omega')$, the population reaches a maximum in the upper state and is said to undergo a "π-pulse". Also as a further justification for our RWA, if we had kept the higher frequency terms instead of the lower frequency terms in Eqn. 4.9 and defined $\Delta = (\omega_0 + \omega)$, the denominators in the above expressions would have been much greater, thereby making excitations due to these terms relatively small.

Further, as the laser detuning increases, the effective oscillation frequency also increases while the maximum excited state population decreases (as displayed in Fig. 4.1a).

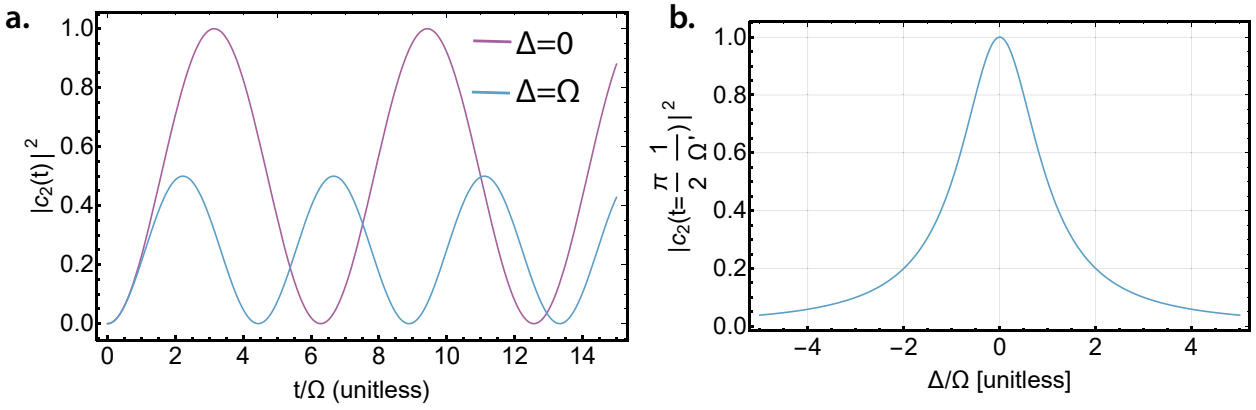

Figure 4.1: Rabi-flopping in a two-level system

(a) Rabi oscillations under two different radiation detuning settings ($\Delta = \Omega$ and $\Delta = 0$). With higher detunings, the maximum population fraction in the excited state decreases and the oscillation frequency increases. **(b)** Maximum excited state fraction, plotted after assuming a perfect π-pulse, as a function of radiation detuning. As the detuning increases, the π-pulse fraction decreases.

4.1.1 Optical Bloch Equations

While the above formalism is quite useful for many systems, it is known that excited states also decay through a process known as spontaneous emission. Although a true derivation of spontaneous emission requires quantization of the electric field, effectively its physical origin can be thought of as being caused by perturbations of the atomic energy level by vacuum electromagnetic modes (related to the zero-point energy of the vacuum field). These perturbations cause uncertainty in the energy of the atomic levels and therefore gives rise to an excited state lifetime through the Heisenberg uncertainty principle. A rigorous treatment of this process is given through the Jaynes-Cummings [JC63] model or Weisskopf-Wigner [Wei35] theory, yielding an effective spontaneous emission rate in a two-level system of

$$\Gamma = \frac{\omega_0^3 |V_{12}|^2}{3\pi\epsilon_0 \hbar c^3} \tag{4.16}$$

While for a single atom, the effect of spontaneous emission would be to interrupt coherent Rabi oscillations by demoting population to the ground state after each emission event, for

an ensemble of atoms, these emission events are uncorrelated. Therefore at short time scales, the collective sample would exhibit Rabi oscillations, but at longer timescales, uncorrelated emission events would causing damping of these oscillations to an eventual average steady-state excited state fraction of the system.

This process is usually studied under the density-matrix formalism. The density matrix operator is defined as

$$\hat{\rho} = |\Psi(t)\rangle \langle \Psi(t)| \tag{4.17}$$

where $|\Psi(t)\rangle = \sum_n c_n(t) |\phi_n\rangle$ (here the phase factors are absorbed into the coefficients for convenience). Therefore the individual matrix elements of the density matrix operator, ρ_{ij} are determined as

$$\rho_{ij} = \langle \phi_i | \hat{\rho} | \phi_j \rangle = c_i \cdot c_j^* \tag{4.18}$$

The evolution of the density matrix is determined by the Heisenberg equation of motion as

$$\frac{d}{dt}\hat{\rho} = \frac{i}{\hbar}[\hat{H}, \hat{\rho}] \tag{4.19}$$

For a two-level system

$$\hat{\rho} = \begin{pmatrix} |c_1|^2 & c_2 c_1^* \\ c_2^* c_1 & |c_2|^2 \end{pmatrix} \tag{4.20}$$

while as detailed above

$$\hat{H} = \hbar \begin{pmatrix} 0 & \frac{1}{2}\Omega_R e^{(i\Delta t)} \\ \frac{1}{2}\Omega_R^* e^{(-i\Delta t)} & \omega_0 \end{pmatrix} \tag{4.21}$$

This leads to the following set of matrix equations

$$\hat{\rho} = \begin{pmatrix} \frac{d}{dt}\rho_{11} & \frac{d}{dt}\rho_{21} \\ \frac{d}{dt}\rho_{12} & \frac{d}{dt}\rho_{22} \end{pmatrix} = \frac{i}{2} \begin{pmatrix} (\rho_{21}\Omega_R^* e^{-i\Delta t} - \rho_{12}\Omega_R e^{i\Delta t}) & e^{i\Delta t}(\rho_{11} - \rho_{22})\Omega_R \\ e^{-i\Delta t}(\rho_{22} - \rho_{11})\Omega_R & (\rho_{12}\Omega_R e^{i\Delta t} - \rho_{21}\Omega_R^* e^{-i\Delta t}) \end{pmatrix} \tag{4.22}$$

which in turn lead to the following set of differential equations

$$\begin{aligned} \frac{d}{dt}\rho_{11} &= \Gamma\rho_{22} + \frac{i}{2}(\tilde{\rho}_{21}\Omega^* - \tilde{\rho_{12}}\Omega) \\ \frac{d}{dt}\rho_{22} &= -\Gamma\rho_{22} + \frac{i}{2}(\tilde{\rho_{12}}\Omega - \tilde{\rho_{12}}\Omega^*) \\ \frac{d}{dt}\tilde{\rho}_{21} &= (i\Delta\tilde{\rho}_{21} - \frac{\Gamma}{2}) + \frac{i}{2}(\rho_{11} - \rho_{22})\Omega \\ \tilde{\rho}_{21} &= \tilde{\rho}_{12}^* \end{aligned} \tag{4.23}$$

where the Γ terms represent spontaneous emission in the system and have been added by hand, and the new variables $\tilde{\rho}_{21} = \rho_{21}e^{-i\Delta t}$ and $\tilde{\rho}_{12} = \rho_{12}e^{i\Delta t}$ have been defined for convenience.

It seems as though I have pulled a sleight of hand by introducing the spontaneous emission terms; however, this addition can be made more formal through the introduction of the relaxation matrix and the master Lindblad equation [BP03] although this formalism will not be discussed in this work.

To obtain the steady state excited state fraction, one simply needs to set all the time derivatives in Eqn. 4.23 to 0, yielding

$$\rho_{22} = \frac{|\Omega|^2}{\Gamma^2} \frac{1}{1 + 2\Omega^2/\Gamma^2 + 4\frac{\Delta^2}{\Gamma^2}} \tag{4.24}$$

This equation can be put in a more illuminating form by making a simple substitution. Let us define a quantity known as the saturation intensity as

$$I_s = \frac{2\pi^2\hbar c\Gamma}{3\lambda^3} \tag{4.25}$$

where λ is the wavelength of the two-level transition.

Given that the intensity of the electric field is

$$I_0 = \frac{1}{2} c \epsilon_0 E_0^2 \tag{4.26}$$

we can now define what is known as the saturation parameter

$$s = \frac{I_0}{I_s} \tag{4.27}$$

After some algebra, we obtain

$$s = 2|\Omega|^2/\Gamma^2 \tag{4.28}$$

This allows us to reexpress the excited state population as

$$\rho_{22} = \frac{1}{2} \frac{s}{1 + s + 4\frac{\Delta^2}{\Gamma^2}} \tag{4.29}$$

which is the common form typically used in the field.

A few observations from the above equations. Firstly, even at infinite s and therefore infinite electric field amplitude, the maximum steady-state excited state population is 1/2. Secondly, the lineshape of the excited-state fraction as a function of detuning is Lorenztian. The maximum of this Lorenztian is determined as

$$\rho_{max} = \rho_{22}|_{\Delta \to 0} = \frac{s}{2(1+s)} \tag{4.30}$$

Using this expression, we can reformulate Eqn. 4.29 as

$$\rho_{22}(\Delta) = \frac{s}{2(1+s)} \frac{1}{\frac{1+s+\frac{4\Delta^2}{\Gamma^2}}{1+s}} = \rho_{max} \frac{1}{1 + \frac{4\Delta^2}{\Gamma^2(1+s)}} \tag{4.31}$$

in order to make it apparent that the full-width half-maximum of this Lorenztian occurs at $\Delta_{FWHM} = \frac{\Gamma}{2}\sqrt{1+s}$. Thus, the width of the Lorentzian increases as the input intensity of the monochramtic driving source increases, a phenomenon [CGG77] known as power broadening (see Fig. 4.2). Experimentally, for high precision determination of transition frequencies, power broadening can be detrimental as it obscures the center of the transition; however, it

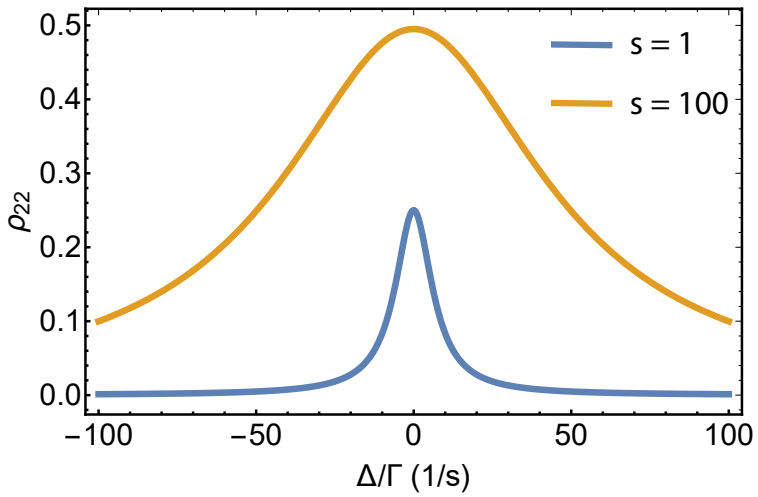

Figure 4.2: Power broadening

Steady state excited state fraction as a function of laser detuning for both $s = 1$ and $s = 100$ conditions. When s is larger, the full-width-half-maximum of the atomic Lorenztian response profile is increased, and the transition is said to be power-broadened.

is advantageous in other situations, such as when searching for narrow transitions of unknown energy.

4.1.2 Einstein Rate Equation Treatment

Often, we are interested in the steady-state electronic populations of a system, for example when experimentally observing laser addressed species over timescales much greater than an atomic lifetime. In these situations, coherent effects get washed out by spontaneous emission events, and a simple linear rate equation model can used to estimate atomic populations.

The standard convention is to assume the rate of both promotion and decay is proportional to the state population. For a two-level system, the required rates are generally labeled through a set of coefficients and describe the following processes

stimulated emission (B_{21})**:** process by which an atom in an excited state is perturbed by an incoming photon and releases an identical photon while being demoted to the ground state

stimulated absorption (B_{12}): process by which an atom in its ground state absorbs an incoming photon and is promoted to its excited state

spontaneous emission (A_{12}): process by which an excited state atom is perturbed by the vacuum field to deexcite to the ground state while emitting a photon (previously described above)

Including these rates leads to a system of differential equations as

$$\begin{aligned} \frac{dN_1}{dt} &= A_{21}N_2(t) + B_{21}\rho(\omega)N_2(t) - B_{12}\rho(\omega)N_1(t) \\ \frac{dN_2}{dt} &= -A_{21}N_2(t) - B_{21}\rho(\omega)N_2(t) + B_{12}\rho(\omega)N_1(t) \end{aligned} \tag{4.32}$$

where $\rho(\omega)$ is the energy density per unit volume per unit angular frequency of the radiation source. We note that the simple stimulated emission and absorption terms presented above describe a monochromatic source, and these expressions become more complicated when radiation widths are considered (see further below).

The spontaneous emission coefficient, A_{12} has already been defined above. Einstein showed quite generally [Ein16], by considering a system in thermodynamic equilibrium, the following relationships exist between A_{12} and B_{12}

$$\begin{aligned} B_{21} &= \frac{\pi^2 c^3}{\hbar\omega_0^3}A_{21} = \left(\frac{\lambda}{2}\right)^2 \frac{c}{\hbar\omega_0}A_{21} \\ B_{21} &= \frac{d_1}{d_2}B_{12} \end{aligned} \tag{4.33}$$

where d_i is the state degeneracy of the i^{th} level.

In order to obtain an explicit formula for the stimulated absorption and emission terms, given how we defined B_{12} above, the absorption cross-section can be expressed [Hil82] as

$$\sigma(\omega) = \frac{d_2}{d_1}\left(\frac{\lambda}{2}\right)^2 A_{21}g(\omega) \tag{4.34}$$

where $g(\omega)$ defines the transition lineshape and satisfies

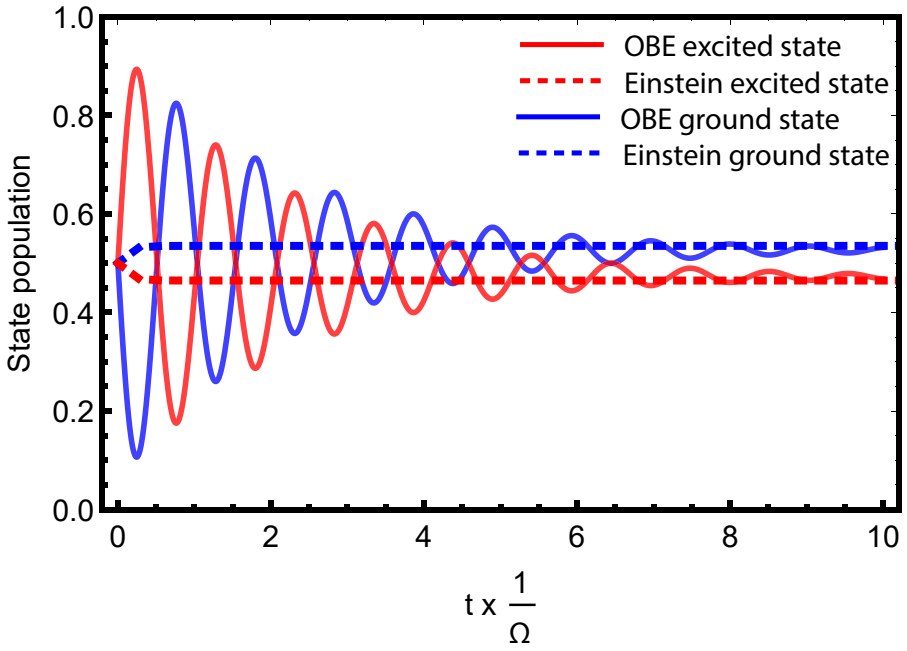

Figure 4.3: Optical Bloch equations vs. Einstein model

The state populations for a two level system as solved by the optical Bloch equations (OBE) (solid lines) as well as the Einstein rate equation model (dashed lines), where the input parameters to the latter was adjusted to yield the same steady state values. We see that the Einstein model neglects coherent oscillations at short timescales but is capable of adequately reproducing the same steady state behavior of the OBE model.

$$1 = \int_{-\infty}^{\infty} g(\omega) d\omega \tag{4.35}$$

For most atomic transitions, $g(\omega)$ can be considered as a Lorentzian; however, different broadening mechanisms, such as Doppler or collisional broadening [HW10], can affect this functional form.

Equipped with the cross-section, from the Beer-Lambert law [Swi62], the total absorption rate, now defined as B^{12}, can be found by integrating the cross-section over the incident photon flux which is given as

$$B^{12} = \int_{-\infty}^{\infty} \frac{d_2}{d_1} \frac{i(\omega)}{\hbar\omega} \sigma(\omega) N_1 d\omega = \int_{-\infty}^{\infty} \frac{d_2}{d_1} \frac{i(\omega)}{\hbar\omega} N_1 \left(\frac{\lambda}{2}\right)^2 A_{21} g(\omega) N_1 d\omega \tag{4.36}$$

where

$$I = \int_{-\infty}^{\infty} i(\omega) d\omega \tag{4.37}$$

where $i(\omega)$ is known as the spectral irradiance of the beam source (power per unit area per unit angular frequency) and I is the total intensity of the radiation source.

Now we consider certain forms of $g(\omega)$ and $i(\omega)$. A typical case to consider is a Lorenztian atomic lineshape of width Γ_A given as

$$g(\omega) = \frac{2}{\pi \Gamma_A} \frac{1}{1 + \frac{4(\omega - \omega_0)^2}{\Gamma_A^2}} \tag{4.38}$$

and a Lorentzian intensity distribution of width of Γ_L, given as

$$i(\omega) = \frac{2I}{\pi \Gamma_L} \frac{1}{1 + \frac{4(\omega - \omega_L)^2}{\Gamma_L^2}} \tag{4.39}$$

this yields a total emission/absorption coefficient of

$$B^{12} = \frac{d_2}{d_1} \left(\frac{\lambda}{2} \right)^2 \frac{I}{\hbar \omega_0} \frac{A_{21}}{\Gamma_L + \Gamma_A} \frac{1}{1 + \frac{4\Delta^2}{(\Gamma_A + \Gamma_L)^2}} \tag{4.40}$$

where Δ is the radiation detuning from the atomic lineshape $\Delta = \omega_0 - \omega_L$. Further, when evaluating the above integral, we made the approximation $1/(\hbar\omega) \approx 1/(\hbar\omega_0)$ since we assumed $g(\omega)$ is sharply peaked about its transition energy. When radiation sources with more complicated lineshapes are used or when additional lineshape broadening mechanisms are present in the system, the above treatment needs to be modified, often resulting in Voigt-like absorption profiles.

After the appropriate convolutions have been made, the resultant absorption coefficient can be substituted back into Eqn. 4.32 using the relation $B_{12}\rho(\omega) = B^{12}$ and thus $B^{21} = \frac{d_1}{d_2} B^{12}$ through Eqn. 4.33.

The predictions using the Einstein rate equation model is compared to the optical Bloch equation solution in Fig. 4.3. Here we notice both models predict the same steady-state

fractions; however, the optical Bloch equations also are sensitive to coherent population oscillations before the steady-state is reached. If long time scales are being considered for a particular problem, the Einstein model is both convenient and sufficient; however, if an experiment is sensitive to coherent effects, caution must be exerted when relying on the Einstein treatment.

4.2 Optical Forces

In addition to transferring population from one state to another, light-matter interactions can also exert useful forces on particles. Although thus far we have only considered laser light classically, i.e. as being comprised of a plane wave electric field, once the electric field is quantized, the light is seen as being composed of photons with characteristic momentum $\hbar k$. Thus, when an atom "absorbs" a photon to be excited to the excited state, the atom is imparted the momentum of the photon. Similarly, when an atom "emits" a photon to be demoted to the ground state, it receives a momentum kick of $\hbar k$ in the direction opposite to emission. Emission occurs in two flavors - either spontaneously, where the emitted photon is ejected in a random direction, or through stimulated emission, whereby an incoming photon "tickles" an excited atom and causes emission of a coherent photon from the atom in the same direction of the incoming photon. While a rigorous derivation of these processes is most readily obtained through electric field quantization [Wys11] (outside the scope of this work), pictoral representations of these processes are presented in Fig. 4.4.

4.2.1 Scattering Forces

Consider a one-dimensional treatment of an atom that traveling antiparallel to the k-vector of an incoming beam of resonant laser radiation. The atom will absorb photons, and thereby gain $\hbar k$ momentum per absorption event along the propagation direction of the laser. The atom will also emit the photons to return to its ground state. The emission process will either occur through stimulated emission, whereby $-\hbar k$ momentum is imparted to the system, or by spontaneous emission, whereby the atom receives a momentum kick in a random direction.

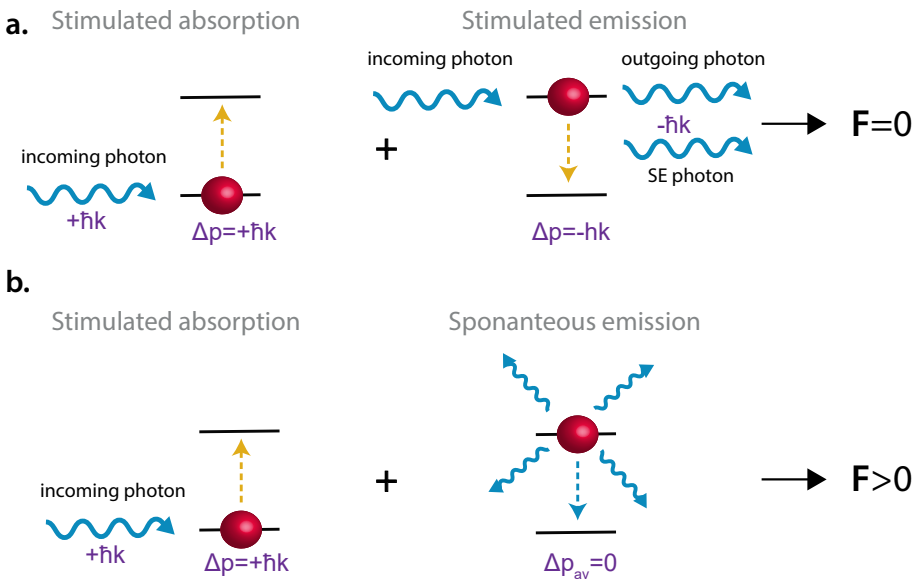

Figure 4.4: Optical forces

(a) A diagram of the momentum exchange during a stimulated absorption/emission cycle from a single beam. The atom absorbs a photon and is promoted to its excited state, receiving a momentum kick of $\hbar k$. The a second photon arrives at the atom and induces stimulated emission where a photon, equal in phase and frequency to the incoming photon, is 'tickeld' out of the atom, demoting it to the ground state and imparting a $-\hbar k$ momentum kick. The total force of this cycle is 0. **(b)** A diagram of a standard stimulated absorption/spontaneous emission cycle. The first step is identical to as in **(a)**; however, in the second step, the atom spontaneously emits. Considering many such cycles, this results in an isotropic emission of photons from the excited state atom, and therefore the atom is also imparted isotropically distributed momentum kicks. Averaging over many cycles, the net momentum exchange is $\hbar k$ and thus the atom experiences a positive force from the beam.

Every absorption event that is followed by a stimulated emission event will result in 0 net momentum being imparted to the atom and therefore 0 net force. However, if we consider absorption events followed by spontaneous emission, we see that the atom, on average, experiences a non-zero force. If we time average over enough spontaneous kicks, the spontaneous emission force will average to zero since the emission pattern is isotropic, leaving the atom with a positive force along the laser propagation direction due to the absorption events (see Fig. 4.4). Therefore, we can express the averaged force the atom experiences due to the laser as

$$\begin{aligned} \langle \vec{F}_s \rangle &= (\text{photon momentum kick}) \times (\text{scattering rate}) \\ &= \hbar \vec{k} \times \Gamma \rho_{22} \end{aligned} \tag{4.41}$$

where we assume an excited state atom spontaneously emits at a rate Γ.

Since at high laser intensities, ρ_{22} saturates to 1/2, this means that a maximum average scattering force of

$$\langle \vec{F}_s \rangle = \frac{1}{2} \hbar \vec{k} \Gamma \tag{4.42}$$

is obtained.

Additionally we can also derive an expression for the approximate minimum possible energy an atom can have when exposed to resonant laser radiation. Even if initially at rest, after one absorption event, then atom will posses a velocity of $v_r = \hbar k/m$, leading to a minimum kinetic energy of

$$E_r = \frac{1}{2} m v_r^2 = \frac{1}{2} \frac{\hbar^2 k^2}{m} \tag{4.43}$$

This energy, known as the recoil energy, can be of order ~ 1 μK for many atomic species; however, it is a temperature rarely reached due to other optical effects, as will be discussed below. However, while the recoil limit is unbroachable in many laser-cooling setups, state-of-the-art cavity cooling techniques can be used to cool atomic species below E_r [WKK12b].

4.2.2 Doppler Cooling

Observing cold atomic and molecular species is a central goal of this thesis, and this section will explore how optical forces can be used to reduce the temperature of these particles.

Earlier, in Eqn. 4.31, we derived an expression for the excited state fraction as a function of Δ, the total detuning of the laser field from the transition energy. However, when considering Δ, one has to consider both the detuning of the laser with respect to the unperturbed atomic transition energy as well as the Doppler shift associated with atomic motion, as

$$\Delta = \omega_L - \omega_0 - \vec{k} \cdot \vec{v} = \Delta_L - \vec{k} \cdot \vec{v} \tag{4.44}$$

where ω_L is the angular frequency of the laser, ω_0 is the transition angular frequency, $\vec{v}$ is the velocity vector of the atom, with the positive direction being defined along the direction of $\vec{k}$, and $\Delta_L = \omega_L - \omega_0$. As we will see shortly, this velocity dependence can lead to a velocity-dependent damping force being exerted on the atom.

To see this, consider a Taylor expansion of the scattering rate about $v = 0$, with the detuning now including the Doppler shift

$$\begin{aligned}
\langle \vec{F}_s \rangle_x &= \hbar k_x \Gamma \rho_{22} = \hbar k_x \Gamma \left(\frac{1}{2} \frac{s}{1 + s + 4\frac{(\Delta_L - k_x v_x)^2}{\Gamma^2}} \right) \\
&\approx \langle \vec{F}_s \rangle|_{v_x=0} + \frac{\partial \langle \vec{F}_s \rangle}{\partial v_x}|_{v=0} \cdot v_x \\
&= \frac{\hbar k_x \Gamma}{2} \frac{s}{1 + s + 4\frac{(\Delta_L)^2}{\Gamma^2}} + 4\hbar k_x^2 \frac{s}{\left(1 + s + 4\frac{(\Delta_L)^2}{\Gamma^2}\right)^2} \left(\frac{(\Delta_L)}{\Gamma} \right) v_x \\
&= \langle \vec{F}_s \rangle|_{v_x=0} + \alpha v
\end{aligned} \tag{4.45}$$

where we have chosen the laser to propagate along the x-axis.

The above force expression for a single beam very much resembles the force expression for a free-falling object subject to air resistance damping. The constant term in the expression, known as the radiation pressure term, provides uniform acceleration while the velocity dependent term damps this motion to a terminal velocity.

However, as the goal is to produce cold atomic species, unless the radiation pressure term is accounted for, the atoms will be unable to reach low kinetic energies. Continuing the analogy with a free-falling system, if the energy of an atomic system initially exists in a wide distribution, as the system is exposed to the resonant laser beam, the final velocity of each individual atom will tend to the same terminal velocity, to first approximation. This will produce an energetically narrow beam with a high forward velocity (in reality our Taylor approximation would break down at this point, but the analogy is still useful to consider).

However, we would really like to maintain an atomic sample with both a narrow energy distribution and an average velocity of approximately 0. In essence, this means the radiation pressure term in the above equation needs to be negated somehow. For a system such as an ion within an ion trap, an electrode potential can produce an an electromagnetic force that directly opposes the radiation pressure term. However, for neutral species, such counterbalancing forces are more difficult to produce since neutrals typically have weaker coupling to electromagnetic fields.

Therefore, in these systems, a counterpropagating beam setup is normally employed to negate the radiation pressure term. Suppose a second beam is introduced into the system that is anti-parallel with the first beam. If we allow the positive direction of the first beam to define the positive direction, the resulting force term for the second beam is

$$\langle \vec{F}_s \rangle_x = -\hbar k_x \Gamma \rho_{22} \tag{4.46}$$

Repeating the same procedure as in Eqn. 4.45 with ($k_x \rightarrow -k_x$) now, we see that resulting Taylor expanded expression will be similar to that of the first beam, except the sign of the radiation pressure term will be switched while the sign of the damping term remains the same . Adding the forces for the two beams together, we end up with

$$\langle \vec{F}_s \rangle_x = 2\alpha v_x \tag{4.47}$$

For cases in which $\omega_L < \omega_0$ (red-detuned), α is negative and thus the atom experiences a damping force with a negative coefficient, leading to velocity compression. On the other

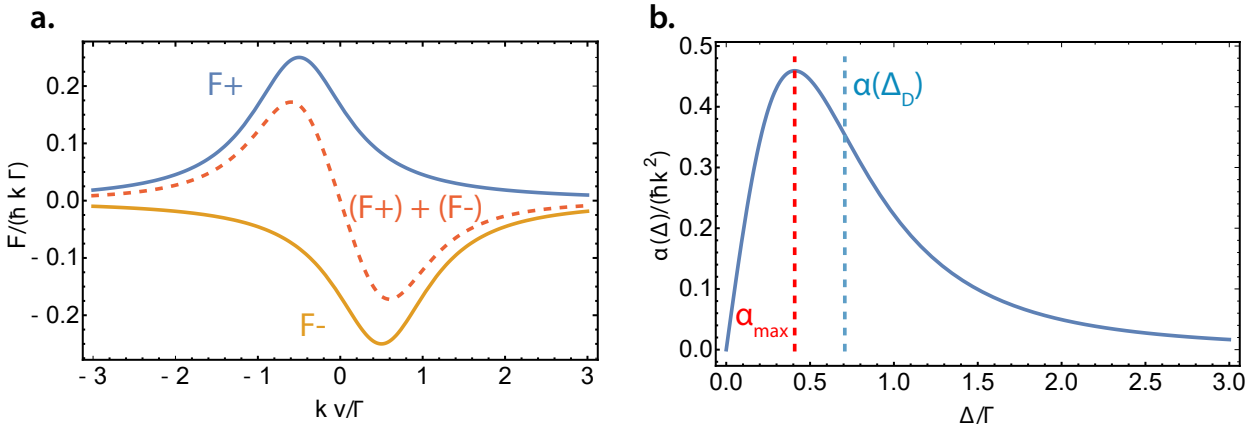

Figure 4.5: Doppler cooling

(a) Force profile as a function of velocity for a beam propagating in the +x direction (F_+), the -x direction (F_-), as well as their composite sum ($F_+ + F_-$). Forces and velocities are expressed in the dimensional parameters, $F/(\hbar k\Gamma)$ and $(kv)/\Gamma$. **(b)** Damping coefficeint, α expressed as a function of detuning. The maximum value of α (α_{max}) differs from the α that yields the Doppler cooling limit, $\alpha(\Delta_D)$, since the latter was chosen to optimize the ratio between velocity damping and spontaneous emission heating while the former was not.

hand, for $\omega_L > \omega_0$ (blue-detuned), the damping force has a positive coefficient, and thus the atom is heated. One key assumption here is that we are in a low s regime such that excited state saturation is not an issue, and thus the beams can be treated independently.

The resulting force curves, using the full force expression instead of the Taylor expansion, are presented for both beams as well as their sum in Fig. 4.5. As can be seen, the velocity damping term is fairly linear for small velocities, as predicted by our Taylor approximation.

In general

$$\dot{v}(t) = \langle \vec{F}_s \rangle_x / m = \frac{2}{m} \alpha v_x \tag{4.48}$$

leading to

$$v_x(t) = v_{x_0} e^{\frac{2\alpha}{m} t} \tag{4.49}$$

where v_{x_0} is the initial velocity of the atom and m is its mass.

Once again, for red-detuned beam configurations, this results in velocity damping with a damping coefficient of $k_d = 2\alpha/m$. The maximum value this coefficient can have is set by the maximum possible value of $\alpha(\Delta_L)$, which is obtained at $\Delta_L = \sqrt{1+s}\Gamma/(2\sqrt{3})$.

Of course, this velocity damping cannot happen indefinitely as eventually the cooling will have to compete with the heating due to spontaneously emitted velocity kicks. To estimate what final temperature the atomic sample will settle at, we can consider the dominant heating and cooling rates of the system.

Consider a six-beam optical molasses cooling configuration, where three pairs of counterpropagating beams are assembled along the x, y, and z axes. The cooling rate is given as

$$\left(\frac{dE}{dt}\right)_{cool} = \langle \vec{F}_s \rangle \cdot \vec{v} = \langle F_x, F_y, F_z \rangle \cdot \langle v_x, v_y, v_z \rangle = 2\alpha v^2 \tag{4.50}$$

With the cooling rate in hand, we must now calculate the heating rate. The heating rate is derived by considering the average added kinetic energy from an absorption/spontaneous emission cycle, assuming a total recoil velocity of $\hbar k/m$ upon emission/absorption of a photon.

We'll start with the spontaneous emission heating rate. Since the emission direction is isotropic, the average added kinetic energy for a single spontaneous emission event can be found by averaging over all possible emission directions as

$$\begin{aligned}\langle \Delta E_{sp} \rangle = \frac{1}{4\pi}\Bigg[\int_0^{2\pi}\int_0^{\pi} \frac{1}{2}m\left((v_x - \frac{\hbar k}{m}\sin(\theta)\cos(\alpha))^2 + (v_y - \frac{\hbar k}{m}\sin(\theta)\sin(\alpha))^2 + (v_z - \frac{\hbar k}{m}\cos(\theta))^2\right) \\ \times \sin(\theta) d\theta d\alpha\Bigg] - \frac{1}{2}m(v_x^2 + v_y^2 + v_z^2) \\ = \frac{\hbar^2 k^2}{2m}\end{aligned} \tag{4.51}$$

Similarly, we can consider the heating due to a single absorption event from a single beam as

$$\langle \Delta E_{ab} \rangle = \frac{1}{2} m \left[\left(v_i - \frac{\hbar k}{m} \right)^2 - v_i^2 \right] \approx \frac{\hbar^2 k^2}{2m} \tag{4.52}$$

where we have assumed we are in the low-velocity limit and our beam is propagating along the i^{th} dimension. Further, in a given emission/absorption cycle, the atom may decay via spontaneous or stimulated emission. However, the average amount of energy transferred to the atom is the same in both cases, as can be gleamed from the above equations. Thus, we will assume all decay occurs spontaneously, for convenience.

Next, we assume the intensities of our beams are low enough such that they can be considered independently. The emission and absorption events happen once every absorption/emission cycle at an overall rate of approximately $\Gamma\rho_{22}$. Thus, combining the heating rates for all six beams in our setup

$$\begin{aligned} \left(\frac{dE}{dt} \right)_{heat} &= 6[\langle \Delta E_{sp} \rangle + \langle \Delta E_{ab} \rangle]\Gamma\rho_{22} = 6 \left(\frac{\hbar^2 k^2}{m} \right) \Gamma\rho_{22} \\ &= \frac{6\hbar^2 k^2}{m} \frac{\Gamma}{2} \frac{s}{1 + s + 4\Delta^2/\Gamma^2} \end{aligned} \tag{4.53}$$

where once again, the factor of 6 comes from the fact that there are six beams in our optical molasses configuration.

At equilibrium the heating and cooling rates are equal, implying

$$\begin{aligned} 2\alpha(\Delta_L)v^2 &= 6\frac{(\hbar k)^2}{m}\Gamma\rho_{22} \\ \rightarrow \frac{1}{2}mv^2 &= \frac{3}{8}\hbar\Gamma(\frac{1}{2}\frac{\Gamma}{\Delta_L} + \frac{2\Delta_L}{\Gamma}) \end{aligned} \tag{4.54}$$

where we have taken the low s limit and neglected the Doppler shift in the scattering rate associated with our heating rate. The expression on the right can be minimized at the Doppler limit detuning, defined as $\Delta_D = \Gamma/2$. At this detuning, we can make the substitution $\frac{1}{2}mv^2 = \frac{3}{2}k_B T$, yielding the Doppler cooling temperature limit

$$T_D = \frac{h\Gamma}{2k_B} \tag{4.55}$$

Cooling below this temperature generally requires more sophisticated schemes, such as Sisyphus cooling, which is not discussed here.

4.2.3 Magneto-Optical Trapping

The optical molasses technique used above will indeed cause velocity phase space compression; however due to the random walk of the atom over time due to spontaneous emission momentum kicks, eventually the atoms will be pushed outside of the intersection region of the six-beam setup, preventing the species from remaining cooled and spatially localized.

For ions, the ion trapping potential is sufficient for spatial localization. Similarly, for neutrals, we would also like to add a position-dependent force, along with our velocity-dependent force, to ensure the atoms remain spatially localized while laser-cooling occurs.

This can be achieved through incorporating magnetic fields that couple to the magnetic sublevels of an atomic system. Imagine a magnetic field that varies linearly through space with the field equal to zero at the origin. Such magnetic fields can be produced through a variety of current coil configurations, such as the anti-Helmholtz configuration which is used in our system and described later.

In the presence of a magnetic field that varies linearly with position, an atomic energy level will experience a Zeeman shift as

$$\Delta E_{B,m_J} = -\vec{\mu} \cdot \vec{B}(z) = \mu_B g_J m_J B_0 z \tag{4.56}$$

where μ_B is the Bohr magneton, g_J is the Lande g-factor, m_J is the magnetic quantum number, B_0 is the magnetic field gradient, and we assume the quantization axis to be along the z-direction of the magnetic field.

Thus, if considering two levels in the atomic system, the resultant energy shift to the transition energy will be the shift of the upper level minus the shift of the lower level, yielding

$$\Delta E_B = \mu_B B_0 z (g_e m_e - g_g m_g) \tag{4.57}$$

where $g_{e(g)}$ and $m_{e(g)}$ are the Lande g-factors and magnetic quantum numbers for the excited (ground) state, respectively. In our particular case, for a Ca Type I MOT, the ground state is the same for all driven transitions and $m_g = 0$. Consequently, the transition energy shift depends on m_e - effectively on whether a σ^+, σ^-, or π transition is being driven.

For σ^+ transitions $m_e = m_g + 1 = 1$ and thus the energy level spacing between the ground and excited state gets *larger* as z *increases*. Similarly, For σ^- transitions $m_e = m_g - 1 = -1$, and thus the energy level spacing between the ground and excited state gets *smaller* as z *increases*.

To exploit this property to create a spatially dependent trapping force, we can consider a counterpropagating beam setup where each beam has opposite left-handed and right-handed circular polarizations at a given point in the trap when measured in the same frame (see Fig. 4.6). On either side of the field zero, the $m_J = -1$ level will be down-shifted in energy since the direction of the magnetic field in a particular point of space sets the quantization axis. Consequently, the polarization of each beam is chosen such that on either side of the field-zero, the beam whose k-vector is oriented towards the field zero is in resonance with the down-shifted $m_J = -1$ level of the excited state, providing spatial confinement. Further, since the frequency of both beams is the same, on each side of the field zero, one beam will be in resonance with the $m_J = -1$ level and provide a confining force, while its counterpropating beam with opposite circular polarization will only be able to weakly address the out-of-resonance $m_J = 1$ level, ensuring anti-confining doesn't occur.

To model this analytically, consider that the total detuning, Δ, from the atomic transition will now also include the Zeeman shift as

$$\Delta = \Delta_L - \vec{k} \cdot \vec{v} + \Delta E_B \tag{4.58}$$

Now, if we consider the averaged force of both the beam with $\vec{k} = \hat{z}$, given as $\langle \vec{F^+} \rangle_z$, as well the beam with $\vec{k} = -\hat{z}$, given as $\langle \vec{F^-} \rangle_z$, the combined scattering force is given as

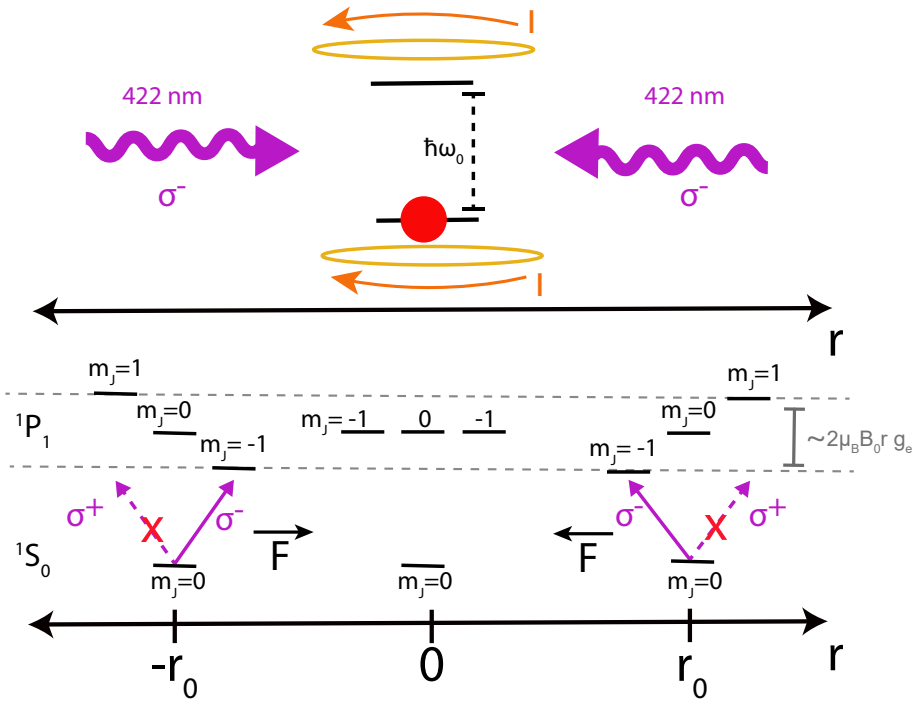

Figure 4.6: MOT level scheme

A Ca atom with a natural ground state ($^1S_0$) to excited state ($^1P_1$) energy splitting of $\hbar\omega_0$ is placed in a magnetic field gradient that adds additional position-dependent Zeeman shifts to the atomic energy levels. In particular, on either side of the field zero, the $m_J = -1$ level will be down-shifted in energy. Counterpropagating beams are introduced into the system such that, on either side of the field-zero, a scattering force is exerted on the atom in the direction *towards the field zero*, providing spatial confinement. On each side of the field zero, one beam will be in resonance with the $m_J = -1$ level and provide a confining force while its partner counterpropating beam will only be able to weakly address the out-of-resonance $m_J = 1$ level, ensuring anti-confining doesn't occur. Pictoral representations of the energy level shifts are presented for different displacements along the radial direction of the trap.

$$\begin{aligned}\langle \vec{F_s} \rangle_z &= \langle \vec{F^+} \rangle_z + \langle \vec{F^-} \rangle_z \\ &= \frac{\hbar k_z \Gamma}{2} \left(\frac{s}{1 + s + 4\frac{(\Delta - k_z v_z + \mu' B_0 z/\hbar)^2}{\Gamma^2}} + \frac{s}{1 + s + 4\frac{(\Delta + k_z v_z - \mu' B_0 z/\hbar)^2}{\Gamma^2}} \right) \\ &\approx 2\alpha v_z - 2\kappa z\end{aligned} \tag{4.59}$$

where $\mu' = \mu_B g_e m_e$ and in the last expression, following a similar procedure as in Eqn. 4.45, a Taylor approximation has been invoked. The resulting expression features α defined as defined in Eqn. 4.45 as well $\kappa = \frac{\mu' B_0}{\hbar k} \alpha$.

Now we both have a velocity-damping force and spatial restoring force, meaning that our atoms can be cooled while they are spatially localized. The spatial restoring force can be thought of as a spring force with characteristic frequency, $\omega_{MOT} = \sqrt{\frac{\kappa}{m}}$, which for standard MOT parameters is typically $\approx 2\pi\times$ 1 KHz. For anti-Helmholtz configurations, the axial magnetic field gradients are typically weaker than the radial ones, resulting is differing trap frequencies in the different spatial dimensions.

While the above analysis was carried out in 1D, it can easily be extended to 3D, as long as we remain in the low-s regime; otherwise more delicate treatments involving the optical Bloch equations are needed [Tar15].

4.2.4 Polarization

Getting the polarization of the incoming beams correct can cause some confusion. The quantization axis of the atom is defined by the magnetic field. Since the Zeeman shift is $\propto m_J B(z)$ (one-dimensional case) this means that the $m_J = -1$ sublevel is going to always be downshifted in the energy. As our MOT beams are red-detuned in order to address the lowest sublevel transition, this means that for proper trapping, we want to arrange our light polarization such that it is σ^- polarized with respect to whatever direction $B(z)$ is pointing. As shown in Fig. 4.7c, for light in which the magnetic field vector and the light k vector are parallel, which is the case for all radial dimensions in the trap due to the anti-Helmholtz configuration, this corresponds to standard left-hand circularly polarized (LHCP) light (with

the handedness defined by k).

However, for the z-dimension, the magnetic field and the light k-vector are antiparallel. Meaning LHCP light is actually projected as right-handed circularly polarized (RHCP) light (σ^+ light) in the frame defined by the magnetic field direction. Therefore, RHCP light must be input to the system for both axial directions in order to drive the desired σ^- transitions (see Fig. 4.7d).

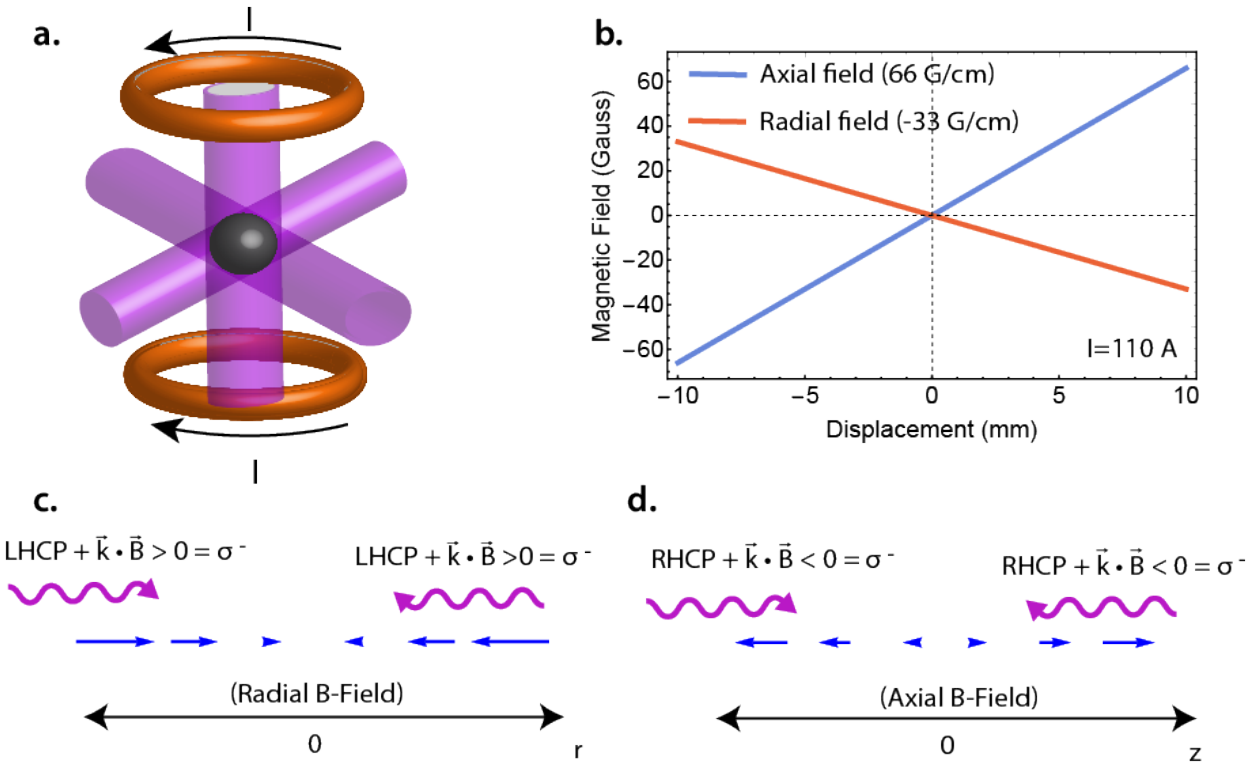

Figure 4.7: MOT Overview

(a) The six-beam optical molasses configuration combined with an anti-Helmholtz coil setup to produce the MOT trapping potential. **(b)** The magnetic field profiles in both the radial and axial dimensions, as a function of displacement form the field zero, taken at 110 A of coil current. **(c)** A diagram showcasing what polarization is needed for each pair of counterpropating beams in the radial dimensions in the MOT setup. Since both beams are parallel with the magnetic field on the side of the field zero in which they are meant to provide a restoring force, they need LHCP polarization to drive the correct σ^- transition. **(d)** A similar argument as in **(c)** is presented for the axial dimension. Now since the k-vector of both beams are anti-parallel to the magnetic field direction in the relevant parts of the trap, RHCP is needed.

CHAPTER 5

Electronic Structure Calculations

A thorough understanding of the electronic properties of molecules and many-electron atoms yields considerable insight into their reaction dynamics and structural properties, and thus solving the electronic Schrödinger equation presented in Eqn. 2.20 is of utmost importance to the work conducted in this thesis. For example, the energetic splitting of rotational levels within a polar molecule, a parameter of extreme relevance for quantum information studies with these species [DeM02, HC18], depends on the electronic effective potential. Further, barriers to reaction can be predicted [PT05] by analyzing the effective potential created by the interaction of electrons on colliding reaction pairs.

As a reminder, the difficulty in Eqn. 2.20 lies primarily in the fact that the $\hat{V}_{ee}$ electron repulsion terms mix the coordinates of all electrons in the system, making the problem increasingly difficult as the number of electrons within a system increases. While analytical solutions to Eqn. 2.20 are generally not possible even for the simplest multi-electron systems, a class of computational techniques has been developed to confront the challenges the electronic Hamiltonian presents. Indeed, such computational chemistry techniques have become one of the most useful ways for researchers to answer questions about the structure of molecules, especially in situations where experimental probing of such structures is difficult [MS17], or even impossible. While the field of computational chemistry is highly sophisticated [SO96, HPO96] and is constantly evolving, only a general overview of core techniques used in the field will be presented here.

5.1 Hartree-Fock Method

The Hartree-Fock method is a technique for predicting electron distributions, amongst other useful properties, in many-electron systems and is one of the most commonly used tools in computational chemistry, often forming the foundation for more elaborate schemes [She00]. As much of the work in this thesis is concerned with diatomics, the method is perhaps best illustrated through application to one of the most basic diatomic molecules imaginable: the two electron/two proton system within the H_2 molecule.

Under the Born-Oppenheimer approximation, the wavefunction of such a system is separable into nuclear and electronic functions and is given as

$$\Psi(\mathbf{R}, \mathbf{r}) = \Psi_N(\mathbf{R_1}, \mathbf{R_2})\Psi_e(\mathbf{r_1}, \mathbf{r_2}) \tag{5.1}$$

where $\Psi(\mathbf{R}, \mathbf{r})$ is the total wavefunction parameterized by both nuclear, $\mathbf{R}$, and electronic, $\mathbf{r}$, coordinates, $\Psi_N(\mathbf{R_1}, \mathbf{R_2})$ is the nuclear wavefunction, and $\Psi_e(\mathbf{r_1}, \mathbf{r_2})$ is the electronic wavefunction.

The nuclear wavefunction can be determined after the electronic eigenvalues, themselves parameterized by $|\mathbf{R_1} - \mathbf{R_2}|$, have been calculated, as discussed in Chapter 2. However, in order to so, electronic wavefunctions must first be determined. How then do we determine the electronic wavefunctions?

We can start by making a simplification. We can pretend that the two electrons in the system do not interact with one another. In this case, the $\hat{V}_{ee}$ potential term would essentially be zero. As the $\hat{V}_{ee}$ operator is the only operator that mixes the electronic coordinates, the electronic wavefunction would then be separable.

Under this approximation, we can model the H_2 electronic wavefunction as

$$\Psi_e(\mathbf{r_1}, \mathbf{r_2}) = \psi_1(\mathbf{r_1})\psi_2(\mathbf{r_2}) \tag{5.2}$$

where the $\psi_i(\mathbf{r_i})$ is known as the *molecular orbital* for the i^{th} electron. What are the molecular orbitals exactly? They are the analog of atomic orbitals within molecules and yield the spatial

probability distributions that electrons in the system may occupy. Unlike with the hydrogen-atom atomic orbitals, the molecular orbitals are usually impossible to solve for analytically. Given this difficulty, they are often expressed as linear combinations of other *basis* functions, and the coefficients of these linear combinations are subsequently optimized using variational methods, to be discussed further below [She00]. Ultimately, the number of basis sets, as well as their ability to span the true Hilbert space of the electronic Hamiltonian, will determine how well these approximate orbitals converge to the exact orbitals [She14].

Moving forward, due to the Pauli exclusion principle, since electrons are fermions, their collective wavefunction must be antisymmetric with respect to exchange of electronic coordinates as

$$\Psi_e(\mathbf{r_1}, \mathbf{r_2}) = -\Psi_e(\mathbf{r_2}, \mathbf{r_1}) \tag{5.3}$$

By itself, the wavefunction in Eqn. 5.2 does not meet the above antisymmetrization condition; however, it can be modified to do so. If the wavefunction in Eqn. 5.2 is a solution to the simplified electronic Schrödinger equation (with the $\hat{V}_{ee}$ terms removed), a state with the coordinates permuted is also a solution, as are linear combinations of such states [SO96]. This means the so-called Slater determinant involving the molecular orbitals in Eqn. 5.2 is also a solution and has the form

$$\Psi_e(\mathbf{r_1}, \mathbf{r_2}) = \frac{1}{\sqrt{2}} \begin{vmatrix} \psi_1(\mathbf{r_1}) & \psi_2(\mathbf{r_1}) \\ \psi_1(\mathbf{r_2}) & \psi_2(\mathbf{r_2}) \end{vmatrix} \tag{5.4}$$

When evaluated, this determinant yields the properly antisymmetrized wavefunction

$$\Psi_e(\mathbf{r_1}, \mathbf{r_2}) = \frac{1}{\sqrt{2}}(\psi_1(\mathbf{r_1})\psi_2(\mathbf{r_2}) - \psi_1(\mathbf{r_2})\psi_2(\mathbf{r_1})) \tag{5.5}$$

This process of antisymmetrization can be generalized to a N-electron system as

$$\Psi_e(\mathbf{r_1}, \mathbf{r_2}, ..., \mathbf{r_N}) = \frac{1}{\sqrt{N!}} \begin{vmatrix} \psi_1(\mathbf{r_1}) & \psi_2(\mathbf{r_1}) & \dots & \psi_N(\mathbf{r_1}) \\ \psi_1(\mathbf{r_2}) & \psi_2(\mathbf{r_2}) & \dots & \psi_N(\mathbf{r_2}) \\ \vdots & \vdots & & \vdots \\ \psi_1(\mathbf{r_N}) & \psi_2(\mathbf{r_N}) & \dots & \psi_N(\mathbf{r_N}) \end{vmatrix} \tag{5.6}$$

To clarify the structure of the Slater determinant, we note that each column vector contains the same molecular orbital, expressed in different electronic coordinates, and each row vector contains the same electronic coordinates, expressed in the different molecular orbitals of the system.

So now we have an understanding of how to create an antisymmetrized wavefunction, comprised of molecular orbital functions. But what do the molecular orbitals themselves look like?

Each molecular orbital, in general, is described by a spatial component and a spinor, in what is known as a spin-orbital

$$\psi_{j,\zeta}(\mathbf{r}_i, \omega_i) = \phi_j(\mathbf{r}_i)\zeta(\omega_i) \tag{5.7}$$

where $\phi_j(\mathbf{r}_i)$ is the spatial component of the j^{th} molecular orbital and $\zeta(\omega_i)$ is a spinor of spin coordinate (ω_i), usually defined as being in one of two states, spin-up, $\alpha(\omega_i)$, or spin-down, $\beta(\omega_i)$. The concept of a 'spin-coordinate' may be odd, but we note that such coordinates are mostly defined just for tracking which electron is associated with which spin-state and are not used explicitly in calculations typically.

Now what do the $\phi(\mathbf{r}_i)$ functions look like? Ideally, they would be the solutions to the full electronic Hamiltonian; however, as this Hamiltonian is analytically unsolvable, one convention, as briefly discussed earlier, is to approximate them as linear combinations of so called *basis functions*. Using these basis functions, the spatial component of the molecular orbital can be expressed as

$$\phi_i(\mathbf{r_i}) = \sum_{\mu} C_{\mu i} \chi_{\mu}(\mathbf{r}_i) \tag{5.8}$$

where $\chi_{\mu}(\mathbf{r}_i)$ are the indexed basis functions and $C_{\mu i}$ are their associated weighting coefficients. Further, the basis functions themselves may take several different forms. One standard approach, known as the linear-combination-of-atomic-orbitals method, is to use a set of hydrogen-like wavefunctions with origins centered at the various nuclei of the system [AF11]. However, calculations within this basis set are often computationally costly. Alternatively, it has been shown that these atomic orbitals can be approximated as a linear combination of simple Gaussian-like orbitals. Given the convenient mathematical properties of Gaussian functions, products and integrals of these functions often have simple, closed-form solutions, leading to huge computational savings [She14].

Aside from the type of functions that are used in these basis sets, how many different functions do the sets contain themselves? *Minimal basis sets*, as one example, refer to the smallest possible basis sets that are typically used to model an N-electron system. These sets approximately consist of one basis function for every normally occupied atomic orbital in the system. For example, within the CO molecule, the C atom contains six electrons distributed amongst the $1s, 2s, 2p_x, 2p_y$, and $2p_z$ atomic orbitals, and the O atom contains eight electrons distributed amongst the same orbitals. Thus, when using a minimal basis set, one would place the 14 electrons of the system in molecular orbitals constructed from the 10 atomic orbitals of the system that are normally occupied in the separated-atom limit, 5 of which are centered on the C atom and 5 of which are centered on the O atom (2 electrons of different spin may occupy a given spatial orbital). We note that even though not all five orbitals are occupied on the C atom, in general all subshell levels are included in the minimal basis set, although this may change based on the system being studied [She14].

While minimal basis sets are convenient for quick-and-dirty calculations, due to their limitations, they do not generally offer accurate predictions of molecular electron distributions and thus are not used for publication quality calculations. When more accurate results are needed, researchers often resort to double-zeta or triple-zeta basis sets, which, in contrast to

minimal basis sets, contain two or three basis functions for every normally occupied atomic orbital in the system, respectively [She14].

In the end, many different basis set sizes and basis set functions may be used, and in general there is a compromise between complexity of basis set and chemical accuracy. The more basis functions that are included, the more flexibility the approximate molecular orbitals will have to resemble the true molecular orbitals of the system, but such flexibility can come at significant computational costs. Thus basis sets are chosen judiciously given the requirements of the problem being solved.

Back to the Hartree-Fock method, once the Slater determinant has been invoked to obtain the electronic wavefunction, we can consider the expectation value

$$E_{HF} = \langle \Psi_e(\mathbf{r}) | \hat{H} | \Psi_e(\mathbf{r}) \rangle \tag{5.9}$$

where

$$\hat{H} = \hat{T}_N + \hat{T}_e + \hat{V}_{NN} + \hat{V}_{ee} + \hat{V}_{Ne} \tag{5.10}$$

as defined in Eqn. 2.15.

According to the variational method, the true ground state wavefunction will yield the lowest energy for E_{HF}, the so called Hartree-Fock energy. Thus, we can vary $C_{\mu i}$ for each electron to minimize E_{HF} and thus get a Hartree-Fock wavefunction that resembles the ground state wavefunction to increasing degrees of accuracy, depending on the quality of the minimization. However, our minimization procedure will be constrained, typically through employing the method of Langrange multipliers [EA07], such that the resulting molecular orbitals are orthornormal with respect to one another, as is required for eigenfunctions of the same operator.

With some effort and clever tricks [EA07, SO96], this optimization problem can be transformed into an eigenvalue-like problem known as solving the Fock-Roothaan-Hall equations [EA07], which can be stated succinctly in matrix notation as

$$\mathbf{FC} = \mathbf{SC}\epsilon \tag{5.11}$$

where $\mathbf{C}$ is the matrix of $C_{\mu i}$ coefficients, ϵ is a diagonal matrix of orbital energies, $\mathbf{S}$ is the matrix of overlap integrals defined as

$$S_{\mu v} = \langle \chi_\mu | \chi_v \rangle \tag{5.12}$$

and $\mathbf{F}$ is the Fock matrix defined as

$$F_{\mu v} = \langle \chi_\mu | \hat{f} | \chi_v \rangle \tag{5.13}$$

where $\hat{f}$ is the Fock-operator defined as

$$\hat{f} = \hat{h} + \sum_j (2\hat{J}_j - \hat{K}_j) \tag{5.14}$$

where $\hat{h}$ is the operator associated with kinetic energy of the electron and the nuclear-electron attraction, $\hat{J}_j$ is an operator accounting for the electron repulsion energy, and $\hat{K}_j$ is a term corresponding to the "exchange" energy between electrons [EA07,RMV16,SO96]. In general, $\hat{f}\,|\Psi_e\rangle = \sum \epsilon_i \,|\Psi_e\rangle$, where ϵ_i is the energy eigenvalue associated with the i^{th} molecular orbital.

Here, the Fock matrix itself depends on the elements of $\mathbf{C}$, meaning in general, the minimization problem is an iterative process where the molecular orbitals that are used to solve the Fock-Roothan-Hall equations are updated after each loop iteration (Fig. 5.1a). This process is continued until the elements of $\mathbf{C}$ have been determined to a level of accuracy such that E_{HF} has converged within a desired tolerance level, at which point it is said that the *self-consistent field (SCF) has converged* [EA07]. At this point, the optimized molecular orbitals can be used to understand structural properties of the molecule as well as to calculate quantities of interest such as dipole moments, effective electronic potentials, etc. [LXC99].

Further, we note that while we neglected $\hat{V}_{ee}$ in making our electronic wavefunction separable, we reintroduce the term in our variational Hamiltonian so that our optimized molecular orbitals account for electron-electron repulsion to some degree.

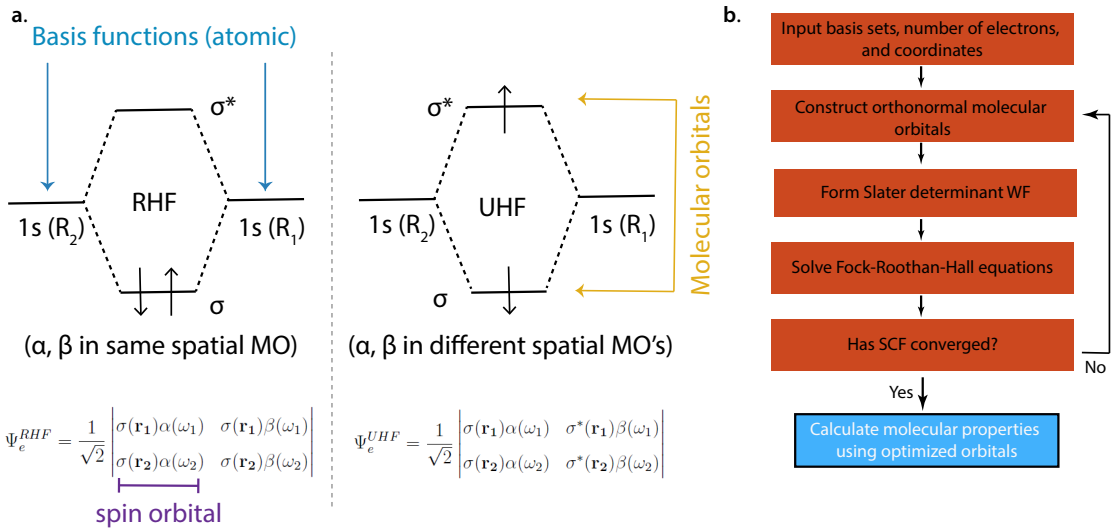

Figure 5.1: Hartree-Fock Method overview

(a) Difference between restricted and unrestriced Hartree-Fock methods. In RHF, each spatial orbital is doubly occupied with electrons of opposing spin. In UHF, electrons of opposing spin may occupy different spatial orbitals, with unpaired electrons being allowed. In both methods, molecular orbitals, σ ,are constructed as linear combination of basis functions, which can often be taken to be hydrogen-like wavefunctions (i.e. 1s, 2s, etc.). **(b)** A conceptual flowchart of the Hartree-Fock method process. Basis sets are used to construct molecular orbitals, which the electrons in the many-body system occupy. A Slater determinant, comprised of spin-orbitals (molecular orbitals multiplied by a spinor), is calculated from these orbitals to produce a properly symmetrized electronic wavefunction. In order to minimize the expectation value of the electronic Hamiltonian, the Fock matrix is initially constructed from Ansantz molecular orbital geometries and the Fock-Roothan-Hall equations are solved to calculate updated geometries. This optimization routine is repeated until the orbital geometries have converged to the desired level of accuracy, at which point it is said the *SCF has converged* and other molecular properties of interest can be calculated.

5.1.1 Restricted Hartree-Fock

The Hartree-Fock method optimizes a given Slater determinant wavefunction, but in general there are many ways in order to construct a Slater determinant. In what is know as a *restricted* Hartree-Fock (RHF) calculation, the molecular orbitals that are used in our N-electron Slater determinant consist of the $N/2$ lowest energy spin-orbitals [She00]. Thus, each spatial orbital is doubly occupied, once with an electron with an α spinor and once with an electron with a β spinor (see Fig. 5.1b). The antisymmetrization in the Hartree-Fock wavefunction will then be accounted for through the spin states instead of the spatial states. For example, consider the following simple two-electron Slater determinant, composed under RHF conditions

$$\begin{aligned}\Psi_e(\mathbf{r_1},\mathbf{r_2}) &= \frac{1}{\sqrt{2}}\begin{vmatrix}\psi_1(\mathbf{r_1}) & \psi_2(\mathbf{r_1})\\ \psi_1(\mathbf{r_2}) & \psi_2(\mathbf{r_2})\end{vmatrix} = \frac{1}{\sqrt{2}}\begin{vmatrix}\phi_1(\mathbf{r_1})\alpha(\omega_1) & \phi_1(\mathbf{r_1})\beta(\omega_1)\\ \phi_1(\mathbf{r_2})\alpha(\omega_2) & \phi_1(\mathbf{r_2})\beta(\omega_2)\end{vmatrix} \\ &= \frac{1}{\sqrt{2}}\phi_1(\mathbf{r_1})\phi_1(\mathbf{r_2})\Big[\alpha(\omega_1)\beta(\omega_2)-\beta(\omega_1)\alpha(\omega_2)\Big]\end{aligned} \tag{5.15}$$

This method works well for closed-shell systems (i.e. every orbital is occupied with two electrons of different spin) in which every electron is paired. Moreover, it has been established that the wavefunction produced by the restricted Hartree-Fock method will be an eigenfucntion of the $\hat{S}^2$ spin operator [SO96]. Consequently, if attempting to produce the ground state wavefunction ($S = 0$) for a particular system, the RHF wavefunction will retain the spin properties of the $S = 0$ state without contamination from other spin-states.

5.1.2 Unrestricted Hartree-Fock

However, when modeling excited states or other open-shell systems, the RHF method is often a poor choice since electrons are necessairly spin-paired in a RHF wavefunction. In these cases, the *unrestricted* Hartree-Fock (UHF) method is used in which N distinct spatial orbitals may be used to construct the N-electron Hartree-Fock wavefunction, each of which is assigned an unconstrained spin orbital (see Fig. 5.1b). Now the molecular orbital optimization is performed as usual in order to minimize E_{HF}. For the two electron system, an example UHF wavefunction is

$$\begin{aligned}\Psi_e(\mathbf{r_1},\mathbf{r_2}) &= \frac{1}{\sqrt{2}}\begin{vmatrix}\psi_1(\mathbf{r_1}) & \psi_2(\mathbf{r_1})\\ \psi_1(\mathbf{r_2}) & \psi_2(\mathbf{r_2})\end{vmatrix} = \frac{1}{\sqrt{2}}\begin{vmatrix}\phi_1(\mathbf{r_1})\alpha(\omega_1) & \phi_2(\mathbf{r_1})\beta(\omega_1)\\ \phi_1(\mathbf{r_2})\alpha(\omega_2) & \phi_2(\mathbf{r_2})\beta(\omega_2)\end{vmatrix} \\ &= \frac{1}{\sqrt{2}}(\phi_1(\mathbf{r_1})\alpha(\omega_1)\phi_2(\mathbf{r_2})\beta(\omega_2) - \phi_2(\mathbf{r_1})\beta(\omega_1)\phi_1(\mathbf{r_2})\alpha(\omega_2))\end{aligned} \tag{5.16}$$

However, since the spins are no longer restricted, the UHF can yield wavefunctions that are no longer $\hat{S}^2$ eigenstates, which means if attempting to model the ground state of a particular system, the UHF wavefunction may in fact be 'contaminated' by higher spin states [AJB91].

Spin contamination results in wavefunctions which appear to emulate the desired spin state, but in fact have portions of higher spin states mixed in. However, despite this drawback, the UHF method will also be able to describe effects such as spin polarization, triplet-spin states, and reactions in which the spin state of the products do not match the spin states of the reactants. To take advantage of the UHF method while avoiding spin contamination, $\langle\hat{S}^2\rangle$ is calculated for the UHF wavefunction to ensure it is within a specified degree of tolerance to the $\hat{S}^2$ eigenstate that is being studied (i.e. if studying a singlet state $\langle\hat{S}^2\rangle_{UHF} \approx \frac{3}{4}\hbar^2$) [SO96].

Lastly, for both the UHF and the RHF method (whose similarities and differences are presented in Fig. 5.1), the computation time for solving the Hartree-Fock equations typically scales $\propto B^4$ [Saa11], where B is number of basis functions used (roughly equal to the number of electrons in the system for minimal basis sets). Therefore, to save computation time, the Hartree-Fock Hamiltonian is often modified to include an effective core potential [Gro00] for the inner electrons while the molecular orbitals for the valence electrons (outer most shell electrons) are optimized. As the valence electrons typically dictate many of the chemical properties of an atomic system, this approximation may still yield accurate results for a variety of chemical properties.

5.2 The Correlation Energy Problem

As noted above, the Hartree-Fock method, whether unrestricted or restricted, does not treat the electron correlation energy fully.

The electron correlation energy, V_{ee} can be considered as a sum of three separate terms [SO96] as

$$V_{ee} = E_J + E_K + E_C \tag{5.17}$$

where E_J is the repulsion energy, E_K is the exchange energy, and E_C is the correlation energy.

Here, E_J has simple classical analog as the electronic repulsion each electron experiences due to the mean electric field produced by all other electrons. However, E_K has no simple classical interpretation and instead is viewed as the energy associated with the electrons experiencing a "force" that prevents them from occupying the same quantum state at the same position in order to satisfy Pauli exclusion.

While not obvious from our simple Hartree-Fock method overview, a more rigorous treatment will illuminate that both E_K and E_J are generally well-treated through the Hartree-Fock method. On the other hand, E_C is not. Physically E_C can be thought of representing additional electrostatic repulsion energy the electrons experience due to faster-timescale movements of the electron clouds that are not reflected in their averaged distributions (E_J).

There are two types of correlation energies discussed in general

$$E_C = E_D + E_S \tag{5.18}$$

where E_D is the dynamic electron correlation energy and E_S is the static electron correlation energy [HG11, Sin07].

Why does the Hartree-Fock method neglect each of these factors? First let us consider E_D. In the Hartree-Fock method, the electron wavefunctions are separable; for a two-particle system, the total electronic wavefunction can be approximated as

$$\Psi_e(\mathbf{r_1}, \mathbf{r_2}) = \Psi_1(\mathbf{r_1})\Psi_2(\mathbf{r_2}) \tag{5.19}$$

This separability is central to forming the Hartree-Fock equations; however, it misses key aspects of the problem. In reality, the electrons' distributions are not independent of one another. For example, classically speaking, the electrons will move in order to avoid the instantaneous position of all other electrons, i.e. their positions are *correlated* and these additional dispersion interactions result in dynamic correlation energy [Sin07]. However, the HF wavefunction cannot take this effect fully into account due to its separability. While the Hartree-Fock wavefunction does take some minor correlations into account due to its antisymmterization, there are much richer dynamics that are missed [Sin07].

E_S is more difficult to get physical intuition for but can be understood by considering a different type of error in the Hartree-Fock method. The Hartree-Fock method assumes that the electronic wavefunction is given by a single *reference* Slater determinant. In general, the electron wavefunction is a general function of N electron coordinates as $\Psi_e(\mathbf{r_1}, \mathbf{r_2}.....,\mathbf{r_N})$. Such a function can be expanded in a variety of basis functions, with each basis function itself being a function of N electron coordinates. Slater determinants themselves are one such sets of basis functions that can be used, and in general an infinite number of such determinants will be able to *exactly* represent the true wavefunction of the system. However, the Hartree-Fock method assumes only one Slater determinant in its wavefunction expansion, not necessarily a valid assumption for many systems. Especially when considering transitions between two molecular states, the Hartree-Fock wavefunction may be a better approximation to one state than the other, leading to differing levels of accuracy in energetic predictions for the two states and therefore large energy level difference errors [HG11].

As comparing the relative energies of molecular levels is of utmost importance in computational chemistry, developing so called "post-Hartree-Fock methods" (see Fig. 5.2) capable of accurately modeling the correlation energy is one of the most important problems in computational chemistry. There are a multitude of methods used to calculate the correlation energy, and the ones most relevant to this thesis are discussed below.

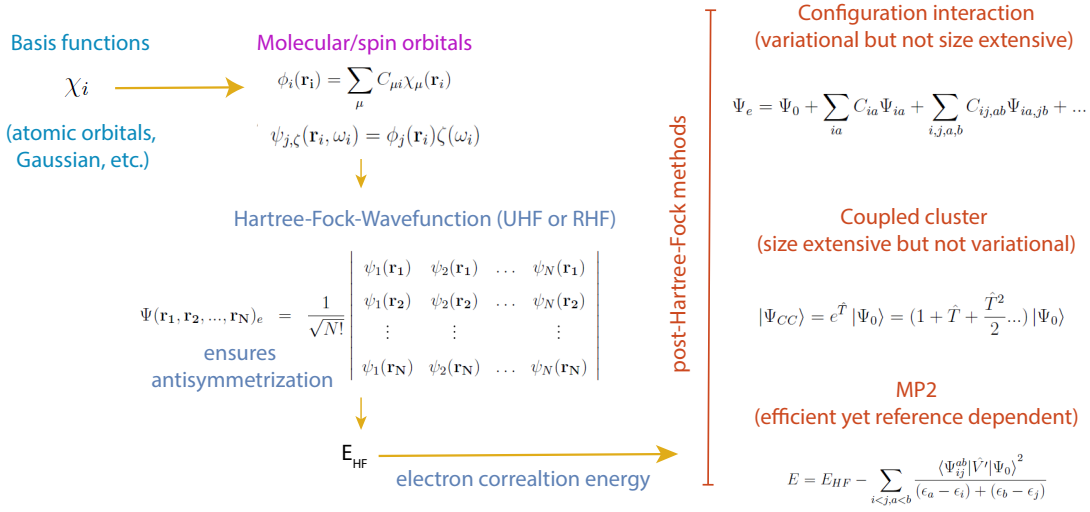

Figure 5.2: Electronic structure calculations overview

A diagramatic overview of the Hartree-Fock method as well as post-Hartree-Fock methods that can be used to account for electronic correlation energy not contained in E_{HF}.

5.2.1 Configuration Interaction

Typically the for a N electron system, the N lowest molecular orbitals are used to construct the Slater determinant wavefunction that is iteratively optimized to yield the minimal Hartree-Fock energy. If there are a total of M orbitals available in a system, this means that $M - N$ orbitals will remain unfilled and are so-called "virtual" orbitals. While virtual orbitals are typically not included in a standard Hartree-Fock calculation, constructing wavefunctions with these orbitals can actually help more accurately account for the electron correlation energy by allowing for additional molecular orbital flexibility.

To better illustrate this point, as an example, again consider the H_2 molecule. In the simplest case, consider molecular orbitals constructed of a basis set of hydrogen wavefunctions, given as $n_l(r_i)$ where n is the principle quantum number and l is the orbital angular momentum of the state, and r_i is the coordinate of the i^{th} electron. For this example, we can restrict ourselves to two molecular orbitals, a so-called bonding orbital

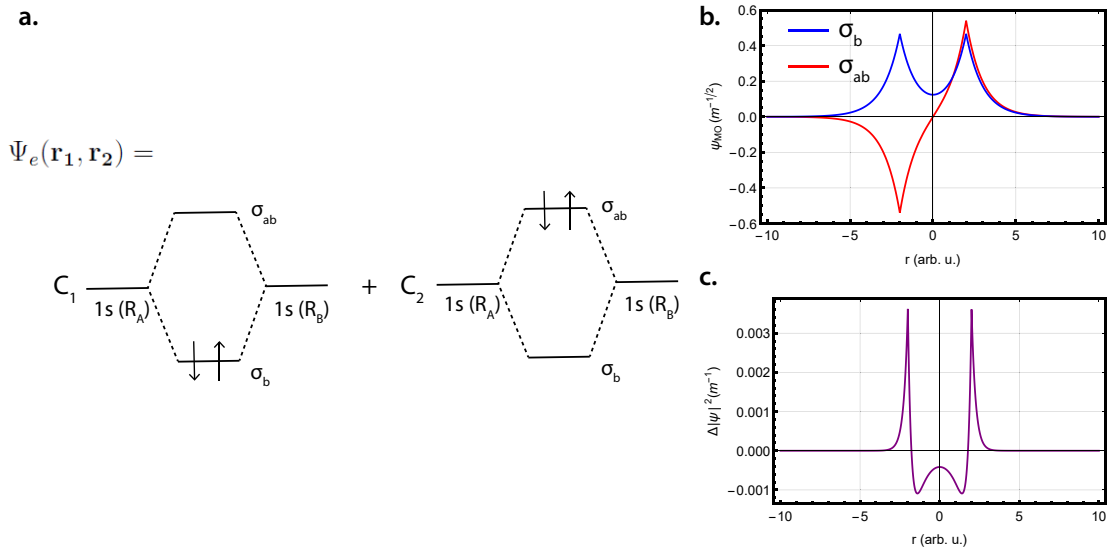

Figure 5.3: Configuration Interaction treatment of the H_2 molecule

(a) In the configuration interaction treatment of the H_2 molecule, the trial wavefunction is assumed to be a linear combination of Slater determinant wavefunctions. While the Hartree-Fock wavefunction contains only bonding orbitals, the excited Slater determinants can also include antibonding orbitals. The expansion coefficients are optimized to minimize the ground state energy of the system. **(b)** Radial electronic wavefunction plots for both the bonding (blue) and antibonding (red) molecular orbitals. The anti-bonding orbital possesses a node at the origin, which leads to lowered electron repulsion as compared to σ_b, but the σ_{ab} also has a higher energy due to the exchange interaction. **(c)** The difference between the radial electron density distribution obtained from the optimized wavefunction in (**a**) and the distribution from the Hartree-Fock wavefunction. As can be seen, by mixing in antibonding orbital character, the electron density between the nuclei is reduced, thereby reducing the electronic-repulsion energy as compared to the Hartree-Fock wavefunction. Since the energy of the system is lowered, it is a more accurate depiction of the true ground state, as predicted by the variational theorem.

$$\sigma_b(r_i) = \frac{1}{\sqrt{2}}(1_S(r_i - R_A) + 1_S(r_i - R_B)) \tag{5.20}$$

and the antibonding orbital

$$\sigma_{ab}(r_i) = \frac{1}{\sqrt{2}}(1_S(r_i - R_A) - 1_S(r_i - R_B)) \tag{5.21}$$

where R_A and R_B are the nuclear positions for the hydrogen atoms in the problem. In a RHF calculation, we can assume both atoms are in the lower energy σ_b bonding orbital, and therefore we obtain a Slater determinant reference wavefunction of

$$\Psi_e(\mathbf{r_1}, \mathbf{r_2}) = \frac{1}{\sqrt{2}} \begin{vmatrix} \sigma_b(r_1)\alpha(\omega_1) & \sigma_b(r_1)\beta(\omega_1) \\ \sigma_b(r_2)\alpha(\omega_2) & \sigma_b(r_2)\beta(\omega_2) \end{vmatrix} = \frac{1}{\sqrt{2}}\sigma_b(r_1)\sigma_b(r_2)\Big[\alpha(\omega_1)\beta(\omega_2) - \beta(\omega_1)\alpha(\omega_2)\Big] \tag{5.22}$$

where the spin portion of the orbitals produces the proper antisymmterization.

However, if we look at the spatial wavefunctions for both the bonding and antibonding orbitals, we see that σ_{ab} has a node at the origin (see Fig. 5.3). In our RHF wavefunction, we only considering the σ_B orbital, which has considerable more electron density near the origin, leading to more dynamical correlation energy. In general, our approximate wavefunction should minimize the energy of the system, according to the variational method. Therefore, if we were to "mix" our excited state anti-bonding orbital with our Hartree-Fock wavefunction, we would perhaps be able to reduce our dynamic correlation energy while still retaining some of the desirable properties of our reference wavefunction, such as a reduced amount of E_J and E_K.

Therefore we can consider another wavefunction consisting of additional excited state Slater determinants as

$$\Psi_e(\mathbf{r_1},\mathbf{r_2}) = \frac{C_0}{\sqrt{2}}\begin{vmatrix}\sigma_b(r_1)\alpha(\omega_1) & \sigma_b(r_1)\beta(\omega_1)\\ \sigma_b(r_2)\alpha(\omega_2) & \sigma_b(r_2)\beta(\omega_2)\end{vmatrix} + \frac{C_1}{\sqrt{2}}\begin{vmatrix}\sigma_b(r_1)\alpha(\omega_1) & \sigma_{ab}(r_1)\alpha(\omega_1)\\ \sigma_b(r_2)\alpha(\omega_2) & \sigma_{ab}(r_2)\alpha(\omega_2)\end{vmatrix} + \frac{C_2}{\sqrt{2}}\begin{vmatrix}\sigma_{ab}(r_1)\alpha(\omega_1) & \sigma_{ab}(r_1)\beta(\omega_1)\\ \sigma_{ab}b(r_2)\alpha(\omega_2) & \sigma_{ab}(r_2)\beta(\omega_2)\end{vmatrix} \tag{5.23}$$

Now we can use the variational energy to optimize the above C_i coefficients in order to minimize the energy of the system [McQ08], with $C_1 = 0$ due to symmetry considerations. If we plot the corresponding electron density of this optimized wavefunction alongside our HF wavefunction electron density, assuming a fixed internuclear spacing, we notice a reduced density in between the two nuclei. In this way, we see that including the excited state can help account for the lack of electron correlation in the HF wavefunction by giving additional flexibility to our trial wavefunction [CMY12].

We can now introduce additional notation to generalize the method. Let us denote a properly symmetrized Hartree-Fock wavefunction, where N electrons have been placed into the N lowest energy molecular orbitals, $\{\phi_1...\phi_N\}$, as

$$\Psi_0 = \Psi(\mathbf{r_1},\mathbf{r_2}...\mathbf{r_N}) = |\phi_1\phi_2....\phi_N\rangle \tag{5.24}$$

If there are M total orbitals in the system then $M-N$ unoccupied virtual orbitals exist. To incorporate excited state character into our wavefunction we can consider adding Slater determinants where the i^{th} molecular orbital has been replaced by the a^{th} virtual orbital as

$$\Psi_i^a = |\phi_1\phi_2...\phi_{i-1}\phi_a\phi_{i+1}...\phi_N\rangle \tag{5.25}$$

We can define Ψ_{ij}^{ab} similarly for double excitations then a general trial wavefunction can be expressed as

$$\Psi_e = \Psi_0 + \sum_{ia} C_i^a\Psi_i^a + \sum_{i,j,a,b} C_{ij}^{ab}\Psi_{ij}^{ab} + ... \tag{5.26}$$

where the sum is carried out across all occupied and all virtual orbitals and the C_i^a and C_{ij}^{ab} terms are the Slater determinant expansion coefficients. Further, higher-order terms corresponding to triple excitations, quadruple excitations, etc. can also be included.

Once these wavefunctions have been constructed, you can then apply the variational method to optimize for the various individual expansion coefficients.

However, in general, there are multiple ways to optimize the above wavefunction. One may choose to iteratively optimize both the coefficients in the expansion of the molecular orbitals themselves as well as the Slater determinant coefficients, a two-fold optimization problem that adds additional computational complexity (used in methods such as the multiconfigurational self-consistent field (MCSCF) method [She04]). Alternatively, one may choose fix the molecular orbitals and to solely optimize the Slater determinant coefficients, as is the case for what is known as *configuration interaction* (CI) calculations.

In general, considering all possible excitations, known as a Full CI calculation, will cause a configuration interaction wavefunction to converge to the true ground state of the system to the highest degree possible within a given basis set [She95]. However, whether or not the configuration interaction will converge to the true ground state energy of the system will depend on the limitations of the chosen basis set.

While in H_2 a full CI calculation can be done rather simply with four total terms (assuming a two molecular orbital basis set), in general the number of excited state determinants scales roughly with the factorial of the number of orbitals in the system (which in turn scales with the number of electrons) as $\approx (M)!/[(N!)!(M-N)!]$ (choose N electrons to occupy M orbitals). Especially when using complex basis sets that span a wider, and therefore more accurate, Hilbert space, this often means including trillions of terms in the configuration interaction wavefunction. Therefore, the configuration wavefunction is often truncated in practice to include only single or double excitations, leading to deviations from the ground state energy. The following acronyms have been developed to describe the level of truncation that is used in a particular calculation:

CIS: (single excitations only)

CISD: (single and double excitations)

CISDT: (single, double, and triple excitations only)

Full CI: (all possible excitations)

5.2.2 Coupled Cluster Method

As Full CI methods are quite cumbersome, often other methods are preferred, such as coupled cluster theory. Similar to the CI, in coupled cluster theory an Ansatz wavefunction is first chosen that is a linear combination of excited state Slater determinants. However, the expansion is different than in the CI method. For coupled cluster theory, the trial wavefunction is formed as

$$|\Psi_{CC}\rangle = e^{\hat{T}} |\Psi_0\rangle \tag{5.27}$$

where

$$\hat{T} = \hat{T}_1 + \hat{T}_2 + \hat{T}_3 \tag{5.28}$$

where $\hat{T}_i$ is the operator that generates a Slater determinant at the i^{th} level of excitation (i.e. singly excited, double excited, etc.)

For example

$$\hat{T}_1 |\Psi_0\rangle = \sum_{ia} t_i^a |\Psi_i^a\rangle \tag{5.29}$$

and

$$\hat{T}_2 |\Psi_0\rangle = \sum_{i,j,a,b} t_{ij}^{ab} |\Psi_{ij}^{ab}\rangle \tag{5.30}$$

where the t_i and t_{ij} are expansion coefficients.

The full couple cluster wavefunction [BM07] is given as

$$
\begin{aligned}
|\Psi_{CC}\rangle = e^{\hat{T}} |\Psi_0\rangle &= (1 + \hat{T} + \frac{\hat{T}^2}{2}...) |\Psi_0\rangle \\
&= (1 + \hat{T}_1 + \hat{T}_2 + \hat{T}_3 + ... + \frac{\hat{T}_1{}^2}{2} + \frac{\hat{T}_2{}^2}{2} + \frac{\hat{T}_3{}^2}{2} + ...\hat{T}_1\hat{T}_2 + \hat{T}_1\hat{T}_3 + \hat{T}_3\hat{T}_2 + ...) |\Psi_0\rangle
\end{aligned}
\tag{5.31}
$$

With Ψ_{CC} in hand, we can now attempt to solve the Schrödinger equation. Assuming the coupled cluster wavefunction is a solution to the Schrödinger equation, we obtain

$$
\hat{H} |\Psi_{CC}\rangle = E |\Psi_{CC}\rangle = E e^{\hat{T}} |\Psi_0\rangle \tag{5.32}
$$

If we multiply the above equation by both $\langle\Psi_0|$, we see

$$
\langle\Psi_0|\hat{H}|\Psi_{CC}\rangle = E \langle\Psi_0|\Psi_{CC}\rangle = E \tag{5.33}
$$

where $\langle\Psi_0|\Psi_{CC}\rangle = 1$ once we assume orthonormality of the determinants in our expansion.

Now we can express the energy of the system as

$$
\begin{aligned}
E = \langle\Psi_0|\hat{H}|\Psi_{CC}\rangle &= \langle\Psi_0|\hat{H}e^{\hat{T}}|\Psi_0\rangle \\
&= \langle\Psi_0|\hat{H}|\Psi_0\rangle + \sum_{ia} t_i^a \langle\Psi_0|\hat{H}|\Psi_i^a\rangle + \sum_{i,j,a,b} t_{ij}^{ab} \langle\Psi_0|\hat{H}|\Psi_{ij}^{ab}\rangle + ...
\end{aligned}
\tag{5.34}
$$

Thus in order to solve for E, one needs to solve for the expansion coefficients.

In order to to this, we can multiply Eqn. 5.32 on the left by $\langle\Psi^*| e^{-\hat{T}}$, where $\langle\Psi^*|$ is one of the excited state determinant terms included in $|\Psi_{CC}\rangle$, yielding

$$
\langle\Psi^*|e^{-\hat{T}}\hat{H}|\Psi_{CC}\rangle = E \langle\Psi^*|e^{-\hat{T}}|\Psi_{CC}\rangle = E \langle\Psi^*|\Psi_0\rangle = 0 \tag{5.35}
$$

where we have once again enforced orthonormality of our determinants. The above equation can be repeated for all Ψ^* to solve for all expansion coefficients in Ψ_{CC}. Greatly simplifying this calculation is that the $e^{-\hat{T}}\hat{H}e^{\hat{T}}$ operator can be expressed using Baker-Campbell-Hausdorf (BCH) expansion and is shown to terminate at the fourth order [BM07].

Full CI and full coupled cluster theory methods generally converge to the same solution as they both include all possible excitations within a given basis set. However, the full expansion coupled cluster wavefunction runs into the same issues as the full CI wavefunction in that number of terms generally scales with the factorial of the number of electrons in the system. Therefore, coupled cluster methods, like configuration interaction methods, usually involve truncating the Ansatz waveform to only include certain excitations. Thus, a coupled cluster calculation is usually specified by the level of truncation used as

CCS: ($\hat{T} \approx \hat{T}_1$)
CCSD: ($\hat{T} \approx \hat{T}_1 + \hat{T}_2$)
CCSD(T): ($\hat{T} \approx \hat{T}_1 + \hat{T}_2$, $\hat{T}_3$ treated perturbatively)
CCSDTQ: ($\hat{T} \approx \hat{T}_1 + \hat{T}_2 + \hat{T}_3 + \hat{T}_4$)
and so on.

There are a number of disadvantages and advantages of coupled cluster (CC) methods with respect to CI calculations. Namely, while CI calculations are variational (i.e. expansion coefficients are varied to minimize E), CC methods are not. There are many reasons for this [BM07], but in the end, the non-variationality generally means that the CC energy cannot be assumed to necessarily be greater than the true ground state energy of the system.

However, there are other advantages. It can be shown that CC calculations are size-extensive [BM07], meaning that the total energy of a non-interacting system is the sum of its individual components, whereas truncated CI methods do not possess this property [BM07]. This is of particular importance in correctly calculating dissociation curves, for example. Consider two noninteracting atoms spaced by R whose energy is $E(A, B, R)$. A size-extensive energy calculation would imply

$$E(A, B, R) = E(A) + E(B) \tag{5.36}$$

an equality truncated CI calculations fail to satisfy [Cre13] due to differing levels of excitation being applied to the combined system versus the separate subsystems. To clarify, for interacting systems, this size-consistency issue would affect truncated CI calculations at any

internuclear separation distance, meaning even $E(A, B, \infty) \neq E(A) + E(B)$, a troubling result indeed (although this can partly be corrected for, through Davidson corrections [Sza05], for example).

This property, along with the fact that coupled clustered correlation energies generally converge more quickly that those obtained from CI calculations [BM07], make CC methods typically preferred over CI calculations, although this may vary system to system. Generally, CCSD(T) is considered the 'gold standard of computational chemistry' [SO96,SL90], yielding highly accurate results while balancing reasonable computation time.

Lastly, in the above sections we have been using the Hartree-Fock wavefunction as a *reference* wavefunction on which all our excitation operators are performed. In general, the reference wavefunction need not be the Hartree-Fock wavefunction; instead, multiple reference wavefunctions may be used, resulting in what is known as a *multirefernce* calculation. While multireference calculations are more expensive, they can become advantageous when calculating transition energies between ground and excited states. In these situations, the reference wavefunctions are chosen judiciously to ensure that the correlation energy calculation for the excited and ground states are performed to similar degrees of accuracy, so transition energies between the states may be better known.

5.2.3 Møsser Plosset Pertubation Theory

Lastly, we may consider perturbative methods as well that are often computationally less expensive that the CI and CC methods. First, we can recall that $|\Psi_0\rangle$ is an eigenfunction of the Fock-operator $\hat{f}$, as defined in Eqn. 5.14.

$\hat{f}$ does not treat electron correlation fully and we can define the 'missing' component as

$$\hat{V}' = \hat{H} - \hat{f} \tag{5.37}$$

where $\hat{H}$ is the full electronic Hamiltonian as defined in Eqn. 5.10. We then can then treat $\hat{V}'$ as a perturbation to $\hat{f}$ as a way to determine how much energy we 'missed out' on with our Hartree-Fock treatment.

According to standard perturbation theory, the first and second order energy corrections terms can be expressed as

$$E \approx E_0 + E_1 + E_2 = \langle\Psi_0|\hat{f}|\Psi_0\rangle + \langle\Psi_0|\hat{V'}|\Psi_0\rangle - \sum_{i<j,a<b} \frac{\langle\Psi_{ij}^{ab}|\hat{V'}|\Psi_0\rangle^2}{(\epsilon_a - \epsilon_i) + (\epsilon_b - \epsilon_j)}$$
$$= \langle\Psi_0|\hat{H} + \hat{f} - \hat{f}|\Psi_0)\rangle + \sum_{i<j,a<b} \frac{|\langle\Psi_{ij}^{ab}|\hat{V'}|\Psi_0\rangle|^2}{(\epsilon_a - \epsilon_i) + (\epsilon_b - \epsilon_j)} = E_{HF} - \sum_{i<j,a<b} \frac{\langle\Psi_{ij}^{ab}|\hat{V'}|\Psi_0\rangle^2}{(\epsilon_a - \epsilon_i) + (\epsilon_b - \epsilon_j)} \tag{5.38}$$

where ϵ_i is the energy of the i^{th} spin-orbital. The substitution was made in the above equation by recalling that E_{HF} is the optimized expectation value of the $\hat{H}$ operator.

In perturbation theory, the second-order sum is carried over all basis states of the system. For us, a complete basis would consist of an infinite amount of N-particle Slater determinants of various degrees of excitation (similar to Full CI). So why do we only consider the doubly-excited terms in our second-order energy? According to Brillouin's Theorem [Sur89], all single-excitation matrix elements will be zero, and triply-excited or higher-excited states will also be zero because the perturbation operator only considers pairwise interactions [Sur89]. This allows for a dramatic simplification of the second-order energy.

Third- and fourth-order perturbation correction terms may be considered as well, but, in general, the computation time for such calculations is non-trivial, and further it has been found that these correction terms generally do not converge. For these reasons, a second-order (MP2) calculation is often used in the field.

MP2 methods do not optimize the Slater orbitals or the reference wavefunction and require only integrals to be performed, offering computational advantages over other post-Hartree-Fock methods. However, since the wavefunction is not optimized, any reference errors associated with Φ_0 and its associated molecular orbitals will be passed along to the MP2 calculation [Cre11]. As with any of the above methods, the strengths and weaknesses of the method have to be assessed when determining if it is appropriate for a given problem.

5.3 Software Suites

Implementing the above iterative algorithms programmatically can be quite challenging; however, fortunately, these routines have been efficiently packaged into a number of commercially available software suites. In fact, the majority of computational chemistry performed for research included in this thesis was performed using the Gaussian [FSL91] and MOLPRO [WKK18] packages. These packages allow convenient platforms for Hartree-Fock, as well as post-Hartree-Fock, calculations to be performed and also allow for density functional theory calculations.

While these packages simplify the computation process, one must be judicious in choosing what type of calculation is appropriate for a given system. As mentioned above, each of these approximation techniques has its weak points, and these vulnerabilities will inform what the most effective way is to choose basis sets, reference configurations, correlation energy calculations, etc. In general, multiple calculations can also be performed at various levels of theory to cross-reference results and better ensure accuracy.

CHAPTER 6

Experimental Implementations

This chapter will provide an overview both of the atomic and molecular species studied in this work as well as the LQT-MOT hybrid trap experimental apparatus in which the species were studied (see Fig. 6.1). Particular emphasis will be placed on the optical and mass spectrometry detection techniques that are used to analyze the electronic state population, velocity, and mass of the studied particles, tools that collectively form the crux of virtually all scientific measurements made in this work. A description of the laser systems utilized in this work, as well as the leak valve apparatus used to introduce controlled amounts of gaseous reagents into our vacuum chamber, will also be provided.

6.1 Vacuum system

If the ambient pressure within the atom-ion trapping volume is too large, reactive and elastic collisions with background gas particles can cause the particles to be lost from the trap. These ejection events are caused either by elastic collisions that impart energies to the atom/ions that surpass their associated trap depths, or by reactive events that convert the trapped particles into other species, both of which are effects that limit trap lifetime. Therefore, to maintain stable trapping environments for both our ions and our MOT, ultra-high vacuum (UHV) conditions ($\lessapprox 10^{-9}$ mbar) are required.

The housing that provides our trapping environment is a 8" Kimball physics extended spherical octagon (MCF800-ExtOct-G2C8A16), which is held at UHV pressure by a Varian sputtering ion pump (VA-911-5034, pumping speed 60 L/s). A titanium sublimation pump (TSP) is also present in the system and further reduces pressure in the chamber by emitting

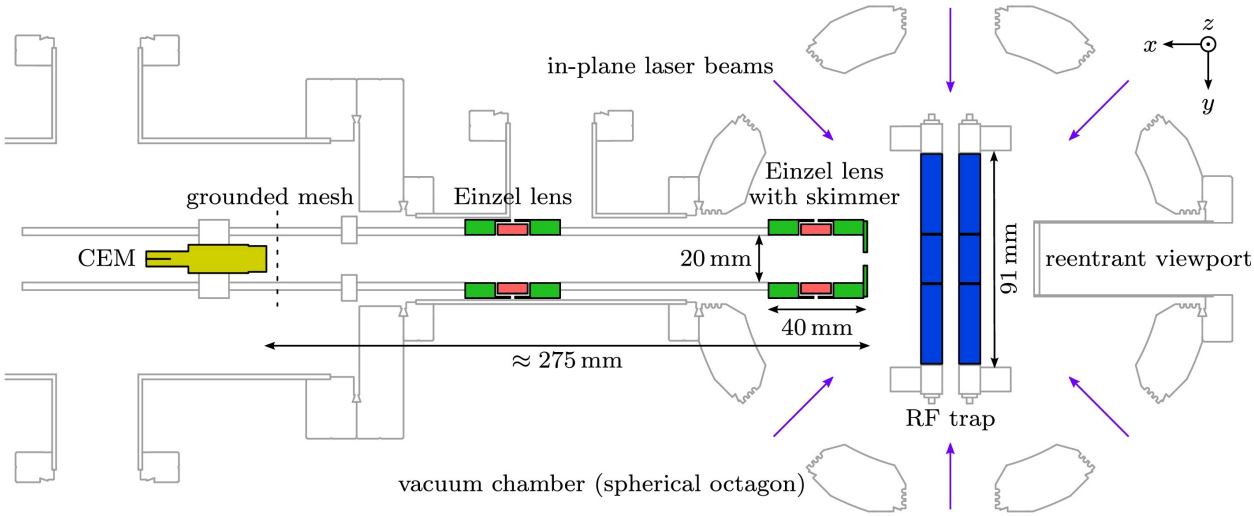

Figure 6.1: MOTion experiment diagram

A schematic diagram of the MOTion apparatus and its key measurement devices, including a depiction of the ToF-MS system, the LQT, and the reentrant viewport used for optical imaging of the ion species. This figure is borrowed from Ref [SSY16].

a stream of titanium that coats the walls of the chamber and binds with background gas particles to form a solid along the chamber walls, thereby reducing the ambient gas pressure.

To be discussed in later sections, a time-of-flight mass spectrometer (ToF-MS) and a leak valve system are also attached to the main chamber, which allow for LQT mass analysis and the controlled introduction of reactive gas particles into the chamber, respectively. The entire vacuum apparatus as well as the required cooling lasers and many of their associated control electronics, are positioned on a 12' x 5' Newport optical table, which is floated to lessen problematic mechanical vibrations that can affect trap/laser stability.

The octagon possesses sixteen 1.33", eight 2.75" and two 8" CF flanges, the majority of which are fitted with optical viewports to allow for camera imaging of the trapped species as well as optical access for the six-beam MOT configuration and the ion cooling beams.

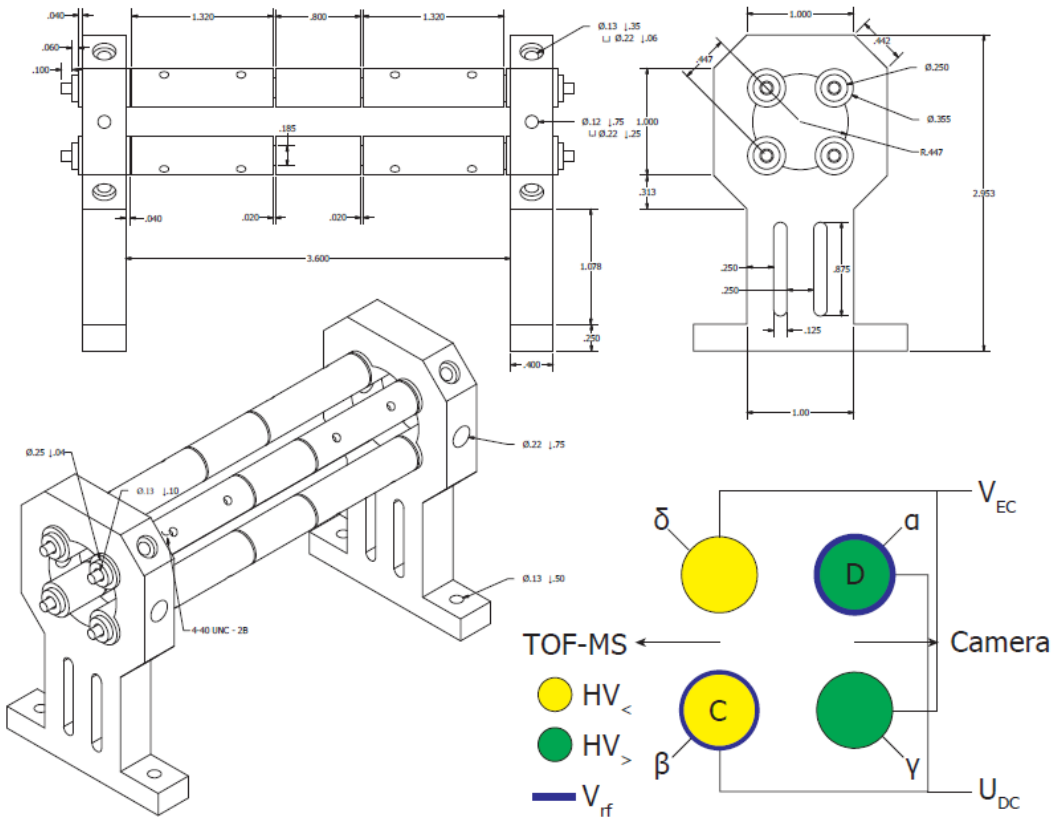

Figure 6.2: Schematic drawing of the LQT

Drawings that display the various dimensions of the LQT utilized in this work. As seen in the lower right hand corner, the α and β rods are equipped with a rf voltage, while all four rods may be assigned an independent DC voltage, allowing for adjustment of the Mathieu a/q-parameters of the trapping potential as well as excess micromotion compensation. Further, high voltage DC pulsing is applied to the α/γ rods and the δ/β rods in order to guide the ions into the ToF-MS. This figure is borrowed from Ref [Sch16].

6.2 The ion trap and the control electronics

6.2.1 The ion trap

The ion trap utilized in this thesis is a standard segmented four-rod linear quadrupole trap (LQT) (see Fig. 6.2 for a diagramatic depiction, borrowed from Ref [Sch16]), where each rod consists of three segments. The initial design of the trap was developed in Ref. [Sul13] and later revised in Ref. [Sch16]. For a more complete description of the engineering specifics, the reader is referred to those sources. Under normal trapping conditions, the α and β rods are supplied with a rf trapping voltage, while the δ and γ rods are not supplied with any rf (see Fig. 6.2 for rod labeling). All four rods may be biased with either HV or DC for ToF-MS extraction and excess micromotion compensation, respectively, as to be discussed below.

6.2.2 Control electronics

The individual rods must be equipped with rf trapping voltages (V_{rf}), DC bias voltages (U_{DC}), and the ability for high voltage (U_{HV}) pulse sequencing for extracting the ions into the time-of-flight apparatus. These requirements are made more stringent by the need for phase and amplitude matching of the applied rf voltages, as well as proper synchronization of the extraction pulses across the four rods. If this synchronization is performed improperly, the ions may experience unnecessary micromotion or may be inefficiently coupled into the mass-spectrometer.

These requirements inspired the development of a sophisticated set of electronics, known as MOTion drive units, that have now been exported to a variety of ion trapping groups throughout the nation. The reader is referred to Ref. [SSY16] for a complete discussion of the MOTion drive units, but a brief overview will be presented here.

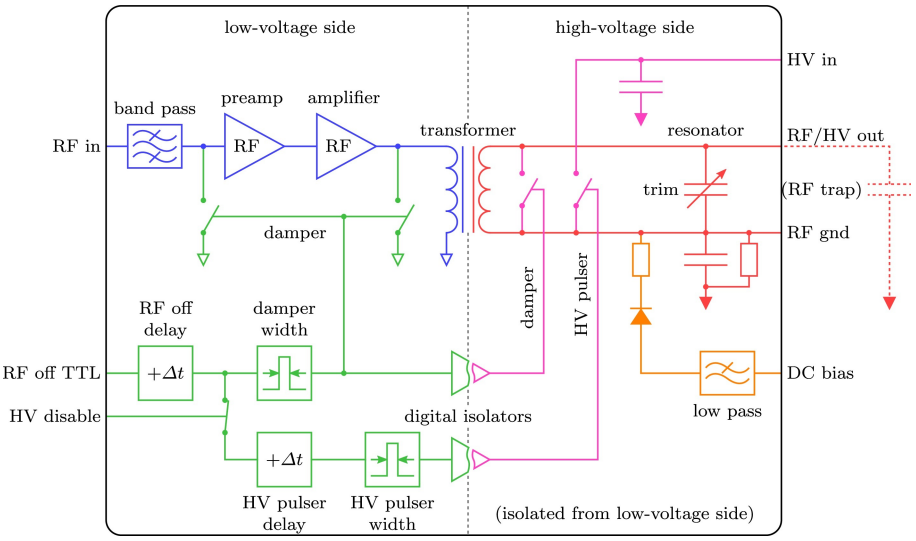

Figure 6.3: Simplified circuit diagram of MOTion drive unit

The circuit is divided into a primary low-voltage (left) and secondary high-voltage (right) side, which are isolated from each other through a toroidal transformer. The low-voltage side consists of rf amplifiers and the primary winding of the rf transformer (blue), as well as timing and damping circuitry (green). The high-voltage side consists of the secondary winding of the transformer along with capacitors that collectively form the resonator circuit (red). In addition, damping and HV pulsing circuitry (purple) and a U_{DC} bias supply is also present on the secondary side. This figure is borrowed from Ref [SSY16].

6.2.2.1 Drive units

There are twelve drive units total, one unit for each segment of the trap, and a simplified circuit diagram for the units is presented in Fig. 6.3 (borrowed from Ref. [SSY16]). Each drive unit is supplied an input rf voltage (supplied via a direct digital synthesis board (DDS), described in 6.2.2.2), which is initially RC-filtered before subsequently being amplified by both a preamplifier and a power amplifier. The power amplifier then drives the primary side of a toroidal transformer with a total turn-number of a few tens.

The secondary side of the transformer consists of an LC circuit, where the total capacitance of the resonant circuit is set collectively by the capacitance of the output cables, rf electrodes, vacuum feedthroughs, and lastly, an adjustable trim capacitor than can be used to fine-tune the resonant frequency (typically set to $\approx 2\pi \times 680$ kHz). One end of the secondary side of the transformer is connected to the rf trap electrode, while the other end is rf grounded via a capacitor, which allows biasing of the rf trap segment with DC voltages, as is required for the HV pulsing and micromotion compensation.

U_{DC} is supplied by a DC power supply that is fed through a low-pass filter and an HV diode (as a protection from U_{HV} to rf ground). Similarly, U_{HV} is applied to rf ground by activating a MOSFET which is supplied by a HV power supply and bypassed with a capacitor. As a result, not only the trap electrode but the entire secondary side of the drive unit is biased with U_{DC} permanently and U_{HV} during pulsing.

Merely turning off the rf source prior to HV pulsing would result in a ring-down time of ~ 10 μs on the secondary side of the transformer, causing problematic effects during ion extraction. To remedy these effects, active damping of the resonator on both its primary and secondary side is achieved using MOSFETs, which essentially short the windings of the rf transformer. Logic circuitry allows adjustment of the delay and duration of both the damping and HV pulsing sequences, and these parameters are further synchronized across all drive units for maximum ToF-MS coupling efficiency.

6.2.2.2 Timing control

The rf signals are generated by four direct digital synthesis (DDS) devices, which each have four channels whose individual frequency, phase, and amplitude can be set programatically. All four DDS devices receive the same 500 MHz reference clock signal for synchronization of the outputs, and further, the output cables are chosen to be of similar lengths to ensure that the signals reach the drive boxes simultaneously.

Additional clocks are also introduced into the system to ensure the buffer input/output sequences and the synchronization of the digital interface of the DDS devices are performed properly [SSY16]. Perhaps most crucially, the additional clocks help ensure that HV pulsing sequences are initiated at consistent rf phases. This helps ensure that the potential gradient the ions are accelerated through during ToF-MS extraction is consistently maintained even as other parameters associated with the rf signal are varied.

These synchronization devices are collectively managed by a microcontroller, which can be sent commands over a serial-to-USB interface coupled to the main experimental control computer or also accessed through the lab wi-fi network.

6.2.2.3 Wiring

The outputs of the drive units are connected to the vacuum chamber over ≈ 175 cm long low-capacitance coaxial cables. These cables have 75Ω mini-SMB connectors and are plugged into one of four printed circuit board (PCB) wiring units positioned on the 1.33" CF-flanges on the vacuum chamber. The PCB interfaces possess receptacles that mate the electrical pins of the vacuum feedthroughs to SMB connectors, and the units also provide the ground connection to the vacuum chamber. On the vacuum side, three wires per feedthrough are connected to the three segments of an electrode (leaving one wire per feedthrough unused).

The interface PCBs also include capacitive pickups, which sample a small fraction of the rf/HV voltage supplied to the segments and can be used for signal monitoring. The pickup signal allows the measurement of the input voltages at each segment with a probe ratio of $\approx 1000 : 1$ (as measured with an oscilloscope with 1 MΩ impedance and typical cable

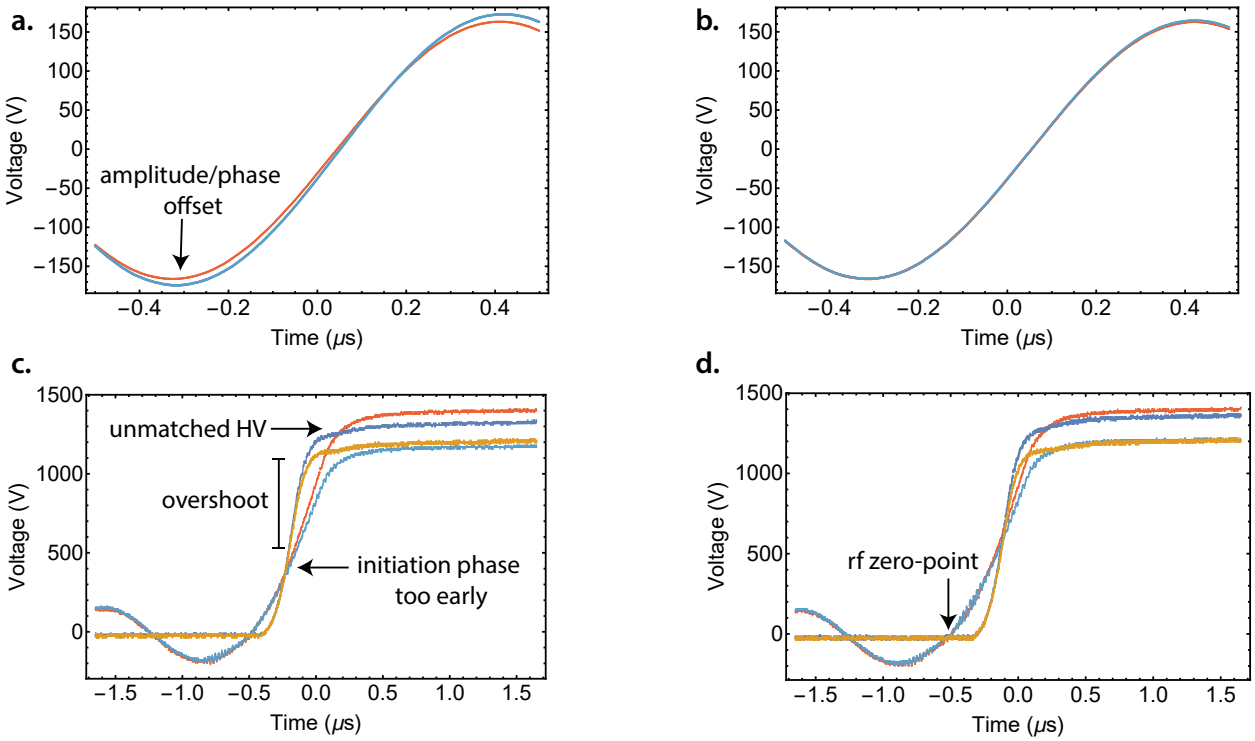

Figure 6.4: Optimized and unoptimized MOTion drive unit outputs

(a) and **(c)** display unoptimized signals from the MOTion drive boxes during both rf output and HV pulsing, as measured through pickup electrodes. In **(a)**, the relative phase and amplitude between the rf applied to diagonally opposed rods in the LQT can be seen to differ. In **(c)**, the asymptotic HV values between the front and back rod pairs both appear to diverge and the phase initiation time for the non-rf rods is chosen too early such that a suboptimal voltage 'overshoot' occurs that will likely compromise the mass resolution and detection efficiency of the ToF-MS. **(b)** and **(d)** display optimized rf output and HV pulse sequences, respectively, that avoid these issues to a large degree.

lengths). These ratios are calibrated against an HV probe (Agilent 10076B) to better than 1% (relative).

6.2.2.4 Optimization

While monitoring the pickup electrodes on an oscilloscope, commands can be sent to the microcontroller to adjust the phase and voltage amplitude of each rf channel such that the produced signals are properly matched. Further, the parameters of the HV extraction

sequence, such as the rf phase at which the sequence is initiated (see Ref. [SCR12] for further details), can also be controlled. Fig. 6.4 displays output traces for both rf output as well as HV extraction sequences both before and after such optimization has been performed.

For the voltage/phase rf optimization, the oscilloscope used to monitor the pickup traces can be interfaced with the experimental control computer through LabVIEW, allowing the phase and amplitude of the rf electrodes to be programmatically varied to minimize their mismatch with one another.

The HV extraction parameters can also be optimized to maximize the detection efficiency and mass resolution of the ToF-MS. There are two main parameters to optimize here - the final voltage each rod will reach and the phase at which the pulse sequence is initiated. The pulse initiation phases and amplitudes are initially coarsely chosen to match the following criteria.

Firstly, for the rods with rf applied (α and β), the initiation phases should be chosen such that the pulse sequence begins at roughly at the rf zero point, where the rf voltages cross the 0 V threshold with a positive slope.

Secondly, the HV values themselves are also adjusted so that each pair of front/back rods asymptote to approximately the same value, as this allows for the ions to be ejected most directly along the ToF-MS axis. Simulations conducted in the SIMION software suite demonstrate that, during an extraction sequence, the ions studied in this work exit the LQT in approximately ~ 1 μs; however, the majority of their motion occurs in the latter 500 ns of this timeframe, when the HV pulses have essentially reached their steady state value (10%-90% rise time of ≈ 250 ns). Thus, choosing the HV amplitudes such that they are well-matched asymptotically is most critical for ToF-MS performance; however, slight offsets from these values may be chosen to account for physical misalignments between the LQT and ToF-MS by 'steering' the ions into the entrance of the spectrometer.

Lastly, the initiation phase of the non-rf rods (δ and γ) are adjusted such that the pulse signals for these rods intersect those of the rf rods (α and β) pulses at roughly half of their respective maximum amplitudes (see Fig. 6.4). This condition is chosen for the following

reason. The rise time of the HV pulse is slightly different for the different MOTion drive units. Primarily, this is because the the MOTion drive units supplying the rf voltage to the α and β rods have a resonant frequency of $\sim 2\pi \times 680$ kHz, while the drive units that supply the HV to the non-rf δ and γ rods have resonant frequencies of $\sim 2\pi \times 1800$ kHz. The boxes have different trapping frequencies to allow us to switch between the two settings if desired; however, in an approximate sense, their different associated capacitances can be understood as causing the two units to have different RC rise times.

Therefore, due to these differences in rise times, for a given pair of front/back rods, if the initiation phase is chosen so that the pulses are well-matched during the beginning of the HV sequence, an 'overshoot' will occur towards the end of the sequence (see Fig. 6.4c), and vice versa. In practice, choosing the initiation phase such that the voltages intersect at roughly half of their asymptotic values balances the amount of 'overshooting' that occurs during early and late portions of the pulse sequence; however, finer optimization is typically performed by observing experimental mass-spectra and adjusting HV phase and amplitude parameters to maximize the corresponding ToF-MS mass-resolution. Ultimately, however, initiation phase selection is a relatively minor consideration when compared to the asymptotic amplitude matching criteria, for reasons mentioned above.

The HV and low-voltage DC signals needed for biasing of the rf electrodes are provided by separate homebuilt, low-noise DC (0-50 V) and HV (0-2 kV) power supplies, engineered by Peter Yu and Christian Schneider. These power supplies are heavily low-pass filtered to ensure that the resultant output signals have minimal frequency components at secular resonances of the ion trap. Table 6.1 provides typical voltage values at which the LQT is operated as well as other parameters related to the trap.

6.3 Atomic and molecular species of interest

Both laser-coolable atomic ions and molecular ions are of interest in this work. The central molecular ion of interest is $BaCl^+$, while the atomic ions of interest are Ba^+ and Yb^+. Both of the atomic ions are simple spin-1/2 systems with a hydrogen-like structure possessing a single

Parameter	Description	Typical Value	Relevant rods
V_{rf}	Trapping rf amplitude	320 V_{pp}	(α, β)
Ω	Trapping rf frequency	$2\pi \times 680$ kHz	(α, β)
V_{EC}	Axial confinement	~0-30 V	(endcap electrodes)
U_{DC}	a-parameter/micromotion compensation	~0-30 V	(α, β, γ, δ)
r_0	Radial electrode spacing	6.81 mm	
z_0	Axial endcap spacing	10.2 mm	

Table 6.1: Table describing the various rf voltages, DC voltages, and spatial dimensions of the LQT in this work.

valence electron. Correspondingly, both can be laser-cooled through standard two-color optical configurations where one beam addresses the central cycling transition and a second beam serves as a 'repump' that reintroduces population that has leaked into metastable levels back into the central cooling cycle. Further, since this work only focuses on laser-cooling of even-mass species, the effects of hyperfine structure can be neglected.

6.3.1 The Ba^+ ion

The level structure for Ba^+ is presented in Fig 6.5a. As can be seen in the figure, the cooling transition (A=$2\pi \times 15.2$ MHz) along the $6s\,^2S_{1/2} \rightarrow 6p\,^2P_{1/2}$ line lies at 493 nm while the repump transition (A=$2\pi \times 4.9$ MHz) along the $5d\,^2D_{3/2} \rightarrow 6p\,^2P_{1/2}$ line is centered at 650 nm, with the metastable $^2D_{3/2}$ state possessing a ~ 80 second lifetime. The ~1:3 branching ratio between the cooling and repump transition is closer to 1 than those found in many other ion laser cooling schemes, and thus the Ba^+ ions can be imaged along either the 650 or 493 nm lines, a convenient feature for avoiding optical scatter in the imaging system, as discussed later.

Further, since both transitions couple to the $^2P_{1/2}$ level, coherent population trapping (CPT) effects result in the creation of non-laser addressed dark states in the system when both beams are present. CPT is a general effect that occurs in so-called Λ cooling systems

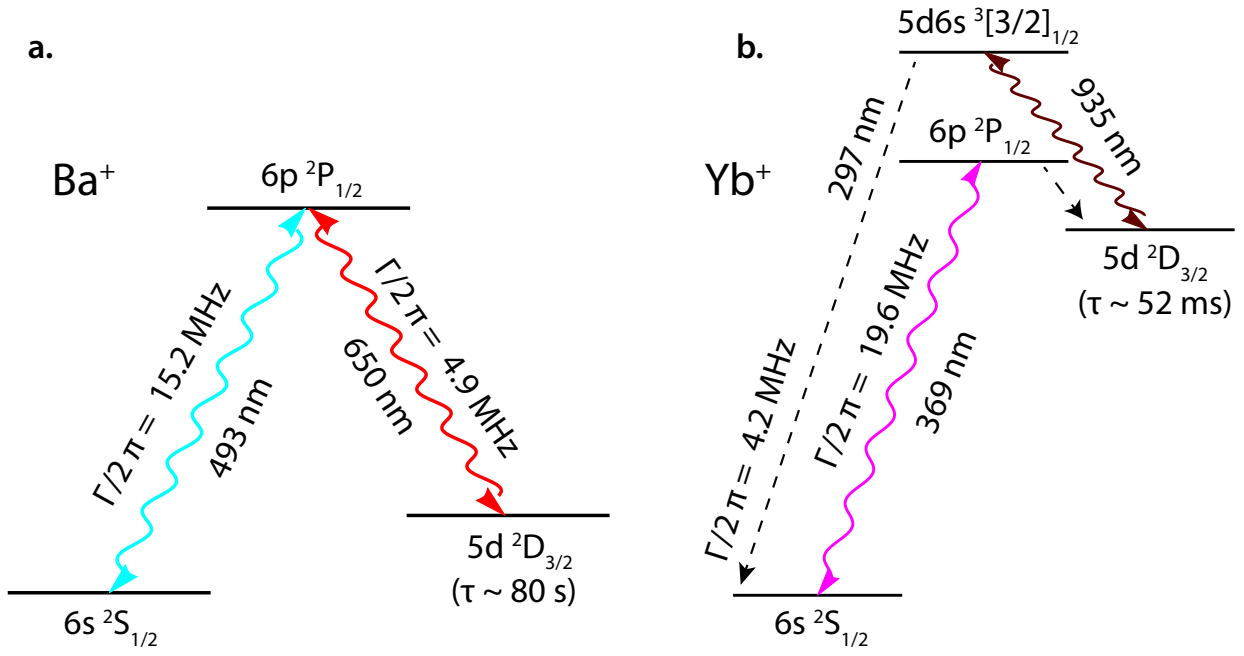

Figure 6.5: Ba^+/Yb^+ laser-cooling diagrams

Energy level diagrams for Ba^+ (**a**) and Yb^+ (**b**). Laser-driven transitions are depicted with squiggly lines whereas relevant spontaneous emission lines are presented with dashed lines. Basic information about the transitions, such as the wavelength and Einstein-A coefficient, are also presented. The lifetimes of relevant metastable states, τ, are presented below each such level.

in which both the repump and cooling transition couple to the same excited state. In Ba^+, when the beams for both of these transitions possess the same laser detuning with respect to the $^2P_{1/2}$ state, optical dark states that are a coherent superposition of the **S** and **D** levels are formed. Ions that fall into these levels are unable to be addressed by the laser fields and thus interrupt the laser-cooling cycle. In order to maintain optical cycling, a non-zero magnetic field is introduced into the system that lessens buildup into these dark states by transferring the dark population into bright states addressed by the lasers. Due to these coherent effects, Einstein-rate-equation models are typically insufficient for accurate Ba^+ steady-state modeling and instead need to be supplanted by optical-Bloch-equation treatments involving all eight levels of the density matrix [SMA17].

6.3.2 The Yb^+ ion

Yb^+, on the other hand, possesses a four-level atomic structure where both the cooling and repump transitions are coupled to different states, removing the difficulties of dark-state formation. In the four-level scheme of Yb^+ (Fig 6.5b), the cooling transition (A=$2\pi \times 19.2$ MHz) lies along the 369 nm $6s\,^2S_{1/2} \rightarrow 6p\,^2P_{1/2}$ line. The $^2P_{1/2}$ level can decay into the $5d\,^2D_{3/2}$ metastable state (lifetime ~ 50 ms), and population from this level is reintroduced into the ground state through the $5d\,^2D_{3/2} \rightarrow 5d6s\,^3[3/2]_{1/2}$ 935 nm transition, where the $5d6s\,^3[3/2]_{1/2}$ level is a mixed state that has a high spontaneous emission branching ratio into the ground state.

The isotope shifts on the cooling and repump lines for adjacent even isotopes of Yb^+ are roughly ~ 4 GHz each, which enables one laser-cooled isotope of Yb^+ to sympathetically cool other non-laser-cooled Yb^+ isotopes while avoiding blue-detuned heating effects, which could be present if the splitting were on the order of hundreds of MHz, as in Ba^+.

6.3.2.1 Ablation loading of atomic and molecular ions

Ions are loaded into the ion trap through laser ablation of targets by a pulsed 1064 nm ND:YAG laser (Continuum Laser's Minilite II series, 5-7 ns pulse width). A single pulse of

the ablation laser strikes the target, positioned roughly ~ 1 in from the center of the ion trap, and causes a plume of ions to be ejected into the surrounding vacuum. Two targets are present in the trap, a Yb^+ metal ingot target, composed of a natural abundance of Yb^+ isotopes and a powdered $BaCl_2$ target, which typically ejects a natural abundance of both Ba^+ and $BaCl^+$ ions. Therefore, ablation loading may be used to load both atomic ions and molecular ions. To avoid excessive electrode charging, we typically limit pulse energies to 2 mJ/pulse, although the system is capable of producing up to $\sim$15 mJ/pulse.

After the firing of the ablation pulse, the trapping rf is momentarily shut off to allow the ejected ion plume to enter the trapping volume uninhibited. After a controllable delay time (typically set to ~ 50 μs), the rf trapping field is switched on again to snare a portion of the ion plume within the ion trap potential. This delay time can be scanned to more efficiently load ions of specific masses and to optimize the overall loading efficiency of the plume as a whole.

Additionally, the ablation pulse energy can also be tuned to control the number of ions emitted by the target. Manipulating the size of the ablation beam will also accomplish this goal, and a standard one-lens configuration is used to focus the beam to the desired spot size on the ablation target. Care must be taken, especially when utilizing high ablation energies, to avoid striking the trap rods with the beam, causing problematic electrode charging that can destabilize the trapped ions.

6.3.3 $BaCl^+$

The molecular ion at the center of this thesis is the $BaCl^+$ molecule. As an ionically bonded molecule composed of two closed-shell atoms, Ba^{2+} and Cl^-, $BaCl^+$ exhibits reduced chemical reactivity compared to other ions [Hud09]. Further, its large dipole moment and convenient rotational splitting make the molecule a promising candidate for quantum information applications, such as the development of a high-fidelity rotational-level qubit [HC18].

Many exciting applications with this molecule require internal state control as well as initialization into the ro-vibrational ground state. While laser cooling has been impres-

State	R_e (a_0)	D_e (cm^{-1})	ω_e (cm^{-1})	$\omega_e\chi_e$ (cm^{-1})	B_e (cm^{-1})
$^1\Sigma^+$	4.89	39103	339.5(7)	1.19(10)	0.0903
$^1\Pi$	6.38	2083	96		0.0528

Table 6.2: Table describing the molecular constants for the $BaCl^+$ $^1\Sigma^+$ and $^1\Pi$ states. Values with error bars are obtained from Ref [BVH15] and subsequent work by the same group, whereas all other values are obtained from Ref. [CSK11] and subsequent work from the Svetlana Kotochigova's group at Temple University.

sively implemented [AAB18,BMN14,KBM17] for this purpose for a select class of molecules, the leaky nature of molecular excited states prevents closed cycling transitions from being identified in many systems. As an alternative, we hope to achieve internal state cooling through sympathetic-cooling collisions with ultracold Ca atoms [Hud09,RSS12], a technique that should be generalizable to many other systems. $BaCl^+$ is particularly well-suited for this method since its electron affinity energetically precludes the molecule from undergoing 2-body chemical reactions with ground-state Ca [Hud09].

As is the case for most atomic and molecular species, the first step to control is spectroscopy. Once the rotational and vibrational transitions within the molecule have been mapped out, methods for robust readout and state control can be developed.

We have collaborated with excellent molecular spectroscopists for this goal. In Ref [BVH15] and in more recent experiments by Michael Heaven's group at Emory University, the vibrational spectroscopic constants were experimentally mapped out for the $^1\Sigma^+$ ground state, while rotational constants have also been extracted for this state from theoretical molecular potentials calculated by Svetlana Kotochigova's group [CSK11] at Temple University. All obtained constants for the $BaCl^+$ system are presented in Table 6.2. While this level of structural characterization has been immensely helpful for vibrational state readout [RSS12, CSK11], finer energy-level resolution will be needed as we push forward towards rotational-state readout and control (see Chapter 12).

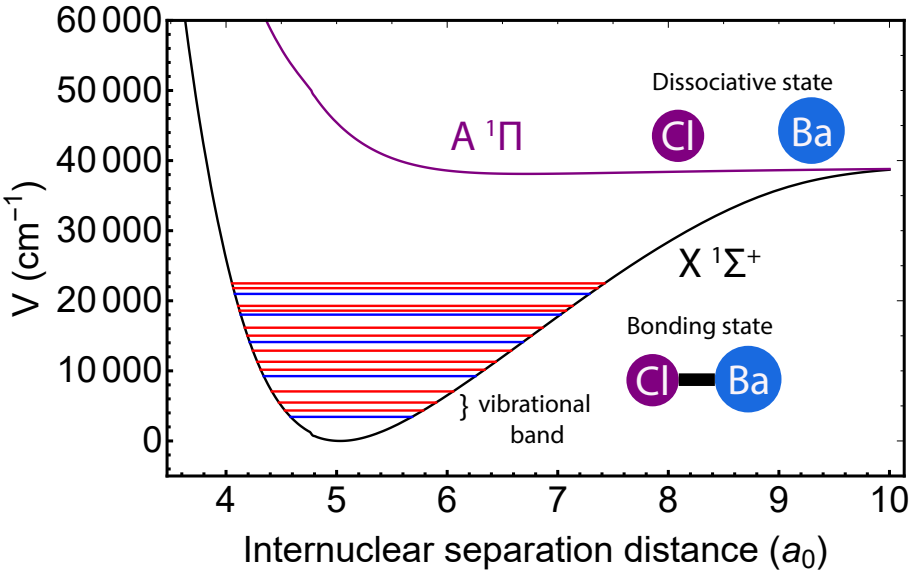

Figure 6.6: $BaCl^+$ molecular potentials

Molecular potentials for the $BaCl^+$ $^1\Sigma^+$ and $^1\Pi_1$ molecular electronic states. The $^1\Sigma^+$ potential yields a series of bound states characterized by rotational and vibrational quantum numbers. Select $(v = v', J = 0)$ band-head states are shown in blue with the remaining states in each v' vibrational manifold shown in red (only a subset of rotational states are shown). The $^1\Pi$ state is a repulsive potential with no bound states; promotion into this potential results in dissociation of the molecule.

Further, aside from the ground state, many electronically excited states in $BaCl^+$ also exist. However, most of the work in this thesis concerns only the ground $^1\Sigma^+$ state as well as the lowest lying dissociative $^1\Pi$ state, shown in Fig. 6.6 (potentials obtained from Professor Hua Guo's group at the University of New Mexico).

Lastly, the $BaOH^+$ and $BaOCH_3^+$ molecular ions are also of interest in this thesis, as they serve as reactants for many of the studied atom-molecular ion reactions, and thus, they will be further discussed below.

6.3.3.1 Molecular ion loading

While $BaCl^+$ can be loaded directly into the LQT through ablation, a number of other molecular ions of interest in this work, such as $BaOH^+$ and $BaOCH_3^+$, can be introduced into the ion trap through reaction. In particular, a background CH_3OH (methanol) gas is

present in our chamber that ultimately limits our Ba^+ trap lifetime to 1000-2000 s due to reactive collisions (reactions with Yb^+ are comparatively suppressed).

Interestingly, the background methanol was unintentionally introduced into the chamber. This most likely was a result of cleaning the vacuum components of our chamber in a supersonic bath of liquid methanol prior to assembling our chamber and a virtual leak forming once the chamber was sealed. However, fortuitously, the methanol reactions have provided the foundation of some of the most interesting chemistry discussed in this thesis [PMS17].

The following reactions [DSL93, LY98] can occur between Ba^+ and CH_3OH

$$\begin{aligned} Ba^+ + CH_3OH &\rightarrow BaOCH_3^+ + H \\ Ba^+ + CH_3OH &\rightarrow BaOH^+ + CH_3 \end{aligned} \tag{6.1}$$

Experimentally, the rate of these reactions can be extracted by obtaining reaction kinetics data in which a sample of Ba^+ ions is initially loaded into to chamber, the sample is allowed to react for variable amount of time, and then all reactant and product species in the LQT are ejected into the ToF-MS, giving an indication of how the relative product/reactant amounts evolve in time.

The data can be fit to the following set of differential equations in order to solve for the various reaction rates of the system

$$\begin{aligned} \frac{dN_{Ba^+}}{dt} &= -(k_{Ba^+\rightarrow BaOCH_3^+} + k_{Ba^+\rightarrow BaOH^+})N_{Ba^+} \\ &\quad + k_{BaOH^+\rightarrow Ba^+}N_{BaOH^+} + k_{BaOCH_3^+\rightarrow Ba^+}N_{BaOCH_3^+} - \Gamma_L N_{Ba^+} \\ \frac{dN_{BaOH^+}}{dt} &= -k_{BaOH^+\rightarrow Ba^+}N_{BaOH^+} + k_{Ba^+\rightarrow BaOH^+}N_{Ba^+} - \Gamma_L N_{BaOH^+} \\ \frac{dN_{BaOCH_3^+}}{dt} &= -k_{BaOCH_3^+\rightarrow Ba^+}N_{BaOCH_3^+} + k_{Ba^+\rightarrow BaOCH_3^+}N_{Ba^+} - \Gamma_L N_{BaOCH_3^+} \end{aligned} \tag{6.2}$$

where $k_{i\rightarrow j}$ refers to the rate of reaction of species i into species j (the density of the methanol vapor is implicitly absorbed into this coefficient) and Γ_L refers to the overall trap loss rate, for example caused by high energy collisions with background gas particles (assumed to be species independent).

The solutions Eqn. 6.2 can be fit to the reaction kinetics data described above to extract the associated rates, as shown in Fig. 6.7.

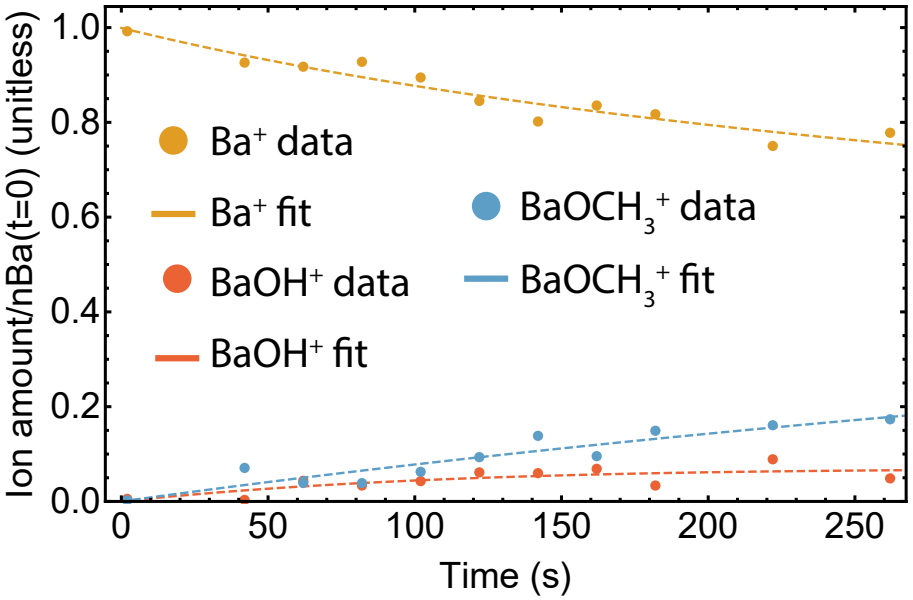

Figure 6.7: Methanol reaction kinetics

Reaction kinetics obtained by loading a Ba^+ sample and allowing it to react for a variable amount of time with the background CH_3OH gas before ejecting the entire ion sample into the LQT. The y-axis is the ion amount of each species present in the LQT at a given instance of time, normalized by the initial amount of Ba^+ present in the system. The solutions of Eqn. 6.2 can be fit to the kinetics data to obtain reaction rates for the formation of $BaOH^+$ and $BaOCH_3^+$.

We note that in Eqn. 6.2 presented above, we allow for both forward and backwards reactions. While the specifics of the potential surface of the (Ba^+ + CH_3OH) pair have not been mapped out to our knowledge, the reactions in Eqn. 6.1 are generally understood to be exothermic [DSL93]. However, at the collision energy of the ions within the LQT, the particles may have enough energy to clear any energetic barriers posed by backward reaction processes, especially if these processes are photon-assisted by beams present in our chamber. Further, photodissociation events may cause any formed molecules to be dissociated into their initial reactant constituents. While we do not have direct knowledge of the exact nature of these back-reactions processes, it appears the best fits to our reactions kinetics data occur when such events are included. In general, these back reactions may be collision-energy or laser-intensity dependent, and the rate-extraction fits should be repeated for any measurement in which these parameters are varied.

With the above rates in hand, rates for other reactions involving $BaOCH_3^+$ and $BaOH^+$ can also be determined, as to be discussed in Chapter 9.

6.4 Time-of-flight mass spectrometer

The time-of-flight mass spectrometer (ToF-MS) is an incredibly powerful tool for characterizing atom-ion chemistry in hybrid trapping systems such as ours. Much of the technical aspects and optimization procedures of the ToF-MS used in our system have been discussed in Refs. [SCR12, SSY16, SSC14]; however, a general overview of the system, including a discussion on the principles of operation, will be given here.

6.4.1 Principles of operation

When attempting to measure ion amount within a LQT, many approaches may be taken. For example, one may place a channeltron detector nearby the LQT and introduce a mass-specific secular excitation signal to one of the trap electrodes [CSK11, HW12]. The species that is excited by this resonant secular excitation will gain energy and eventually be ejected from the LQT, and a portion of these purged ions will hit the channeltron detector, registering an ion-

number-dependent signal. The resonant frequency can then be swept across other masses, and the process can be repeated to gain a mass spectrum of the trap. While straightforward to implement, this technique suffers from low detection efficiency and does not allow for simultaneous mass readout of multiple ion species.

Another approach, as detailed in Refs. [SCR12, SSY16, SSC14], is radial time-of-flight mass spectrometry. In this approach, after an ion sample has been loaded in a LQT, the trapping rf is extinguished and a HV pulse is applied to both the front and back pair of rods. The front pair is set to a lower voltage as compared to the back pair, creating a potential gradient that accelerates the ion towards the front pair of electrodes.

After passing the front pair of electrodes, the ions pass through a grounded skimmer plate (diameter ≈ 5 mm) and enter a field-free drift tube. The velocity that the ions possess upon entering the drift tube is dependent on the mass of the species and is given approximately as

$$q\Delta V = \frac{1}{2}mv_f^2 \tag{6.3}$$

where ΔV is the potential difference which the ions are accelerated through, m is the mass of the ion, and v_f is its final velocity. A more thorough treatment of the process is presented in Ref. [WM55], but the gist is that the heavier the mass the slower the final velocity.

A channeltron detector is placed at the end of the drift tube (≈ 254 mm). As a cluster of ions collide with the channeltron, the device outputs an ion-number-dependent current which can be read on an oscilloscope. The oscilloscope tracks this current as a function of time, which can be read as a string of time-tagged voltages on the oscilloscope monitor. This current is also dependent on the channeltron gain, which is in turn set by the detector bias voltage (typically held at $\approx$1700 V).

By monitoring the channeltron output as a function of time, one can simultaneously measure the ion amount of a wide range of masses in the LQT, as shown in Fig. 6.8. The narrower the time-width of the mass cluster peaks, the greater the mass resolution. Therefore the various time and voltage parameters in ToF-MS extraction sequence are optimized to

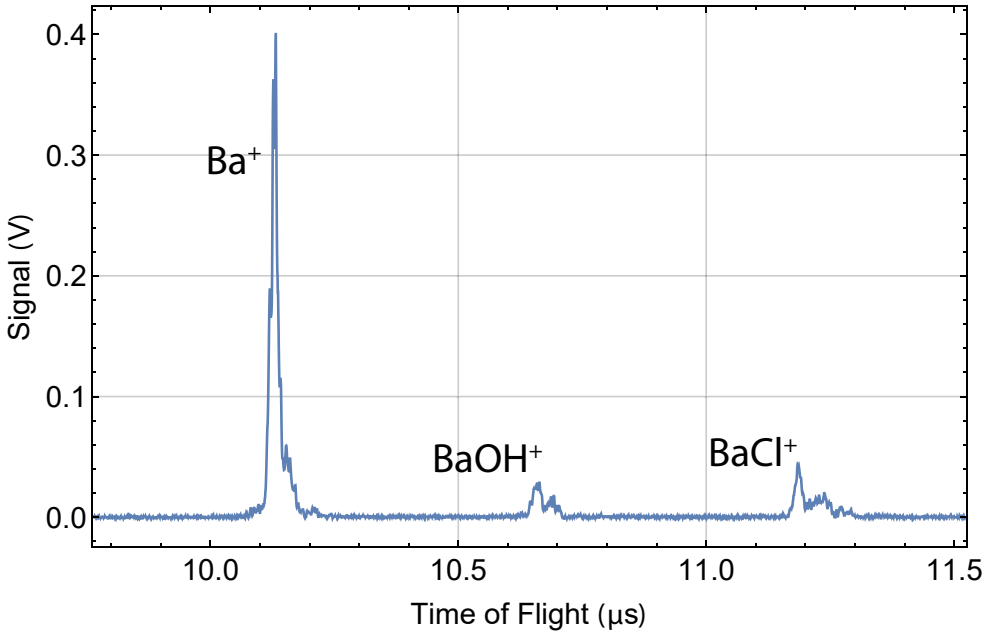

Figure 6.8: Sample ToF-MS mass spectrum

Channeltron voltage as a function of time. As can be seen, the Ba^+, $BaOH^+$, and $BaCl^+$ species reach the detector at different times, allowing their ion numbers to be individually resolved.

ensure that each mass cluster arrives at the channeltron detector at as uniform of a time as possible while satisfying other constraints in the system.

The skimmer, which has a roughly 6 mm circular diameter, serves multiple purposes in this process. Firstly, it prevents ions that are ejected extremely off-axis (with respect to the axial dimension of the flight tube) from reaching the channeltron detector. If these ions reached the detector they would have severely bent trajectories, meaning their path length would be longer and they would reach the detector at a later time, broadening the time-width of the channeltron signal and thereby compromising the mass-resolution. Thus the skimmer rejects these ions, improving mass-resolution while sacrificing detection efficiency to a slight degree.

The second purpose the skimmer serves is allowing for a two stage acceleration scheme. Initially described in Ref [WM55], a two stage acceleration scheme involves accelerating the ions from $V_{LQT}(z) \rightarrow V_2 \rightarrow 0$ V, as opposed to a single stage acceleration scheme that accelerates the ions as $V_{LQT}(z) \rightarrow 0$ V. In our system, the back (~ 1400) and front (~ 1200)

rod voltages, V_1 and V_2 respectively, set $V_{LQT}(z)$ and V_2, while the skimmer is held at ground.

Note that $V_{LQT}(z)$ is position dependent because the ion cloud has a non-zero spatial width (~ 500 μm radial width). The potential field created in the LQT during pulsing can roughly be thought of as that produced by a parallel plate electrodes, where $V_{LQT}(z) = Ez$ where E is the electric field between the rods. Thus, the position of the ion within the LQT will determine what initial voltage it feels when the HV is pulsed.

Therefore, the ions closer to the front rods accelerate through less of a potential difference than ions positioned further from the front rods. Thus, while having a shorter path length to the detector, the front-most ions also have a smaller drift-tube velocity than the back-most ions.

Of course, in a single-stage scheme, this isn't necessarily an issue if one could choose to vary the position of the detector to find the location where the back-most ions have exactly 'caught up' to the front most ions; however, this parameter is not convenient to vary experimentally and further may conflict with other design considerations, such as placement of ion-focusing optics. Therefore, these effects in general lead to broadening of the time-width of each mass cluster, significantly impairing mass-resolution.

The two-stage scheme depicted in Fig. 6.9 improves on this method by splitting the acceleration into two stages. Essentially there are two effects to consider in the system: 1) the fact that the front-most ions have a smaller path length to the detector and thus will reach the detector first given the same velocity, 2) the fact that the back-most ion will in general experience a larger potential difference and thus will reach a larger drift-tube velocity than the front-most ions. Ideally, one would balance the velocity difference between the back-most and front-most ions such that both species reach the detector at the same time, and the two-stage process allows just this flexibility.

In the first stage, the ions are accelerated through a potential difference of $V_{LQT}(z) \rightarrow V_2$. The larger $V_{LQT}(z)$-V_2 is, the larger the difference in exit velocity between the front-most and back-most ions. On the other hand, if $V_{LQT}(z) \approx V_2$, the ions will hardly accelerate at

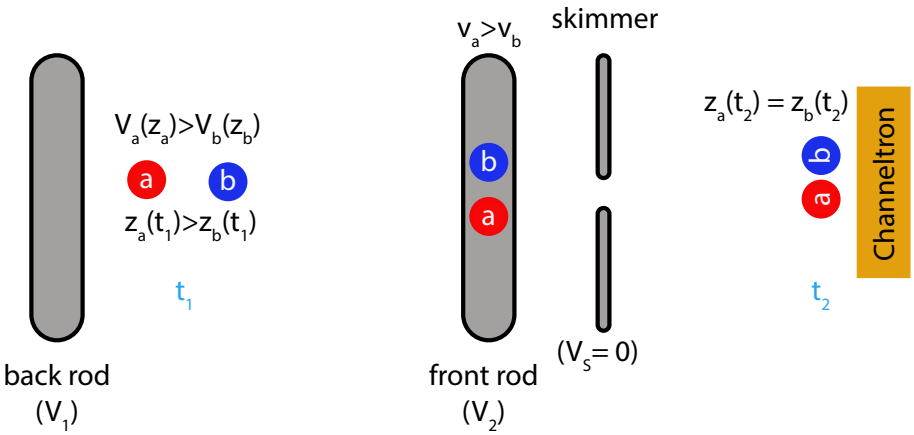

Figure 6.9: Two-stage acceleration in the ToF-MS

Sequence of events in a two-stage acceleration scheme in a ToF-MS. The back rod is set to V_1 while the front rod is set to V_2. Thus, at t_1, the moment the HV is pulsed, the ion towards the back rod, ion a, experiences a higher potential than ion b; however, ion a's position, z_a, is also further from the detector than ion b's position, z_b ($z_a(t_1) > z_b(t_1)$). Consequently, the velocity of ion a when it reaches the front rod is larger than that of ion b ($v_a > v_b$ at this point), but ion b reaches the front rod before ion a does temporally. After reaching the front rod, both ions are then accelerated through of potential difference of $V_2 \rightarrow 0$ V as they pass through the grounded skimmer. V_1 and V_2 are adjusted so that the ions reach the detector at essentially the same time ($z_a(t_2) = z_b(t_2)$), with their difference in drift tube velocities accounting for their initial difference in position in the LQT.

all through the first process, and consequently, their final velocity will be set by the $V_2 \rightarrow 0$ V stage, which is the same for all ions. In this way, one can tune V_2, as well as V_1, strategically such that, at the position of the detector, the path length difference is optimally balanced by the velocity dispersion effect, as detailed with great clarity in Ref. [WM55] and displayed schematically in Fig. 6.9.

In addition to the two-stage scheme, in order to establish a large detection efficiency, ion trajectories in both the radial and axial planes must be adjusted to prevent ion loss due to collisions with the chamber wall. The ion trajectories upon exiting the LQT differ in both of these planes, largely due to the skewed aspect ratio of the LQT and its associated extraction potential. To correct this astigmatic ion beam, we employ two Einzel lenses with differing focusing strengths, which are set by the voltages applied to the Einzel electrodes. The first Einzel lens, positioned directly after the skimmer, approximately collimates the ions in the axial plane and sufficiently decreases the divergence in the radial plane to avoid ion loss. A second Einzel lens, added closer to the channeltron detector, slightly focuses ions in the axial plane while approximately collimating the ions in the radial plane [SCR12]. In practice, the voltages of both Einzel lens are scanned in order to optimize the detection efficiency of the system; however in general, there is a compromise between detection efficiency and mass-resolution that must be struck, since allowing more ions with off-axis trajectories to reach the channeltron also results in broadening of the time-width of each mass cluster peak.

Table 6.3 provides typical voltage parameters at which the ToF-MS is operated and Fig. 6.10 presents a diagram of the entire system. Once again, we note that the front rods have a slight voltage offset to allow for 'beam-steering' of the ion beam to account for spatial misalignment of the LQT with respect to the channeltron detector.

6.4.2 Optimization

There are many ways to coarsely optimize the ToF-MS operating settings experimentally, and we choose an iterative approach. V_1 and V_2 are coarsely set by the Wiley/McLauren condition and initially these values are fixed. We then adjust the HV pulse initiation phase

Description	Typical Value (V)	Relevant rods
Front rod pulse voltage	1209	δ
Front rod pulse voltage	1195	β
Back rod pulse voltage	1386	(γ, α)
First Einzel lens voltage	940	
Second Einzel lens voltage	610	
Channeltron bias voltage	1700	

Table 6.3: Table describing the various rf voltages, DC voltages, and spatial dimensions of the LQT in this work.

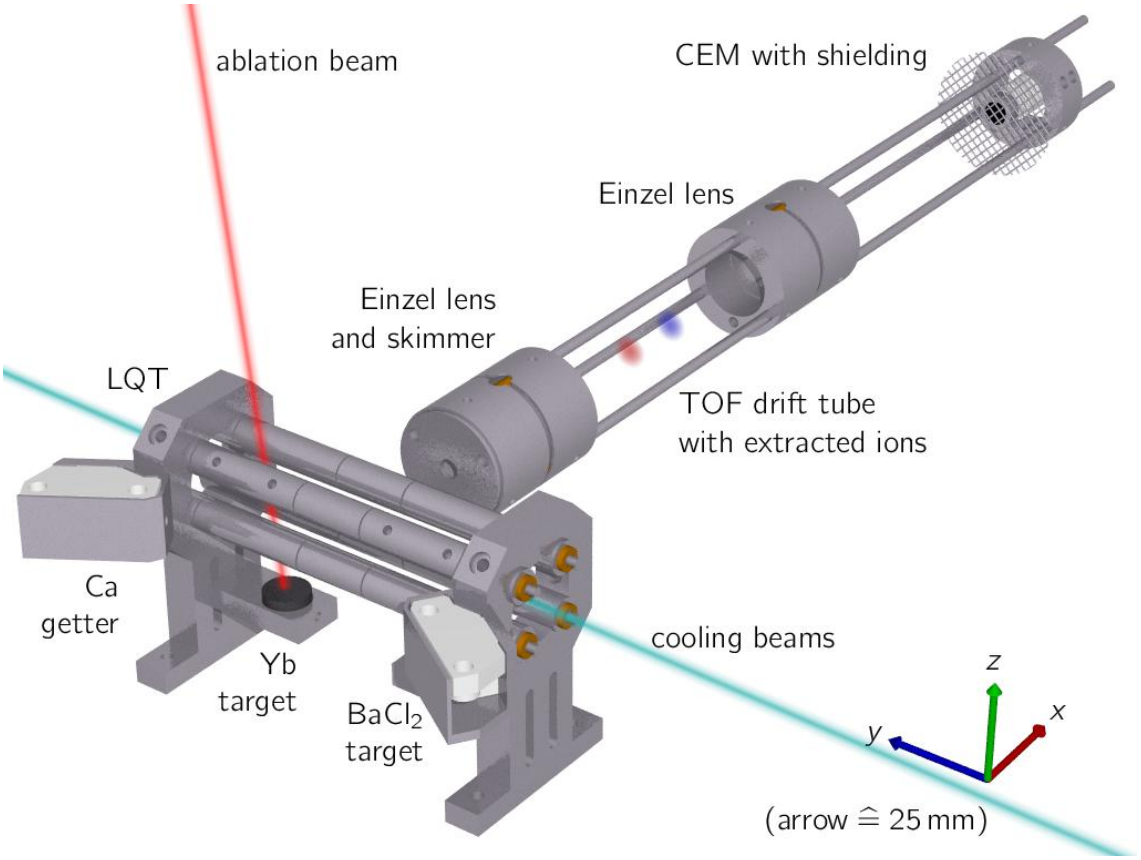

Figure 6.10: Digram of MOTion trap coupled into a ToF-MS

Diagram of a series of ion clusters being ejected from the the MOTion trap LQT into the ToF-MS. Also depicted are the Yb and $BaCl_2$ ablation targets used for LQT loading as well as the Ca getter units employed for loading the MOT.

to match the criteria presented in the Sec. 6.2.2.4. At this point, we load samples of ions into the ion trap and adjust the offset on the front rods, while both Einzel lenses are grounded, to maximize detection efficiency. This coarsely optimizes the 'beam-steering' of the ions onto the detector. At this point, the front Einzel lens is turned on and its voltage is varied to maximize detection efficiency, and then the same process is repeated for the second Einzel lens.

At this point, either the V_1-V_2 or the initiation phase can be adjusted and the process can be repeated, eventually yielding settings that offer an acceptable local maximum for detection efficiency. Once detection efficiency has been optimized, we can turn our heads to mass resolution. At this point, essentially all parameters (pulse initiation phase, Einzel lens voltages, extraction voltages) can be finely varied to essentially 'throw-away' off axis ions that are reaching the detector, thereby reducing detection efficiency while increasing mass resolution. Fortunately, there is not much of a need for a mass resolution greater than $m/\Delta m \approx 500$, a value easily achievable with even modest optimization when studying directly laser-cooled and sympathetically-cooled species [SSC14]. Fig. 6.11 displays a resulting isotopically resolved mass spectrum for a sample of laser-cooled $^{138}Ba^+$ ions, along with its sympathetically cooled dark isotopes.

Most of these optimization routines are performed using the laser-cooled species of interest (Ba^+, Yb^+) in this work. Of course, some of the effects of the Einzel lens focusing and the HV pulse sequence may also be mass-dependent. For example, extremely light ions may accelerate over a larger distance during the rise time of the HV pulse and therefore may be affected differently by the beam steering. This could potentially result in off-axis entry into the field free drift tube that could complicate Einzel lens focusing. For the work conducted in this thesis a m/z ratio range of ≈80-200 is studied, a range in which none of the mentioned effects appear to differ significantly.

One way this can be verified is by initializing a sample of Ba^+ in the LQT and allowing the sample to react into $BaOH^+$ and $BaOCH_3^+$. The entire sample can then be ejected into the ToF-MS, and the summed ion amount, normalized by initial ion amount through fluorescence imaging for example (see Sec. 6.5.1), can be monitored as a function of reaction

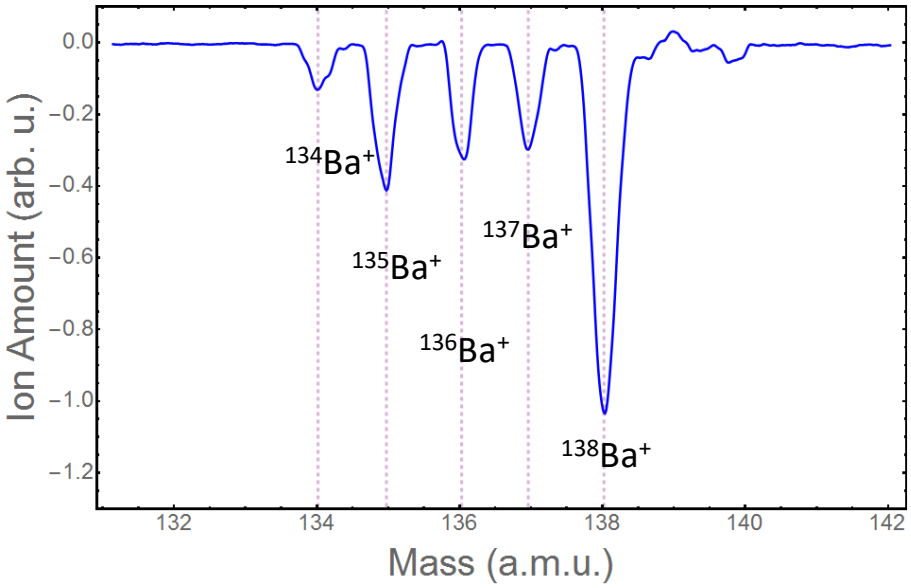

Figure 6.11: Optimized ToF-MS spectrum

The resultant mass-spectrum from a sample of laser-cooled $^{138}Ba^{+}$ ions, as well as its sympathetically cooled natural isotopes, obtained after optimizing the ToF-MS parameters

time. If the decay rate of total ion number is consistent with 0 over the timescale studied, it is a good indication that detection efficiency is not varying much as a function of mass. Indeed, if the detection efficiency of the higher-mass species was quite lower, we would expect a statistically significant decay as reaction products are lost during the extraction process (the reaction rate should be faster than the trap loss rate to avoid a complications here). Of course, this measurement also assumes that the studied reactions do not have exit channels that would result in LQT ejection, i.e. trap ion number is conserved throughout reaction.

While the above-mentioned routine can check for heavier-mass detection efficiency changes, similar checks, when possible, should also be performed for lower-mass regions if relevant to experiments.

6.4.3 Mass-timing calibration

The relationship between ToF arrival time and mass for a given species is given by $t_a = k_a\sqrt{m_a} + t_0$ where t_a is the arrival time for the species of interest, m_a is the mass of the species of interest, k_a is a proportionality constant, and t_0 is an offset time. The ToF-MS

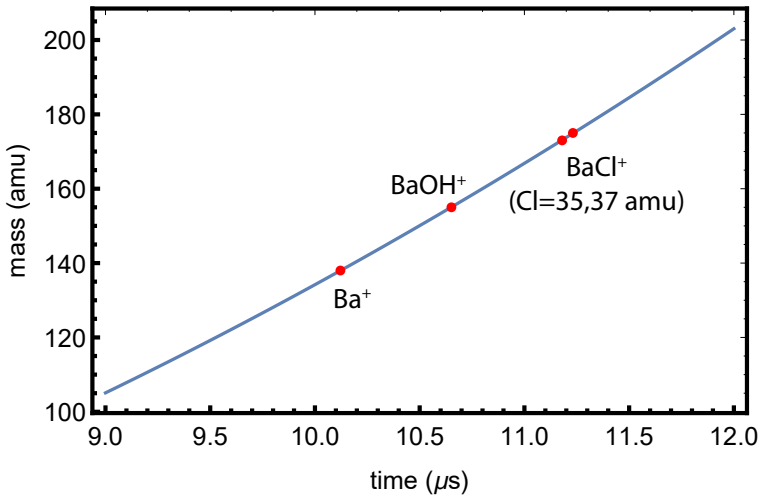

Figure 6.12: Mass-timing ToF-MS calibration

Measurements of ion mass plotted as function of channeltron arrival time for Ba^+, $BaOH^+$, and $BaCl^+$. Also presented is the fit to the inverted equation presented in Sec. 6.4.3, with t_0=1.30(3) and $\gamma_a = \frac{1}{k_a^2}$=1.77(1).

is calibrated by measuring channeltron arrival times for species of known masses in our system (isotopes of $BaCl^+$, Ba^+, $BaOH^+$, and $BaOCH_3^+$) and performing a fit using the above functional form to determine k_a and t_0 (see Fig. 6.12). Once these constants have been determined, mass-identification for unknown species in the LQT can be performed.

There are two main sources of mass determination error to consider. Firstly, there is an uncertainty in peak arrival time associated with the temporal spread of each species' ToF signal. To this end, a Gaussian fit is applied to each mass signal to extract the arrival time uncertainty. Secondly, statistical errors in our actual ToF-MS calibration can be determined from the fit errors to the free parameters in the above arrival time equation. In addition to the errors associated with the parameters themselves, the accuracy of our mass determination for unknown species in the trap increases as the mass of these unknown species nears the calibration masses, since the calibration is inherently well known at these points. For example, Ca^+ is further away in mass from its nearest calibration mass (Ba^+ - 137.9 amu) than BaO^+ is ($BaOH^+$ - 154.9 amu), and while both species are still isotoptically resolvable, the associated calibration-related mass determination error is greater for the former.

This calibration-based error is calculated from spreads in 95% confidence interval bands applied to our calibration fit, assuming ion arrival time uncertainties as determined by the above-mentioned Gaussian mass signal fit. By adding our confidence interval uncertainty in quadrature with the mass error determined from propagating error through the arrival time equation, we can extract conservative overall mass determination errors.

6.4.4 ToF-MS Performance

After optimization has been performed, single Ba^+ ions may be loaded into the LQT and ejected into the ToF-MS to assess the single ion detection efficiency. The number of ions can be counted prior to ToF-MS ejection via optical imaging (see Sec. 6.5), and this value can be compared to the resultant integrated ToF-MS spectrum. This process is first repeated for a single ion multiple times, and the detection efficiency for the channeltron registering a detectable response above a determined discrimination level is roughly $\sim 30\%$. In addition to this detection efficiency, this is also a variation in detector response, as the channeltron response current also has a distribution. For a single ion, this distribution is shown in Fig. 6.13a.

However, in reality, the detector gain is also dependent on output-current, and thus, the response also varies with ion number as saturation occurs. This response is investigated in Fig. 6.13b where ion number is varied and the channeltron output is observed after ejection of the sample in the ToF-MS. Here, ion number is initially counted in two ways.

Firstly, for low ion numbers that can be counted optically, we use camera imaging to count the number of resolvable particles. Secondly, for larger three-dimensional structures, we fit spatial dimensions to fluorescence images of the crystal, assuming prolate spheroid density profiles, and then multiply the resultant ion volume by the space-charge limited density to extract ion numbers (see Sec. 6.5.1 for details).

The results of such a measurement are presented in Fig. 6.13b. As can be seen from the figure, at low ion numbers, where the amount of ions is individually countable, we see a roughly linear response; however, the response function becomes non-linear as ion number

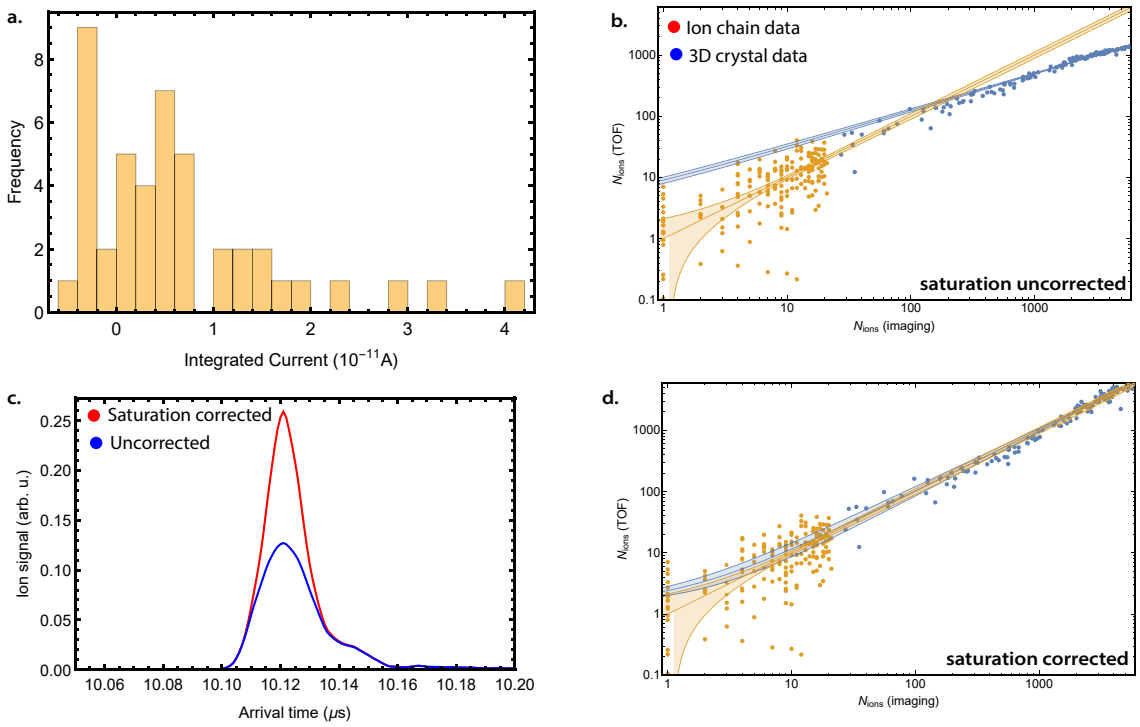

Figure 6.13: ToF-MS calibration and saturation correction

(**a**) A histogram of the integrated detector current when a single ion is detected in the ToF-MS. For a single ion, non-detection events are distinguished from detection events based on whether the detector voltage surpasses a certain discrimination level during the detection time window (not depicted in the plot), with an overall detection efficiency of $\sim 30\%$. (**b**) Laser-cooled Ba^+ ions are initialized in the LQT, and the total ion number is counted in one of two ways. For linear chains, single-ion-resolved optical detection is used, and for non-single-ion-resolvable 3D structures, spatial estimates of the crystal size are used to extract ion number values. After the ions are initialized, they are ejected into the ToF-MS, and a scatter plot is created to compare the optically-measured ion number to the integrated ToF-MS detector response. Here, the y-axis is proportional to the total integrated current from the channeltron and is converted into an effective ion number by fitting the equation $y = mx + b$ to the low-ion-number data, with determination of m providing the necessary conversion factor. Fits to the detector response are applied to both low-ion-number and high-ion-number data, with the fit coefficients for the two data sets being visibly different, implying detector saturation. Here, the solid lines denote the fit and the bands represent 90% confidence intervals. (**c**) Due to detector saturation the voltage profile of the channeltron output has to be transformed by Eqn. 6.4. In the plot, this function is applied to the mass-spectrum of a Ba^+ crystal, with the saturation effect quite significant (here total ion number is taken to be proportional to the integrated ion signal curve). (**d**) The calibration in (**b**) is repeated after applying the saturation correction function to the mass spectra, and the discrepancies between the low-ion-number and high-ion-number fits is greatly reduced.

is increased and saturation becomes an issue.

Saturation can be a problem for reaction rate experiments where reactant/product number is relied upon to extract rate constants. Therefore, we develop a method to account for detector saturation by applying the following function to each voltage in our mass spectrum

$$V_c(t) = V(t)e^{41.9543\,V(t)^{1.9765}} \tag{6.4}$$

where $V_c(t)$ is the saturation corrected voltage and $V(t)$ is the uncorrected voltage, with the functional form of the correction function empirically chosen to minimize saturation errors.

When Eqn. 6.4 is applied point-by-point to each voltage in the obtained mass spectra (Fig. 6.13c) and the calibration curve is replotted, we see a much more linear response at both low and high ion numbers, as shown in Fig. 6.13d. Indeed, the form Eqn. 6.4, which may seem unusual, was empirically chosen and optimized to match such a criteria. Of course, our saturation model assumes saturation is instantaneous and only depends on the detector voltage at a given instant of time. However, in reality, detector 'dead time' may play a role, and the history of previous voltages prior to a particular point may also affect that point's degree of saturation. However, given the quality of the fit shown in Fig. 6.13d, such effects may play a minor role. Further, this calibration also depends on factors such as detector age and gain and thus should be repeated regularly for accuracy, especially when the channeltron bias current has been altered. Lastly, the calibration is also dependent on knowledge of the ion-number-density, which in turn is subject to errors in trap secular frequency determination (see Eqn.6.5).

However, limitations aside, the above calibration allows for reasonably accurate ion number predictions for ion numbers ranging from a few tens to a few thousands, which will become of critical importance for quantum chemistry work discussed later in this thesis.

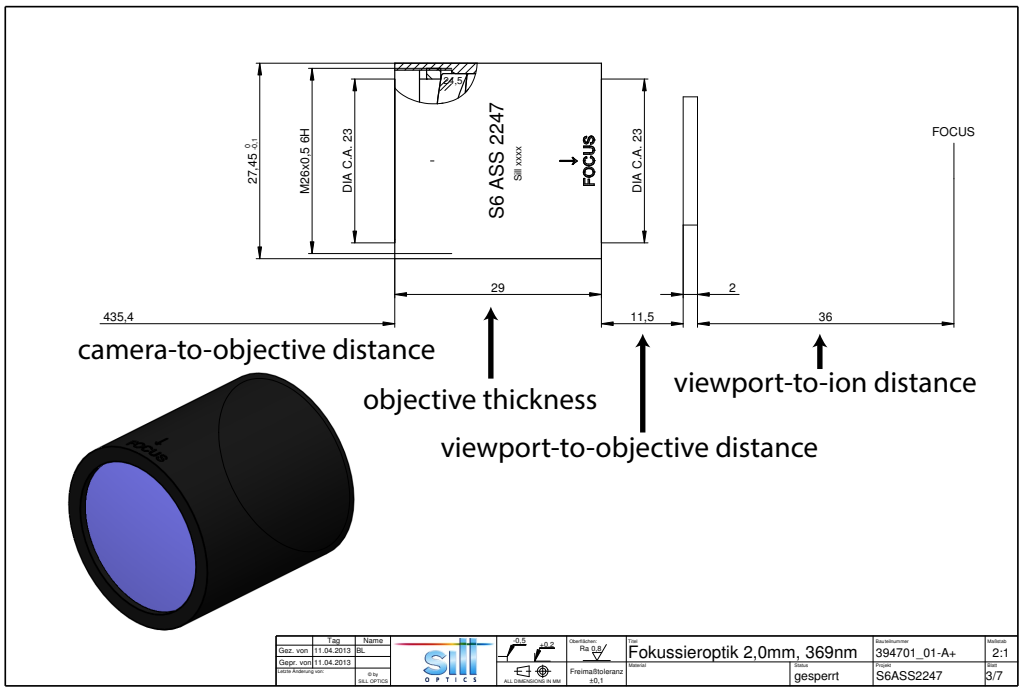

Figure 6.14: Reentrant imaging system dimensions

Dimensions of the reentrant imaging system, expressed in mm. The reentrant flange allows the objective to be placed roughly 50 mm from the ion, allowing for a total NA of 0.23

6.5 Imaging system

Electron-multiplying-charged-coupled-device (EMCCD) cameras (model Andor Luca-R, 1000 x 1000 pixels, 8 μm x 8 μm pixel size) are used to optically image the ionic and atomic species in this work. There are three main cameras used for this type of imaging: one camera that is positioned along a reentrant flange (DUV 2 3/4" sapphire viewport, MPF) aligned with the center of the LQT and two other cameras positioned along 1.33" viewports (UV Fused Silica), positioned at a relative angle (16°, 28°) and (-16°, 28°) with respect to the reentrant camera (azimuthal angle, polar angle) (assuming the axial dimension of the MOT coils sets the z direction of the trap).

For the reentrant camera, relevant dimensions of the objective (Sill Optics) imaging system is shown in Fig. 6.14, with the system having an overall imaging magnification of ~ 8

and a NA of 0.23. As the reentrant camera has by far the largest solid angle of the three cameras, it is the primary choice for imaging small ion crystals. In addition to the objective, a 2" mirror is also included in the optical setup to allow for redirection of the ion image. In addition, a filter wheel is included to allow for switching of the optical filters in the imaging system, which allows for Ba^+ ions to be imaged with either 650 nm or 493 nm light, Yb^+ ions to be imaged with 369 nm light, or even Ca atoms to be imaged with 422 nm light.

We note that 650 nm imaging of Ba^+ is particularly useful since only 493 nm light is typically used in the radially-oriented beams employed to provide the cooling necessary to create stable ion chains. As these beams also cause a majority of the optical scatter in the system due to their geometry, imaging on the 650 nm line can be very convenient. Typical camera settings used when studying ions are 100 ms exposure time, 4 x 4 binning, and an EM gain of 200.

The other two cameras imaging systems' consists primarily of a single 75 mm lens arranged in the 2f-2f configuration to provide a magnification of 1. Optical filters are again used in these systems, with the most commonly used filter a 369 nm/493 nm/422 nm tri-band-pass-filter that allows imaging of all three Yb^+/Ba^+/Ca species, a convenient feature when determining spatial atom-ion overlap factors. When imaging the Ca MOT, these cameras are typically run without EM gain at settings of 25 ms exposure time and 1 x 1 binning.

6.5.1 Ion number measurements from imaging

One of the most useful quantities that can be calculated through imaging, especially for the quantum chemistry experiments in this thesis, is the number of ions present in an ion sample. For laser-cooled species arranged in a chain, such as in Fig. 6.15a, this is a fairly straightforward matter of counting. As seen from Fig. 6.15a,c, non-laser cooled species that are sympathetically cooled are also observable.

However, when dealing with three dimensional structures where the ions are no longer individually countable, other approaches must be taken. The approach that is taken will depend on the phase of matter that the ions are in.

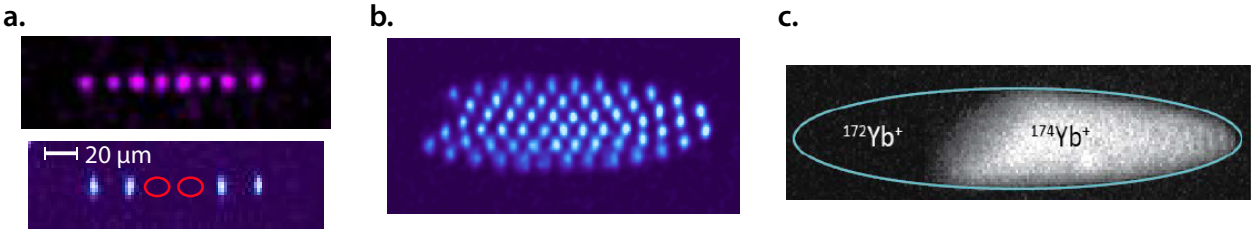

Figure 6.15: Ion fluorescence imaging

(**a**) False color images of linear chain of laser-cooled Yb^+ ions (top) and bi-sample of laser-cooled Ba^+ ions with two sympathetically cooled $BaCl^+$ ions (red circles denote their position). (**b**) Images of a resolved two dimensional crystal of Ba^+ ions. (**c**) Images of a non-single-ion-resolvable 3D crystal of laser-cooled $^{174}Yb^+$ and sympathetically cooled $^{172}Yb^+$. The two species spatially separate due to the radiation pressure on the $^{174}Yb^+$ ions.

If in the crystal phase, we can say that the ion has a constant density throughout its volume. The maximum possible density obtainable can be calculated as follows. Assume isotropic conditions such that ($\omega = \omega_x = \omega_y = \omega_z$). Consider a test charge positioned at a general radial distance r' from the center of the sphere - the maximum possible density will occur when the centripetal force inwards due to harmonic potential exactly equals the Coulomb repulsion along the outward radial dimension, calculated from Gauss's Law as

$$\begin{aligned} F_\omega &= F_C \\ m\omega^2 r' &= \frac{Q_{enc}}{4\pi\epsilon_0 r'^2} = \frac{Q^2 \rho_{max} V_{enc}}{4\pi\epsilon_0 r'^2} \\ &= \frac{Q^2\rho_{max}}{4\pi\epsilon_0 r'^2}\frac{4}{3}\pi r'^3 = \frac{Q^2\rho_{max}}{3\epsilon_0} r' \\ \rightarrow \rho_{max} &= \frac{3\epsilon_0 m}{Q^2}\omega^2 \end{aligned} \tag{6.5}$$

where $Q_{enc}(V_{enc})$ is the amount of charge (volume) enclosed at a radial distance r' from the sphere center and ρ_{max} is the maximum ion number density (charge density $= Q \times \rho_{max}$).

The expression yields an approximate maximum density for ions within an ion trap, a quantity typically only achievable at laser-cooled conditions. For the LQT conditions in this work, $\rho_{max} = 10^8$ cm^{-3}.

With ρ_{max} in hand, for ion crystals, the spatial density distribution can be modeled using

a prolate spheroid function as follows:

$$\rho(x,y,z) = \begin{cases} \rho_{max} & \frac{x^2}{r_x^2} + \frac{y^2}{r_y^2} + \frac{z^2}{r_z^2} \leq 1 \\ 0 & \frac{x^2}{r_x^2} + \frac{y^2}{r_y^2} + \frac{z^2}{r_z^2} > 1 \end{cases} \tag{6.6}$$

where r_x, r_y, and r_z are the spatial lengths of our ion crystal.

Given knowledge of these spatial dimensions, we can calculate the total ion number as $N_{tot} = \rho_M \frac{4}{3}\pi r_x r_y r_z$, but first we must calculate the spatial dimensions. For most LQT's, the radial dimensions are degenerate, meaning $r_x = r_y$.

Further we can assume all laser-cooled ions in the sample are fluorescing at the same rate. This approximation is valid as long as the waist of the cooling beam is much bigger than the sample size and excess micromotion doesn't add a significant Doppler shift to the ions at the crystal outskirts. In this regime, fluorescence is directly proportional to ion number, and thus, we can use knowledge of the spatial distribution of the fluorescence profile, obtained from our ion image, to infer the ion-number spatial distribution.

Our camera image compresses a three-dimensional into a two-dimensional image by essentially integrating along the axis of the camera, in this case, one of the radial dimensions of the LQT.

Thus, the total camera counts obtained from the camera, F(x,z), is given as

$$F(x,z) = T_E \int_{-\infty}^{\infty} \rho(x,y,z)dy \tag{6.7}$$

where T_E is a factor incorporating the scattering rate of the ions and the overall efficiency of the imaging system (including optical losses due to solid angle, absorption, etc.)

Now to determine r_x (r_z), using the camera image of our ion crystal, we can sum over all pixels in the remaining axial (radial) direction, effectively yielding

$$\begin{aligned} F(x) &= T_i \int_{-\infty}^{\infty}\int_{-\infty}^{\infty} \rho(x,y,z)dydz = T_E \rho_{max} \frac{\pi r_z (r_x - x)(r_x + x)}{r_x} \\ F(z) &= T_i \int_{-\infty}^{\infty}\int_{-\infty}^{\infty} \rho(x,y,z)dydx = T_E \rho_{max} \frac{\pi r_x (r_z - z)(r_z + z)}{r_z} \end{aligned} \tag{6.8}$$

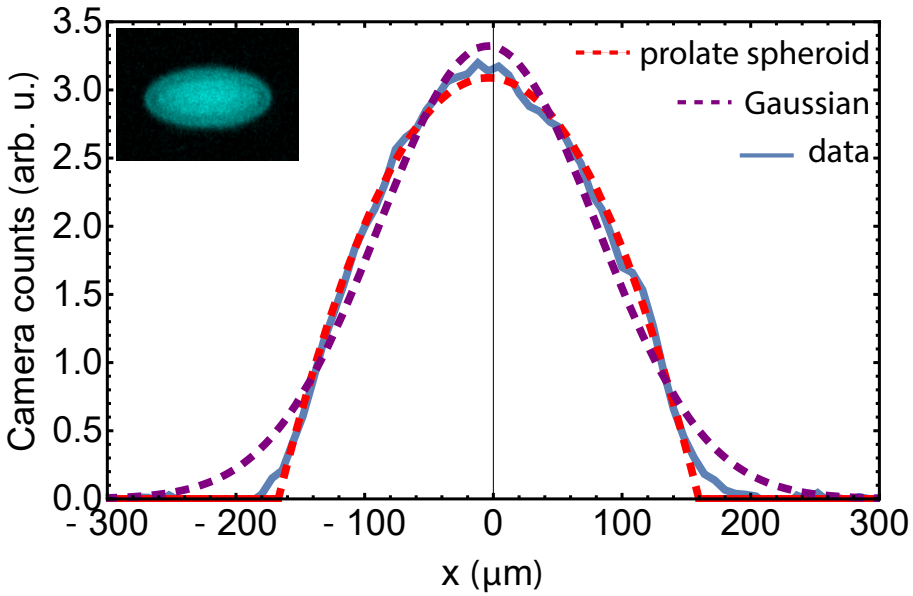

Figure 6.16: Ion fluorescence spatial profiling

Fluorescence profile (which is proportional to the ion number density profile) of an ion image as a function of radial displacement from the null (x dimension). Here the camera pixels have been summed along the axial dimension of the trap (z). The profile is fit to both a prolate spheroid and a Gaussian function. Since the sample is crystallized, the prolate spheroid offers a much better fit, with the Gaussian fit overestimating the density at at the peak as well as the wings. The camera image being analyzed is presented as an inset.

where the first equation is vald for $-r_x \leq x \leq r_x$, the second equation is valid for $-r_z \leq z \leq r_z$, and we have assumed $r_x = r_y$.

After fitting the above profiles to the summed camera images (Fig 6.16) we can extract the r_x and r_z values, allowing us to also extract the total ion number and the ion-number density profile.

If in the liquid or gas phase, the situation shifts. The peak density of the sample now depends on the secular temperature and is given as $\rho_0(T)$, with the scaling approximately $\propto T^{-3/2}$ [CSK11]. We can also say the ion density in a particular dimension will scale according to the Boltzmann factor associated with its secular potential as $\propto e^{-\frac{m\omega_i r_i^2}{k_b T}} = e^{-\left(\frac{r_i}{r_{i0}}\right)^2}$, where r_{i0} is the characteristic length scale of the ion cloud in the i^{th} dimension. Therefore the overall ion number density can be expressed as

$$\rho(x,y,z) = \rho_0(T) e^{-\left(\frac{x}{r_{x0}}\right)^2} e^{-\left(\frac{y}{r_{y0}}\right)^2} e^{-\left(\frac{z}{r_{z0}}\right)^2} \tag{6.9}$$

and once again

$$F(x,y,z) = T_E \rho(x,y,z) \tag{6.10}$$

$\rho_0(T)$ can be difficult to directly experimentally probe; however, the r_{x0}, r_{y0}, and r_{z0} length scales can be determined by following a similar fitting procedure as above, allowing a relative ion-number density to be determined.

With theses spatial values in hand, the total fluorescence, F_{tot}, can be expressed as

$$F_{tot} = \int F(x,y,z) dV = T_i \rho_0(T) \pi^{3/2} r_{x0} r_{y0} r_{z0} \tag{6.11}$$

Here, we can also recall $F_{tot} = T_E N_{tot}$. Therefore, if we can determine the amount of total camera counts for a single ion (effectively T_E), we can divide F_{tot} by this value to get N_{tot}. Of course, this method has its limits, and at larger ion sizes, Doppler shifts due to excess micromotion at large LQT radial displacements, as well as beam size issues, may prevent accurate fluorescence fits from being obtained.

6.5.2 Micromotion compensation and mass-filtering

DC voltages can be placed on the trap rods to compensate for stray electric fields. In general, if such fields are present, they will shift the ion off the trap null, and it is possible to probe for such displacements optically. For example, if an ion is off the trap null, if V_{rf} is increased, its position should shift towards the true trap center as the radial potential tightens. However, if the ion is already on the null, it should essentially remain motionless as V_{rf} is scanned. Thus, to compensate for stray electric fields, the position of a trapped ion can be observed as V_{rf} is switched between two values, and the shim voltages of the LQT can be adjusted until ion motion appears minimal upon rf switching.

However, our camera will not be able to resolve ion displacements along the camera axis, since the obtained image is only sensitive to motion orthogonal to the camera axis. To account for shifts in this direction, we can apply the same technique as above while instead varying the a-parameter of our trap. If a DC voltage is jointly applied to rods α/β, an a-parameter will be introduced into the trap that will in general compress ions to a plane connecting the γ/δ rods. If the ion has a positional offset along the direction of the camera axis, it will thereby be compressed to this plane, allowing for optical detection of this motion. Like before, shim voltages can be adjusted until negligible motion upon a-parameter modulation is observed.

These two methods are performed iteratively while shims are adjusted until the shim voltages have converged to within ~ 10 mV, as set by our control software (actual voltage on the rods may be slightly different). Procedurally, the voltages on the α/γ rods are adjusted in equal steps concurrently, and same goes for the γ/β rod pair. This allows for adjustment of the ion position along experimentally convenient axes in the LQT. Further, the optimization protocol is most easily performed using a 1D chain of ions for maximum sensitivity to positional shifts.

The success of the optimization relies on the rf being properly phase/voltage matched at both settings, as well as the DC voltage needed for the a-parameter being applied equally to both rods. Both of these checks can be performed by monitoring the proper voltage probe

for each rod upon V_{rf} and a-parameter switching.

6.5.3 Mass-filtering

Due to the nature of LQT stability regions, changing the a-parameter of the trap is very useful for destabilizing undesired ions (often $BaOCH_3^+$ and $BaOH^+$), when such ions are heavier than the ions of interest being studied (see Sec. 3.1.1). To accomplish this mass-filtering, a triangle voltage ramp ($\sim$ 1 sec period) can be applied to a pair of diagonally opposed rods to raise the a-parameter of the trap to a certain level before returning it to its base value. The a-parameter needed to eject the undesired ions will vary based on V_{rf}.

However, this method will only be able to deplete heavier ions. To remove lighter ions, the q-parameter of the trap may be raised, or the trap may be operated at a q-value such that a nonlinear resonance causes the undesired ions to be purged [DW69]. Lastly, a resonant tickle, at the mass-dependent secular frequency (typically $\sim$40-60 kHz at $V_{rf} = 160V$) of the undesired ion, may be placed on one of the trap rods to selectively expel [SKD00] the mass species from the trap.

6.6 Leak valve system

6.6.1 System overview

Ablation loading is a simple and robust technique; however, it is also stochastic and results in often inconsistent amounts of ions being loaded in the LQT. Much of this stochasticity can be circumvented by loading a large number of ions initially, and then 'whittling' the ions down to the required size by manipulating the Matheui a and q parameters to make a portion of the ions unstable. However, when multiple ion species are being loaded into the LQT via ablation, such as is the case with Ba^+ and $BaCl^+$ bi-samples, the ratio of these species loaded into the LQT is often also inconsistent, making it more difficult to correct for using mere post-ablation mass-filtering.

An alternative to this method is to initialize a sample of a particular ion species into the

LQT and then introduce a controlled quantity of reactive gas to induce reactions with the ions until they have formed a desired amount of product ions. For the purposes of this work, the following reaction is most useful

$$Ba^+ + CH_3Cl \rightarrow BaCl^+ + CH_3 \tag{6.12}$$

Thus, by introducing controlled amounts of CH_3Cl in our vacuum chamber, we can engineer bi-crystals with precise $Ba^+/BaCl^+$ ratios. When conducting quantum chemistry experiments, where knowledge of initial amount of reactant is crucial, or when conducting proposed quantum information experiments, where a specific number of $BaCl^+$ molecules may be needed to form an entangled qubit system [HC18], having such control will be highly desirable. The apparatus created to produce these controllable gas bursts is described below.

The leak valve system, depicted in Fig. 6.17, consists of two stages - a primary stage where a constant pressure ($\sim$100 mBar) of reactant gas is maintained, and a secondary stage attached directly to the MOTion chamber that is connected to the primary stage through a piezo-controllable leak valve.

Primary Stage

The CH_3Cl gas is produced from a Praxair gas cylinder (part numnber MC 3.5-LP5) hooked up to a Matheson single stage regulator (3396 Series). The regulator connects to a stainless steel flexible bellow line that feeds into a VCR cross. On one end of the cross is a MKS Pirani gauge (part number 103170014SH) used to monitor the CH_3Cl pressure on the primary stage. Another end of the cross connects to stainless steel bellow that feeds into a scroll pump (Agilent, IDP-3) that can be used to purify the system before introducing the methyl chloride gas.

The final cross end feeds into a bellow that itself feeds into a VCR tee. One end of the T is connected to a valved nitrogen line. The valve can be opened to overpressure the primary side with nitrogen, allowing for flushing of the system when a gas cylinder needs to be changed, for example. The other end of the tee connects directly the piezo doser. We also note that a ball valve is placed after the Matheson regulator to allow for convenient

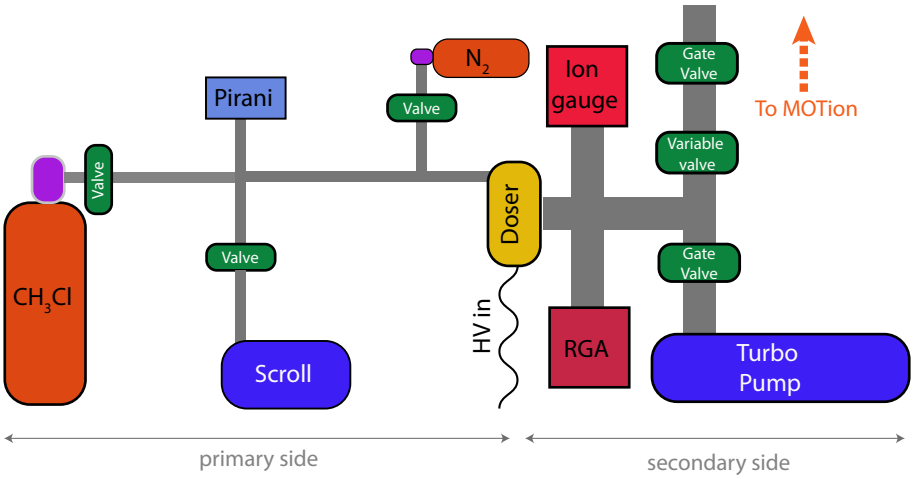

Figure 6.17: Leak valve system schematic diagram

Schematic diagram of the leak valve system, which consists of a primary side where a high pressure of reactant gas in maintained and a secondary side that a controlled amount of gas is leaked into, with this gas eventually flowing to the MOTion chamber. See text for specific part numbers for the various components.

exchange of gas cylinders. Moreover, a needle valve is placed prior to the scroll as a means to control how much pumping, if any, is occurring on the primary side.

CH_3Cl is a toxic chemical and thus should be handled delicately. The exhaust from the scroll line is fed into a ALTEF Gas Sampling Bag (Restek 22958) through brass and Viton connectors (McMaster 5346K12/5119K32). When ready for removal, this bag should be valved off and taken to a fume hood before the gas is released.

Secondary Stage

The primary stage is connected to the secondary stage through a piezo doser (input CF 1.33", output CF 2 3/4 "). The doser (Oxford Applied research, PLV1000) can be fed a voltage between 0-1000 V to open the piezo valve to various degrees. A HV pulser unit designed by Elizabeth West is used to send HV pulses to the devices. However, we note it is best to send signals with rise times of $\sim$100 ms or so to the unit to avoid exciting mechanical resonances in the piezo.

For further control of the valve, a tightening nut that clamps the piezo to the sapphire

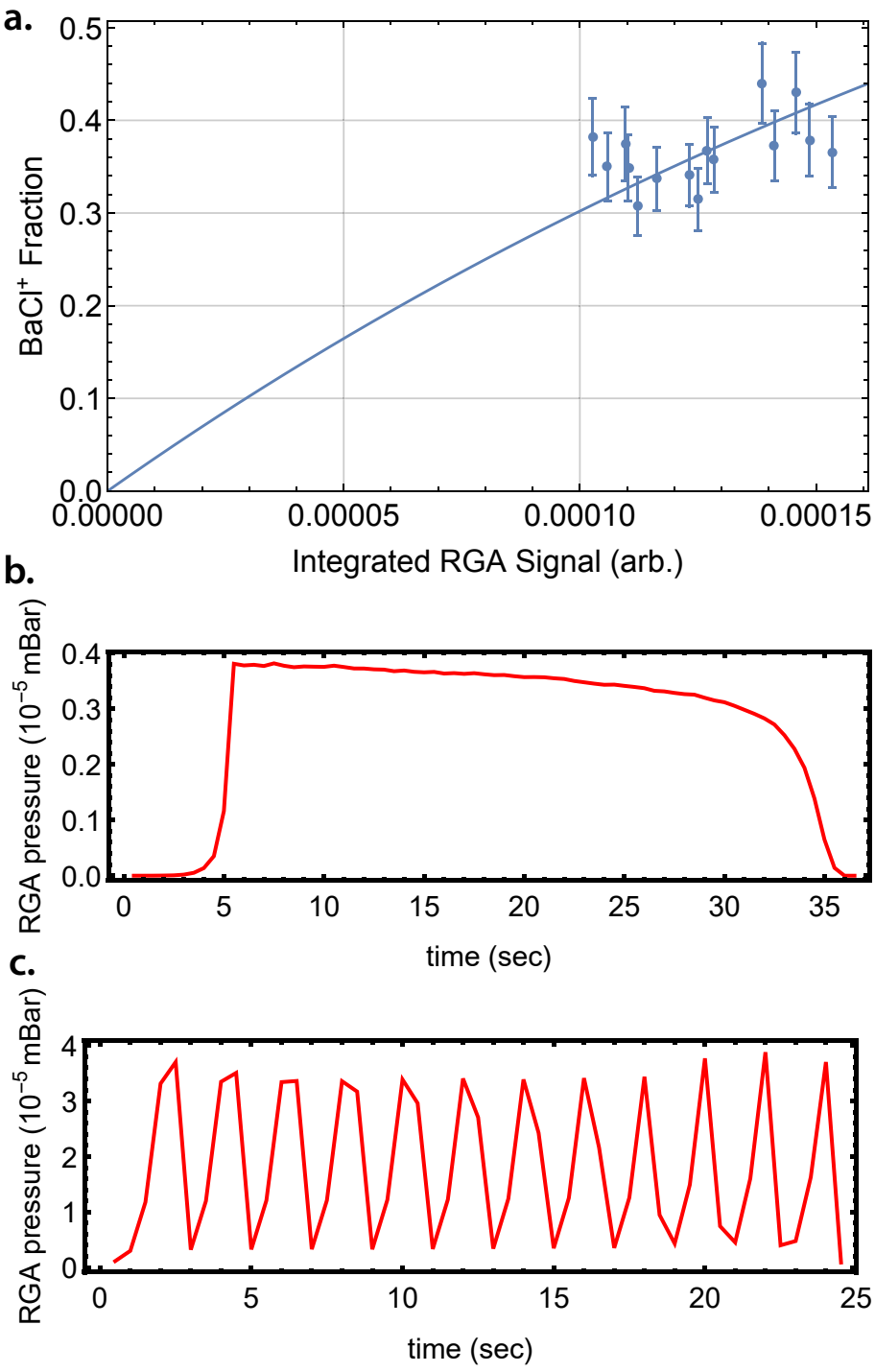

Figure 6.18: Leak valve reaction loading

(**a**) $BaCl^+$ fraction (normalized by total ion amount) as a function of total integrated CH_3Cl leak pressure. (**b**) Leak valve response when a constant HV is applied to the doser and then suddenly switched off. (**c**) Leak valve response of the doser system when using sending a stream of ~0.5 sec period TTL pulses to the doser (pump out time is longer than the pulse time).

seat that controls the valve can be adjusted to afford greater dynamic range of pressure flow. On the secondary side is also a residual gas analyzer (SRS, RGA 200) and an ion gauge (MKS, 100005980) as well as turbomolecular pump (Agilent, TPS Flexy 304FS) which is backed by an Agilent Scroll pump (SHG 100). The entire secondary side is connected to the MOTion chamber through a gate valve located near the second Einzel lens on the ToF-MS. Before the gate valve is a variable leak valve (Duniway, VLVE 1000), which can be adjusted to further control how much gas enters the MOTion chamber and also acts as a convenient safety-stop in case anything malfunctions with the system.

6.6.2 Leak valve system performance

The performance of the leak valve can be tested by leaking in various amounts of CH_3Cl gas and observing $BaCl^+$ formation. The voltage waveforms applied to the doser can be varied depending on the application. One may apply fast voltage pulses, resulting in a plume of gas in the chamber that is quickly pumped out by the ion and turbomolecular pumps (with just the ion pump the decay time is $\sim$5 seconds, but with both pumps, this lifetime is more like $\sim$1 sec). The fast bursts are most useful when only a small amount of $BaCl^+$ is needed; however, the valve response to fast voltage pulses can be somewhat inconsistent, and thus the amount of gas leaked in does vary pulse to pulse (Fig. 6.18b).

Alternatively, one may choose to operate the piezo at a constant voltage, allowing reactions to occur until a suitable amount of $BaCl^+$ has formed, at which point the voltage is switched off (Fig. 6.18c). This generally results in more consistent gas flows but may be difficult to implement when only single $BaCl^+$ ions are needed.

As an experimental demonstration of the reaction loading, $BaCl^+$ formation as a function of gas input is displayed in Fig. 6.18a. The amount of gas input into the system is measured by the RGA; however, since the RGA is spatially separated from the ion trap by several low-conductance apertures, only a fraction of this pressure actually reaches the ions. As can be seen, the amount of $BaCl^+$ in the trap can be controlled by merely changing the amount of gas input into the chamber.

6.7 Ca MOT hardware and profiling

6.7.1 Anti-Helmholtz coils

The magnetic field gradient necessary for the MOT trapping potential is produced by a pair of current coils arranged in the anti-Helmholtz configuration. The coils are powered by a HP 6683A power supply (0-32 V, 0-160 A), and are usually operated at ∼95 A of current. A full description of the dimensions of the anti-Helmholtz coils, including coil number, diameter, and thickness, as well as a more analytical treatment of the resulting magnetic field gradient, is given in Refs. [SDC16, Sul13].

In practice, the magnetic field zero is slightly offset from the ion trap center. To correct for this, a bias current can be placed on the top coil through means of a second power supply (HP-6033A, 0-20 V, 0-30A) that is added in parallel with the top coil. By adding current to the top coil but not the bottom coil, the magnetic field zero can be scanned across the axial dimension of the MOT trapping potential.

The location of the magnetic field zero can be experimentally determined by loading a sample of laser-cooled Ba^+ ions into the LQT and adjusting the shim current until the ions are maximally dark, which occurs due to CPT effects when the ions are not exposed to a state-mixing magnetic field.

Usually when operating with an anti-Helmholtz current of ∼95 A, a shim current of ∼ 7 A will center the magnetic field zero on the ions; however, when performing an experiment with laser-cooled Ba^+, the shim current is kept at ∼ 5 A to ensure CPT effects do not impede hinder cooling. Near the field zero, the measured field gradient per unit current is 0.527 G/(cm A) along the anti-Helmholtz axis and 0.2635 G/(cm A) along the radial direction [Sul13].

Our current coils are spaced relatively far away from our field zero due to the large vacuum chamber needed to house the ion trap. Consequently, relatively high currents are needed to produce the necessary MOT trapping potential, which in turn generate significant heat loads. The coils themselves are constructed from copper tubing that can be water cooled

(Small Tube Products) and also possess a Kapton coating performed by S&W Wire Co.

Chilled water is pumped through the coils, in parallel, dropping from about 270 PSI to the house return pressure of about 40 PSI. At typical operation of about 95 A through each coil, the temperature measured via a thermocouple adhered to the outer portion of the coil equilibrates to roughly 65 (45) C in the top (bottom) coil (the top coil tends to get hotter than the bottom coil, likely due to internal debris that obstructs water flow). To avoid runaway heating in the event of a cooling failure, the temperature reading on each coil is used to interlock the HP-6683A power supply via the alarm function on an Omega CN9600 temperature controller. If a temperature above the setpoint is detected, the alarm function shorts the interlock pins on the HP-6683A power supply, disabling it.

6.7.2 Getter units and Ca loading

Ca atoms are introduced into the MOT trapping region through two calcium getter sources (Alvatec) contained in MACOR housings that are mounted to the end caps of the LQT (Fig. 6.10). While two getter units are present, during MOT operation current ($\sim$ 5 A) is flowed (HP 6256B, 0-10V, 0-20A) through just one of the units, which heats the unit and creates a calcium vapor which sprays into the MOT trapping volume through an aperture of the housing. When installing a new getter, it must first be 'popped' by running the units at a current between $\sim$4-6 A (where the current is increased at roughly $\sim$1 A/hr), at which point an argon signal will be visible, which can be monitored on the RGA. A turbmolecular pump should also be connected to the vacuum housing during this process to pump any background gasses emitted from getter unit. Ideally, the lowest possible getter current needed to produce the Ca MOT density required by a particular experiment should be used to maximize getter lifetime.

The Ca atoms are quite hot as they exit the getter units ($\sim$ 1000 K), and thus they must be slowed down to temperatures lower than the MOT trap depth, which is of order a few Kelvins. For this purpose, beams detuned by roughly -4Γ and -10Γ, arranged in a power ratio of roughly 1:1, respectively, are aimed directly at the aperture of the getter unit to slow

the velocity of the emitted Ca atoms. This simple setup provides satisfactory trap loading efficiency, but may be replaced by other techniques, such as white light [ZOH91] slowing or chirped slowing [EBH85] for further MOT loading efficiency gains.

Once the Ca atoms have been loaded into the MOT, various parameters of the optical system can be manipulated to adjust the position of the MOT, which is critical for maintaining good overlap with the ionic species. The MOT is created by beams arranged in the standard six-beam optical molasses configuration. The power balancing between each pair of counterpropagating beams is controlled by a half wave plate (HWP) that feeds into a polarizing beam splitter (PBS) that splits the beam into a pair that are later sent through quarter-wave plates (QWP) (to obtain the correct circular polarization) before entering the chamber.

By changing the power balancing between a pair of counterpropagating beams, the MOT can be moved along the axis of the beam pair. We note that this may change the equilibrium position of the MOT to one that is not centered on the magnetic field zero, meaning the detuning of each σ^+ and σ^- beam from its associated transition may in general be different (off the field zero, both beams no longer address the σ^- transition, see Sec. 4.2.4 for further clarification). While this may seem counterintuitive for trapping, we note that since the MOT is stable at this new equilibrium position, it must be experiencing no net force. Therefore, the difference in power between the beams makes up for the difference in effective detuning from their associated transitions, leading to balanced scattering forces and thus stable trapping of the MOT at a position displaced from the field zero. We note that since the magnetic field gradient is twice as strong in the axial dimension as it is in the radial dimension, half the power should be used in the axial beams as in the radial beams in order to create a spherically symmetric MOT sample. Further, beam pointing can also be used to change the intersection region of the beams, and hence the MOT location, and to increase/decrease the effective MOT density.

The number of atoms loaded into the MOT is also quite sensitive to alignment of the deceleration beams with the getter beam source, and therefore, this parameter should also be varied during routine MOT alignment.

6.7.3 Density profiling

Knowledge of the MOT density is critical for accurate determination of the atom-ion reaction rate constants measured in the quantum chemistry experiments in this work, as the overall reaction rate scales proportionally with the atomic density. In order to measure this parameter, we employ a standard absorption imaging technique.

The density of the MOT, due to the linear restoring force present in the system, can be modeled as spherical Gaussian as

$$\rho(x,y,z) = \rho_0 e^{-\left(\frac{x}{\omega_x}\right)^2} e^{-\left(\frac{y}{\omega_y}\right)^2} e^{-\left(\frac{z}{\omega_z}\right)^2} \tag{6.13}$$

According to Beer's Law [Swi62], if a resonant beam is directed towards the sample, the intensity of the incoming beam will be attenuated as

$$\begin{aligned} \frac{dI(x,y,z)}{dz} &= -I(x,y,z)\sigma_a(\lambda_0)\rho(x,y,z) \\ \rightarrow \frac{dI(x,y,z)}{I(x,y,z)} &= -\sigma_a(\lambda_0)\rho(x,y,z)dz \end{aligned} \tag{6.14}$$

where $\sigma_a(\lambda_0)$ is the absorption cross-section at wavelength λ_0.

We are interested in the intensity change in the beam as it passes through the entire sample, so we can integrate the above equation integrate across the z-dimension as

$$\begin{aligned} \int \frac{dI(x,y,z)}{I(x,y,z)} &= -\int_{-\infty}^{\infty} \sigma_a(\lambda_0)\rho(x,y,z)dz \\ \ln\left(\frac{I_f(x,y)}{I_i(x,y)}\right) &= -\int_{-\infty}^{\infty} \sigma_a(\lambda_0)\rho(x,y)e^{-\left(\frac{z}{\omega_z}\right)^2}dz \\ &= -\pi^{1/2}\sigma_a(\lambda_0)\rho(x,y)\omega_z \end{aligned} \tag{6.15}$$

where $I_f(x,y)$ is the final intensity after the beam has passed through the MOT and $I_i(x,y)$ is the corresponding initial intesntiy prior to MOT exposure.

We are really interested in solving for the peak density, ρ_0, so we can rearrange the above formula, using $\rho(x,y) = \rho_0 e^{-\left(\frac{x}{\omega_x}\right)^2} e^{-\left(\frac{y}{\omega_y}\right)^2}$ as

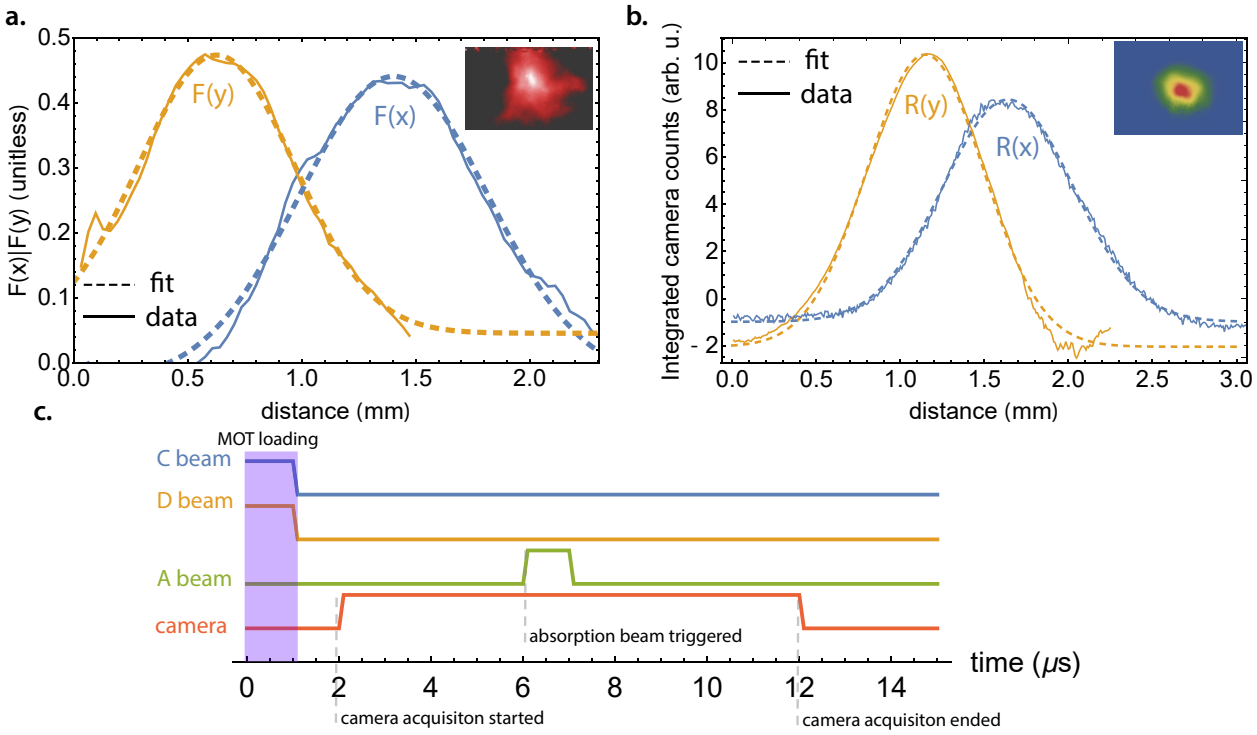

Figure 6.19: MOT density and spatial profiling

(**a**) Fits to integrated absorption images in both the x ($F(x)$) and y ($F(y)$) dimensions, as well as the camera count profiles the fits were applied to. The absorption image from which the fits were obtained is shown as an inset. (**b**) Similar to (**a**) except now the fits are applied to a fluorescence image. Specifically, the fits are applied to the camera count profiles along the x ($R(x)$) and y ($R(y)$) dimensions. These fits allows for extraction of MOT spatial dimensions, and as mentioned in the text, can also be calibrated to yield atomic densities. (**c**) Absorption measurement timing sequence. The MOT is loaded to its steady state density. The cooling beams (C beams) and deceleration beams (D beams) are then switched off the release the MOT. 5 μs later, an absorption beam (A beam) is introduced for 1 μs to probe the MOT density. The camera, whose minimum exposure time is 10 μs, is triggered slightly before the A beam trigger to capture the pulse event. The whole timing sequence can be repeated with no MOT initially present to obtain a control image.

$$-\ln\left(\frac{I_f(x,y)}{I_i(x,y)}\right) = \pi^{1/2}\sigma_a(\lambda_0)\omega_z\rho_0 e^{-\left(\frac{x}{\omega_x}\right)^2} e^{-\left(\frac{y}{\omega_y}\right)^2} \tag{6.16}$$

In the above formula, let $T(x,y) = \left(\frac{I_f(x,y)}{I_i(x,y)}\right)$. $I_f(x,y)$ can be obtained experimentally by first shining a beam through the MOT and then having the output be directed towards one of the Andor Luca cameras. After this image has been obtained, the process can be repeated with no MOT present to obtain $I_i(x,y)$ and then two images can be subsequently divided, resulting in the desired $T(x,y)$ matrix.

Now Eqn. 6.17 can be integrated over both the x and y dimensions to yield

$$\begin{aligned} F(x) &= \int_{-\infty}^{\infty} -\ln T(x,y)dy = \pi\sigma_a(\lambda_0)\omega_z\omega_y\rho_0 e^{-\left(\frac{x}{\omega_x}\right)^2} \\ F(y) &= \int_{-\infty}^{\infty} -\ln T(x,y)dx = \pi\sigma_a(\lambda_0)\omega_z\omega_x\rho_0 e^{-\left(\frac{y}{\omega_y}\right)^2} \end{aligned} \tag{6.17}$$

As shown in Fig. 6.19, ω_x and ω_y can both be extracted from Gaussian fits to the integrated $T(x,y)$ camera pixel matrices (experimentally, summing over all pixels in a particular dimension is treated as equivalent to integration over that dimension).

Once ω_x and ω_y have been determined, we can assume that $\omega_z = \sqrt{\omega_x\omega_y}$, since this quantity cannot be measured easily experimentally.

The fits that produce ω_i have the form $A_i e^{-\left(\frac{(r_i - r_{i0})}{\omega_i}\right)^2}$ where A_i is an amplitude coefficient and r_{i0} allows for a spatial offset of the MOT from whatever is defined as the coordiante system origin. As can be seen From Eqn. 6.17

$$\begin{aligned} A_i &= \pi\sigma_a(\lambda_0)\omega_z\omega_i\rho_0 \\ \rightarrow \rho_0 &= \frac{A_i}{\pi\sigma_a(\lambda_0)\omega_z\omega_i} \end{aligned} \tag{6.18}$$

In general, two measurements of ρ_0 may be made from the x and y dimension fits, and the peak MOT density is generally taken to be the average of these measurements.

On resonance, $\sigma_a(\lambda_0)$ is given as

$$\sigma_a(\lambda_0) = \frac{2J'+1}{2J+1}\frac{\lambda_0^2}{2\pi} \tag{6.19}$$

where $J'(J)$ is the rotational quantum number of the upper (lower) state ($J' = 1, J = 0$ in this case).

6.7.3.1 Experimental considerations

When taking an absorption image, it is important to select the absorption beam exposure time carefully. In general, it is best to pick the shortest time possible while yielding resolvable signals, and this value is typically $\sim 1\mu$s. At times much longer than this, the MOT ballistically expands while absorbing the beam, smearing out its spatial profile. Moreover, the beam also exerts a scattering force on the MOT, and given enough time, this effect may also morph the Ca density profile.

Lastly, in a typical absorption image cycle, shown in Fig. 6.19c, the MOT is first loaded into the chamber and then the cooling beams are extinguished. A brief $\sim$ 5 μs delay is included to allow for a majority of excited state atoms to fall into the ground state, and then the absorption beam is introduced ($\sim$ 1 μs exposure) from the output of a fiber coupler aligned with one of the CF 1.33" chamber viewports. While the absorption beam is introduced, a camera image is also captured. The camera exposure time is set to camera minimum of 10 μs, although ideally this would perhaps be closer to the absorption beam pulse time to limit background scatter. The process is repeated with no MOT present as a control.

One might think, to save time, that one could take both an absorption image and a control in the same duty cycle by reintroducing the absorption beam after the MOT has ballistically expanded out of the trapping region. However, AOM's are used as optical switches to control both the cooling beam and the absorption beam timing. Due to AOM heating, the amount of light that couples into the absorption beam fiber changes as a function of time during the AOM duty cycle. To avoid these effects, the control and absorption images are therefore taken using the same delay time after switching on the absorption beam AOM (in separate

imaging cycles).

6.7.4 'Shortcut' density profiling

Experimentally obtaining absorption images can be a little time consuming due to the need to need to cycle over several MOT lifetimes. However, once an initial density measurement has been made, a 'shortcut' measurement may be made for future density measurements that only involves standard fluorescence images.

Say that the overall total number of counts collected by our camera from the fluorescing MOT is R_C. This quantity can be expressed as

$$\begin{aligned} R_C &= \Gamma\rho_{22}\Omega GEN_{atoms} \\ &= \Gamma\rho_{22}\Omega GE\int \rho(x,y,z)dV \\ &= \Gamma\rho_{22}\Omega GE\pi^{3/2}\omega_x\omega_y\omega_z\rho_0 \end{aligned} \tag{6.20}$$

where Ω is the solid angle of the imaging system, G is the camera gain, E is the optical efficiency of the imaging system (includes losses due to optical filter absorption, reflectances at the objective, etc.), and N_{atoms} is the total number of atoms in the system. $\{\omega_x, \omega_y, \omega_z\}$ are defined as above. Shown in Fig. 6.19, ω_x and ω_y can be obtained easily through fits to simple fluorescence images, without invoking the more complicated procedures needed for absorption imaging (see Sec. 6.7.3.1).

Thus, the density can be calculated as

$$\rho_0 = \frac{R_c}{\Gamma\rho_{22}\Omega GE\pi^{3/2}\omega_x\omega_y\omega_z} = C\frac{R_c}{\omega_x\omega_y\omega_z} \tag{6.21}$$

where C is a coefficient that can be determined by calibrating to a MOT of known density, as determined by absorption images. While the above relation means that density profiles can be obtained from simple fluorescence images; the C coefficeint needs to be remeasured frequently, as thermal beam drifts in the system can change the amount of scatter in the system and thus the number of photons collected by the imaging system. Further, often

times parameters like the excited state fraction are changed in a measurement which will generally change C as well. Therefore, it is often more reliable to use absorption imaging for accurate density measurements.

6.7.5 MOT lifetime measurements

The time evolution of the atom number in the MOT can be understood by the following simple differential equation

$$\frac{dN}{dt} = -\Gamma_L N(t) + L \tag{6.22}$$

where N is the MOT atom number, Γ_L is atom loss rate, and L is the atom loading rate. L is set by the getter current and the efficiency of the deceleration beams in allowing atoms to enter the MOT, while Γ_L is primarily set by leakages in the laser-cooling cycle that populate dark states that cannot be laser cooled as well as background gas collisions.

The solution to Eqn. 6.22, given initial conditions $N(0) = 0$, is given as

$$N(t) = \frac{L}{\Gamma_L}(1 - e^{-\Gamma_L t}) \tag{6.23}$$

Experimentally, Γ_L can be measured by initializing the chamber with no MOT beams present but the getter unit on. Then the MOT beams can be introduced for varying amounts of time, and a fluorescence image can be taken at the end of each sequence. The total fluorescence, which is proportional to the total atom number, can then be plotted as function of time to extract Γ_L and the MOT lifetime, $\tau = \Gamma_L$, can be extracted (see Fig. 6.20). As we will see in Ch. 7, τ is heavily determined by how efficient the repump used in the MOT is (multiple repump pathways are available) and can vary from $\sim 80 - 4000$ ms.

6.7.6 MOT Temperature

According to a simple Boltzmann model, the probability of an atom occupying a position x in the MOT is $P(x) \propto e^{-(x/\omega_x)^2}$. If the atom is released from the trapping potential

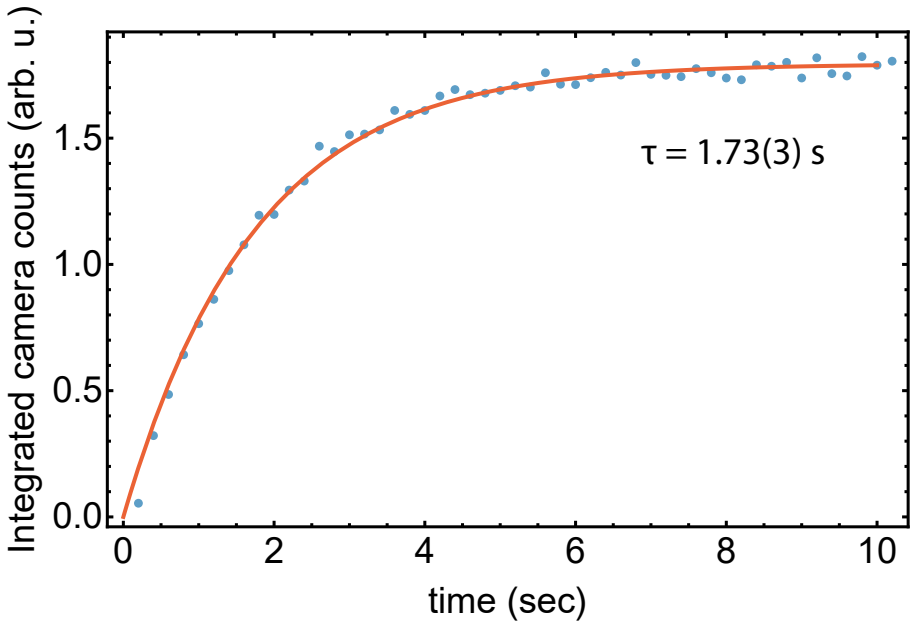

Figure 6.20: MOT lifetime measurement

The chamber in initialized with the getters on but no beams present. The cooling beams are turned on for variable amounts of time, at which point a camera image is taken. The integrated camera counts, as a function of time, are plotted and an exponential fit is applied to extract a MOT lifetime of $\tau = 1.73(3)$ s.

when it has a velocity v, we would expect the updated probability distribution to look like $P(x(t)) \propto e^{-((x+vt)/\omega_x)^2}$, in a process known as ballistic expansion.

Now to understand our MOT's spatial probability distribution as a function of time, $P(x(t))$, we need to consider the fact that our MOT is a thermal source and thus has a velocity probability function $P_v(T) \propto e^{-\frac{mv^2}{2k_BT}}$, where T is the temperature of the sample. Convolving the two factors, we see that

$$\begin{aligned} P(x,t) &\propto \int e^{-((x+vt)/\omega_x)^2} e^{-\frac{mv^2}{2k_BT}} dv \\ &\propto e^{-\left(\frac{x}{\omega_x + \frac{2k_BT}{m}t^2}\right)^2} \end{aligned} \tag{6.24}$$

Here we use the velocity probability distribution instead of the speed probably distribution since we are interested in velocity vectors (i.e. $v_x + t \neq -v_x + t$).

Thus, it can be seen that $P(x(t))$ is the similar to $P(x)$, except ω_x has been replaced with a time dependent length scale, $\omega_x(t,T)$ as

$$P(x,t) \propto e^{-\left(\frac{x}{\omega_x(t,T)}\right)^2} = e^{-\left(\frac{x}{\omega_x(t=0)^2 + \frac{2k_BT}{m}t^2}\right)^2} \tag{6.25}$$

where

$$\omega_x(t,T) = \sqrt{\omega_x(t=0)^2 + \frac{2k_BT}{m}t^2} \tag{6.26}$$

Experimentally, we can monitor the evolution of $\omega_x(t,T)$ by initializing a MOT and then extinguishing our cooling beams. We then allow our MOT to expand for a variable amount of time, and then image our MOT to determine its spatial distribution, effectively extracting a $\omega_x(t_0,T)$ value for a given amount of delay time, t_0. We can then fit the functional form of $\omega_x(t,T)$ to our data, using T as a fit parameter, in order to extract the temperature of our sample (see Fig. 6.21).

For the $\sim$5 mK temperature of our sample, ballistic expansion results in a majority of the MOT atoms leaving the trapping region in under a millisecond. Due to the optical efficiency of our imaging system, direct fluorescence imaging cannot be used on these timescales.

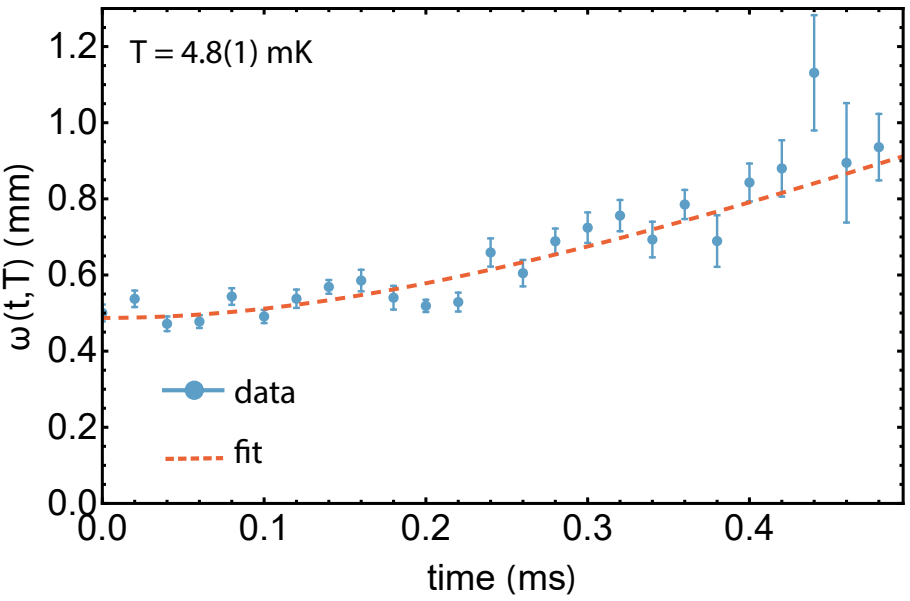

Figure 6.21: MOT ballistic expansion

The evolution of the MOT size as a function of time after the cooling beams have been extinguished. The rate at which this expansion occurs is indicative of the temperature of the sample. After fitting the Eqn. 6.26 to the data, a temperature of 4.8(1) mK is extracted for the MOT sample (error bars given by 68% confidence interval bands.

However, absorption imaging, due to it's increased sensitivity, can be used to probe these timescales. Thus MOT images are obtained by performing MOT absorption images at a set of hold times. We note that since the act of taking an absorption image affects the MOT position dynamics, we take only one absorption image per imaging cycle.

Lastly, for the temperatures studied in this work, this analysis extends to all three spatial dimensions. However, in our setup, we only monitor the MOT in the dimension consistent with the axial dimension of the LQT, since the LQT rods block a large portion of our absorption beam in the orthogonal dimension, preventing the MOT from being imaged at expansion distances greater than $\sim$500 μm.

Further, if our MOT was much colder, in the μK regime for example, we would also have to consider the effect of gravity along the z dimension of expansion. This would involve performing our above treatment with $e^{-((z+vt)/\omega_z)^2} \rightarrow e^{-\left((z+vt-\frac{1}{2}gt^2)/\omega_z\right)^2}$ for analysis of the MOT spatial profile along the axis parallel with Earth's gravitational field.

6.8 Magnetic trap

In addition to the MOT, a magnetic trap also exists within our system. The magnetic trap potential energy due to our anti-Helmholtz coil configuration can be expressed using the electronic state Landé g-factors, g_F, as

$$U_B = -\vec{\mu}_M \cdot \vec{B} = g_F \mu_B m_J B_0 |z| \tag{6.27}$$

where U_B is the magnetic trap potential energy, $\vec{B}$ is the trap magnetic field, B_0 is the magnetic field gradient, and $\vec{\mu}_M$, the magnetic moment, is given by $-g_F \mu_B \vec{J}/\hbar$, where μ_B is the Bohr magneton and $\vec{J}$ is the total angular momentum vector.

Why the absolute value |z|? Here we assume, if an atom is placed into a particular m_J state when it enters the trap, its orientation will remain fixed with respect to the magnetic field direction as it moves through the trap. Thus, the magnetic sublevel orientation will adiabatically respond to the changing magnetic field direction, meaning the dot product in Eqn. 6.27 will always have the same sign, and thus the absolute value is introduced. However, in general, this adiabatic behavior need not exist. If the atoms spend enough time near the field zero, their quantization axis will no longer be well-defined and the atoms may project into other m_J states, and this effect has indeed been observed to cause magnetic trap loss through so-called Majorana transitions [Maj32].

Due to the dependence of U_B on m_J and g_F, only atoms in states where $g_F m_J > 0$ will have stable trapping forces. For states populated during Ca laser-cooling, these states are the $|^3\mathrm{P}_2,\ m_J = 1,\ 2\rangle$, $|^3\mathrm{P}_1,\ m_J = 1\rangle$, $|^1\mathrm{P}_1,\ m_J = 1\rangle$, and $|^1\mathrm{D}_2,\ m_J = 1,\ 2\rangle$ electronic levels. In general, all of these states are populated to some degree through leakages in the Ca laser cooling cycle.

However, since the last three states have very short radiative lifetimes (< 2 ms) compared to that of the $^3\mathrm{P}_2$ state ($\sim$118 min), after only a few milliseconds, the magnetic trap contains purely $|^3\mathrm{P}_2\rangle$ atoms. Further, due to the smaller potential depth of the $|^3\mathrm{P}_2,\ m_J = 1\rangle$ atoms, the atomic density of the magnetically trapped $|^3\mathrm{P}_2,\ m_J = 2\rangle$ atoms is $\sim$10x larger, resulting in a magnetic trap dominated by $|^3\mathrm{P}_2,\ m_J = 2\rangle$ Ca atoms. Essentially, as atoms fall into the

$|^3\mathrm{P}_2\rangle$ state, they are lost from the Ca laser-cooling cycle but are also simultaneously loaded into the magnetic trap, allowing a steady-state population to form in the latter.

Often the magnetically trapped atoms are used as reactants to study atom-ion chemistry. We note that above we have defined m_J with respect to the trap magnetic field direction; however, when considering reactions with ionic species, the relative velocity vector between the reagent pairs that defines the reaction is isotropically distributed, meaning the Ca m_J sublevel is not controlled along the reaction quantization axis.

6.8.1 Magnetic trap density

In many experiments in this thesis, the magnetically trapped atoms will be used as a chemical reactant to explore the reactivities of triplet states, allowing comparison of these reactivities to those of other excited levels. However, in order to extract reaction rate constants, magnetic trap densities must be estimated.

While absorption imaging methods, discussed in Sec. 6.7.3, are typically used to assess the density of atom traps, the magnetic trap is not dense enough for this technique to yield resolvable values using current techniques. Thus, alternative methods must be pursued. Primarily, we make separate measurements of the magnetic trap atom number and spatial distribution, and combine these measurements to obtain an approximate density.

6.8.1.1 Magnetic trap atom number

In order to measure the trapped atom number, a MOT is first loaded, which in turns loads $|^3\mathrm{P}_2\rangle$ atoms into the magnetic trap. The MOT cooling beams are extinguished for roughly 50 ms. At this time, due to ballistic expansion, any atoms that were trapped in the MOT have exited the trapping region, essentially leaving only the magnetically trapped atoms.

Optical pumping is now utilized to transfer the magnetically trapped triplet atoms into the ground state, through introducing a beam resonant with either the $4s4p\,^3P_2 \rightarrow 4s4p\,^3D_2$ transition (445 nm) or the $4s4p\,^3P_2 \rightarrow 4p^2\,^3P_2$ transition (430 nm). The upper levels in these transitions decay primarily to the $4s4p\,^3P_2$ level or to the $4s4p\,^3P_1$ state, which decays to

the ground state with a lifetime of ~ 300 μs. Thus, after ~ 1 ms of optical pumping, nearly all of the magnetically trapped population should reside in the ground state (see Fig.6.22c).

When the optical pumping beam is introduced, the MOT cooling beams are also introduced into the chamber. The transferred atoms are then recaptured into a MOT, and fluorescence from the magnetically trapped atoms is collected for $\sim$10 ms. We note that it takes roughly 5-10 ms for the atoms to be retrapped by the MOT cooling beams, so often it is best to have the cooling beams on for this amount of time time before collecting fluorescence (see Fig.6.22b).

However, fluorescence from a small amount of non-magnetically-trapped atoms loaded into the MOT from the getter source is also recorded during this interval. Fortunately, since the MOT loading time is typically $\gtrsim$100 ms, this background is negligible, and further, it can easily be accounted for through background subtraction. The deceleration beams may also be turned off during this recapture process, further minimizing the background rate.

After the fluorescence image has been obtained, by using a calibration of fluorescence to atom number based on observing a Ca MOT of known density, total magnetic trap atom numbers can be calculated. However, no spatial information about the magnetic trap is offered by this measurement since the trap is optically depopulated before fluorescence collection.

Aside from atom number measurements, this process can easily be modified to capture magnetic trap lifetime information as well, as shown in Fig.6.22a. In this case, the 50 ms hold time is varied to include larger hold times, and the atom number is probed as a function of time, allowing τ_M, the magnetic trap lifetime, to be extracted (assuming an exponential decay model).

Further, this decay curve allows for prediction of the atom number at a hold-time of 0 s, which is the magnetic trap atom number that is reached during steady-state MOT conditions, a quantity often relevant to reaction rate calculations.

A few final notes - if conducting a measurement where a steady-state magnetic trap is needed (which in turn requires a steady-state MOT), be careful to block the optical

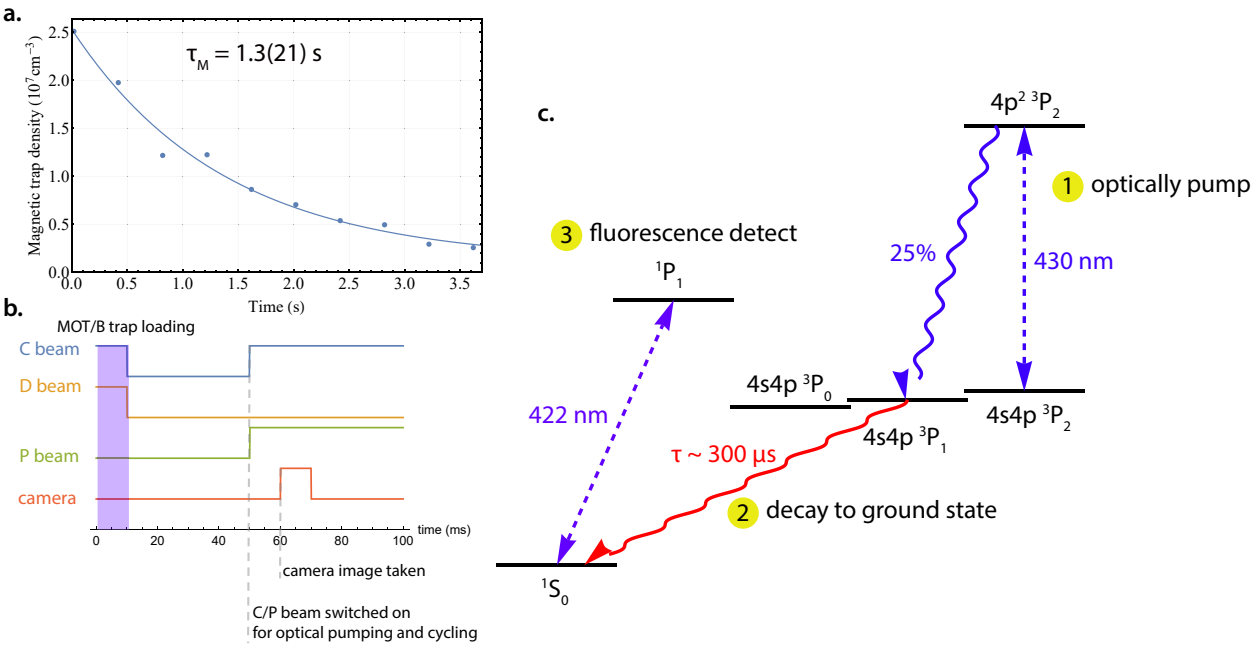

Figure 6.22: Magnetic trap atom number profiling

(**a**) Magnetic trap density as a function of time after the MOT has been switched off, with an extracted lifetime of 1.3(21) s. The magnetic trap atoms are presumably lost from the trap over time due to collisions with background gas particles and non-adiabatic transfer into non-trapped states. (**b**) Timing sequence for a magnetic trap atom number measurement. The MOT, and consequently the magnetic trap, are first loaded to their steady state values ($\sim$ 5 s). Then the cooling beams (C beam) and deceleration beam (D beam) are extinguished. The MOT ballistically expands away in roughly $\sim$ 1 ms. $\sim$ 50 ms after the MOT has been extinguished, the optical pumping beam (P beam) is introduced to transfer population to the ground state. At the same time, the C beam is introduced to retrap them into a MOT. After $\sim$ 10 ms, a vast majority of the triplet atoms have been reintroduced into the MOT, and a 10 ms camera image is acquired. The total captured camera counts on the image can subsequently be converted to an atom number. (**c**) The optical pumping scheme is displayed diagrammatically. (1) First, $^3P_2$ atoms are transferred to the $^3P_1$ state by pumping atoms from the former state to the $4p^2\ ^3P_2$ level which has a 25% decay the latter state, meaning after a few optical cycles the population is essentially all transferred. (2) Second, atoms in the $^3P_1$ state, which has a $\sim$ 300 μs lifetime, decay to the ground state. (3) Lastly, the C beams are introduced to capture fluorescence from the transferred atoms.

pumping beam during MOT operation. A small amount of pumping light, even on the level that leaks through an AOM employed as an optical switch, can result in significant magnetic trap depopulation. Lastly, the distance over which the MOT beams can recapture atoms efficiently is $\sim$ 7 mm, and as we will see shortly, this is a distance much greater than the dimension of the magnetic trap, ensuring the atoms are efficiently recaptured and subsequently counted. However, this recapture range can vary with cooling beam power, and therefore, experiments should be performed to measure this recapture range before any serious density measurement is performed. If the recapture range is too small, the magnetic trap atoms will not be efficiently reintroduced into the MOT, resulting in artificially low density measurements.

6.8.1.2 Spatial magnetic trap estimate

The magnetic trap spatial profile needed for atom number density calculations, and thus rate constant extraction, is obtained by monitoring how the reaction rate of the triplet atoms with an ionic reactant varies as a function of displacement from the trap center. The reaction rate is proportional to the density, meaning the reaction rate spatial profile is effectively proportional to the trap density spatial profile, all other factors being the same.

The position of the ionic reagent can conveniently be scanned across the axial dimension of the LQT by manipulating the endcap voltages, allowing for local probing of the magnetic trap density over a distance of $\sim$ 8 mm. The most convenient ionic reactant to use is $BaCl^+$, which participates in the following reaction:

$$\begin{aligned} Ca(^3\mathrm{P}_2) + BaCl^+ &\rightarrow Ba^+ + CaCl \\ &\rightarrow Ca^+ + BaCl \end{aligned} \tag{6.28}$$

In general, the density of the magnetic trap can be profiled as

$$\rho_M(r) = \rho_{M_0} e^{\frac{-\sqrt{r^2+4z^2}}{\omega_B}} \tag{6.29}$$

where ρ_{M_0} is the peak density of the magnetic trap, $r(z)$ is the radial (axial) position of

the ions with respect to the magnetic trap center, and ω_B is the spatial length scale of the magnetic trap. Here, the asymmetry between the r and z dimensions occurs since the magnetic field gradient is twice as strong in the z dimension.

In order to calculate the spatial overlap of the magnetic trap and the ions, the center of the magnetic trap is first identified by observing a Ba^+ laser-cooling fluorescence dip due to coherent-population-trapping (CPT) at the magnetic field zero of the system. Subsequently, a bias current is applied to the anti-Helmholtz coils utilized for constructing the MOT trapping potential. The bias current shifts the magnetic field zero, and thus the center of the magnetic trap, by a fixed distance, z_0, away from the ions (typically chosen to be ≈ 500 μm) in the axial dimension, ensuring that CPT effects do not complicate reaction rate data acquisition. The radial distance of the ions from the center of the magnetic trap is then tuned by adjusting the endcap voltages of the LQT, and reaction rates are measured at various atom-ion spatial offsets (see Fig. 6.23).

Assuming an axial offset of z_0, at each position in the LQT, the ions experience a local magnetic field density, $\rho_M(r)$, of

$$\rho_M(r) = \rho_{M_0} e^{\frac{-\sqrt{r^2+4z_0^2}}{\omega_B}} \tag{6.30}$$

$\omega_B = 0.98(11)$ mm, as determined through fits (see Fig. 6.23) to the above-mentioned reaction rate data (error expressed at 68% confidence interval). For clarity, we emphasize that the axial and radial dimensions referenced here refer to the conventional dimensions of the anti-Helmholtz coil geometry and not the LQT trapping potential. We note that this measurement was performed at a current of 95 A, and the trap size will need to be scaled, or the measurement repeated, for density measurements at other gradient strengths.

Interestingly, if one were to predict ω_B theoretically from Eqn. 6.27, assuming of a 4 mK Ca temperature and known values for the magnetic field gradients, Landé factor, and other atomic properties, one would predict a magnetic trap size $\omega_B \approx 7$ mm. The fact that our measured size is much smaller might point to other effects in the system, such as rf knifing [BBM00], playing a role in reducing the trap size.

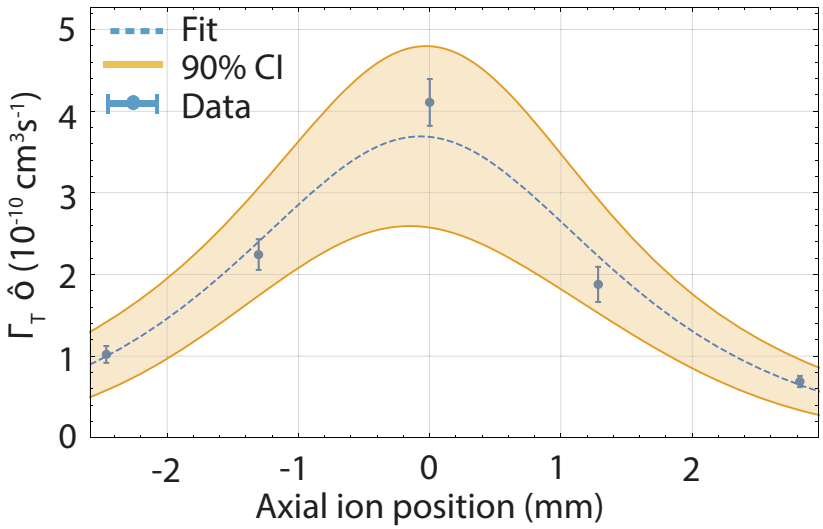

Figure 6.23: Magnetic trap-ion overlap

The measured Ca 4s4p $^3P_2$ reaction rate constant, Γ_T, multiplied by the geometric atom-ion overlap factor, $\hat{O}$, obtained at different spatial offsets between the ion sample and the center of a magnetic trap of pure triplet atoms. The corresponding fit curve (dashed line) along with its 90% confidence interval (CI) (yellow band) are displayed as well. The functional form of the fit curve (Eqn. (6.30)) allows for approximate estimation of the magnetic trap density profile. For both plots, each data point consists of approximately 100 measurements, where error bars represent one standard error.

As a technical note, it is imperative in the above measurements to limit the amount of reactions that occur between $BaCl^+$ and the Ca MOT - ideally we want the ions to only interact with the magnetically trapped atoms. To this end, we initially displace the atoms $\sim$4 mm away from the center of the MOT while the magnetic trap is being loaded. We then switch off the MOT and immediately 'shuttle' the ions to the position in the trap where we would like to probe the magnetic trap density. Since the lifetime of the magnetic trap is $\sim$ 2 s, the ions can react with the pure magnetic trap for this duration. At this point, the ions are again far-displaced from the center of the trap, the MOT is reloaded, and the process is repeated. This shuttling method minimizes MOT/ion overlap while still allowing magnetic trap interactions, and further will be used several more times in the measurements discussed in this thesis.

With the atom number and magnetic trap spatial estimates in hand, we can estimate the

magnetic trap peak density from the relation

$$\begin{aligned} N_{mag} &= \int \rho_{M_0} e^{\frac{-\sqrt{r^2+4z_0^2}}{\omega_B}} dV \\ &= \int_{-\infty}^{\infty} \int_0^{2\pi} \int_0^{\infty} \rho_{M_0} e^{\frac{-\sqrt{r^2+4z_0^2}}{\omega_B}} r dr d\theta dz \\ &= 4\pi\omega_B^3 \rho_{M_0} \\ &\rightarrow \rho_{M_0} = \frac{N_{mag}}{4\pi\omega_B^3} \end{aligned} \tag{6.31}$$

Typically densities are of order $\sim 10^7$ cm^{-3}, although this density is largely dependent on factors such as getter current and MOT density.

6.9 Atom-ion overlap factor

One of the most important quantities to calculate experimentally is the atom-ion overlap factor, as this factor is integrated into reaction rate calculations and will also determine the rate of atom-ion sympathetic cooling. Essentially the overlap factor affects the average atomic density that the ion sample experiences. This average density, ρ_{av}, can be expressed as

$$\rho_{av} = \rho_0 \hat{O} = \rho_0 \int \hat{\rho}_{MOT}(x,y,z)\rho_I(x,y,z)dV \tag{6.32}$$

where $\hat{O}$ is the atom-ion overlap factor, $\hat{\rho}_{MOT}(x,y,x)$ is the peak-normalized MOT density, and $\rho_I(x,y,z)$ is the spatial ion probability distribution, which has the integral normalized property

$$1 = \int_{-\infty}^{\infty} \rho_I(x,y,z)dV \tag{6.33}$$

Physically speaking, from above, we see that the average density the ions experience is simply the expectation value of the MOT density integrated over the spatial probability distribution of the ion - a quantity given as $\rho_0\hat{O}$.

The overlap integral will depend on the functional forms of both the MOT and ion density.

In one of the simplest cases, we can consider $\rho_I(x,y,z)$ to have an ellipsoidal Gaussian form and the $\hat{\rho}_{MOT}(x,y,z)$ to have a spherical Gaussian form. Consequently, the atom-ion overlap factor $\hat{O}$, can be calculated as

$$\begin{aligned}\hat{O} &= \int \hat{\rho}_{MOT}(x,y,x)\rho_I(x,y,z)dV = \int e^{-\frac{x^2+y^2+z^2}{\omega_M^2}}\rho_{I0}e^{-\frac{(x-x_0)^2}{\omega_x^2}}e^{-\frac{(y-y_0)^2}{\omega_y^2}}e^{-\frac{(z-z_0)^2}{\omega_z^2}}dv \\ &= \prod_{i\in(x,y,z)}\frac{\rho_{i0}\sqrt{\pi}\omega_M\omega_i}{\sqrt{\omega_M^2+\omega_i^2}}e^{-\frac{x_0^2}{\omega_M^2+\omega_i^2}}\end{aligned} \tag{6.34}$$

where ρ_{I0} is the coefficient of normalization for $\rho_I(x,y,z)$. The MOT size is characterized by spatial length ω_M, where the ion distribution is characterized by ω_x, ω_y, and ω_z. The ion distribution also can generally be offset from the center of the MOT by a displacement $\langle x_0, y_0, z_0\rangle$.

ω_M, ω_x, ω_y, and ω_z can all be estimated conveniently through fluorescence images of the atom and ions. Thus, the only remaining quantities that need to be calculated for the overlap calculation are the spatial offsets. To estimate these values, we rely on the two EMCCD cameras situated along the 1.33" CF Flanges, each of which can produce a two-dimensional image of both the atoms and ions.

In each image, a vector from the center of the MOT to the center of the ion can be drawn to determine the atom-ion offset in the imaging plane. However, from a single image there no information regarding offsets along the camera axis; rather this information must be inferred from combining information from both images.

First, consider the atom-ion offset vector within the frame of each camera image as

$$\begin{aligned}\mathbf{o}' &= \langle x', y', z'\rangle = x'\hat{e}'_x + y'\hat{e}'_y + z'\hat{e}'_z \\ \mathbf{o}'' &= \langle x'', y'', z''\rangle = x''\hat{e}''_x + y''\hat{e}''_y + z''\hat{e}''_z\end{aligned} \tag{6.35}$$

where $\mathbf{o}'$ is the frame of the first camera $\mathbf{o}''$ is the frame of the second camera. Recall from earlier discussions that the first camera axis is rotated 16° azimuthally from the reentrant camera axis and the second camera is rotated - 16° from the reentrant camera axis. Here, we

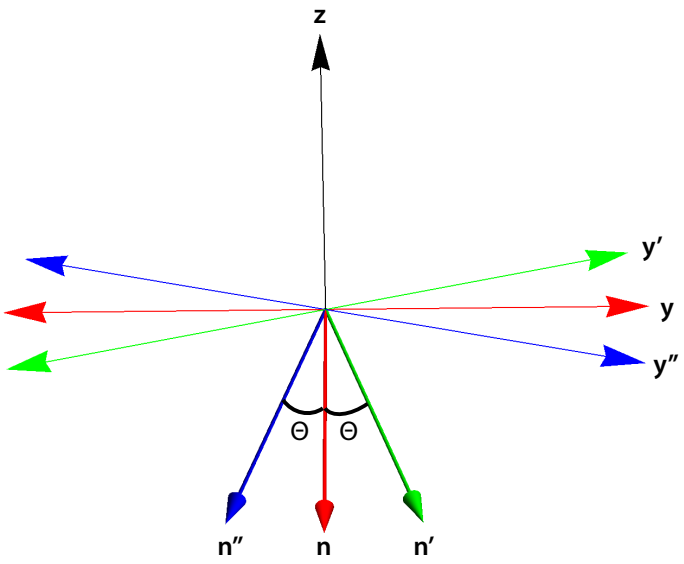

Figure 6.24: Camera reference frames

Coordinate systems for all three camera planes, ignoring polar angle rotations. The atom-ion imaging cameras are rotated -θ and +θ azimuthally with respect to the reentrant camera. Here $\hat{n}$, $\hat{n'}$, and $\hat{n''}$ represents the normal vector to the three cameras, and all three cameras share the same z-axis.

ignore the polar angle rotation of both cameras with respect to the reentrant camera frame since the ion cloud spatial distribution is symmetric to polar rotations. $\hat{e}'_i/\hat{e}''_i$ are the basis vectors in the respective imaging frames, with $\hat{e}'_x/\hat{e}''_x$ being the normal vector to the camera planes. Once again, since x' and x'' lie along the camera axes, they cannot be determined from a lone image.

It is convenient to represent both offset vectors within the same frame, and in this case, the reentrant camera frame is most prudent. Once again, in all camera frames the x-basis vector represents the vector normal to the camera frame (referred to as $\hat{n}$ in Fig. 6.24 for convenience).

Expressed in the reentrant frame

$$\begin{aligned} \hat{e_i}' &= R(\theta)\hat{e_i} \\ \hat{e_i}'' &= R(-\theta)\hat{e_i} \end{aligned} \tag{6.36}$$

for $i \in \{x, y\}$ where $R(\theta)$ is the rotation matrix defined as

$$R(\theta) = \begin{pmatrix} \cos(\theta) & -\sin(\theta) \\ \sin(\theta) & \cos(\theta) \end{pmatrix} \tag{6.37}$$

The z-axis is the same in all frames since we are not considering polar angle rotations.

Thus the ion position, P, expressed in the $\mathbf{o}'$ frame is

$$\begin{aligned} P_{\mathbf{o}'} &= x'\hat{e}'_x + y'\hat{e}'_y + z'\hat{e}'_z \\ &= x'(\hat{x}\cos(\theta) + \hat{y}\sin(\theta)) + y'(-\hat{x}\sin(\theta) + \hat{y}\cos(\theta)) + z'\hat{z} \\ &= \hat{x}(x'\cos(\theta) - y'\sin(\theta)) + \hat{y}(y'\cos(\theta) + x'\sin(\theta)) + z'\hat{z} \end{aligned} \tag{6.38}$$

Similarly in the second camera frame

$$\begin{aligned} P_{\mathbf{o}''} &= x''\hat{e}''_x + y''\hat{e}''_y + z''\hat{e}''_z \\ &= x''(\hat{x}\cos(-\theta) + \hat{y}\sin(-\theta)) + y''(-\hat{x}\sin(-\theta) + \hat{y}\cos(-\theta)) + z''\hat{z} \\ &= \hat{x}(x''\cos(\theta) + y''\sin(\theta)) + \hat{y}(y''\cos(\theta) - x''\sin(\theta)) + z''\hat{z} \end{aligned} \tag{6.39}$$

In reality, both cameras are imaging the same object, so $P_{\mathbf{o}'} = P_{\mathbf{o}''}$. Thus we can express both vectors in the reentrant coordinate system and set their components equal to one another. This results, most simply, in the relation $z'' = z'$, as well as

$$\begin{aligned} x''\cos(\theta) + y''\sin(\theta) &= x'\cos(\theta) - y'\sin(\theta) \\ y''\cos(\theta) - x''\sin(\theta) &= y'\cos(\theta) + x'\sin(\theta) \end{aligned} \tag{6.40}$$

After some algebra, this yields

$$x' = \frac{y'' - y'\cos(2\theta)}{2\cos(\theta)\sin(\theta)} \tag{6.41}$$

We can examine this case for two special cases. If $\theta = \frac{\pi}{4}$, then the two camera normal vectors are orthogonal and $x' = y''$, i.e. the camera-axis offset for the first camera is given exactly by the offset along one of the basis vectors of the second camera. This situation would be the most convenient in the lab; however, experimentally it is unobtainable in our system due to limitations on the placement of viewports. Secondly, if $\theta = 0$ there is no solution to the above equation, as the two camera axis are parallel and thus there is no way to determine offsets along the camera axis from the resulting 2D camera images, unless such information is inferred from the amount of defocusing occurring in the imaging system.

Using the above relation, the total atom-ion offset vector is given as

$$\mathbf{o} = \hat{x}\left(\frac{y'' - y'\cos(2\theta)}{2\sin(\theta)} - y'\sin(\theta)\right) + \hat{y}\left(y'\cos(\theta) + \frac{y'' - y'\cos(2\theta)}{2\cos(\theta)}\right) + \frac{z' + z''}{2}\hat{z} \quad (6.42)$$

where the average of the z-offsets is taken to account for experimental imperfections.

Once $\mathbf{o}$ has been determined, it can be plugged into Eqn. 6.34 to yield the overlap factor. Similarly, after $\mathbf{o}$ has been determined, Eqn. 6.34 can be adapted to include other ion/atom density functional forms of interest, such as prolate spheroid functions for ion crystals or magnetic trap profiles for the atoms.

Also as a final note, the spatial dimensions of the MOT are measured in the rotated camera frames; however, for transformation into the reentrant frame in which the overlap integral is calculated, we make the following approximations

$$\{\omega_x, \omega_y, \omega_z\} = \{\sqrt{\omega_z \omega_y}, \frac{\omega_y' + \omega_y''}{2}, \frac{\omega_z' + \omega_z''}{2}\} \quad (6.43)$$

6.10 Laser systems

There are several laser systems in the lab used to provide optical fields necessary for laser cooling, dissociation transitions optical pumping, and other atomic and molecular manipulations. These systems range from commercially purchased units to homebuilt sysems. A brief discussion of the laser systems in the lab, as well as their locking mechanisms, will be given here.

6.10.1 External cavity diode lasers: the 650 nm, 493 nm, 672 nm, and 369 nm systems

The most standard homebuilt laser systems in our lab are external cavity dioder lasers (ECDL) arranged in the standard Littrow configuration. In this setup, a laser diode, typically equipped with an anti-reflection coating, is housed within a temperature controlled mount and further collimated with an aspheric lens. The collimated output is directed at a diffraction grating, and the $m = -1$ order of the grating is directed into the laser diode, providing optical feedback. Thus, the lasing mode is determined by the length of the cavity formed between the grating and the rear facet of the diode, which also sets the laser wavelength.

Further, the angle of the grating with respect to the diode will also determine the frequency of the light that is fed back into the laser, and thus the diode laser output frequency. Therefore, a piezo element (typically Thorlabs AE0203D08F) is integrated into the opto-mechanical mount that houses the diffraction grating (typically either Thorlabs Polaris or LINOS Lee's mount) to allow for fine frequency tuning. All components are typically mounted to an aluminum base plate, which itself is fixed to an aluminum diecast box (Hammond Manufacturing 1550Z139BK), which can be sealed with rubber gasket. The entire box is placed on top of a layer of vibration damping material (sticky blue stuff) which is spread over large hunk of metal, which in turn rests on top of sorbethane or Neoprene feet that are placed on our floated optical table - offering many layers of vibration isolation.

In general, the temperature of the diode, the temperature of the base plate, the grating piezo voltage, and the diode current all offer ways to tune the effective cavity length of the system and thus what the frequency output of the system is. Changing these parameters strategically in conjunction is often key to obtaining the largest 'mode-hop-free' tuning range where laser frequency can be tuned continuously without 'jumps' to adjacent cavity modes (in our homebuilt systems this value is usually ~ 4 GHz).

Typically, the grating-diode spacing is chosen to be less than $\lesssim 1$ in. The shorter this distance, the longer the free-spectral-range (FSR) of the cavity. In general, a large FSR will

lead to less mode-hoping. However, the shorter the diode-grating spacing, the less a given change in piezo length will affect the feedback frequency fed into the diode, leading to a smaller frequency sweeping dynamic range.

There are many different temperature and current controller units incorporated into these laser systems, with a majority of them manufactured by MogLabs or Wavelength Electronics or produced in house by Peter Yu and Christian Schneider. The performance of each of these units varies, and thus whichever unit best matches the constraints of a particular application should be used.

6.10.2 Titanium Sapphire Laser System

A titanium sapphire (ti-sapph) SolsTis-ECD-X unit was purchased from M2 Lasers. This laser has $\sim$ 4 W optical output from 700-1000 nm that can also be frequency doubled to allow probing of the 350-500 nm spectral region as well ($\sim$500-1000 mW of doubled light power).

The ti-sapph cavity is pumped by a 15 W 532 nm pump laser from Lighthouse Photonics (Sprout G). Unlike a bowtie frequency doubling cavity, multiple cavity modes across the ti-sapph crystal gain profile can resonate within the cavity. Thus, for single frequency output, optical elements are introduced into the cavity to induce frequency-specific optical losses, allowing a single mode to resonate. For coarse tuning, an intracavity bi-fringent filter (BRF) can be tilted to varying degrees (offering tuning at the $\sim$ 500 GHz level). In addition, an etalon is also present within the ti-sapph cavity, and it itself acts an optical filter that only allows frequencies that match a certain resonance condition to propagate in the crystal cavity. The etalon length can be tuned via a piezo, allowing for frequency control on the order of $\sim$100 MHz. Lastly, a piezo-element is also positioned within the ti-sapph cavity that can be used to scan the cavity length, and further, a feedback voltage can be applied to the piezo for laser locking purposes.

The output of the laser can also be fed into a reference cavity for further line narrowing to the $\sim$kHz level; however, the reference cavity can also make long-term laser locking more

difficult. Even without the reference cavity, the normal ti-sapph cavity output has a linewidth on the order of 1 MHz, which is perfectly adequate for many applications.

The ti-sapph fundamental output can be directed into a bow-tie doubling cavity for frequency doubling. A number of doubling crystals, each with $\sim$ 20 nm of doubled light tuning range, have been purchased for use with the system. The doubling power output will depend on the gain profile of the ti-sapph fundamental output, which is peaked near $\sim$800 nm; however, in general, up to $\sim$ 1 W of doubled light can be obtained.

Control of the BRF, the cavity etalon, the reference cavity, and the ECD-X unit is handled electronically through the M2 ICEBLOC control system, which has a software interface that can be linked to the wi-fi network within the lab. There are a variety of sensors that can observed through the ICEBLOC system, which also is equipped with two BNC outputs for signal monitoring. Namely these include photodiodes within both the ti-sapph and ECD-X cavity as well as error signals for the etalon, reference cavity, and ECD-X locks.

6.10.3 Alignment procedures

A general alignment procedure for the system goes as follows (the user manuals for the system can be consulted for more thorough details). Use the BRF to coarse tune to the desired wavelength, and then use the etalon control to navigate to the desired wavelength to within $\sim$100 MHz. Ideally, keep the etalon control setting as close to 50% as possible for optimal performance. Then adjust the ti-sapph cavity coupling mirror (see Fig. 6.25a) using the x/y dimension mirror mount knobs (but not the z knob) to maximize the cavity output, as determined by the intracavity photodiode.

Once this has been done, engage the etalon lock and proceed to optimizing the ECD-X unit if needed. The ECD-X can be aligned through iterative adjustment of the input coupling and output coupling mirrors of the cavity (M1 and M4 in Fig. 6.25b) as well as the doubling crystal tilt angle, controlled through a micrometer. All mirrors and crystal faces in the cavity should be cleaned with methanol-moistened lens cleaning tissues if performance is suboptimal. In general, dust is the single most common issue for poor system performance

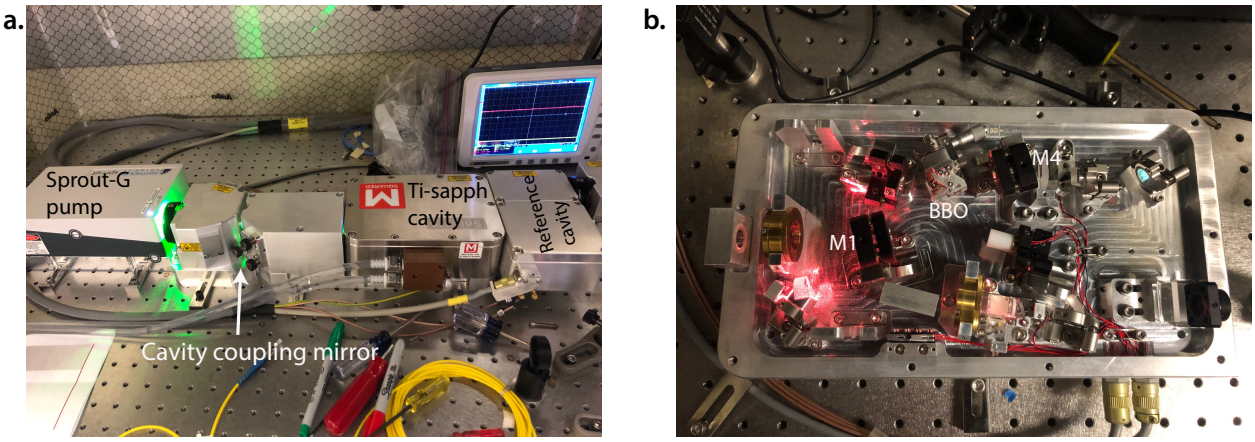

Figure 6.25: M2 laser system

(**a**) Image of the M2 SolStis system, with the 532 nm pump, the ti-sapph cavity coupling unit, the ti-sapph cavity, and the reference cavity all visible. (**b**) An image of the ECD-X unit which consists of a BBO crystal in a bowtie cavity configuration. The input (M1) and output (M4) coupling mirrors should be adjusted during cavity alignment for maximum power output.

throughout both the Solstis and ECD-X units.

Once the power had been optimized in the ECD-X, once again as measured by an intra-cavity photodiode visible on the ICEBLOC system, the error signal can be adjusted through manipulation of various photodiode gain and offset voltage settings involved in Hänsch-Couillard cavity lock employed to stabilize the system. After performing these steps, the lock can be engaged and the laser is ready for use.

6.10.4 ND:YAG and Pulsed Dye Laser system

A Q-switched Nd:YAG laser (Spectra-Physics Quanta Ray Lab-170 Series) provides the high energy pulsed (10 ns width) light used to drive many of the dissociation events in this thesis. The fundamental output of the system is 1064 nm ($\sim$ 750 mJ/pulse) but a series of BBO crystals housed in a frequency doubling unit within the system allow for simultaneous output of both 532 nm ($\sim$ 350 mJ/pulse) as well as 355 nm ($\sim$ 150 mJ/pulse) light. The linewidth of the fundamental is typically $\sim$ 2 GHz, but the unit is also equipped with a seeder laser that, when activated, can lead to Fourier limited linewidths of $\sim$ 50 MHz. In addition, a

separate BBO crystal can be introduced into the path of the 532 nm output to produce FHG 266 nm light (∼50 mJ), which will be featured in the rotational state readout schemes discussed later in this thesis.

To perform photodissociative spectroscopy of molecular ions, we use a pulsed dye laser (Sirah Cobra Stretch PDL, dual grating configuration 1800 lines/mm, .05 cm^{-1} linewidth) combined with a Sirah Precision Scan frequency-doubling unit whose output can be tuned from 205-280 nm using two BBO crystals (205-215 nm and 215-280 nm) and an assortment of Exalite (p-dioxane solvent) and Coumarin (methanol solvent) dyes. Additional crystals and solvents can be purchased to afford even greater tuning range. Optimizing the many different components of the system is quite complex and the user manual should be consulted for a thorough treatment of alignment procedures.

An auto-tracking unit can be used to automatically angle-tune the BBO crystals in order to optimize the second-harmonic generation; however we have found that it is sufficient to tune this semi-manually using a look-up table for motor positions for the tuning unit based on desired wavelength. Frequency-doubled light typically can have pulse energies up to ∼4 mJ at 10 Hz repetition rates. Scanning is primarily achieved by a LabVIEW vi which generates a signal that is fed back to the PDL cavity grating position following the input of a wavelength value recorded by an external wavemeter.

6.10.5 Toptica 422 Laser System

To drive the Ca cooling transition in this work, we employ a Toptica TA-SHG-110 laser system. The unit includes a 845 nm diode housed in the patented Toptica 'hockey puck mount' that enables a mode-hop free fundamental tuning range of roughly ∼30 GHz. The 845 nm output is sent through a tapered amplified (TA) that boosts the fundamental power to ≈ 2W. The amplified light is then sent through a bowtie doubling cavity featuring a BBO crystal for 422 nm output (∼200-350 mW, depending on alignment). A piezo fastened to one of the bowtie mirrors allows for PDH locking of the internal cavity.

When optimizing power output of the system, the TA coupling mirror may first be

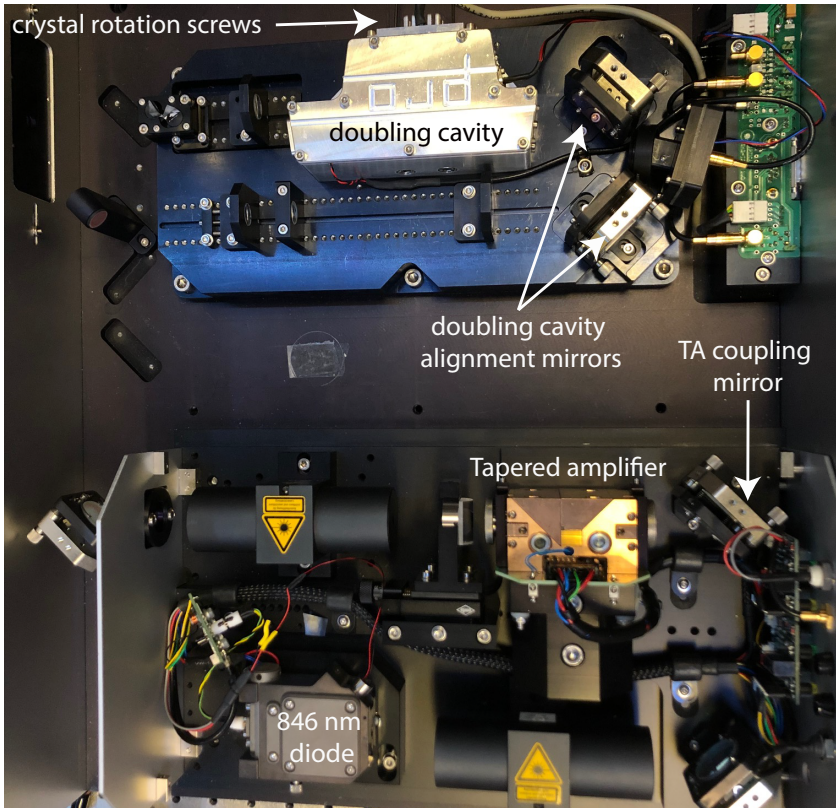

Figure 6.26: Toptica TA-SHG-110 laser system

An image of the Toptica TA-SHG-110 laser system including the IR diode, the tapered amplifier, and the doubling cavity, along with their associated coupling mirrors and relevant adjustment knobs.

adjusted for maximal IR output while still permitting doubled light output (see Fig. 6.26). Then both the doubling cavity input coupling and the doubling crystal rotation angle can be co-optimized for maximum blue output. If additional power optimization is needed, the angle of the cavity mirrors themselves may also be adjusted; however, this is not typically necessary during week-to-week maintenance.

A set of electronics from Toptica are used for the following purposes:
(DTC 110): temperature control of the laser diode/TA/doubling crystal
(DCC 110): current control of the laser diode/TA
(PDD 110): error signal generation for the cavity PDH lock
(PID 110): PDH locking circuitry for the doubling cavity
(SC 110): cavity piezo scanning unit

The diode current/temperature setpoints are typically 107mA/22.4° C, while the corresponding values for the TA are 2730 mA/28.4° C. In particular, stable laser locking is extremely important to the power output of the laser, and thus, the parameters of the PDD 110 and PDH 110 should be checked regularly for ideal system performance.

A portion of the beam output from the Toptica (∼10 mW) is picked off and sent to a saturated absorption lock, referenced to an Ca vapor cell (detailed in Refs. [Sul13, SDC16]). The lock provides feedback to the diode grating within the Toptica unit and is set such that the Toptica emits light at $\omega = \omega_0 + 85$ MHz, when ω_0 is the frequency of the cooling transition.

There are essentially four frequencies that are required from the Toptica output for our MOT setup: (1) a $-\Gamma$ detuned cooling beam ($\sim$ 30 mW), (2) an on-resonance beam for absorption imaging ($\sim$ 2 mW), (3) a -4Γ detuned deceleration beam ($\sim$ 40 mW), 4) a -10Γ detuned deceleration beam ($\sim$ 40 mW). The frequencies are produced from the AOM setup in Fig. 6.27. The overall power of the cooling beams may be conveniently adjusted through installing a variable ND filter wheel (Thorlabs NDM2) in the cooling laser beam path, a feature often used for controlling excited state population, as to be discussed later in this work.

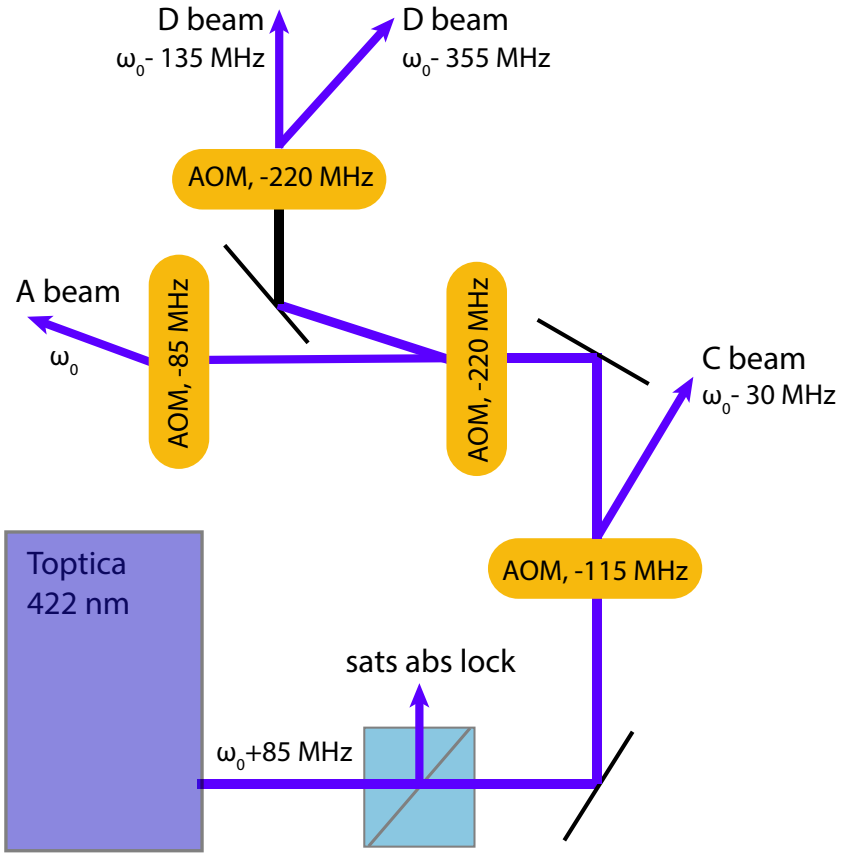

Figure 6.27: MOT beam setup

The beam setup for the MOT system. The output of the Toptica is locked to a saturated absorption lock, with a lock frequency of $\omega_0 + 2\pi\times85$ MHz, where ω_0 is the Ca $^1S_0 \rightarrow ^1P_1$ transition frequency. The first AOM shifts this beam to ω_0 - $2\pi\times30$ MHz, creating the cooling beam (C beam). Two subsequent AOM's create the two deceleration beams (D Beams), which are set to ω_0 - $2\pi\times135$ MHz and ω_0 - $2\pi\times355$ MHz. Lastly the zeroth order AOM beams are finally directly to a +85 MHz AOM which can be used to create an on-resonance beam of frequency ω_0, for absorption imaging.

6.10.6 Laser-locking: wavemeter lock

Essentially all of the laser locking in the lab (aside from the Toptica saturation absorption lock) is performed through software locks referenced to a High Finesse WSU-2 wavemeter (14 channel, ~ 2 MHz accuracy). The wavemeter is fiber-connected to two 8 channel multiplexers (product number MC8) with fiber-coupled inputs, one with wavelength coverage from ≈360 nm - 650 nm and a second capable of reading $\approx$ 650 nm - 1100 nm light. Each port on the switch can be fed a separate laser beam sample, and the channel exposure times can be varied until stable readings are produced.

The wavemeter itself came pre-frequency-calibrated from the manufacturer, but, to account for frequency drifts over time, is periodically re-calibrated to our Ca saturated absorption reference. The frequencies for most of the atomic transitions of relevance to this work are presented in Table 6.4.

The wavemeter reading of each laser can be used as a reference for standard PID locking, whereby the wavemeter reading is compared to a reference value and a correction signal is generated. In our lab, this correction signal takes the form of a voltage that is sent to a piezo element that controls the length of a particular laser cavity.

The correction voltage,$V_c(t)$ is defined by the standard k_P, k_I, and k_D parameters as

$$V_c(t) = S\left(k_P e(t) + k_I \int_0^t e(t')dt' + k_D \frac{de}{dt}\right) \tag{6.44}$$

where $e(t) = \lambda(t) - \lambda_0$ where $\lambda(t)$ is the signal as a function of time, λ_0 is the signal reference, and S is the overall feedback sensitivity. The proportional gain (k_P) terms handles instantaneous offsets with respect to λ_0 while the integral term (k_I) handles longer-term offsets that can accumulate in a feedback system. The derivative term (k_D) offers an additional degree of flexibility but is rarely utilized in our feedback loops (k_D=0).

The WSU unit is also equipped with a 8 channel DAC card that can be used to generate feedback signals. The S, λ_0, k_P, k_I, and k_D parameters for each feedback signal can be specified, and further each feedback signal can be linked to a wavemeter channel, whose readings serve as the $\lambda(t)$ for the feedback loop. All these parameters can be conveniently

Transition	Frequency (THz)	Use	Laser system
$^{174}\mathbf{Yb}^{+}$			
$6s\,^2S_{1/2} \rightarrow 6p\,^2P_{1/2}$	811.291296	369 nm cooling	Homebuilt ECDL
$5d\,^2D_{3/2} \rightarrow 5d6s\,^3[3/2]_{1/2}$	320.571886	935 nm repump	Homebuilt ECDL
$^{172}\mathbf{Yb}^{+}$			
$6s\,^2S_{1/2} \rightarrow 6p\,^2P_{1/2}$	811.292610	369 nm cooling	Homebuilt ECDL
$5d\,^2D_{3/2} \rightarrow 5d6s\,^3[3/2]_{1/2}$	320.569285	935 nm repump	Homebuilt ECDL
$^{138}\mathbf{Ba}^{+}$			
$6s\,^2S_{1/2} \rightarrow 6p\,^2P_{1/2}$	607.426130	493 nm cooling	Homebuilt ECDL
$5d\,^2D_{3/2} \rightarrow 6p\,^2P_{1/2}$	461.311765	650 nm repump	Homebuilt ECDL
$^{40}\mathbf{Ca}$			
$4s^2\,^1S_0 \rightarrow 4s4p\,^1P_1$	709.078379	422 nm cooling	Toptica TA-SHG-110
$3d4s\,^1D_2 \rightarrow 4s5p\,^1P_1$	446.150863	672 nm repump	Homebuilt ECDL
$3d4s\,^1D_2 \rightarrow 4s4f\,^1F_3$	614.393495	488 nm repump	M2 SolStis/ECD-X
$3d4s\,^1D_2 \rightarrow 4snp\,^1P_1$	662.057231	453 nm repump	M2 SolStis/ECD-X
$3d4s\,^1D_2 \rightarrow 4s5f\,^1F_3$	688.180929	436 nm repump	M2 SolStis/ECD-X
$3d4s\,^1D_2 \rightarrow 4s7p\,^1P_1$	706.783089	424 nm repump	M2 SolStis/ECD-X
$3d4s\,^1D_2 \rightarrow 4s6f\,^1F_3$	729.478413	411 nm repump	M2 SolStis/ECD-X
$4s4p\,^3P_2 \rightarrow 4s4d\,^3D_2$	672.612130	445 nm ^{3}P$_2$ optical pumping (preferred)	M2 SolStis/ECD-X
$4s4p\,^3P_2 \rightarrow 4s4d\,^1D_2$	659.014100	455 nm ^{3}P$_2$ optical pumping	M2 SolStis/ECD-X
$4s4p\,^3P_2 \rightarrow 4p^2\,^3P_2$	696.586670	430 nm ^{3}P$_2$ optical pumping (preferred)	M2 SolStis/ECD-X
$4s4p\,^3P_1 \rightarrow 4p^2\,^3P_2$	699.760770	428 nm ^{3}P$_1$ optical pumping	M2 SolStis/ECD-X
$4s4p\,^3P_0 \rightarrow 4p^2\,^3P_1$	698.724110	429 nm ^{3}P$_0$ optical pumping	M2 SolStis/ECD-X

Table 6.4: Frequencies of a majority of the atomic transitions used in this thesis, as determined by the WSU-2 wavemeter. Due to calibration drifts at the time of each measurement, these readings are subject to ~ 100 MHz error.

controlled via the High Finesse software, which also allows for simple viewing of wavemeter channel readings as a function of time. For experiments, in which wavemeter readings need to be extracted *in situ*, we communicate with the wavemeter through the LabRAD software interface. Further, if all 8 outputs of the WSU DAC card are occupied, feedback voltages can also be generated through other DAC cards connected to the central experimental control computer, with control software for the feedback loops generated in LabVIEW.

6.11 Experimental control software

National Instruments (NI) LabVIEW is used for instrumentation and timing control in the experiment. The experimental control computer has three data acquisition (DAQ) cards. First, there is a PCIe 6537 50 MHz digital I/O card which, in conjunction with an occasionally-used digital pulse generator (Quantum Composer 9518+), handles all the timing requirements of the experiment. Analog input and output capabilities are covered by a PCI 6236 and a PCI 6230 card, which handle current and voltage readings, respectively.

CHAPTER 7

Ca electronic structure and laser-cooling pathways

Ca atoms are used extensively in this thesis as both a chemical reactant and a sympathetic coolant. For the former, knowledge of the exited state populations while laser-cooling is critical for being able to determine state-specific rate constants. For the latter, obtaining high MOT densities is important for ensuring the rate of cooling exceeds the heating rate due to blackbody radaition and background gas collision events. This chapter is dedicated to investigating the electronic structure of Ca; in particular, we will identify a series of repumping transitions that may be used to increase typical MOT densities by a factor of ~ 10. In addition, we will also explain how electronic state populations are modeled during Ca laser cooling.

7.1 Background motivation

The magneto-optical trap (MOT) [al87] is an integral part of atomic and molecular physics, where it is the starting point for a variety of experiments including precision tests of fundamental physics [al15], studies of quantum many-body physics [al16], and production of ultracold molecules [RSS12,BMN14]. At present, atomic MOTs have been constructed for atoms within Groups 1, 2, 6, 12, and 18, as well as the lanthanides. Extension to atoms in other Groups is often limited by the availability of appropriate laser technology for driving the necessary cooling transitions and complications due to the electronic structure of the atom. For example, if there are multiple electronic states below the upper electronic state of the primary laser cooling transition, then radiative decay into these lower levels can severely reduce, and even eliminate, the laser cooling force. For these reasons, the Group

1 atoms, with their lone optically active, unpaired electron, provide the simplest, and often best performing, MOTs.

Nonetheless, the same 'complications' that can limit the laser cooling process often host interesting and useful phenomena. A prime example of this is the presence of ^3P states of Group 2(-like) atoms, which, while detrimental to the performance of a standard MOT, allow the construction of next-generation optical atomic clocks that can outperform the Cesium standard [LBY15]. One such MOT of this type is the Ca MOT. Calcium MOTs have been utilized in atomic optical clock experiments using the 657 nm $^3P_1 \leftarrow {}^1S_0$ intercombination line [SDS04, DSL05, WOH06] and have significant appeal due to their simplicity of construction as portable optical frequency standards [Vut15]. However, despite this appeal, the details of the Ca electronic structure lead to relatively poor performance of Ca MOTs, including a short trap lifetime limited by optical pumping into dark states and a low achievable peak atomic density. This is one reason other Group 2(-like) atoms such as Sr, Yb, and Hg have become more popular choices for optical frequency standards [LBY15, DK11].

Given the potential of Ca as a portable frequency standard, as well as its utility in our own experiments as a sympathetic coolant for molecular ions [RSS12], we have performed a detailed combined experimental and theoretical study of Ca MOT operation. Specifically, relativistic many-body calculations are performed for the first 75 energy levels of the Ca atom, providing reliable electronic structure and transition matrix elements for this multi-electron atom. The results of this calculation are incorporated into a rate equation model for the populations in the Ca atom, which is used to evaluate specific repumping schemes and identify seven promising transitions. In total, we experimentally investigate five alternative repumping schemes and find that all of them yield Ca MOTs with lifetimes and atom numbers improved by $\sim 10\times$ over the traditional scheme described in Ref. [GH01]. The best of these schemes, which utilizes repumping to a highly configuration-mixed state with a 453 nm repumping laser, produces a Ca MOT with lifetime, number, and density improved over the standard MOT by $\sim 25\times$, $\sim 20\times$, and $\sim 6\times$, respectively.

In the remainder of this paper, we first present the details of the relativistic many-body calculation of the Ca energy levels and the resulting rate equation model of the Ca

populations. We then use this rate equation model to explain the poor performance of the traditional Ca MOT. From this work, we propose seven alternative MOT operation schemes and experimentally investigate five of them. We characterize the differences in these MOT operation schemes, reporting the achievable MOT lifetimes, density, and trapped atom numbers, as well as the necessary repumping laser frequencies. We conclude with discussion of the ideal repumping scheme for Ca MOT operation and possible extension to other Group 2(-like) atoms.

7.2 Relativistic many-body calculations of atomic structure

The analysis of MOT performance requires estimates of electric-dipole transition rates between the 75 lowest-energy levels of Ca, including both spin-allowed and spin-forbidden (intercombination) transitions. While the energy levels are well established, transition rates among the first 75 lowest-energy states (811 possible channels) are not known completely, although there are a number of theoretical and experimental determinations. The earlier theory work provides oscillator strengths for spin-allowed transitions for levels up to $4s10s$, $4s9p$, $4s6d$, and $4s5f$, respectively [Mit93, BF94, LH96, HLH99]. Most of these calculations are non-relativistic with a limited number of low-lying levels treated with *ab initio* relativistic methods. The data on transition probabilities for intercombination transitions and transitions involving the $4s6f$ states are scarce [PKR01, SJ02, FT03]. In literature, 111 experimental transition rates are available [ZBR00, Smi88, Kos64, SR81, PRT76, LH87, ALB09, HWW85, HP86, HR86, KRR16, Mor04, SO75, UHF83, UHF82]. The incompleteness of transition rate data motivated us to generate a full set of the 811 required transition rates. To this end we used methods of relativistic many-body theory. *Ab initio* relativistic calculations are necessary as the analysis requires inclusion of transition amplitudes that are non-relativistically forbidden.

Calcium is an atom with two valence electrons outside a tightly bound core. We employ a systematic formalism that combines advantages of both the configuration interaction (CI) method and many-body perturbation theory (MBPT), the CI+MBPT method [DFK96].

Table 7.1: Comparison of CI+MBPT transition energies ΔE (cm^{-1}) and rates A_{if} ($10^8 \times \mathrm{s}^{-1}$) with NIST-recommended transition energies and 16 out of the available 111 experimental transition rates along with their uncertainties.

States		ΔE, cm^{-1}		A_{if}, $10^8\,\mathrm{s}^{-1}$		
Initial	Final	CI+MBPT	NIST	CI+MBPT	Exp.	Deviation (%)
$4s4p\ ^1P_1$	$4s^2\ ^1S_0$	23491	23652.304	2.170	2.182(12) [ZBR00]	-0.5(5)
$4p^2\ ^1S_0$	$4s4p\ ^1P_1$	18846	18133.972	0.778	0.754(21) [Smi88]	3.2(2.9)
$4p^2\ ^1D_2$	$4s4p\ ^1P_1$	17691	17067.543	0.576	0.683(11) [HWW85]	-16(1)
$3d4p\ ^1D_2$	$3d4s\ ^1D_2$	13901	13985.779	0.341	0.358(9) [SR81]	-4.7(2.4)
$4snp\ ^1P_1$	$4s^2\ ^1S_0$	44383	43933.477	0.325	0.284(39) [PRT76]	14(16)
$4s4f\ ^1F_3$	$3d4s\ ^1D_2$	19943	20493.953	0.312	0.31(6) [LH87]	1(19)
$4s7p\ ^1P_1$	$4s^2\ ^1S_0$	46975	45425.358	0.130	0.148(21) [LH87]	-12(12)
$4s7s\ ^1S_0$	$4s4p\ ^1P_1$	21724	20624.234	0.068	0.113(5) [Smi88]	-40(3)
$4s4d\ ^1D_2$	$4s4p\ ^1P_1$	14169	13645.983	0.160	0.154(4) [Smi88]	3.9(2.7)
$4s6d\ ^1D_2$	$4s4p\ ^1P_1$	22324	21337.526	0.057	0.080(3) [Smi88]	-29(3)
$4s5p\ ^1P_1$	$3d4s\ ^1D_2$	14259	14881.981	0.130	0.147(3) [SR81]	-12(2)
$4s6p\ ^1P_1$	$4s^2\ ^1S_0$	41788	41679.008	0.092	0.157(22) [PRT76]	-41(8)
$4s6s\ ^1S_0$	$4s4p\ ^1P_1$	17451	17038.131	0.014	0.052(4) [Smi88]	-73(2)
$4s4p\ ^1P_1$	$3d4s\ ^1D_2$	1041	1802.670	0.0000534	0.0000368(100) [LH87]	45(39)
$4s4p\ ^3P_1$	$4s^2\ ^1S_0$	15180	15210.063	0.0000274	0.0000302(7) [HR86]	-9.3(2.2)
$3d4p\ ^1F_3$	$3d4s\ ^1D_2$	18651	18688.259	0.057	0.165(7) [SR81]	-65(1)

The CI+MBPT method has been used extensively for evaluation of atomic properties (see, e.g., Ref. [DP11] for optical lattice clock applications and references therein). Relativistic effects are included exactly, as the formalism starts from the Dirac equation and employs relativistic bi-spinor wave functions throughout the entire calculation. In our treatment, the CI model space is limited to excitations of valence electrons. Contributions involving excitations of core electrons are treated within MBPT. In this approach, we first solve for the valence electron orbitals and energies in the field of the core electrons. The one-electron effective potential includes both the frozen-core Dirac-Hartree-Fock (DHF V^{N-2}) and self-energy (core-polarization) potentials. The self-energy correction is computed us-

ing second-order MBPT diagrams involving virtual core excitations. At the next step, the computed one-electron valence orbitals are used to diagonalize the atomic Hamiltonian in the model space of two valence electrons within the CI method. The CI Hamiltonian includes the residual (beyond DHF) Coulomb interaction between the valence electrons and their core-polarization-mediated interaction. The latter was computed in the second-order MBPT. This step yields two-electron wave-functions and energies. Finally, with the obtained wave-functions we calculated the required electric-dipole matrix elements. In calculations of transition rates we used experimental energy intervals and the computed CI+MBPT matrix elements.

We used two independent CI+MBPT implementations: (i) by the Reno group (see the discussion of the earlier version in Ref. [Der01]) and (ii) a recently published package [KPS15]. The practical goal of the calculations was not to reach the highest possible accuracy, but rather to generate the large amount of data needed for the transition array involving the 75 lowest-energy levels. An additional computational challenge was the inclusion of high angular momenta states, e.g., the $4s5g\ ^3G$ state. The Reno code was run on a large basis set but without including core-polarization-mediated interaction in the CI Hamiltonian due to considerable computational costs. The production runs with the package of Ref. [KPS15] employed a smaller basis set (due to code limitations) but treated the correlation problem more fully. Our final values combine the outputs of the two codes. The bulk of the results comes from the package of Ref. [KPS15]. These results are augmented with the rate data involving $4s8s$ states from the Reno code due to the limited number of roots in the package of Ref. [KPS15].

We assessed the quality of the calculations by comparing the CI+MBPT energies with the NIST recommended values [KRR16] and CI+MBPT transition rates with 111 available experimental values (see subset in Table 7.1) [ZBR00, Smi88, Kos64, SR81, PRT76, LH87, ALB09,HWW85,HP86,HR86,KRR16,Mor04,SO75,UHF83,UHF82]. The CI+MBPT energy intervals for tabulated transitions agree with NIST values to better than 1000 cm^{-1}. To quantify the error of the CI+MBPT transition rates, we calculate the relative deviation from the experimental values, $E_{if} = 100\frac{A_{if,calc}-A_{if,exp}}{A_{if,exp}}$, with standard errors corresponding

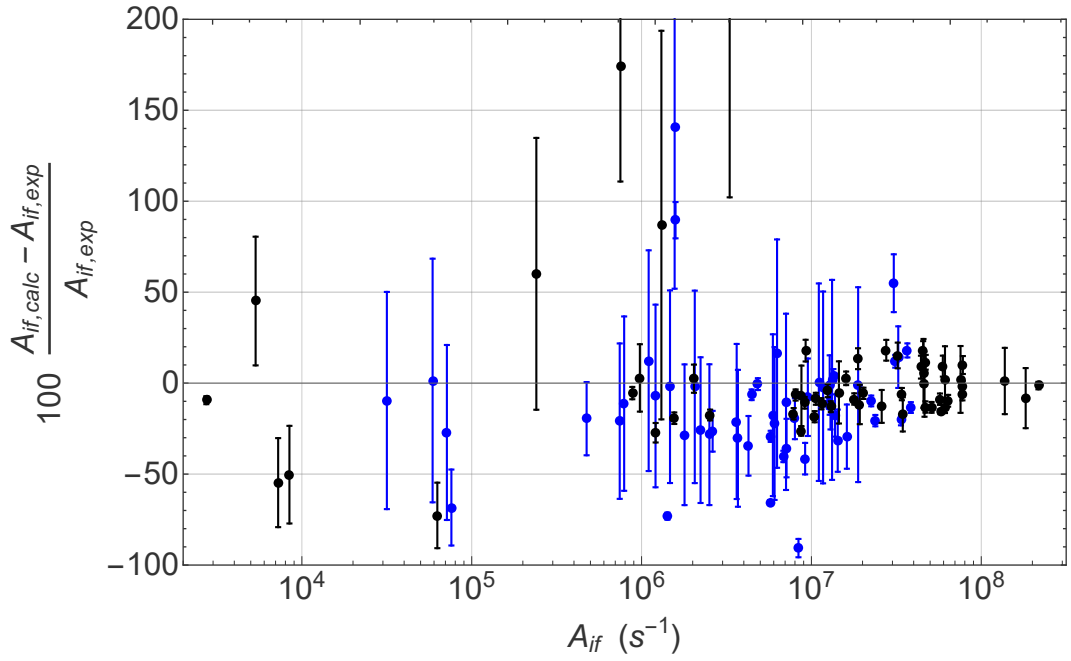

Figure 7.1: Comparison of the calculated CI+MBPT transition rates with 111 available experimental data. Transitions involving a state with orbital angular momentum $l \geq 3$ or principal quantum number $n \geq 6$ are shown in blue. All other transitions are shown in black. Error bars correspond to the experimental error.

to the experimental errors (see Fig. 7.1). The weighted root mean square of E_{if} yields an estimate of the error of the CI+MBPT transition rates. We determine this error for two subsets of transitions: The first includes all transitions involving a state with orbital angular momentum $l \geq 3$ or principal quantum number $n \geq 6$, where both faithful numerical representation and inclusion of correlations are important, and yields an average error of 48%. The second subset includes all other transitions and has an average error of 13%. This difference in error is reflective of the computational difficulty of obtaining transition rates for these subsets of transitions. For some transitions, the deviation of our theoretical transition rates from experiment is large; to remedy this, we replace our calculated transition rates with experimental values when the deviation is greater than twice the experimental error or the experimental error is less than our expected error.

7.3 Rate equation model of Ca electronic state populations

Using the 811 calculated CI+MBPT transition rates augmented by experimental transition rates as previously described, we create a rate model including the first 75 excited states of calcium. As an example, the differential equation for state i with a monochromatic laser driving from state i to state k is given by

$$\frac{d}{dt}N_i = \sum_{j>i} A_{ji}N_j - \sum_{j<i} A_{ij}N_i - \frac{N_i}{\tau_{Loss}} + A_{ki}\frac{\pi^2 c^3}{\hbar\omega_{ik}^3}\frac{I_l}{2\pi c}\frac{\Gamma_k}{(\omega_{ik}-\omega_l)^2 + \frac{\Gamma_k^2}{4}}\left(N_k - \frac{2j_k+1}{2j_i+1}N_i\right) \quad (7.1)$$

where N_i is the number of atoms in state i, A_{ij} is the decay rate of state i to j, τ_{Loss} is the time in which an uncooled atom drifts outside of the MOT region (for our parameters, this value is 1.7 ms for the $4s4p\ ^3P_0$ and $^3P_2$ states and ∞ otherwise), c is the speed of light in a vacuum, $\hbar$ is the reduced Planck constant, ω_{ik} is the angular transition frequency between state i and k, ω_l (I_l) is the angular frequency (intensity) of the applied laser, Γ_k is the natural linewidth of state k, and j_i is the total angular momentum quantum number of state i [Foo05].

To determine the effect of the errors in the CI+MBPT transition rates on the lifetime of the MOT, we randomly vary each of the 811 transition rates according to their expected error. Using these modified transition rates, we numerically solve the coupled differential equations to extract a MOT lifetime. We repeat this process 1000 times and report the mean and the standard deviation of the resulting MOT lifetimes.

7.4 Evaluation of the standard Ca MOT operation

The standard implementation of a Ca MOT is formed by laser cooling on the strong $4s4p\ ^1P_1 \leftarrow 4s^2\ ^1S_0$ transition at 423 nm in the presence of an anti-Helmholtz magnetic field with gradient of 60 G/cm in the axial direction. This transition incurs loss from the laser cooling cycle primarily due to decay from the $4s4p\ ^1P_1$ state to the $3d4s\ ^1D_2$ state. This $^1D_2$ state, as shown in Fig. 7.2, decays to the $4s4p\ ^3P_1$ (83% branching) and $^3P_2$ (17% branching) states with a total lifetime of 1.71 ms [HR86]. The $^3P_1$ state decays to the ground state with a lifetime of 0.331 ms, while the $^3P_2$ state has a lifetime of 118 minutes, leading to loss from the laser cooling cycle [HR86,Der01]. This loss, which is proportional to the $4s4p\ ^1P_1$ state population, limits the lifetime of the Ca MOT and according to the rate model with our experimental parameters leads to a MOT lifetime of 27(5) ms. As detailed later, we experimentally observe a MOT lifetime of 29(5) ms in this configuration.

To extend the MOT lifetime, a repumping laser is usually added to drive the $4s5p\ ^1P_1 \leftarrow 3d4s\ ^1D_2$ transition at 672 nm in order to return electronic population in the $3d4s\ ^1D_2$ level to the laser cooling cycle before it decays to the $4s4p\ ^3P_1$ and $^3P_2$ states [KS92]. In this configuration, the rate equation model predicts that the MOT lifetime is increased to 86(18) ms for our experimental parameters. As detailed later, we experimentally observe a MOT lifetime of 93(6) ms in this configuration.

Interestingly, it is often assumed that the lack of a further increase in the MOT lifetime with this repumping scheme is due to an incomplete depletion of the $3d4s\ ^1D_2$ state, which is in turn due to unfavorable branching ratios in the $4s5p\ ^1P_1$ state [KS92]; this state decays primarily back to the $3d4s\ ^1D_2$ state and only weakly back in the cooling cycle. However,

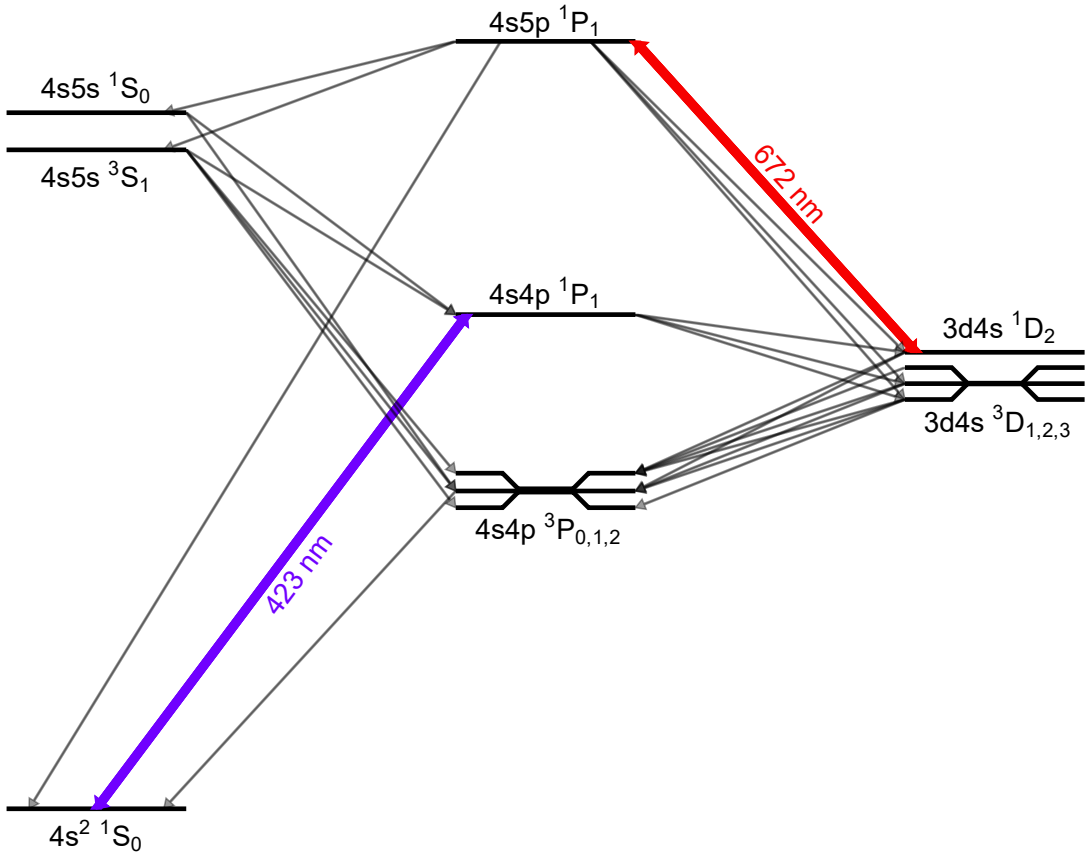

Figure 7.2: Relevant level structure for operation of a standard calcium MOT. Laser cooling is accomplished on the 423 nm $4s4p\ ^1P_1 \leftarrow 4s^2\ ^1S_0$ transition. Atoms that decay to the $3d4s\ ^1D_2$ state are repumped back into the cooling cycle via the 672 nm $4s5p\ ^1P_1 \leftarrow 3d4s\ ^1D_2$ transition, while those in the long-lived $4s4p\ ^3P_{0,2}$ states are lost from the MOT.

the rate equation model reveals that the MOT lifetime is actually limited by the decay of the $4s5p\ ^1P_1$ state to the $4s5s\ ^3S_1$, $3d4s\ ^3D_1$, and $3d4s\ ^3D_2$ states, all of which decay primarily to the $4s4p\ ^3P_{0,1,2}$ states, as shown in Fig. 7.2 and first pointed out in Ref. [OBF99]. Specifically, according to the theoretical calculations, the $4s5p\ ^1P_1$ state decays indirectly to the lossy $4s4p\ ^3P_0$ and $^3P_2$ states at a total rate of 8×10^4 s^{-1}, while the $3d4s\ ^1D_2$ state decays to the $4s4p\ ^3P_2$ state at a rate of only 80 s^{-1}. With this understanding, the natural question arises: *Is there an alternative repumping scheme that would suppress the loss into these triplet states?*

7.5 Evaluation of alternative Ca MOT operation schemes

The ideal repumping laser out of the $3d4s\ ^1D_2$ state would quickly transfer population from the $^1D_2$ state back into to the cooling cycle with perfect efficiency. With this idealized scheme, the rate model predicts a lifetime of 3.0(4) s with our MOT parameters. This lifetime is limited by the decay of the $4s4p\ ^1P_1$ state to $3d4s\ ^3D_1$ and $^3D_2$ states and is thus dependent on the $4s4p\ ^1P_1$ state population; lowering the $4s4p\ ^1P_1$ state population by decreasing 423 nm cooling laser intensity while maintaining reasonable MOT performance can extend the lifetime by $\sim 2\times$. Since this lifetime is similar to lifetimes set by other effects in most systems, such as collisions with background gas, it is likely unnecessary for the majority of applications to employ a more complicated multi-laser repumping scheme out of the ^{3}P states like that used in Sr [LBY15], especially since the longer lifetime of the $3d4s\ ^1D_2$ and $4s4p\ ^3P_1$ in Ca make this scheme less efficient.

Therefore, for this work we choose to only explore single-laser repump transitions from the $3d4s\ ^1D_2$ state with high branching ratios back into the laser cooling cycle. With this metric, we find that within the first 75 electronic states, there are seven reasonable alternative repumping transitions from the $3d4s\ ^1D_2$ state, shown in Fig. 7.3, which go to states in the $^1P_1$ and $^1F_3$ manifolds. Using the rate equation model with our standard MOT parameters, we calculate the expected MOT lifetimes for these transitions, which are limited by optical pumping into the $^3P_{0,2}$ states, and present the results in Table 7.2.

Of these seven transitions, five are accessible by lasers available to us and we explore them using a standard six beam Ca MOT described in Ref. [RSS12]. Briefly, in this system, laser cooling is provided by driving the $4s4p\ ^1P_1 \leftarrow 4s^2\ ^1S_0$ cooling transition with a total laser intensity of 63 mW/cm^2 detuned 34.4 MHz below resonance. The Ca MOT is loaded from an oven source placed ~ 3.5 cm away from the MOT. Atoms from the oven are decelerated by two 'deceleration beams' with intensities 110 mW/cm^2 and 53 mW/cm^2 and detunings below resonance of 109 MHz and 318 MHz, respectively. The 672 nm traditional Ca MOT repump laser has an intensity of 11 mW/cm^2.

For each single-beam repumping scheme, we characterize the MOT performance by mea-

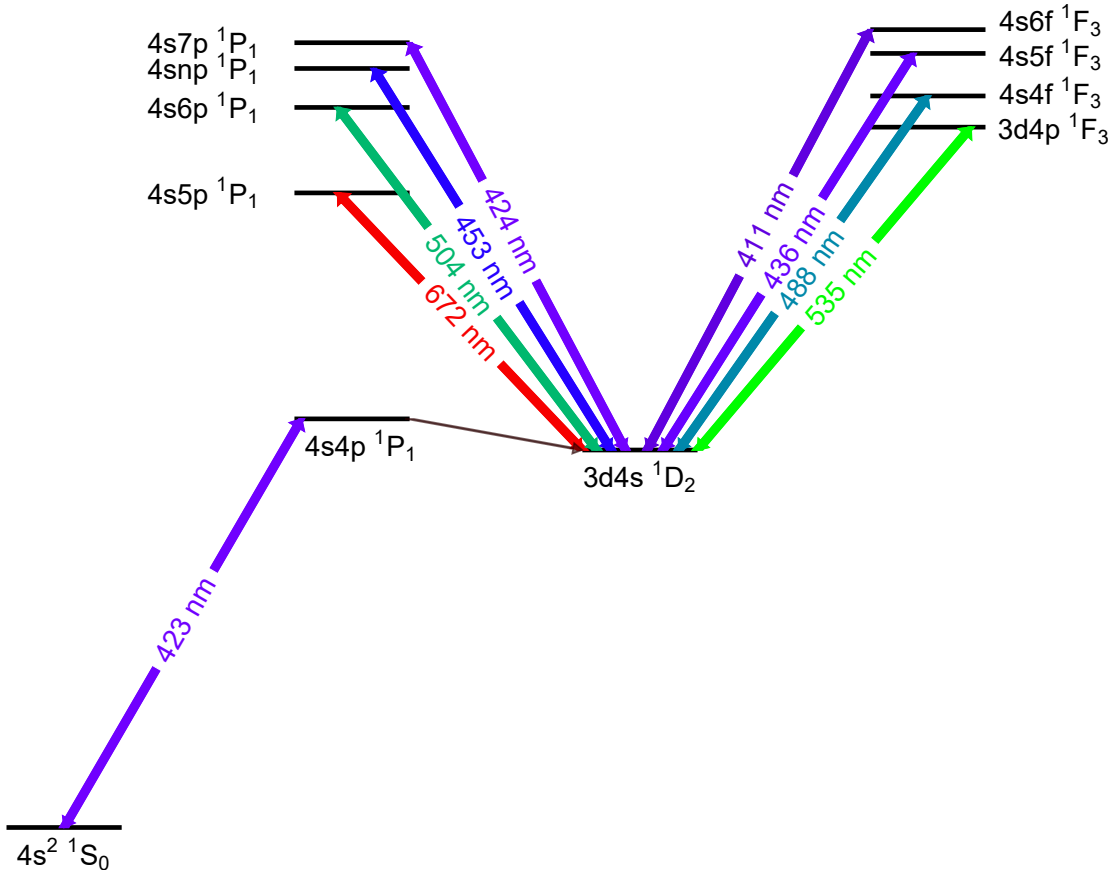

Figure 7.3: Simplified calcium electronic level structure showing the eight repumping transitions considered here. All transitions except the 504 nm and 535 nm have been studied experimentally. The overall best Ca MOT performance is found when pumping to a highly configuration-mixed state, labeled as $4snp\ ^1P_1$, using the 453 nm $4snp\ ^1P_1 \leftarrow 3d4s\ ^1D_2$ transition.

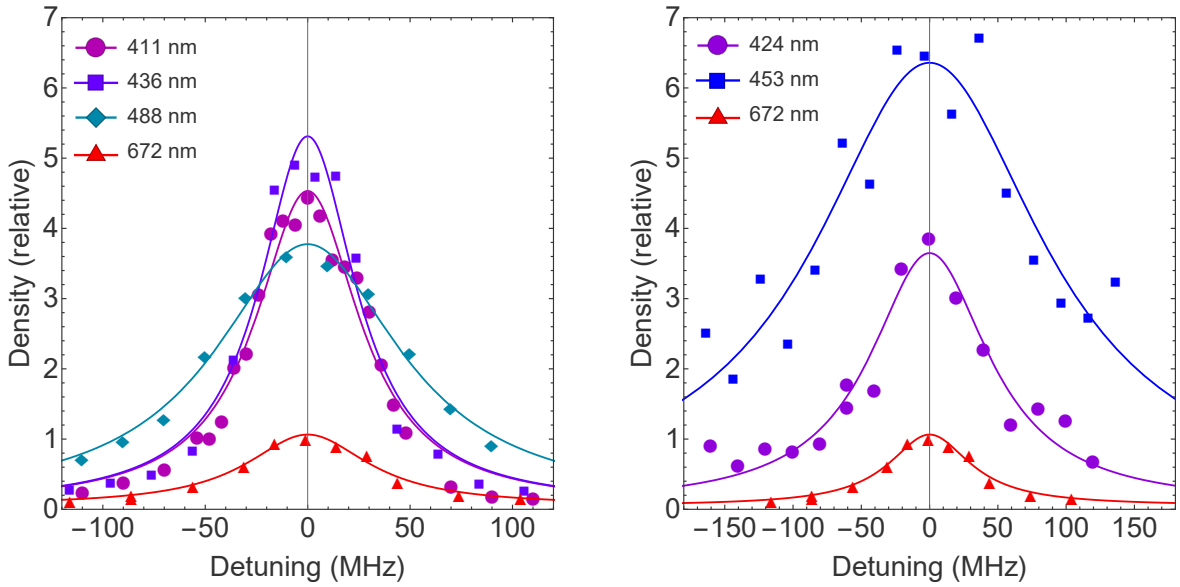

Figure 7.4: Measured calcium MOT density as a function of repumping laser detuning for the (a) $^1F_3$ and (b) $^1P_1$ repump transitions. Experimental data are shown by points, while Lorentzian fits are shown as lines. All measured densities are scaled to the peak MOT density achievable with the standard 672 nm repumping scheme.

suring the MOT density, lifetime, and temperature. The density is measured using absorption imaging on the $4s4p\ ^1P_1 \leftarrow 4s^2\ ^1S_0$ transition. The MOT lifetime, τ, is extracted by using fluorescence imaging to observe the number of trapped atoms, N, as the MOT is loaded from the oven at rate R and fitting the data to the form $N(t) = R\tau\left(1 - e^{-t/\tau}\right)$. The temperature, T, is found from the ballistic expansion of the Ca atoms after the MOT trapping beams are extinguished. For this measurement, the e^{-1} waist of the cloud is extracted from absorption images taken after a variable time of expansion, and T is extracted by fitting this data to the form $w(t > 0) = \sqrt{w(t = 0)^2 + \frac{2k_B T t^2}{m}}$, where k_B and m are the Boltzmann constant and the mass of the Ca atom, respectively. The results of these measurements are shown in Fig. 7.4-7.5 and Table 7.2. All of the experimentally explored alternative repumping schemes produce significantly denser MOTs at roughly the same temperature with longer lifetimes.

Somewhat surprisingly, repumping to $^1F_3$ states leads to similar or sometimes better MOT performance than repumping to $^1P_1$ states. Population promoted to the $^1F_3$ states

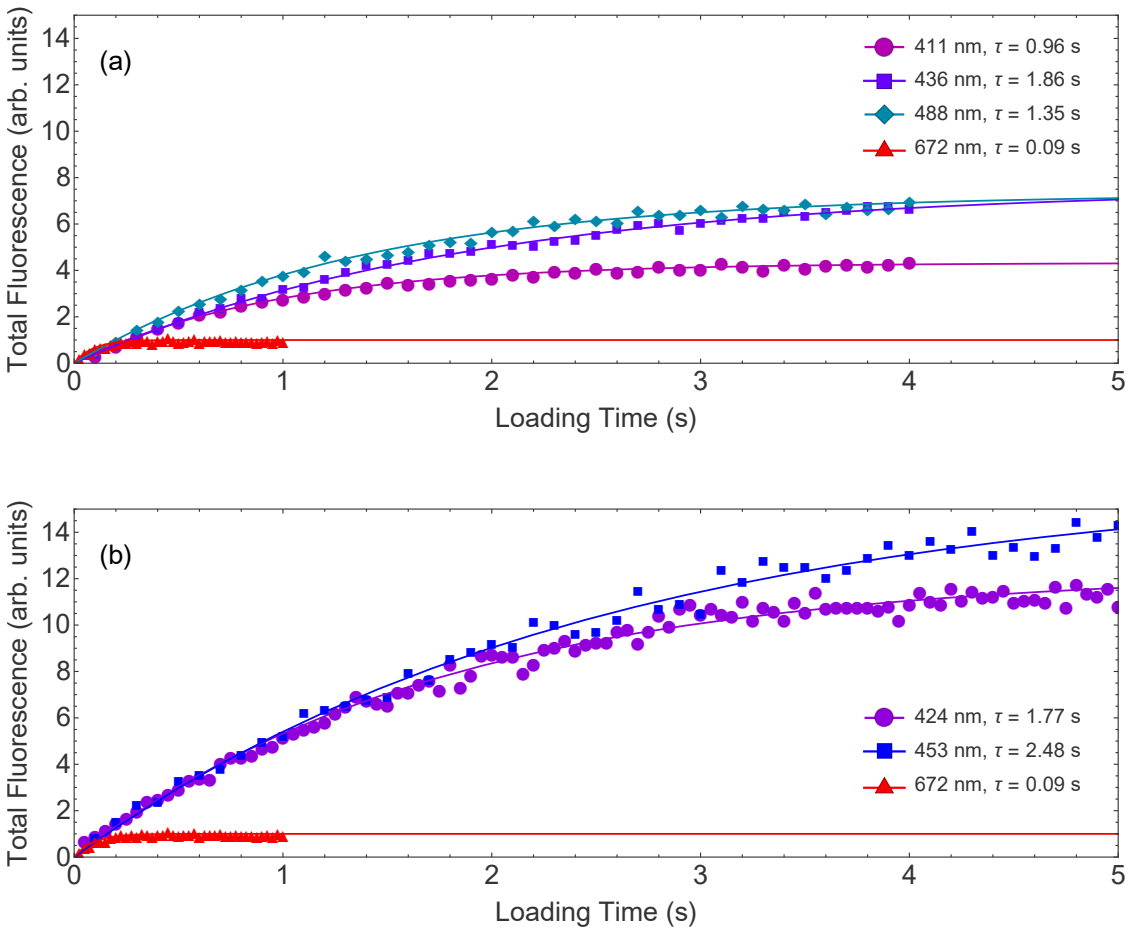

Figure 7.5: Measured Ca MOT loading curves for the (a) ${}^1F_3$ and (b) ${}^1P_1$ repump transitions, MOT fluorescence is plotted as a function of time elapsed after the cooling lasers are turned on; curves fitted to $N(t) = R\tau\left(1 - e^{-t/\tau}\right)$ are shown alongside the data.

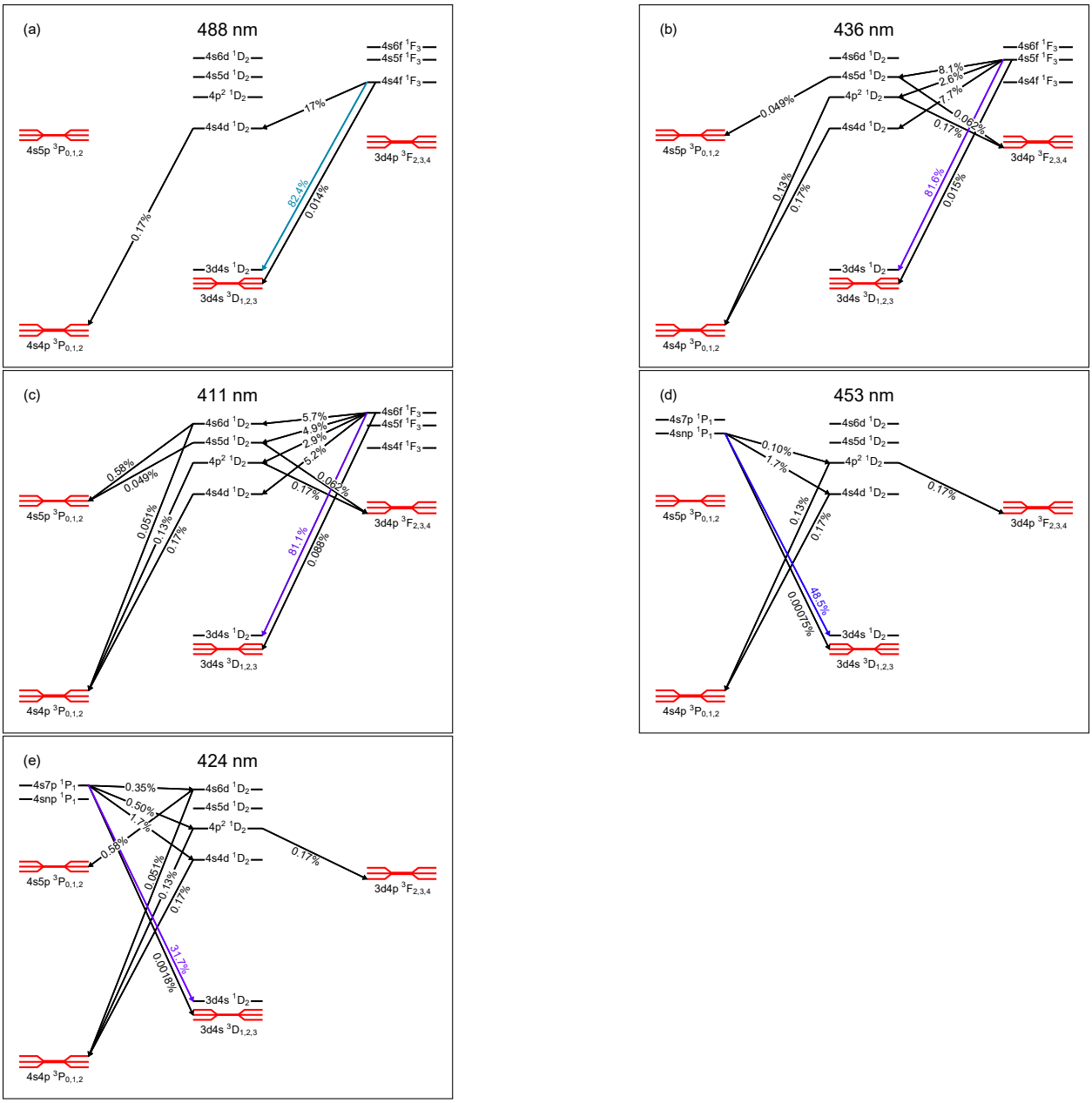

Figure 7.6: Simplified electronic energy level structures illustrating the main loss channels for the experimentally tested repumping schemes. $^1F_3$ repumps are shown in (a), (b), and (c), and $^1P_1$ repumps are shown in (d) and (e). Here we show only the most significant pathways into lossy triplet states, shown in red. The omitted decays dominantly return to the main cooling cycle. Using only these branching ratios and the natural linewidths of the upper states, one can compare the approximate relative MOT lifetimes for each transition. This simple model reproduces the lifetime ordering of the more comprehensive 75-level rate equation model and also matches experimental results.

quickly decays to states with term $^1D_2$, which in turn primarily decay to the $4s4p\ ^1P_1$ state. During this cascade, there is less decay into states of triplet character as compared to decays from some of the $^1P_1$ repumping states. Thus, despite the more complicated repumping pathway, repumping to the $^1F_3$ states can be very effective.

The relative performance of the $^1F_3$ repumping schemes can be explained by their branching pathways into lossy triplet states. The total MOT loss rate due to loss from an upper repump state is given by $\frac{d}{dt}N = -\Gamma_i f_{Loss} N_i$, where N is the total number of atoms in the MOT, N_i is the number of atoms in the upper repump state, Γ_i is the natural linewidth of the upper repump state, and f_{Loss} is the fraction of decays which lead to decay into the triplet states directly or indirectly. Of the three $^1F_3$ repump transitions experimentally tested, we approximate the relative values of N_i by comparing the average number of repump transition cycles required before decay into another state. We use the calculated linewidths Γ_i along with the most significant loss pathways to estimate f_{Loss}.

Summarizing from Fig. 7.6, the $4s4f\ ^1F_3$ state decays with $\sim 17\%$ branching into the $4s4d\ ^1D_2$ state, which has a branching of $\sim 0.2\%$ into the $4s4p\ ^3P_2$ state. The $4s5f\ ^1F_3$ state decays to the $4s4d\ ^1D_2$, $4p^2\ ^1D_2$, and $4s5d\ ^1D_2$ states with $\sim 8\%$, $\sim 3\%$, and $\sim 8\%$ branching, respectively. The $4p^2\ ^1D_2$ state decays to triplet states with $\sim 0.3\%$ branching, and the $4s5d\ ^1D_2$ state decays to triplet states with $\sim 0.1\%$ branching. The $4s6f\ ^1F_3$ state decays with branching ratio $\sim 5\%$, $\sim 3\%$, $\sim 5\%$, and $\sim 6\%$ into the $4s4d\ ^1D_2$, $4p^2\ ^1D_2$, $4s5d\ ^1D_2$, and $4s6d\ ^1D_2$ states respectively, the last of which decays with $\sim 0.6\%$ branching into the $4s5p\ ^3P_1$ state. Using this method with only the branching ratios shown in Fig. 7.6 and the natural linewidths of the upper repump states, we predict that the lifetime of the MOT τ_{488}, τ_{436}, τ_{411}, using a 488 nm, 436 nm, or 411 nm repump should obey the relaton: $\tau_{436} > \tau_{488} > \tau_{411}$. This agrees with the observed MOT lifetimes. For the same reason, we expect repumping to the $3d4p\ ^1F_3$ state with a 535 nm laser will exhibit poor performance. One can use this method to quickly estimate relative performances of potential repump transitions without developing a comprehensive rate model.

Similarly, the MOT performance when repumping to the $4s6p\ ^1P_1$ and $4s7p\ ^1P_1$ states relative to the traditional $4s5p\ ^1P_1$ state is understood by their primary branching ratios

Table 7.2: Summary of the results of this work. Each row of this table lists the calculated and measured properties of an individual repumping scheme, with the most efficient repump transition to the $4snp\ ^1P_1$ state in bold. We attribute deviations between the model prediction for the MOT lifetime and the measured lifetime to inaccuracies in the calculated transition rates. These inaccuracies are expected to be higher for the high-lying F-states, in agreement with the larger deviations seen between model and data for these states. The experimental errors include statistical and systematic uncertainties.

State	λ (nm)	f (THz)	ρ_0 (cm^{-3})	N	τ(s), model	τ (s), exp.	T (mK)	Ca^+ Production (relative)
$4s5p\ ^1P_1$	672	446.150837(13)	$7.5(7)\times10^9$	$3.7(3)\times10^6$	0.086(18)	0.093(6)	4(1)	$\equiv 1$
$3d4p\ ^1F_3$	535	–	–	–	0.14(11)	–	–	–
$4s6p\ ^1P_1$	504	–	–	–	2.3(3)	–	–	–
$4s4f\ ^1F_3$	488	614.393495(22)	$2.1(2)\times10^{10}$	$2.7(2)\times10^7$	0.73(16)	1.35(6)	5(1)	0.9(1)
$4snp\ ^1P_1$	**453**	**662.057231(22)**	$\mathbf{5.0(5)\times10^{10}}$	$\mathbf{7.8(7)\times10^7}$	**2.4(3)**	**2.48(8)**	**5(1)**	**0.8(1)**
$4s5f\ ^1F_3$	436	688.180929(22)	$2.8(3)\times10^{10}$	$2.8(3)\times10^7$	0.99(15)	1.86(7)	4(1)	1.4(2)
$4s7p\ ^1P_1$	424	706.783089(10)	$2.9(3)\times10^{10}$	$5.9(5)\times10^7$	2.2(3)	1.77(6)	5(1)	1.7(2)
$4s6f\ ^1F_3$	411	729.478413(22)	$2.5(2)\times10^{10}$	$1.6(1)\times10^7$	0.45(10)	0.96(3)	4(1)	3.1(4)
Ideal	–	–	–	–	3.0(4)	–	–	–

into triplet states. The $4s6p\ ^1P_1$ state decays with $\sim 0.006\%$ branching into the $3d4s\ ^3D_2$ state, and the $4s7p\ ^1P_1$ state decays with $\sim 0.002\%$ branching into the $3d4s\ ^3D_2$ state, while the $4s5p\ ^1P_1$ state decays with $\sim 0.9\%$ branching into the $3d4s\ ^3D_1$, $3d4s\ ^3D_2$, and $4s5s\ ^3S_1$ states.

Interestingly, the best MOT performance, in terms of number, density, and lifetime, is achieved by repumping to a highly configuration-mixed state, which we label as $4snp\ ^1P_1$. Our calculations find this state is primarily composed of the mixture $4s7p$ (43%), $4p3d$ (28%), and $4s8p$ (13%). The high performance of this repumping transition arises from two facts. First, its primary branching ratio to triplet states is $\sim 0.001\%$ and the lowest of all repumping transitions explored here. Second, it exhibits a very high branching ratio of $\sim 43\%$ directly back to ground $4s^2\ ^1S_0$ state.

Because the lifetime of the MOT when operating with the 453 nm repump (~ 2.5 s) is close to the idealized limit set by intercombination transitions from the $4s4p\ ^1P_1$ state (3 s),

we vary the intensity of the 423 nm cooling laser to measure the lifetime of the MOT as a function of the $4s4p\ ^1P_1$ state population. Fig. 7.7 shows our results alongside the predicted lifetime from the rate model and the calculated limit of $0.24/\rho_{pp}$ s^{-1} set by the decay from the $4s4p\ ^1P_1$ state indirectly to the lossy $4s4p\ ^3P_0$ and $^3P_2$ states – here ρ_{pp} is the population fraction in the $4s4p\ ^1P_1$ state. Our results show that the lifetime of the MOT in this scheme approaches this fundamental limit for any Ca MOT with a single repump out of the $3d4s\ ^1D_2$ state. Therefore, repumping at 453 nm provides nearly the optimum performance for any imaginable single-repump scheme in Ca.

Trapping calcium atoms in a MOT also provides us with a cold sample convenient for metastable state spectroscopy. We take advantage of this as well as the effect a repump laser has on the total number of atoms and fluorescence of a MOT to measure the transition energies of several repump transitions. Using a low repump laser intensity to minimize power broadening, we measure MOT fluorescence on the $4s4p\ ^1P_1 \leftarrow 4s^2\ ^1S_0$ transition as we scan a given repump frequency. As the repump laser comes into resonance, the number of atoms in the MOT and the fluorescence drastically increase. We use a HighFinesse Angstrom WS Ultimate 2 wavelength meter calibrated to the Ca $4s4p\ ^1P_1 \leftarrow 4s^2\ ^1S_0$ transition via a saturated absorption lock to measure the absolute frequency [SMD11]. Our results are shown in Table 7.2, where the reported uncertainties account for the following potential errors: the absolute accuracy of the wavelength meter, the error in the Lorentzian fits, the Zeeman effect for a $M_J = \pm 1$ transition, the DC Stark effect, the AC Stark effect, and the uncertainty in the Ca $4s4p\ ^1P_1 \leftarrow 4s^2\ ^1S_0$ transition frequency.

7.6 Ca^+ production

Due to its relatively light mass and high ionization potential, Ca is especially useful in hybrid atom-ion traps as a sympathetic coolant [RSS12]. However, as was recently identified [al11, SDC16], Ca MOT operation can produce Ca^+ and Ca_2^+ through multi-photon and photo-associative ionization, respectively. These ions then produce an unwanted heat load during the sympathetic cooling process. While techniques exist to cope with these nuisance

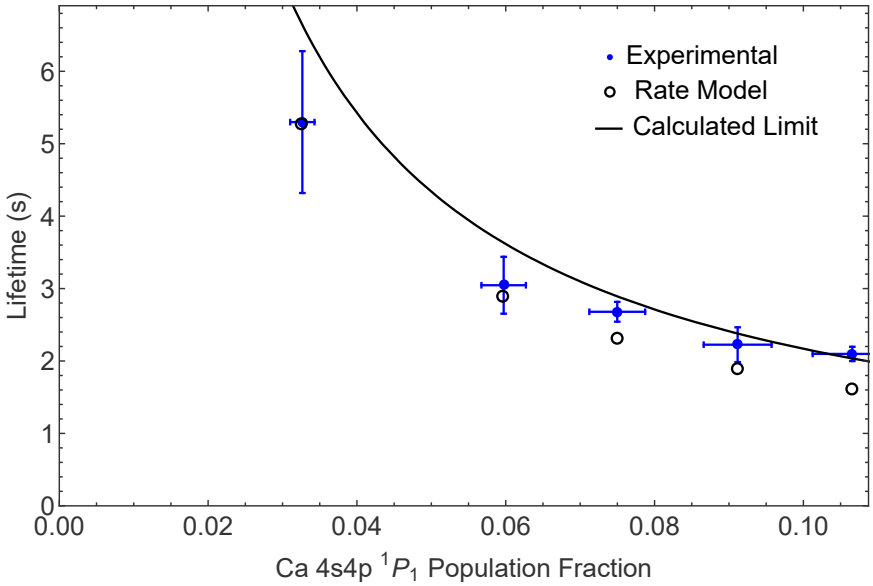

Figure 7.7: Measured Ca MOT lifetime as a function of $4s4p\ ^1P_1$ state population with a 453 nm repump. The measured lifetimes are shown alongside the rate model predictions and a curve representing the fundamental limit for any single repump laser scheme in a Ca MOT. This limit is the result of decay from the $4s4p\ ^1P_1$ state indirectly to the $4s4p\ ^3P_0$ and $^3P_2$ states and is found as $0.24/\rho_{pp}$ s^{-1}, where ρ_{pp} is the population fraction of the Ca $4s4p\ ^1P_1$ state.

ions [SDC16], it is advantageous to keep their production rate as low as possible. Therefore, we use time of flight mass spectrometry [SCR12, SSC14, SSY16] to measure the density normalized Ca^+ production rate for each of the tested repump lasers and compare to the Ca^+ production rate with a 672 nm repump. As shown in Table 7.2, we find that the largest Ca^+ production rate occurs with the 411 nm repump, a factor of 3.1 compared to the Ca^+ production rate with the 672 nm repump. The 453 nm repump, which resulted in the MOT with the longest lifetime, highest density, and largest number of atoms also yields the lowest Ca^+ production rate.

7.7 Summary

In summary, we propose seven alternatives to the traditional 672 nm repumping scheme for a Ca MOT and experimentally explore five of them. We find that all five produce significant

improvements in MOT density and lifetime. Three of these repumping transitions appear particularly convenient from a technological perspective since they occur at wavelengths that are accessible by diode lasers, *i.e.* 453 nm, 424 nm, and 411 nm – with the middle transition of this list occurring at nearly the same wavelength as the cooling transition in Ca. The overall best MOT performance occurs for repumping at 453 nm on the $4snp\ ^1P_1 \leftarrow 3d4s\ ^1D_2$ transition and results in a $\sim 6\times$ and $\sim 25\times$ improvement in density and lifetime, respectively, over the standard scheme. According to our rate model, this lifetime is near the maximum theoretical lifetime that can be achieved in a Ca MOT with a single repump laser from the $3d4s\ ^1D_2$ state.

In all cases, the relative performance of the different repumping schemes can be understood by their branching into triplet states. Electronic population in these states typically ends up in either the $4s4p\ ^3P_0$ or $^3P_2$ state, which due to their long spontaneous emission lifetimes are lost from the MOT. For this reason, if a Ca MOT lifetime beyond that of ~ 5 s is desired it would be necessary to add additional lasers to repump from the $4s4p\ ^3P_0$ and $4s4p\ ^3P_2$ states as is done in Sr [LBY15]. If the MOT is not limited by other factors such as background gas collisions, we estimate this would extend the lifetime to ~ 29 s. If a further increase in the lifetime is required, it would be necessary to repump from the $4s4p\ ^3P_1$ state, which would completely close the laser cooling cycle. However, even if these lasers are added, given the longer lifetime of the $3d4s\ ^1D_2$ state as compared to its analogue in Sr, it will likely be necessary to retain the 453 nm repump for optimal MOT operation.

Finally, due to their similar atomic structure it may be possible to apply this repumping scheme in other Group 2(-like) atoms. For example, in Sr MOTs we speculate that repumping on the $5s8p\ ^1P_1 \leftarrow 4d5s\ ^1D_2$ transition at 448 nm may be beneficial since it would return population from the $4d5s\ ^1D_2$ more quickly than in the typically employed scheme and thereby increase the achievable optical force. A likely less efficient, but perhaps technologically simpler repumping pathway would be to drive the $5s6p\ ^1P_1 \leftarrow 4d5s\ ^1D_2$ transition at 717 nm. In both of these cases, however, it may be necessary to retain the lasers used to repump population from the $5s5p\ ^3P_0$ and $^3P_2$ states as the larger spin-orbit mixing in Sr increases the parasitic intercombination transitions from *e.g.* the $5s5p\ ^1P_1$ state.

We would like to thank M. Kozlov for help with the CI-MBPT package [KPS15]. We also thank an anonymous referee for compiling a list of 111 experimentally measured transition rates for Ca I. This material is based upon work supported by the National Science Foundation Graduate Research Fellowship under Grant No. DGE-1650604. This work was supported by the National Science Foundation (PHY-1205311 and PHY-1607396) and Army Research Office (W911NF-15-1-0121 and W911NF-14-1-0378) grants. YMY thanks support of the National Natural Science Foundation of China, Grant No. 91536106.

CHAPTER 8

High resolution atom-ion collision energy control

Control of collision energy during atom-ion reactions is crucial for comparing measured cross-sections to long-range capture models and may even be used to identify resonance features. Here, we demonstrate an ion shuttling technique for high-resolution control of atom-ion collision energy by translating an ion held within a radio-frequency trap through a magneto-optical atom trap. The technique is demonstrated both experimentally and through numerical simulations, with the experimental results indicating control of ion kinetic energies from $0.05 - 1$ K with a fractional resolution of ~ 10 and the simulations demonstrating that kinetic energy control up to 120 K with a maximum predicted resolution of ~ 100 is possible, offering order-of-magnitude improvements over most alternative techniques. Lastly, we perform a proof-of-principle chemistry experiment using this technique and outline how the method may be refined in the future and applied to the study of molecular ion chemistry.

8.1 Background motivation

Reactant collision energy can strongly influence the kinetics and product outcomes of a reaction, revealing fundamental properties about the underlying chemical system [BON15, KSS16, GMG12]. Consequently, there has been much work on creating methods capable of precisely controlling this parameter. Lee, Herschbach, and coworkers developed the crossed molecular beam apparatus to explore the effect of collision energy on the angular distributions of products in neutral-neutral reactions, revolutionizing the field of gas-phase chemistry [LML69]. Other groups [SKS15, HGS12, AS17] have since extended the technique to the millikelvin regime with improved energy resolution, enabling observations of quantum

scattering resonances in reaction rates [KSS16, VOC15, KWS15, DXW10]. In this work, we take a step towards enabling similar high-resolution studies of ion-neutral reactions, which have been observed to play an important role in the formation of the interstellar medium and other astrophysical processes [IOG10, SB08, MSA99, RGM10], by developing a novel technique for controlling collision energy in these systems.

Early efforts to control collision energies in ion-neutral systems, such as the SIFT [SS96, Arm04] and CRESU [RM87, RP95] techniques, combined gas-discharge ion sources with neutral beams of tunable temperature. Current implementations of these experiments are typically restricted to collision energies of $\sim 10 - 500$ K with fractional energy resolutions of $\sim 10 - 100$ [SR00], depending on neutral beam parameters. We define the fractional resolution of a distribution X as $R_X = \overline{X}/\sigma_X$ where $\overline{X}$ and σ_X are the average and standard deviation of X, respectively.

Ion-neutral reaction experiments have recently been extended to laser-cooled hybrid systems [Fig. 8.1(a)] capable of accessing millikelvin temperatures [ZW18, ZRP11, HD14], where they have been used to explore reaction rate dependencies on conformational and electronic states [CDK13, SRK12, HW12, RSK11, RZS12] and to produce novel chemical species [PMS17]. The majority of these hybrid systems contain radio-frequency (rf) ion traps, and typically the atom-ion collision energy is controlled by manipulating the ion excess micromotion energy, either by using electric fields to displace the ions from the rf trap null [ZPS10,ZPR10,HW12] or by changing the size of the ion sample [HHF13,GCc09,PMS17].

Upon displacing an ion from the rf trap null, the ion excess micromotion energy distribution approximately follows that of a simple harmonic oscillator [Fig. 8.1(b)]. Mathematically, the trajectory of a trapped ion in in the low Mathieu-q limit can be approximated [BMB98] as

$$r(t) = r_0(1 + \frac{q}{2}\cos(\Omega t))\cos(\frac{q}{2\sqrt{2}}\Omega t) \tag{8.1}$$

where $r(t)$ is the ion radial coordinate at time t, r_0 is the ion's initial radial displacement, and q is the Mathieu-q parameter, given as $q = \frac{2eV_{RF}}{mr_0^2\Omega^2}$, where e is the electronic charge and m is the mass of the ion. This motion consists of harmonic oscillation at a secular trap

frequency, $\frac{q}{2\sqrt{2}}\Omega$, modulated by faster micromotion oscillation at the rf drive frequency of the ion trap. Under laser-cooled conditions, the secular portion of the ion's motion is cooled to ≤ 1 mK. This energy is negligible relative to the micromotion energy of the ion [CSR13], and consequentially, the ion velocity can be modeled as follows

$$v(r_0, t) = -r_0 \Omega \frac{q}{2} \sin(\Omega t) \tag{8.2}$$

The velocity probability distribution function is then given by the probability distribution function for a classical harmonic oscillator at frequency Ω as

$$P(r_0, v) = \begin{cases} 0 & \left(\frac{q\Omega}{2r_0}\right)^2 < v^2 \\ \frac{1}{\pi}\sqrt{\frac{1}{\left(\frac{q\Omega}{2r_0}\right)^2 - v^2}} & \left(\frac{q\Omega}{2r_0}\right)^2 \geq v^2 \end{cases} \tag{8.3}$$

$P(r_0, v)$, which depends on the initial ion radial position, can further be weighted by the ion spatial density distribution as

$$P_V(v) = \int n_{ion}(r, z, \phi) P(r, v) dV \tag{8.4}$$

where P_V(v) is the ion velocity probability distribution and $n_{ion}(r, z, \phi)$ is the integral-normalized ion-density distribution expressed in cylindrical coordinates, whose parameters are characterized through fits to fluorescence images obtained by our EMCCD camera. After obtaining the velocity probability distribution, it is then straightforward to calculate E_{col}, the average collision energy, as

$$\int P_V(v) \frac{1}{2} \mu v^2 dv \tag{8.5}$$

where μ is the reduced-mass of the atom-ion system. The kinetic energy distribution can also be found by obtaining $P_V(v)$ and performing a change of variable.

Thus is a single ion is displaced from the trap null to vary its energy, following the above steps, the resulting energy distribution stretches from 0 K to twice its average value, with the average energy varying quadratically with radial displacement (all energies in this work are expressed in units $J/k_B = K$). Similarly, when using crystal size to tune the collision energy, each ion at a distinct radial position within the crystal has a unique harmonic distribution,

and upon averaging over all radial positions, the resultant energy distribution is peaked at low energies with a high-energy tail [Fig. 8.1(b)]. While the average kinetic energy of an ion sample can be precisely controlled using both of these techniques, their energy resolution is ≈ 1, making it difficult to measure energetically narrow features. Further, micromotion interruption collisions [CSH14] and calculations of the atom-ion spatial overlap [RSS12] may provide further complications for these micromotion-based techniques as collision energy is scanned. In particular, ions held within rf traps integrated into atom-ion hybrid systems are known to settle into Tsallis law energy distributions characterized by power-law tails after undergoing several collisions with an atomic sample [CSH14, RW17], thereby leading to extreme high energy collision events that can jeopardize controlled collision energy studies. While active laser-cooling can mitigate many of these concerns, in certain cases they can still be nontrivial; however, the intricacies of such considerations will be omitted for simplicity in the following discussion.

Thus, other techniques have been developed to avoid these drawbacks and achieve higher energy resolutions. For example, Zeeman [CCJ17, DTS15] and Stark decelerators [OBH12] have been coupled to ion traps to probe atom-ion collision energies in the $\sim 10-100$ K range with an energy resolution of ~ 50 [PFL09]. In other work, Eberle [Ebe16] and coworkers recently demonstrated a novel method that uses optical "push" beams to precisely control the motion of atom clouds for kinetic energies ranging from $\approx 10-500$ mK with a resolution of ≈ 10.

Here, inspired by Eberle *et. al.* [Ebe16], we describe a simple alternative that can be immediately used in most existing hybrid systems. In this technique, ions are translated at fixed velocities across a neutral sample by adjusting their axial trapping potential, maintaining the ions on the rf trap null throughout the process. At constant translational ion velocity, R_E is primarily limited by the micromotion energy of the ion crystal [Fig. 8.1(b)] and can exceed values of 100. In what follows, we describe the experimental system, investigate the shuttling technique through both experiment and simulation, and identify parameters where constant velocity ion motion can be approximately realized.

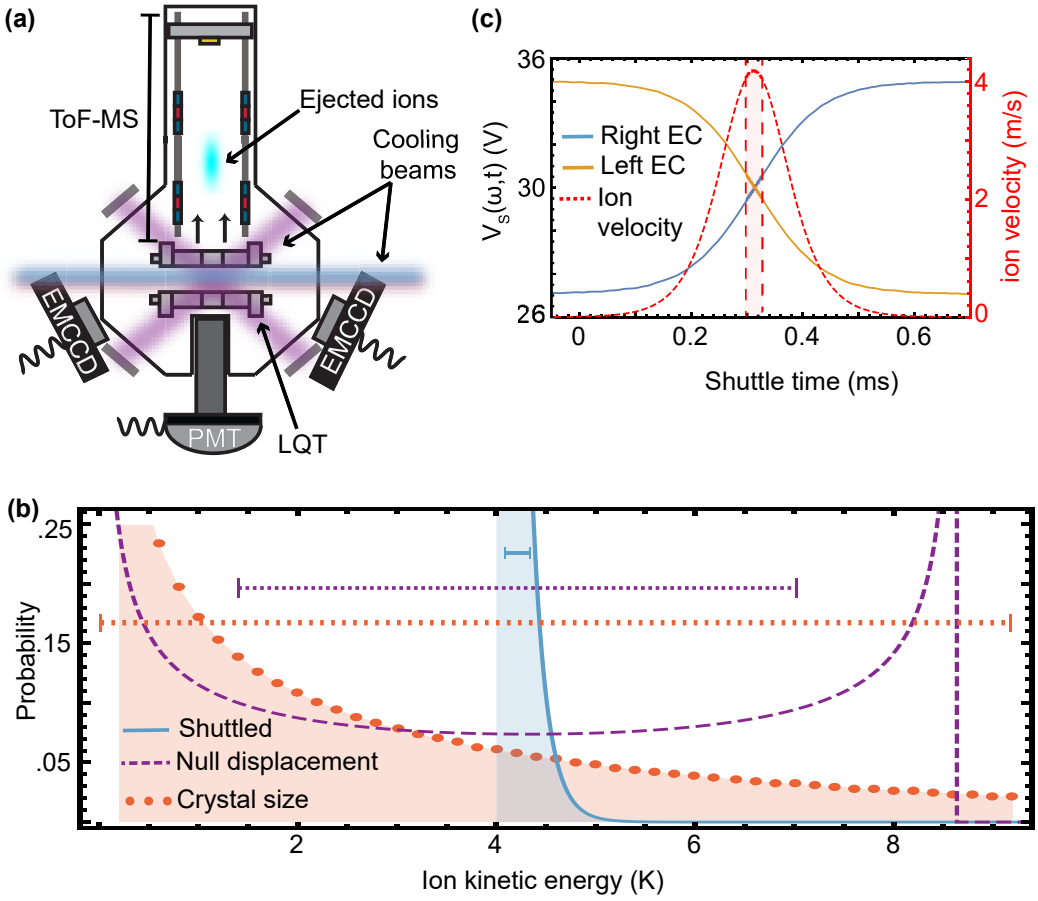

Figure 8.1: Shuttling procedure and energy resolution

(a) Schematic of the MOTion trap apparatus displaying an ion cloud being ejected from the 12-segment LQT (3 segments per rod) into the ToF-MS, with arrows denoting the direction of ejection. **(b)** Energy distributions, derived from approximate Mathieu equation solutions, of a Yb^+ sample tuned to an average kinetic energy of ~ 4 K through ion chain displacement from the trap null, crystal size tuning, and idealized shuttling at a constant velocity of a crystal with an initial micromotion energy of ~ 100 mK. The standard deviations for each distribution are denoted by horizontal scale bars. **(c)** Voltage waveforms measured on the right and left endcap electrodes (EC) of the LQT, as well as the corresponding predicted ion velocities, expressed as a function of shuttle time. The waveforms follow the $V_S(\omega, t)$ profile, presented in Eq. 8.8, with $V_{DC} = 30$ V, $V_{amp} = 5$ V, $\gamma = 0.18$, and $\omega = 2\pi \cdot 95$ Hz. The portions of the waveform where the ions are stationary are not shown for clarity. The shaded region denotes the approximate period of overlap between the shuttled ions and the MOT.

8.2 Shuttling principles

For small displacements from the ion trap center, the electrostatic potential in the axial dimension z at time t is given as $U_{ax}(z,t) \approx \frac{\kappa V_{end}}{z_A^2}(z - z_0(t))^2$, where κ is a factor associated with the ion trap geometry, V_{end} is the endcap voltage, z_A is the endcap electrode spacing of the LQT, and $z_0(t)$ is the time-dependent axial equilibrium position of the trap. In our system, $\kappa \approx 0.02$ and $z_A \approx 10.2$ mm. By adding a time-dependent voltage waveform between right and left endcap electrodes [Fig. 8.1(c)], $z_0(t)$, and hence the ion crystal position, can be modulated at a speed proportional to the time derivative of the applied waveform. By changing the ramping speed of the waveform while keeping the peak-to-peak voltage constant, the translational velocity of the ion, and thus the ion kinetic energy E, can be conveniently controlled.

Experimentally, an arbitrary waveform generator produces the endcap voltage waveforms that modulate the ion axial position. Output from the generator is amplified and low-pass filtered to remove any electrical noise near secular resonances of the trapped ions.

When the modulation technique is used in conjunction with laser cooling, the motion of the resulting system can be described as a damped harmonic oscillator (DHO):

$$m\ddot{z} = -k_{eff}(z,t)(z - z_0(t)) + F_\beta(\dot{z}), \tag{8.6}$$

where m is the mass of the ion of interest, $k_{eff}(z,t)$ is the effective spring constant of the moving endcap potential, approximated as $q\frac{d^2}{dz^2}U_{ax}(z,t)$ where q is the charge of the ion of interest, and $F_\beta(\dot{z})$ is a velocity-dependent damping force with an e^{-1} motional damping time constant β (units s^{-1}) determined by the laser parameters of a given Doppler-cooled system. Higher order terms are neglected.

In order to achieve well-controlled energy resolution, the ion position should adiabatically follow the moving equilibrium position of the axial potential. However, if the Fourier transform of z_0(t) possesses frequency components near secular resonances of the ion, the shuttling motion may excite secular oscillations and heat the ion. To avoid this, we raise the trap axial confinement, thereby increasing the ion secular frequency above these frequency

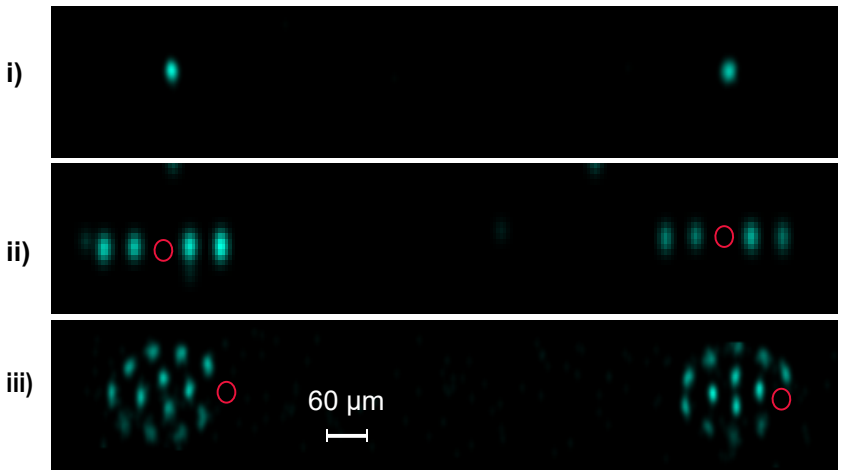

Figure 8.2: Ion shuttling imaging

False-color experimental fluorescence images of Yb^+ ions undergoing shuttling presented for the following cases: i) a single ion, ii) a five-ion chain with one non-laser-cooled dark isotope, iii) a two-dimensional Coulomb crystal with one embedded dark isotope. As the ions spend $\sim 90\%$ of the time at the trajectory endpoints, their fluorescence is only evident in these locations.

components, and strategically choose a ramping waveform less prone to ion heating.

Waveform optimization is a well-studied problem in the quantum information community [HYO08, BOV09, BOV11, RLB06]. In this work, when transporting an ion from one shuttling endpoint to another, we implement a hyperbolic tangent profile similar to that presented in Ref. [HYO08], given by

$$f_{tanh}(\tau) = \frac{\tanh(2\alpha\tau - \alpha)}{\tanh\alpha} \tag{8.7}$$

where τ is the shuttle time as a fraction of total shuttle duration and α is a parameter that characterizes the slope of the function, chosen to have a value of 4 in the work presented here. While a linear profile would seem to produce a flatter velocity profile at the trajectory midpoint, such a profile, once Fourier-decomposed, may possess frequency terms near secular resonances of the ion that could lead to secular heating, especially at high shuttle energies. The hyperbolic profile, while exhibiting a larger velocity spatial dependency, avoids these effects while still allowing for sufficient velocity control over the narrow region of MOT interaction such that other effects, such as excess micromotion compensation, are generally the limiting factor to energy resolution (see Section 8.4).

To meet the demands of our experiment, additional modifications were made to the applied shuttling waveform. Firstly, the waveform was chosen to be periodic in time to allow for waveform frequency, and thus ion velocity, to be varied while not affecting other experimental parameters, such as the time-averaged spatial overlap between the atom and ion sample [SRK12]. Secondly, the waveform was constructed such that the ions remain at the stationary endpoints for a majority of the shuttling period, allowing sufficient laser cooling time to dampen any excitations that may occur during the transport process. A natural choice of waveform that satisfies the above criteria, shown in Fig. 8.1(c), is given by the following piecewise function:

$$V_S(\omega,t) = \begin{cases} V_{DC} - V_{amp} & 0 \le t < \frac{T}{2}(1-\gamma) \\ V_{DC} + f_{tanh}(\frac{t-\frac{T}{2}(1-\gamma)}{\frac{T}{2}\gamma})V_{amp} & \frac{T}{2}(1-\gamma) \le t < \frac{T}{2} \\ V_{DC} + V_{amp} & \frac{T}{2} \le t < \frac{T}{2}(2-\gamma) \\ V_{DC} - f_{tanh}(\frac{t-\frac{T}{2}(2-\gamma)}{\frac{T}{2}\gamma})V_{amp} & \frac{T}{2}(2-\gamma) \le t < T \end{cases} \tag{8.8}$$

where ω is the angular shuttle frequency, V_{DC} is the base endcap voltage, V_{amp} is the amplitude of the shuttle waveform, $T = \frac{2\pi}{\omega}$ is the shuttle period, and γ is a factor that determines the ratio of stationary time to shuttled time during the ion trajectory. For a standard shuttle with an endpoint-to-endpoint distance of $\sim$1 mm, parameters are chosen as follows: V_{DC} $\sim$ 30 V, $V_{amp} \sim 2$ V, $\gamma \sim 0.1$, and ω can be tuned as desired from $\sim 2\pi \cdot (0 - 500)$ Hz, providing control of the ion kinetic energy from $\approx 0.01 - 10$ K. For reference, the axial secular frequency of our trap is typically chosen to be $\approx 2\pi \cdot 30 - 150$ kHz for the range of axial confinements explored in this work.

Fluorescence from the laser-cooled Yb^+ ions was collected with an EMCCD while shuttling. Shuttling images are presented in Fig. 8.2 for a single ion, a five-ion chain, and a two-dimensional Coulomb crystal, the last two of which are embedded with a non-laser-cooled Yb^+ isotope, indicating that this technique may also be used with sympathetically cooled species, such as molecular ions.

8.3 Experimental investigation of technique

8.3.1 Fluorescence detection while shuttling

Understanding the energy dynamics of the shuttled ions requires knowledge of their velocity distribution. In order to experimentally characterize this distribution, a $^{174}Yb^{+}$ crystal was shuttled over a ≈ 1 mm distance by applying $V_S(\omega, t)$ to the endcap electrodes of the ion trap. The EMCCD in our imaging system was replaced with a PMT to record the ion photon scattering rate throughout the shuttling process.

The photon scattering rate of laser-cooled Yb^{+} can be approximated [MS03] as

$$\Gamma_{scatt}(v_z) = \frac{\Gamma}{2}\frac{s}{1+s+4\frac{(\delta - k_z v_z)^2}{\Gamma^2}} \tag{8.9}$$

where Γ is the transition linewidth, s is the saturation parameter of the cooling laser, given as I/I_s where I is the intensity of the laser beam and I_s is the saturation intensity of the transition, δ is the detuning of the laser from resonance, k_z is the magnitude of the k-vector of the axially-aligned cooling laser, and v_z is the z-component of the ion velocity. The scattering rate is insensitive to micromotion or secular motion in the radial dimension.

8.3.2 Ensemble and spatial averaging of velocity distributions

For a single shuttled ion, the velocity-dependent scattering rate (see Eq. 8.9) during each PMT time acquisition bin ($\sim$ 10 ns width) can be used to measure $v_z(t)$. In order to enhance the PMT signal in the experiment, we interrogate an ensemble of ~ 100 ions, and consequently, the velocities extracted in each time bin are ensemble averages of the total axial velocity distribution, defined as $\langle v_z \rangle$ (Sec. 8.8). Here, we define the ensemble average of a data set X as $\langle X \rangle$.

Further, the shuttled ions are only overlapped with the neutral sample at the center of the ion trap for a small portion of their trajectory. Therefore, the relevant resolution to consider is the resolution of $[\langle v_z \rangle]_S$, the velocity distribution with weighting factors determined by the spatial overlap of the ions at each shuttle time with an atom sample of characteristic length

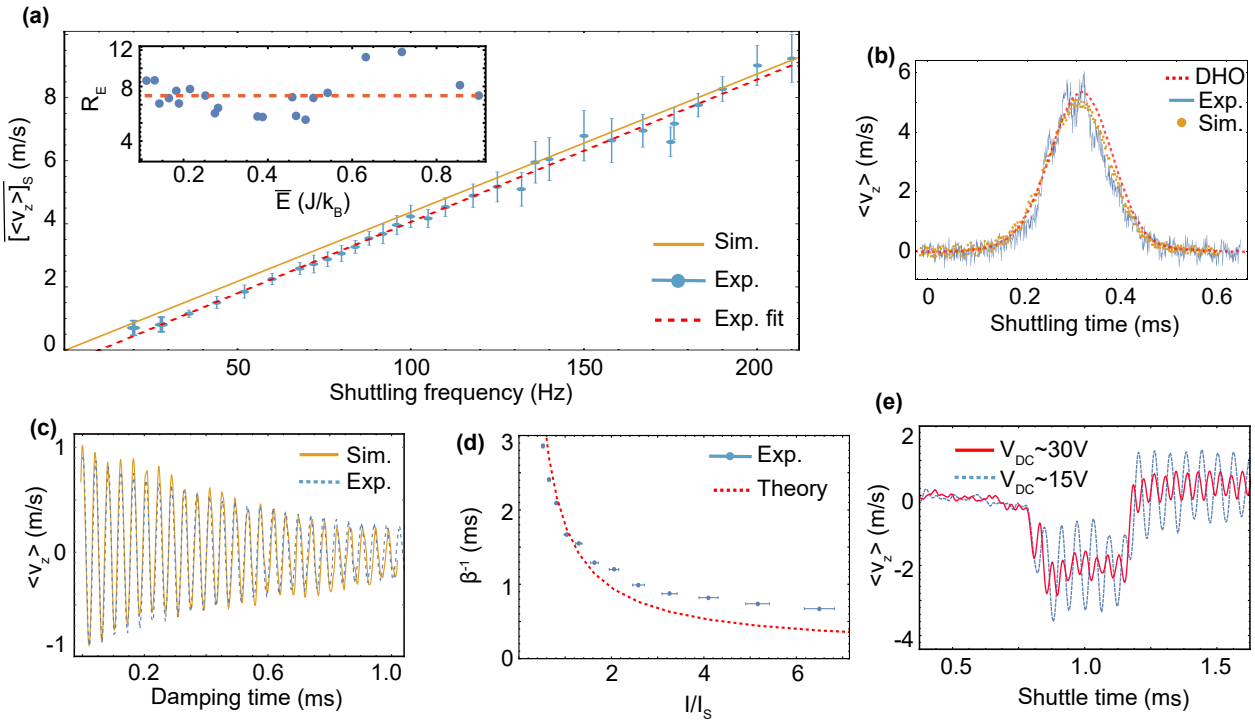

Figure 8.3: Doppler velocimetry and large crystal simulation results

(a) Experimentally measured $\overline{[\langle v_z \rangle]_S}$ of a ~ 100 ion crystal obtained through Doppler velocimetry at different shuttling frequencies, where the error bars are displayed at the 1σ level. The experimental results show reasonable agreement with MD simulations. A linear fit applied to the experimental data shows that varying the shuttle frequency modifies the axial velocity of the trapped ions in the expected way. The inset shows the corresponding mean kinetic energies and energy resolutions obtained at the various shuttling frequencies, with the dotted line referring to the average resolution. Note here that the plot refers to averages and resolutions of the distribution $[\langle \hat{E}_z \rangle]_S$ (see text), but the subscript was omitted in the plot for clarity. **(b)** Experimental $\langle v_z \rangle$ values, obtained as a function of shuttle time at a shuttle frequency of 120 Hz, are compared to results of a MD simulation and the predictions of a 1D damped harmonic oscillator model. **(c)** The effects of laser cooling on damping secular motion from both simulation and experiment. The saturation parameter used to construct the laser cooling force in the simulations was tuned until β matched well with experiment. **(d)** Experimental damping timescales are obtained as a function of laser cooling saturation parameter and are compared with predictions from a rate equation model. Horizontal and vertical error bars are expressed at the 1σ level, with the latter being smaller than the data points **(e)** Measured $\langle v_z \rangle$ as function of shuttle time for two different axial confinement strengths. The shuttle was performed with a linear ramping profile more prone to ion heating than $f_{tanh}(t)$ in order to accentuate the increase in energy resolution that is possible with greater axial confinement.

scale w_A (Sec. 8.9). Here, we define the spatially-weighted distribution of a data set X as $[X]_S$ [Pat14]. For optimal resolution, the neutral sample should be placed at the center of the ion trajectory where the ion velocity is most constant.

8.3.3 Simulation parameters

The experimental results are compared to predictions of molecular dynamics (MD) simulations conducted with the SIMION 8.1 software package [Dah00], as shown in Fig. 8.3(a) and 8.3(b). The simulation software employs finite difference methods to numerically solve Laplace's equation for a given set of electrodes and point charges, allowing for determination of ion trajectories and energy distributions. Time-dependent trapping potentials were incorporated into the simulation to properly include the effects of micromotion, and ion-ion repulsion was treated by superimposing the Coloumb interaction from co-trapped ions with the potential produced by the quadrupole trap electrodes. The simulations were performed using 100 ions, approximately equivalent to the number used during the experiment, and also employed a laser-cooling damping force whose velocity profile was derived from a simple four-level rate equation model.

In order to optimize the accuracy of the simulated laser cooling force, both in experiment and simulation, the ions were initialized in the LQT, non-adiabatically transported between trajectory endpoints through a square-wave-like voltage ramp, and subsequently observed as the laser cooling force damped the motion of the excitation [Fig. 8.3(c)]. The saturation parameter of the simulated laser cooling force was adjusted until the e^{-1} decay constant β matched that observed in experiment. We also investigated how this damping timescale varied with laser cooling intensity by repeating the above measurement at various laser powers [Fig. 8.3(d)]. The results are comparable with those expected from our rate equation cooling model and are instructive when considering what laser cooling parameters to implement while shuttling. Namely, one should operate in a laser cooling regime such that the time spent at the shuttle endpoints during each cycle is much longer than the damping time, ensuring the ions are sufficiently cooled before the next shuttle cycle begins. Further, the

simulations confirm that at experimental conditions, the laser cooling damping force does not significantly influence the trajectory of the ions while shuttling.

8.3.4 Analysis of results

The experimental and simulated results for $\overline{[\langle v_z \rangle]_S}$ are in reasonable agreement [Fig. 8.3(a)]. Both exhibit a linear relationship with waveform frequency, affirming that w_A can be varied to predictably control the velocity, and thus collision energy, of the ions. The trajectory for the ions assuming a damped harmonic oscillator model, shown in Fig. 8.3(b), also appears to describe the ion motion well, confirming that the model may be used to gain intuition about the shuttling procedure. We attribute minor discrepancies between the simulation and experiment, such as differing damping timescales and amplitudes of secular oscillation while shuttling, to imperfect voltage matching due to unmeasured electrode charging and rf pickup, minor discrepancies in laser cooling velocity profiles, and effects not considered in the simulation such as micromotion interruption collisions with background gas particles.

The experimental energy resolution can also be compared to predictions from simulation. $\overline{[\langle \hat{E}_z \rangle]_S}$, defined as $\frac{1}{2}m(\overline{[\langle v_z \rangle^2]_S})$, was scanned over $\approx 0.01-1$ K over the velocities explored in Fig. 8.3(a), with probing of higher kinetic energies precluded by difficulty in discriminating between scattering rates at large v_z. Shown in the inset to Fig. 8.3(a), the measured ensemble-averaged axial energy resolutions, $R_{[\langle \hat{E}_z \rangle]_S}$, were determined to be ≈ 10, in agreement with simulations.

However, the resolution of the non-ensemble-averaged kinetic energy distribution, $[E_z]_S = \frac{1}{2}m[v_z^2]_S$, is the more relevant quantity to consider when characterizing collision energy control since it is sensitive to center-of-mass frame velocity dispersions. Measuring $R_{[E_z]_S}$ involves knowing the velocities of each individual ion, information unavailable with our velocimetry technique. Therefore, we utilize the simulations to estimate this quantity and obtain $R_{[E_z]_S} \approx 6$ (Sec. 8.10).

Experimental average velocity distributions were also obtained at various levels of axial confinement, and, as expected, higher axial confinement offered superior resolution. To

exaggerate this effect, we performed a shuttle using a linear ramping profile prone to ion-heating and observed that increased confinement more effectively suppressed secular oscillations [Fig. 8.3(e)]. Probing of even higher axial confinements was prohibited in our system by technical considerations.

8.4 Single ion and molecular ion simulation results

While Section 8.3 demonstrates large ion samples can be successfully shuttled, the resolution is maximized when used with a single ion, where ion heating effects are minimal and the ion shuttling energy can dominate over its micromotion energy. In this section, kinetic energy will refer to the total kinetic energy of the ion, including both axial and radial motion.

While our experimental optical detection efficiency prevents extensive single ion measurements, reasonable best-case-scenario simulations are performed with a single Yb^+ ion utilizing the electrode geometry of the MOTion trap and the laser cooling profile described in Section 8.3. Further, laser cooling while shuttling was necessary in the work discussed in Section 8.3.1 for Doppler velocimetry purposes, but in general laser cooling may be switched off during transport if, for example, finer control of ion electronic state populations is desired. However, we choose to maintain laser cooling throughout the shuttling process in the following simulations for consistency with the simulations performed in the previous section. The end-to-end shuttle distance, experimentally limited to ≈ 1 mm by the field of view of our imaging system, is increased to ≈ 2 mm to enhance energy resolution. Further, idealized waveforms were implemented in the simulation instead of the waveforms measured in the experiment, where unintended filtering due to trap electronics and rf pickup caused slight waveform distortion.

These simulations, presented in Fig. 8.4(a), were performed at two different axial confinements ($V_{DC} = 150$ V and 35 V) and once again indicate that confinement plays a pivotal role in determining energy resolution. When the endcap voltages were raised to 150 V in the simulation, the rf voltage amplitude was also increased by a factor of 2 relative to the low-confinement case to prevent radial defocusing caused by the increased axial confinement.

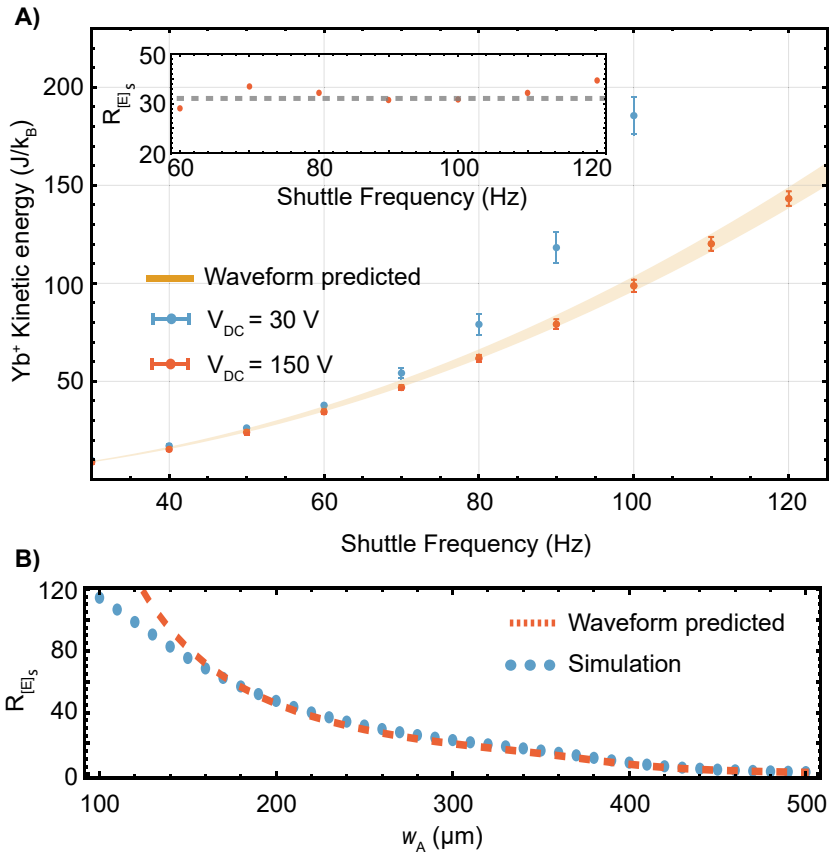

Figure 8.4: Single ion simulation results

(a) Total kinetic energy for a simulated single ion shuttled at various waveform frequencies, using two separate axial confinements. The simulations performed at the higher axial confinement display higher energy resolutions and exhibit less significant secular oscillations, as evidenced by their adherence to the waveform-predicted energy, shown in bands. Error bars are expressed at the 1σ level. The inset to the figure shows $R_{[E]_S}$, the total kinetic energy resolution including both axial and radial motion, for the high axial confinement simulations, with the average resolution of ≈ 35 denoted by the dotted line. Low axial confinement simulations produced average energy resolutions of ≈ 20. **(b)** $R_{[E]_S}$ of a simulated ion shuttled at ≈ 100 K of kinetic energy as a function of neutral cloud spatial dimension. The results are compared to the resolutions that would be expected if the ions perfectly followed the motion of the equilibrium position without any micromotion or secular excitation.

At high enough axial confinements, further resolution improvement is eventually limited by the need to operate at increasingly large rf voltages to avoid this defocusing effect, forcing the trap towards high Mathieu q-parameter regimes where the ions become unstable.

At higher energy in particular, the results presented in Fig. 8.4(a) indicate that low axial confinement can facilitate secular excitation of the ion motion. The excitation can cause the ion to either lag or lead the equilibrium position of the moving potential during MOT interaction, increasing the ion kinetic energy spread. At high enough energies, the shuttling process is no longer adiabatic, leading to large-scale secular oscillations that significantly broaden the ion kinetic energy distribution, as evidenced in the increasing energy spreads for the low axial confinement points in Fig. 8.4(a). However, increasing the axial confinement postpones this behavior until higher energies. For $V_{DC} = 150$ V, the ion position follows $z_0(t)$ closely for kinetic energies up to 120 K while the kinetic energy resolution, $R_{[E]_S}$, approaches 35 for $E \gtrsim 2$ K. Here the resolution is limited by a combination of increased micromotion energy at the large axial confinement, minor secular excitation during transport, and non-uniformities in the velocity profile of the shuttling waveform.

On the other hand, for $E \lesssim 2$ K where secular oscillations play less of a role, the resolution is ultimately limited by excess micromotion compensation techniques, which are typically accurate to within ~ 10 mK in quadrupole traps with dimensions similar to that used in this work. In this low energy regime, $V_{DC} \approx 5$ V is optimal since the reduced confinement limits micromotion from radial defocusing, permitting $R_{[E]_S} \approx 20$.

While a 250 μm neutral cloud size was assumed when computing the energy resolutions in Fig. 8.4(a), further resolution increases can be realized by reducing the size of the neutral atom sample, thereby also reducing the sampled velocity spread of the ion trajectory. Often the spatial dimensions of neutral atom traps can be conveniently tuned using optical or magnetic fields, with some atom systems, such as dipole traps, approaching 5 μm in size [ZFT09]. In Fig. 8.4(b), R_E is shown as function of w_A, with resolutions in excess of 100 predicted for atom traps nearing the 100 μm regime. Conversely, resolution may also be improved by increasing the distance between shuttling endpoints for a fixed atom cloud size. Increases in shuttle distance would also have the added benefit of mitigating secular oscillations as

a lower frequency waveform with Fourier components further spaced from ion secular resonances could be used to obtain a given shuttle velocity. However, this improvement would come at the expense of more difficult micromotion compensation, as to be discussed below.

The simulations do not consider the effect of atom-ion collisions on the ion trajectory; however, at experimental atomic densities ($\approx 10^{10}$ cm^{-3}), over the range of energies explored in the simulations, there is a $\approx 10^{-3}$ probability of a collision occurring with the MOT atoms in a given shuttle cycle. Therefore, any deviations from the expected ion motion caused by collision events are not expected to influence the energy of subsequent collisions, as there is only a $\approx 10^{-6}$ probability of a second collision occurring before the ion motion is reinitialized through laser cooling at the trajectory endpoints. Additionally, to reduce the effect of background gas collisions on the ion trajectory, the technique may be used in ultra-high vacuum conditions.

Further, the technique may ultimately be limited by effects unconsidered in the simulations, such as patch potentials and electrode charging, that make it difficult to optimally micromotion compensate at each trajectory position, especially given the comparatively large size of the utilized ion trap and the limited number of compensation electrodes.

For example, in our system, if excess micromotion compensation is performed at the center of the shuttling trajectory, we experimentally observe ~ 100 mK of uncompensated excess micromotion at the trajectory endpoints 2 mm displaced from the center point. While proper compensation throughout the trajectory may be a challenge in certain applications, we note that proper compensation in the narrow region of MOT interaction is most important for determining collision energy resolution, as the micromotion amplitude of the ion motion generally adiabatically follows any local uncompensated electric field (see Sec. 8.11 for a more detailed treatment on the effects of excess micromotion on the shuttling process). Further, axial micromotion may provide additional complications, although radial micromotion will likely dominate this effect. Through simulations performed using our system, we observe less than a < 2 mK difference in ion energy due to axial micromotion between the center of our shuttling trajectory and a point displaced 2 mm from the center; however, experimental imperfections may further increase this value.

To minimize these effects, the appropriate electrode shim voltages can first be identified for the ions at each trajectory position while the ions are stationary. Subsequently, the shim voltages can be updated while shuttling to ensure uniform micromotion compensation as the ion transits from one endpoint to the other. Additionally, excess micromotion compensation techniques, such as photon cross-correlation spectroscopy [BMB98] or parametric excitation [KPB15], may be used to compensate micromotion with greater precision and maintain ions with excess micromotion energies nearing $\lesssim 5$ mK.

While the precise kinetic energy control of laser cooled species is beneficial, ultimately this technique may be most useful when applied to molecular ion chemistry, where it can be used to detect nuances in long range capture models [SLG16] and possibly illuminate rotational and vibrational resonance features that have thus far evaded current techniques. To explore this possibility, simulations are performed while shuttling two laser cooled Ba^+ ions and a sympathetically cooled $BaCl^+$ molecular ion, with the resulting energy distributions of the molecular ion depicted as a function of shuttle frequency and trajectory position in Fig. 8.5(a) and Fig. 8.5(b), respectively. In contrast to Yb^+, Ba^+ possesses a Λ level-structure system, and thus, the three-level optical Bloch equations are solved to account for coherent-population-trapping effects in the simulated laser cooling force.

The results from the simulation demonstrate that, similar to the Yb^+ single-ion case, energy resolutions for $BaCl^+$ approaching 40 are achievable assuming a neutral atom cloud size of 250 μm, a value over a order-of-magnitude greater than that offered by alternative micromotion-based techniques in this energy range and one that can be further improved by changing the axial confinement and employing a smaller atom cloud size, as discussed earlier in this section. At kinetic energies below 1 K and when combined with a light mass atomic partner that would yield a low reduced mass, this resolution may be sufficient to resolve reaction resonance features, which have been predicted to have collision energy widths of order $\sim 1 - 10$ mK [SRA15], although the particulars of the resonance of interest and control of the systematics alluded to above will ultimately determine if this is feasible. Here, the collision energy is proportional to the reduced mass of the atom-ion system, and in most current hybrid systems the average and the width of its distribution are typically a

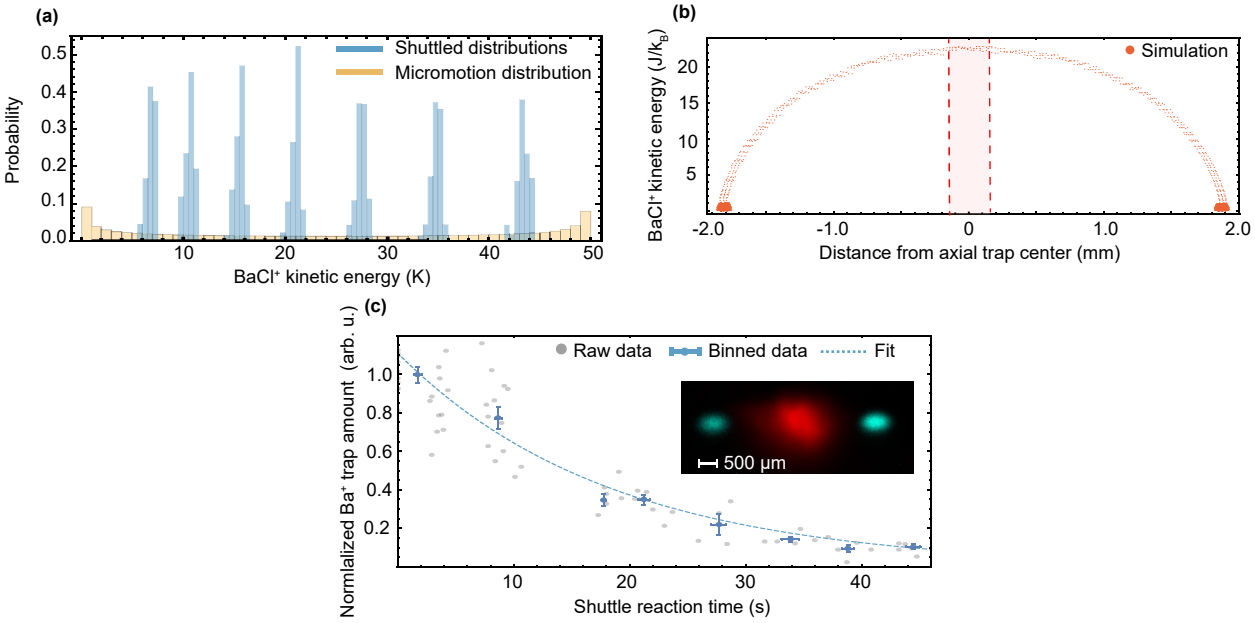

Figure 8.5: Controlled chemistry implemented with ion shuttling

(a) Simulated energy distributions for a single shuttled $BaCl^+$ molecular ion sympathetically cooled by two laser-cooled Ba^+ ions. The shuttled distributions are presented for a variety of shuttle frequencies and are compared to the theoretical distribution obtained from using the excess micromotion of a single ion to access an average kinetic energy of ≈ 25 K. **(b)** Simulated $BaCl^+$ kinetic energy as a function of axial ion position while shuttling. The dashed lines enclose the 250 μm effective region of MOT interaction where the ion velocity is approximately constant. **(c)** Decay of Ba^+ amount from the LQT as a function of shuttling time when a Ca MOT is placed at the center of the trajectory. The inset displays superimposed experimental fluorescence images of a ~ 500-ion Ba^+ sample and a Ca MOT containing roughly one million atoms taken while performing a shuttling reaction rate measurement. The large ion sample utilized in the experiment was initially liquid upon loading into the LQT and remained so while shuttling.

factor of $\approx 1 - 10$ smaller than the corresponding kinetic energy values.

8.5 Demonstration of technique for charge exchange reaction investigation

As a proof-of-principle experiment, a cloud of ≈ 500 Ba^+ ions was loaded into the LQT and shuttled through a Ca MOT located at the center of the ion trajectory at an average kinetic energy of 14(4) K. Here the resolution was limited by the inherent excess micromotion energy of the three-dimensional crystal. Fig. 8.5(c) shows the decay of Ba^+ ion amount in the LQT, measured by the ToF-MS [PMS17], as a function of shuttling duration due to charge-exchange collisions with ground-state Ca. The inset to Fig. 8.5(c) presents superimposed images of the atoms and ions obtained during shuttling, with each image taken using separate laser line optical filters. The geometric overlap between the atoms and ions was measured by phase-triggering the EMCCD cameras on the shuttling waveform to acquire ion images, and hence ion positions, at various points along their trajectory. This technique allowed for the effective imaging of ions with velocities $\lesssim 50$ m/s, bounded by effects related to the minimum camera exposure time of 10 μs. For velocities in this range, the ions are seen to follow the expected shuttling trajectory, and numerical simulations are used to verify this trend at higher collision energies. After the overlap factor was verified, measured atomic densities were used, in a manner similar to Ref. [PMS17], to calculate a total reaction rate of $2.4(4) \times 10^{-11}$ cm^3s^{-1}, a value consistent with a previously measured result [SRK12] after ion excited state fraction normalization.

This proof-of-principle experiment demonstrates that this technique can be used to measure accurate rate constants for reactions between laser-cooled species and neutrals, paving the way for similar studies incorporating sympathetically cooled molecular ions.

8.6 Conclusion

Blending techniques from the quantum information and hybrid trapping communities, we have demonstrated a method for controlling ion-neutral collision energy based on ion axial position modulation that is capable of offering energy resolutions, $\overline{E}/\sigma_E$, from $\sim 10-100$ over

kinetic energies ranging from $\approx 0.05 - 120$ K. This combination of both range and resolution improves on alternative techniques that typically compromise one for the other. In addition to investigating the technique through experiment and simulation, we also performed a reaction rate measurement by shuttling laser-cooled atomic ions, and we suggested how the shuttling method may be implemented in future experiments to study molecular ion chemistry.

Further, the technique can be immediately implemented in currently existing hybrid traps with little experimental overhead. The shuttling procedure is also quite adaptable, and properties such as axial confinement, neutral atom size, and endpoint-to-endpoint shuttle distance can be custom-tailored to a variety of experimental conditions to obtain desired energy resolutions while obeying most experiment-specific constraints.

Additional improvements may further increase the effectiveness of the technique. Ion traps with mulitple-segmented endcap electrodes that can more reliably compensate micromotion and produce more pure harmonic potentials throughout the trap may be utilized, allowing the ions to be shuttled over longer axial distances and while minimizing their acceleration in the MOT region. Further, if laser cooling during transport is necessary for a particular application, Doppler shifting of the ions while shuttling may be problematic if constant electronic state populations are desired. To this end, one may choose to appropriately adjust the frequency of the Doppler cooling laser while shuttling in order to produce a constant effective laser detuning. In addition, a imaging system with higher capture efficiency and a radial probe beam may be used to apply the Doppler velocimetry technique towards detecting the radial micromotion of single ions while shuttling and thus set more realistic bounds on excess micromotion compensation.

Lastly, the waveforms utilized in this proof-of-principle study were largely chosen out of convenience and speed of implementation. While sufficient for the purposes of this work, they are by no means optimal. More sophisticated waveforms [Osw15, FGP14, CLM16] that maintain flatter velocity profiles while not inducing secular heating may be used if even finer energy resolution is required.

This material is based upon work supported by the National Science Foundation Graduate Research Fellowship under Grant No. DGE-1650604. This work was also supported by the National Science Foundation (Grant No. PHY-1255526) and Army Research Office (Grants No. W911NF-15-1-0121 and No. W911NF-14-1-0378).

8.7 Corollary calculations and measurements

The following section summarizes ancillary measurements and calculations that were performed to complement the above study.

8.8 Doppler-cooling velocimetry

In order to extract experimental velocities for shuttled ion samples, we first take a linescan of a sample of stationary ions where ion fluorescence is collected by the PMT at various cooling beam detunings, allowing for determination of both s and δ in Eq. 8.9 in the manuscript. Laser cooling detunings are determined from a calibrated High Finesse wavemeter coupled directly to the laser beams in our system.

Once these two parameters have been determined, the ions can then be shuttled while their total photon scattering rate is measured by the PMT during each acquisition time bin ($\sim$ 10 ns). For a single ion, after normalizing by the stationary ion count rate, a time-dependent ratio, η(t), is produced which can be used to solve the equation $\eta(t) = \frac{\Gamma_{scatt}(v_z(t))}{\Gamma_{scatt}(v_z=0)}$ for $v_z(t)$. This velocimetry technique is only effective at determining motion along the axial propagation direction of our cooling beam and is insensitive to micromotion or secular motion in the radial dimension.

Furthermore, since the stationary count rate of our sample changes over the course of the experiment, due to ion depletion caused by background gas reactions or slight laser power fluctuations, we renormalize our background ion count rate by collecting ion fluorescence from the stationary endpoints of the trajectory during each shuttling procedure. We also collect a stationary ion count rate at each point along the shuttle trajectory to ensure that ion

fluorescence changes are indeed caused by velocity changes and are not a result of differing laser cooling alignment or light collection efficiency along the trajectory.

Due to the low optical detection efficiency of the system, an ensemble of ions must be interrogated in order to produce a measurement with an adequate signal-to-noise ratio on reasonable experimental timescales. Consequently, the resulting PMT signal yields the collective sum of photons captured from the entire crystal of ions, making individual ion motion indiscernible. Our velocimetry technique therefore effectively measures $\langle \eta(t) \rangle = \frac{\sum_i \Gamma_{scatt}(v_z^i)}{N\Gamma_{scatt}(v_z=0)} \approx \frac{\Gamma_{scatt}(\langle v_z \rangle)}{\Gamma_{scatt}(v_z=0)}$, where $\langle \eta(t) \rangle$ is the ensemble average count ratio, N is the total number of ions in the system, v_z^i is the axial component velocity of the i^{th} ion, and $\langle v_z \rangle$ is the ensemble average axial velocity of the entire system. The latter approximation is justified in our regime since the dispersion of velocities is expected to be low during the shuttling process, as evidenced by simulations described in Section 8.3.

8.9 Spatial and ensemble averaging of distributions

The velocity and also the energy of the shuttled ions exists as a distribution in two separate dimensions. Firstly, for a multi-ion sample, at a given instance of time, the ions reside in a distribution of velocities within the crystal itself. The ensemble-averaged measurements extract the mean of this distribution while remaining insensitive to its spread, which is determined by ion-ion collision events and differences in excess micromotion energy. Secondly, this distribution of velocities within the crystal also changes as a function of shuttle time as the ions evolve along their trajectory, meaning all ensemble-averaged measurements will change as well. To assign weighting factors to each measurement, we consider the spatial overlap of the ions at each instance of time with a neutral sample located at the center of the trajectory.

The neutral atom density distribution is approximately Gaussian. The spatial weighting factor associated with the velocity or energy measured in each time bin along the trajectory is defined as $w_b = \frac{e^{-(z_b/w_A)^2}}{\lambda}$ where z_b is the position of the ion during the b_{th} time bin, w_A is the e^{-1} decay length scale of the atomic density distribution, and λ is a normalization factor

chosen such that $\sum_b w_b = 1$. After the weighting factors have been calculated, the mean and standard deviations of the weighted distribution can be computed to yield the relevant distribution resolutions [Pat14].

8.10 Experimental energy resolution

We note the distinction between the energy distributions $[\langle \hat{E}_z \rangle]_S$ and $[E_z]_S$. $[E_z]_S = \frac{1}{2}m[v_z^2]_S$ while $[\langle \hat{E}_z \rangle]_S = \frac{1}{2}m([\langle v_z \rangle^2]_S)$. $[\langle \hat{E}_z \rangle]_S$ only approximately describes the average kinetic energy of the sample as it assumes this quantity is proportional to $[\langle v_z \rangle^2]_S$ instead of $[\langle v_z^2 \rangle]_S$, the latter of which is incapable of being measured in experiment. However, this approximation is reasonable if the energy dispersion of the sample is expected to be small, as suggested by simulations.

Further, $[\langle \hat{E}_z \rangle]_S$ is a distribution of ensemble-averaged energies and is distinct from $[E_z]_S$, the distribution of the non-ensemble-averaged axial kinetic energies. The latter is the more relevant distribution to consider when characterizing overall atom-ion collision energy control as it contains information on the spread of the entire axial energy distribution and not just the spread in the average energy of the sample. The simulations predict $R_{[E_z]_S} \approx 6$, while $R_{[\langle \hat{E}_z \rangle]_S} \approx 10$ was measured from experiment. $R_{[E_z]_S}$ is smaller than $R_{[\langle \hat{E}_z \rangle]_S}$ for a variety of reasons. For example, within a large ion crystal, the ions may experience slightly different potentials at different points within the crystal and therefore reach different peak velocities, dispersing their overall energy distribution while keeping their average energy constant.

8.11 The effect of micromotion on shuttling trajectories

An uncompensated offset electric field will displace the ion from the rf trap null and lead to excess micromotion energy. Currently, in our system, excess micromotion energy is compensated by iteratively changing the Mathieu-q and Mathieu-a parameter of our trap and adjusting compensation voltages on the LQT electrodes until the ion position changes minimally with trap parameter modulation, as verified through camera imaging. Ultimately

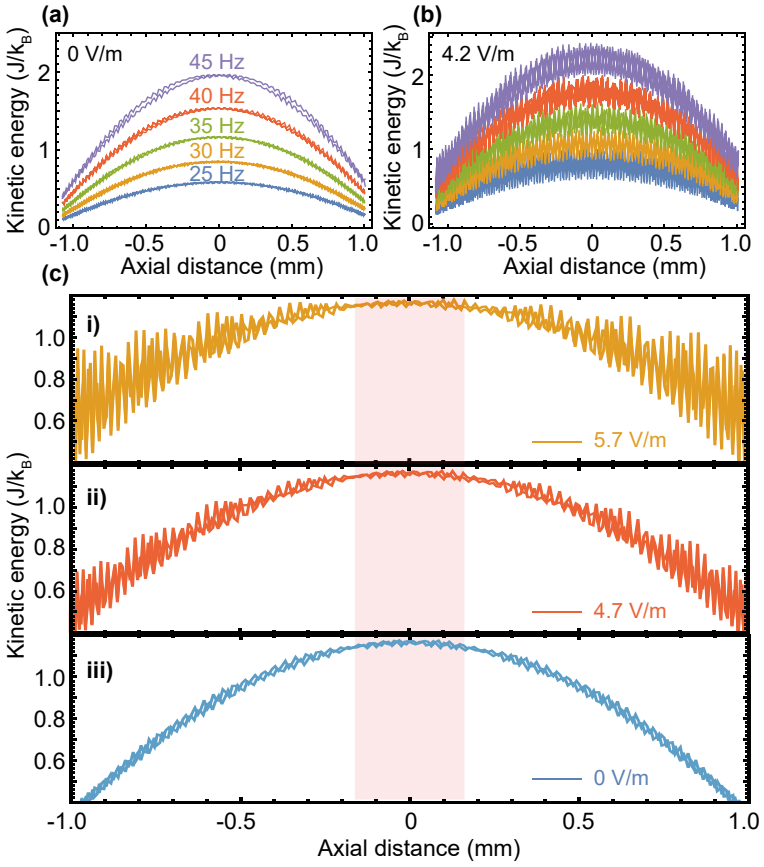

Figure 8.6: Effects of micromotion on shuttling energy

(a) Energy as a function of axial shuttle distance for a single ion in a perfectly excess micromotion compensated system at various shuttling frequencies. **(b)** The same simulations in (a) repeated with an additional electric field offset of 4.2 V/m. The micromotion broadens the energy distribution and shifts the average energy upwards from the perfectly compensated simulations in (a). The 4.2 V/m offset is consistent with what can currently be compensated in our system.**(c)** Simulations of an ion being shuttled with radial electric field gradients of varying strengths **(i-iii)** imposed upon the ion. The ions are assumed to be perfectly compensated at the center of the trajectory with the electric field rising linearly in a symmetric fashion for displacements from the center. The labels reflect the maximum electric field the ions experience at the outer points of the trajectory. As can be seen in the figure, the ions respond nearly adiabatically to the local micromotion compensation at a given point along the trajectory, making the energy resolution of the ions during MOT interaction less sensitive to the energy resolution of the ions at other points in the trajectory. Approximate regions of MOT interaction are shaded in red (color).

our technique is limited by our imaging resolution of ≈ 5 μm, leading to excess micromotion uncertainties of ≈ 30 mK. This value could certainly be improved with more sophisticated micromotion-compensation techniques, such as photon correlation spectroscopy or parametric excitation, that have been shown to limit displacements from the null to ≈ 1 μm [BMB98,KPB15], which would potentially result in roughly a factor of 25 improvement in the minimum excess micromotion energy obtainable in our system.

To illustrate how excess micromotion would affect the shuttling trajectory, we performed additional simulations with a single ion being shuttled at low energy, where micromotion more significantly affects energy resolution. In the simulations, stray voltages were imposed on trap electrodes to cause a constant ≈ 5 μm shift of the ion from the trap null during shuttling (approximately equal to our current micromotion compensation limits), and the results were compared to a perfectly compensated case. The trap and shuttling parameters utilized during these simulations are as follows: $V_{DC} = 5$ V, $V_{amp} = 1.2$ V, $\gamma = 0.03$, and $\omega \sim 2\pi \cdot (25 - 45)$ Hz.

As can be seen in Fig. 8.6(a) and (b), the additional micromotion energy leads both to an upward shift in average kinetic energy as compared to the compensated case and a broader energy distribution. Under perfect compensation, kinetic energy spreads of $\lesssim 10$ mK are obtainable, whereas this number is increased to $\lesssim 100$ mK in the simulations with excess micromotion.

Due to stray fields and patch potentials on the electrodes, the offset electric field experienced by the ion may not always be constant and may change during the shuttling trajectory. However, the closest sources of charge that could produce such fields reside on the trap rods, and thus these fields are expected to scale as $\sim 1/(r_0 - r_e)^2$, where r_e is the electrode radius of our trap rods. While the charges could be arranged in a cluster of any size, point sources may be particularly problematic since without neighboring charges to broaden their potential, the electric field they produce may change significantly along the shuttling trajectory.

Given the large dimensions of the trap relative to the shuttle trajectory, we can approx-

imate the potential of these fields as

$$\Phi(r,z) = \frac{Q}{4\pi\epsilon_0}\frac{1}{(r^2+z^2)^{1/2}} \approx \frac{Q}{4\pi\epsilon_0}\frac{1}{r}\left(1-\frac{1}{2}\left(\frac{z}{r}\right)^2\right) \tag{8.10}$$

which leads to an radial electric field gradient with respect to the trap axial dimension along the trap null of

$$\begin{aligned}\frac{\partial}{\partial z}E_r(r,z)|_{r\to(r_0-r_e)} &= \frac{\partial}{\partial z}\frac{\partial}{\partial r}\Phi(r,z)|_{r\to(r_0-r_e)} \\ &\approx \frac{Q}{4\pi\epsilon_0}\frac{z}{(r_0-r_e)^4}\end{aligned} \tag{8.11}$$

where $\Phi(r,z)$ is the electrostatic potential due to a point charge on a rod located a trap electrode, Q is the charge of the point charge of interest, ϵ_0 is the vacuum permittivity of free space, r is the radial dimension of the trap, $E_r(r,z)$ is the component of the electric field in the radial direction, and $(r_0 - r_e)$ is the distance between the surface of the electrode and the center of the trap ($r_0 - r_e = 4.1$ mm in our system).

While the magnitude of the electric field at any given trajectory point can certainly be significant enough to pull the ion off the null, the fields vary approximately linearly as a function of axial distance. Therefore, we investigated the influence of a linearly varying electric field gradient on the shuttling procedure.

Using the same simulation parameters as in the above-mentioned excess micromotion simulations, we initialized an ion with idealized micromotion compensation at the center of the shuttling trajectory. We then also included an offset electric field that varied linearly with axial trap distance, serving to push the ions off the null as they progressed further from the trajectory center point during the shuttle.

As the total charge producing such patch potentials is difficult to estimate, the results for a variety of reasonable electric field strengths are presented in Fig. 8.6(c). Even though the ions experience significant excess micromotion at the trajectory endpoints, since the changes in radial displacement from the null occur gradually, the ions can respond nearly adiabatically to the local excess micromotion amplitude at each trajectory position. Therefore when the ions reach the MOT region, where the micromotion has been compensated adequately, they

experience very little excess micromotion. For all field gradients explored in Fig. 8.6(c), the kinetic energy widths are predicted to be within 10% percent of the perfectly compensated value of 14 mK, assuming $\omega_A = 200$ μm.

Of course, multiple charge patches could result in a stronger gradient along the axial trap dimension. If the gradient is strong enough, the ions could respond non-adiabatically to sudden changes in radial positions along the shuttling trajectory, inducing radial secular oscillations that could significantly compromise the energy resolution. However, when imaging the ions while stationary at various points along the trap axis, no such electric field profile is observed, and the ions are found to be within ≈ 10 μm of the trap null at all points along the trajectory for given set of micromotion compensation shimming voltages (while operating the trap at radial secular frequency of $\approx 2\pi \cdot 45$ kHz). Additionally, all fields explored in Fig. 8.6(c) above 4.2 V/m produces ion displacements from the null greater than that observed experimentally, further reducing the likelihood that strong electric fields that could compromise ion energy resolution exist in our system. These results indicate that if compensating micromotion throughout the trajectory is technically infeasible for a give experimental setup, the less challenging task of compensating in the narrow region of MOT interaction may provide similar results.

CHAPTER 9

Synthesis of a mixed hypermetallic oxide

Hybrid trapping platforms provide excellent environments for the control and study of chemical reactions; however, up until this point, the vast majority of such research has been performed using atoms and atomic ions. Such studies have produced fascinating results; however, extending these techniques to more complex polyatomic molecules would allow the tools of ultracold physics to be applied to systems of greater interest to the chemistry and biology communities.

Hypermetallic alkaline earth (M) oxides of formula MOM have been studied under plasma conditions that preclude insight into their formation mechanism. We present here the application of emerging techniques in ultracold physics to the synthesis of a mixed hypermetallic oxide, $BaOCa^+$. These methods, augmented by high-level electronic structure calculations, permit detailed investigation of the bonding and structure, as well as the mechanism of its formation via the barrierless reaction of Ca (^3P_J) with $BaOCH_3^+$. Further investigations of the reaction kinetics as a function of collision energy over the range 0.005 K to 30 K and of individual Ca fine-structure levels compare favorably with calculations based on long-range capture theory.

9.1 Background motivation

Molecules usually contain their constituent atoms in well-defined ratios predicted by classical theories of valence. Hypervalent species, however, are well known, and provide an opportunity to look more deeply into chemical bonding [NSG02] and to anticipate and predict new chemical species and structures that may have exotic or useful properties [UOY10]. An

interesting class of hypervalent molecules is the hypermetallic alkaline earth (M) oxides of form MOM. Theory reveals the bonding in these linear molecules as donation of an electron from each metal atom to the central O atom, resulting in a system in which the central atom is closed shell, inhibiting coupling between the radical centers on the terminal metal atoms. As a result, the singlet-triplet splitting is very small and its prediction sensitive to the level of theory applied. The hypermetallic alkaline earth oxide BeOBe and its cation have recently been investigated by Heaven and coworkers using a range of spectroscopic tools, augmented by high-level electronic structure calculations [MBH09, ABH11]. For BeOBe, the singlet was found to be the ground state, just 243 cm^{-1} below the triplet. Theoretical predictions of bonding and structure have also been reported for MgOMg [OBS11], CaOCa [BSG12], and SrOSr [OJS13].

Given these properties, MOM molecules and their cations provide an opportunity to benchmark quantum chemical calculations and explore bonding in molecules containing M atoms in the +1 oxidation state, which have recently been produced and are expected to be useful for inorganic synthesis [GJS07]. For mixed hypermetallic oxides MOM', dramatic effects on the electronic structure, single-triplet splitting, and excited state spectra may be expected to result from breaking the metal atom symmetry, leading to unusual inorganic diradicaloid systems [Abe13]. In addition, for the mixed cations the asymmetric hole distribution impacts both the dipole moment and bonding. All of these properties could be tuned through choice of metal atoms for applications such as nonlinear optics, materials science, or as synthetic intermediates [NC15]. One challenge to such investigations is to develop a means to synthesize these molecules under controlled conditions and probe the pathways leading to their formation. Cations are a natural first target for such investigations as they can be manipulated and detected with great ease and sensitivity.

Emerging techniques in ultracold physics are now being adapted to the study of chemical systems, bringing new capabilities to probe reaction dynamics and mechanisms [EDP15, DKW11, Hud16]. Recently, a study of the reaction of conformers of 3-aminophenol with laser-cooled Ca^+ ions revealed a fascinating dependence on conformational state [CDK13]; quantum state resolved collisions between OH and NO [KWS12], as well between N_2^+ and

Rb [HW12], have been observed; and quantum effects were found to have a major impact on state-resolved KRb reactions [ONW10]. Reactions involving polyatomic reagents are a compelling target for such studies as these techniques may be used to cool these species into a limited number of quantum states, as well as provide precise control over reaction conditions. Here we describe use of a magneto-optical atom trap coupled to an ion trap and time-of-flight mass spectrometer to synthesize a mixed hypermetallic alkaline earth oxide, $BaOCa^+$. These methods, augmented by high-level electronic structure calculations, permit detailed investigation of the properties of this molecule as well as the mechanism of its formation via the barrierless reaction of Ca (^3P_J) with $BaOCH_3^+$.

9.2 Experimental characterization of reaction

The collision energy of the trapped ions and atoms in this study, defined as E/k_B, where E is the kinetic energy of the collision complex and k_B is the Boltzmann constant, ranged from 0.005 K to 30 K, depending on the size of the ion crystal loaded into the LQT. A standard Ba^+ crystal was used as a sympathetic coolant for other trapped ions (Fig. 9.1B). In a typical experimental sequence, Ba^+ ions were initially loaded into the LQT through laser ablation of a $BaCl_2$ target. From this initial sample, a small number of $BaOH^+$ and $BaOCH_3^+$ ions were created by the reaction of Ba^+ with CH_3OH [DSL93] introduced into the vacuum chamber at a pressure of $\sim 10^{-10}$ Torr. The $BaOCH_3^+$ molecules were translationally cooled by the Ba^+ crystal. Recent studies [RSS12] indicate that collisions with the ultracold Ca atoms of the MOT should also cool their ro-vibrational internal degrees of freedom; however, absent spectroscopy of $BaOCH_3^+$, we assume an internal temperature of < 300 K, bounded by the temperature of our vacuum chamber. Once a sufficient number of $BaOCH_3^+$ molecules were produced, $BaOH^+$ ions could be removed from the LQT by resonantly exciting their motion at a mass-specific secular frequency; afterwards, the purified sample was immersed in a radius r $\approx$0.6 mm cloud of three million Ca atoms at 0.004(2) K (Fig. 9.1B). After a variable immersion time, t_i, the voltages of the LQT were adjusted to eject the ions into the ToF, yielding mass spectra (Fig. 9.1C). The ToF spectra indicated the formation of a

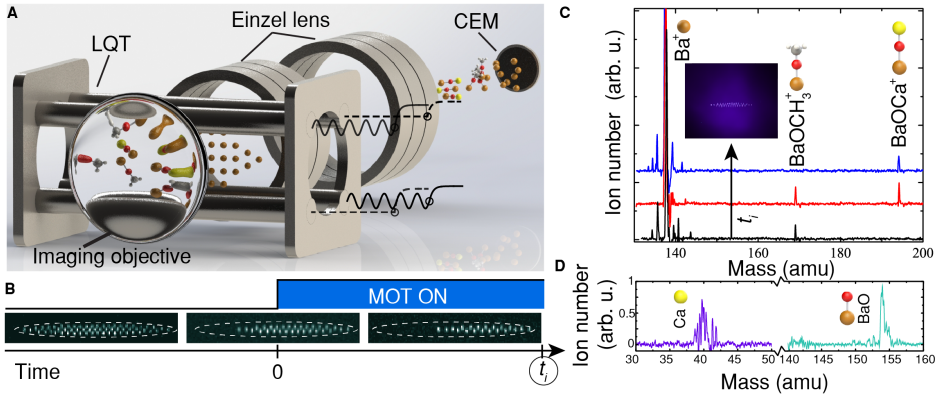

Figure 9.1: Experimental schematic of the hybrid system and ToF apparatus

(A) A schematic of the experimental apparatus, including the LQT, the high voltage pulsing scheme (shown as solid and dashed lines), and the ToF. **(B)** An illustrative experimental time sequence that depicts initialization of a Ba^+ crystal, production of $BaOCH_3^+$ (visualized as dark ions in the crystal) through reactions with methanol vapor, and subsequent MOT immersion. **(C)** Sample mass spectra obtained after ejecting the LQT species into the ToF after various MOT immersion times, t_i, along with an inset depicting a superimposed fluorescence image of an ion crystal immersed in the Ca MOT. **(D)** Mass spectra of photofragmentation products collected after inducing photodissociation of $BaOCa^+$. The identified photofragments were used to verify the elemental composition of the product.

reaction product with mass-to-charge ratio m/z of 193(1) amu, which is consistent with that of $BaOCa^+$ (193.9 amu). We confirmed the assignment by introducing a photodissociating laser into the LQT and analyzing the dissociation fragments of the molecule (see Sec. 9.9). Depending on which dissociation pathway was resonant with the laser, fragments were detected with mass-to-charge ratios of either 40(1) amu or 153.7(3) amu, consistent with Ca^+ and BaO^+, respectively (Fig. 9.1D).

9.3 Electronic Structure Calculations

To aid in the interpretation of the experimental results, electronic structure calculations were performed for the Ca + $BaOCH_3^+ \rightarrow BaOCa^+$ + CH3 reaction [WKK12a, FTS09]. Optimized geometries for $BaOCH_3^+$ and $BaOCa^+$ and their fragments were obtained from density functional theory (DFT) using the triple-zeta correlation consistent basis sets (cc-pwCVTZ on calcium and barium and cc-pVTZ on hydrogen, carbon, and oxygen) and the B3LYP density functional. The inner shell electrons of calcium and barium were described by an effective core potential (ECP). Harmonic vibrational frequencies were computed at all stationary points. The calculated vibrational frequencies were used to characterize the stationary points as minima or saddle points and to obtain vibrational zero point energies. Coupled cluster theory including single and double excitations with perturbative triples, denoted CCSD(T), was used to estimate thermochemical energy differences. To check the validity of the DFT geometries for this problem, the CCSD(T) energies of the stationary points were recalculated at geometries obtained from second-order Møller-Plesset (MP2) theory, and the changes in thermochemical energy differences were less than 1 kcal/mol. DFT and MP2 offer different approaches to the electron correlation problem, but they predict geometries of generally comparable accuracy. Discrepancies between them would be an indication that a higher level of theory should be used, but their agreement here suggests such methods are not warranted. The electronic structure calculations were performed using the Gaussian 09 and Molpro 2012 program packages [WKK12a, FTS09].

The calculated results show the Ca ($^1S_0$) + $BaOCH_3^+ \rightarrow BaOCa^+$ + CH_3 reaction to be exothermic by 5.3 kcal/mol at the CCSD(T)/cc-pVTZ level of theory. Interestingly, at this level of theory, most of the exothermicity results from a loss of vibrational zero point energy between reactants and products. At the more expensive CCSD(T)/cc-pV5Z level of theory, the heat of reaction is increased to 8.4 kcal/mol.

In mixed hypermetallic oxides, the electronic degeneracy of the metal atom locations is removed and our calculations predicted electron localization on the Ca atom due to its higher ionization potential (Fig. 9.2A). This conclusion was supported by a natural bond

order analysis assigning partial charges of +1.67 to barium and +0.91 to calcium in BaOCa. Calculations also indicated the ion has a significantly larger permanent dipole moment (2.80 D) than neutral BaOCa (1.32 D), again supporting principal removal of Ba-centered electron density upon ionization. The first strong electronic transition in $BaOCa^+$ corresponds to transfer of this electron density from Ca to Ba. As this electron does not strongly participate in the molecular bonding, the associated Franck-Condon factors are moderately diagonal and may allow optical cycling and detection [BMN14]. We calculated the ionization energy of BaOCa to be 4.18 eV, slightly higher than in BaOBa (experimentally reported as 3.87 eV (28)) but closer to BaOBa than CaOCa, calculated to be 4.90 eV.

The dipole moment calculation was performed at the B3LYP/cc-pVTZ level, using broken symmetry unrestricted Hartree-Fock (UHF) for the singlet neutral, whereas the singlet-triplet splitting was calculated at the projected third-order Møller-Plesset (PMP3/cc-pVTZ) level of theory, again using broken symmetry UHF for the singlet neutral. Further, the ionization energy was determined at the CCSD(T) with UHF reference/cc-pVTZ level.

The intrinsic reaction coordinate (IRC) calculation, depicted in Fig. 9.2B, was performed at the B3LYP/cc-pVTZ level of theory, revealing the existence of two bound $BaOCH_3Ca^+$ complexes, one in the entrance channel and one in the exit channel. The structure and relative energy of both of these structures are investigated at the CCSD(T)/cc-pVTZ level of theory, indicating the existence of a barrier to the reaction, whose height is 10.2 kcal/mol. The IRC calculations were performed using the Hessian based predictor-corrector integrator method of Hratchian and Schlegel. The Hessian was recomputed at each integration step.

It is possible that multi-reference effects may be significant in this system. To assess the need for a multi-reference description, valence complete active space (CAS) multi-configurational self-consistent field (MCSCF) calculations were performed on all the singlet and triplet structures presented in Fig. 9.2A. The weight, defined as the square of the configuration interaction (CI) coefficient, of the reference Hartree-Fock configuration is shown to be 94% in the triplet state and 80% in the singlet for the transition state (TS) structure, indicating that multi-reference effects play a role in the singlet, but not the triplet, TS. The second most important configuration in the singlet TS has a weight of 13%, while all others

are found to be less than 2%. Natural orbital analysis of the broken symmetry UHF wavefunction for the singlet TS shows two natural orbitals with significant fractional occupation (1.2 and 0.8), indicating the broken symmetry UHF gives an approximate description of the two most important configurations in the CAS wavefunction. A CCSD(T)/VTZ calculation using the broken symmetry UHF wavefunction as a reference results in a 3.4 kcal/mol increase in the barrier height. Further, CI coefficients for the remainder of the structures along the triplet pathway demonstrate reference configuration weights ≈93%, allowing us to conclude that multi-reference effects would not significantly alter the conclusions of our computational study (Table 9.1).

Calculations for neutral BaOCa predicted that, like BeOBe, it is a diradicaloid system with a similarly small singlet-triplet splitting of only 407 cm^{-1} but with very different energies for the radical centers. The small singlet-triplet splitting in neutral MOM' molecules is a manifestation of the spin uncoupling on the metal centers. The reaction experimentally studied in this work produces the $BaOCa^+$ cation and a CH_3 coproduct, two doublets whose spins are uncorrelated, and thus, the singlet-triplet splitting vanishes and the potential energy surfaces are degenerate.

9.4 Experimental search for reaction pathway

Given that the predicted barrier is insurmountable at experimentally realized collision energies and that the tunneling probability through the barrier is negligible, we hypothesized the observed synthesis occurred through an electronically excited state of the Ca reactant. To test this explanation, we varied the Ca electronic state populations via control of the Ca MOT lasers and measured the resultant changes in $BaOCa^+$ production. The excited state populations of the Ca atoms were determined from a rate equation model spanning 75 electronic states that incorporated the intensities and detunings of all near-resonant laser fields present in the MOT trapping volume [MPY17]. The chemical reaction rate for the $Ca + BaOCH_3^+ \rightarrow BaOCa^+ + CH_3$ reaction is given by $\Gamma = n_{Ca} k_t$, where n_{Ca} is the Ca atom number density and k_t the total reaction rate constant, which is found as $k_t = \sum_i p_i k_i$,

Stationary point	Singlet surface configuration weights (%)	Triplet surface configuration weights (%)
Ca	100(0)	100(0)
$BaOCH_3^+$	94.8(0.5)	94.8(0.5)
Entrance channel complex	88.7 (7.3, 1.6)	95.8(0.6)
Transition state	80.3(13.1, 1.8)	94.5(0.5)
Exit channel complex	93.9(0.8)	94.8(0.5)
$BaOCa^+$	99.2(0.7)	99.2(0.7)
CH_3	96.7(0.4)	96.7(0.4)

Table 9.1: MCSCF calculations to assess multi-reference effects

CAS MCSCF calculations were performed on all singlet and triplet structures displayed in Fig. 9.2A to verify multi-reference effects do not play a significant role in our computational study. The weight, as given by the square of the CI coefficient, of the Hartree-Fock configuration is presented for the triplet and singlet structures, along with the weights of the second most significant configuration in parenthesis. For select cases along the singlet surface where the weight of the Hartree-Fock configuration is shown to be less than 90%, the weight of the third most significant reference configuration is also subsequently presented in parenthesis, with all such configurations having weights less than two percent. While secondary configurations appear to be most significant in the singlet transition state, a CCSD(T)/VTZ calculation involving a broken symmetry UHF wavefunction incorporating the two most significant reference configurations indicates a barrier height increase of 3.4 kcal/mol, further confirming the existence of a barrier to reaction along the singlet surface. The initial reactant and final product states have the same configuration weights for both the singlet and the triplet, explaining their equivalency in the table.

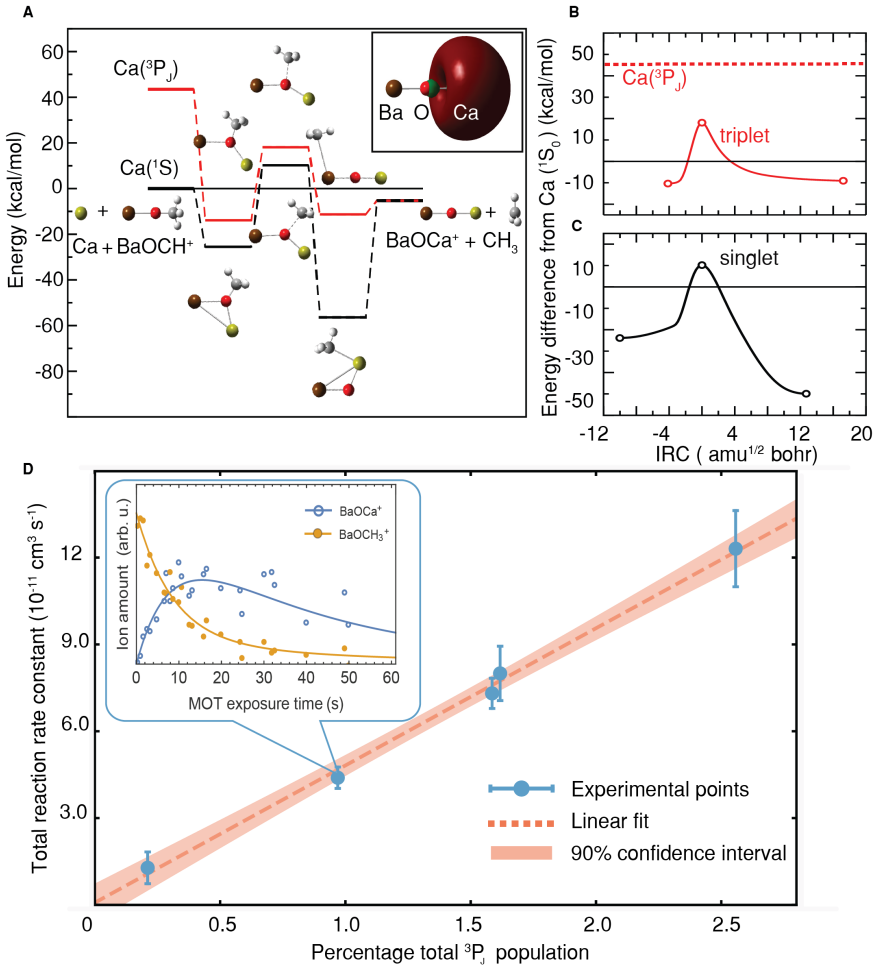

Figure 9.2: $BaOCa^+$ production mechanism

(A) Energy of stationary points along the Ca $^1S_0$ (black) and ^3P_J (red) reaction pathways calculated at the CCSD(T)/cc-pV5Z level of theory. The corresponding energies for the singlet (triplet) pathway in kcal/mol are, from left to right, 0 (43.5), -25.5 (-13.9), 10.2 (18.1), -56.4 (-11.3), and -5.3 (-5.3). The presence of a barrier in the Ca $^1S_0$ pathway precludes reaction at low temperature, while the transition state in the triplet pathway is well below the energy of the reactants and does not prevent the exothermic reaction to $BaOCa^+$ and CH_3. The geometries of the complexes at each stationary point are shown below (above) the singlet (triplet) pathway. The inset displays the linear geometry of the $BaOCa^+$ molecule and its open shell highest occupied molecular orbital. **(B-C)** Energy along the IRC for both the singlet (B) and triplet (C) surfaces calculated at the B3LYP/cc-pVTZ level of theory. The circles correspond to the stationary points in (A), and all energies are given with respect to the ground state reactants. **(D)** Experimental total reaction rates plotted as a function of aggregate triplet Ca population, presented alongside a linear fit to the data (weighted by the reciprocal of the standard error squared) and its corresponding 90% confidence interval band. Experimental uncertainties are expressed at the one-sigma level. The inset shows the temporal evolution of both $BaOCH_3^+$ and $BaOCa^+$ amounts, normalized by initial Ba+ number, in the LQT as a function of MOT exposure time as well as the solutions of differential equations globally fit to 250 kinetic data points in order to extract reaction rate constants, with a reduced chi-square statistic of 1.03 specifying the goodness-of-fit to the displayed data set.

where p_i and k_i are the population and reaction rate constant of the i^{th} Ca electronic state, respectively. The total reaction rate constant was experimentally measured by monitoring the amount of both $BaOCH_3^+$ and $BaOCa^+$ present in the LQT as a function of interaction time with a Ca MOT of known density. The solution of a differential equation incorporating all measured loss and production rates for each molecular ion due to photodissociation, chemical reactions, and background loss was then fit to the reaction kinetics data in order to determine k_t.

This system of differential equations is similar to that presented in Eqn. 6.2, except additional reaction and loss pathways have been included to account for interactions with the MOT and potential photodissociation processes. The general differential equation given for the ion number of the i^{th} species in the trap, N_i, is determined as

$$\frac{dN_i}{dt} = -\eta_{Ca}\hat{O}_{Ca}k_{i,CEX} - \sum_{j,l}\eta_l\hat{O}_l k_{i+l\rightarrow j}N_i + \sum_{j,l}\eta_l\hat{O}_l k_{j+l\rightarrow i}N_j - \lambda_L N_i \tag{9.1}$$

where $\hat{O}_n$ is overlap factor for the ions with the n^{th} neutral sample, $k_{i,CEX}$ is the charge-exchange rate constant between the i^{th} ionic species and Ca, $k_{i+a\rightarrow j}$ is the reaction rate constant for the $i + a \rightarrow j$ reaction, η_n is the atom-number density for the n^{th} neutral reactant, and λ_L is the loss rate associated with photodissociation and natural trap loss. The main neutral reactants of interest are Ca, in its various electronically excited states, and CH_3OH. Here, we present the charge-exchange processes outside the summation for clarity. Lastly, back reactions are included in the above differential equation for thoroughness, but these processes do not necessarily occur for all reactions and their associated rate constants may fit to 0 when compared to the data.

The experimentally measured reaction rate exhibited no statistically significant dependence (see Sec. 9.8.1) on the population of the singlet Ca electronic states involved in the laser cooling process, i.e. the $4s^2\ ^1S_0$, $4s4p\ ^1P_1$, $4s5p\ ^1P_1$ and $3d4s\ ^1D_2$ states. This observation is consistent with preliminary theoretical calculations, which suggested that a reaction barrier, similar to that of the Ca ($^1S_0$) + $BaOCH_3^+$ channel, exists on all of these singlet channels.

Studies have shown [MPY17, OBF99] spin-forbidden optical transitions lead to the pro-

duction of a small number of Ca atoms in the 4s4p ^3P_J states (Fig. 9.3C) in Ca MOTs. Though atoms in these metastable states are not trapped by the MOT force, they are continually produced, leading to a steady-state population in the trapping volume. Further, controlling the MOT lasers can vary the electronic populations in these states and reveal how they affect the reaction rate in a manner similar to studies of the singlet state. In particular, the primary method for varying population in the ^3P_J levels is controlling the power of the 423 nm beam, which is used to drive the cooling transition for the MOT. The 423 nm beam intensity directly can affect the amount of population in the $^1P_1$ state and, since the ^3P_J levels are populated primarily through decay channels from the $^1P_1$ state, also has an effect on the total ^3P_J population.

The observed reaction rate as a function of total population in the 4s4p ^3P_J states is shown in Fig. 9.2D, with a characteristic kinetics data set and the corresponding fitted solutions shown in the inset. Here, the linear dependence of the reaction rate constant on the 4s4p ^3P_J population was shown to be consistent with zero vertical intercept, suggesting that the observed formation of $BaOCa^+$ initiates predominantly along the triplet Ca (^3P_J) + $BaOCH_3^+$ surface. While non-adiabatic interactions from the excited singlet surfaces coupling to other electronic states could permit reaction despite the calculated barriers, the experimental observations indicate that these effects, if present, do not play a significant role. Additionally, since the collected data is sensitive to reaction entrance channel, but not necessarily to the surface along which the reaction completed, events where coupling from the triplet surface to the singlet surface occurred and resulted into reaction would not be experimentally distinguishable from reactions evolving exclusively along the triplet surface.

9.5 Verification of triplet reaction pathway

In order to verify the Ca ^3P_J pathway of the reaction, we performed two additional experiments. First we measured the reaction rate of Ca atoms in a single internal quantum state, the $|^3P_2, m_J = 2\rangle$ state, by loading MOT atoms in this state into a magnetic trap and overlapping them with the ions. This experiment showed unequivocally that the reaction

occurs between a Ca atom in the $^3\mathrm{P}_J$ state and a BaOCH_3^+ ion. In the second experiment, we employed additional optical pumping lasers to populate only a single $^3\mathrm{P}_J$ state during Ca MOT operation, enabling the extraction of fine-structure-resolved reaction rate constants for the ^{3}P states.

Under normal MOT operation, multiple energy levels in the laser cooling cycle are populated simultaneously. Although the triplet population data in Fig. 9.2D suggests the $^3\mathrm{P}_J$ pathway of the reaction, it is possible that other electronic states may be contributing to the observed reaction through non-adiabatic processes. The magnetic trap, introduced above, provides a means to isolate a sample of triplet Ca atoms and ensure that reaction initiates on the triplet surface. The magnetic trap, a separate atom trap from the MOT whose non-optical trapping force is produced by the MOT field gradients, serves as a nearly pure reservoir of Ca triplet atoms since only atoms in the $|^3P_2, m_J = 2\rangle$ state have large enough magnetic moment to produce significant atomic trap densities.

In the magnetic trapping experiment, ions were first initialized as described earlier. To ensure that reaction only occurred between the magnetically trapped Ca atoms and BaOCH_3^+ molecules, the voltages of the LQT were adjusted such that BaOCH_3^+ ions were first displaced from the center position of the MOT by $\sim$3 mm, corresponding to a displacement of $\sim$5 MOT radii, precluding background reactions from direct MOT-BaOCH_3^+ overlap. After the magnetic trap was loaded to capacity, the MOT was depleted by extinguishing the atom cooling beams, removing any background Ca MOT atoms from the magnetic trap region within $\sim$5 ms. The endcap voltages were then adjusted to shuttle the ion crystal to the center of the magnetic trap, allowing it to react directly with a nearly pure sample of $|^3P_2, m_J = 2\rangle$ atoms for the duration of the magnetic trap lifetime ($\sim$1000 ms), and this process was repeated up to 100 times for each ion crystal. Here, m_J is defined with respect to the trap magnetic field direction, whereas the relative velocity vector defining the reaction is isotropically distributed, meaning the Ca m_J sublevel is not controlled along the reaction quantization axis.

BaOCa^+ accumulation in the LQT was observed to increase with BaOCH_3^+ magnetic trap immersion time, whereas the chemical reaction rate for a control case, where an optical

pumping laser was used to depopulate $^3P_2$ atoms throughout the experiment and thus deplete the magnetic trap, was consistent with zero (Fig. 9.3B). When $|^3P_2, m_J = 2\rangle$ atoms were present in the magnetic trap, a reaction rate constant of $\sim 10^{-9}$ cm^3/s was measured, consistent with the reaction rate measurement described earlier. Here, fluorescence imaging and spatial estimates of the magnetic trap derived from the magnetic field gradients of the MOT were used to estimate the $^3P_2$ atom number density needed for the rate constant calculation. The uncertainty of this estimate prevents a more precise measurement of the reaction rate constant.

Therefore, to find more accurate reaction rate constants and to resolve the rate constant for each of the ^3P_J fine-structure states, optical pumping lasers were used to deplete population from two ^3P_J levels simultaneously, isolating population in a single triplet state while reaction kinetics data were measured. All three measured fine-structure resolved reaction rate constants (Fig. 9.4D) were of order 10^{-9} cm^3/s, with the $^3P_1$ state exhibiting the largest rate constant value of $5.4(9) \times 10^{-9}$ cm^3/s. These results are in reasonable agreement with predictions from a long range capture theory (see below).

9.6 Triplet reaction pathway and long-range capture model

Having concluded experimentally that the synthesis of $BaOCa^+$ occurs via the triplet channel, electronic structure calculations, as described earlier, were performed to characterize the Ca (^{3}P) + $BaOCH_3^+ \rightarrow BaOCa^+ + CH_3$ reaction. Although the general features of the triplet potential energy surface leading to the two product doublet molecules were similar to those discussed above for the ground state, the transition state for reaction on the triplet surface (Fig. 9.2C) was calculated to be 25.4 kcal/mol (CCSD(T)/cc-pVTZ) below the energy of the reactants (Fig. 9.2, A and B), meaning the reaction proceeds without barrier for each ^3P_J fine-structure state. The ground state and triplet potential surfaces both have entrance channel complexes that feature a strongly bent Ba-O-Ca backbone with the methyl attached to the oxygen while retaining the pyramidal sp3 configuration. The ground state exit channel shows a strongly bound complex with the methyl chemically bound to

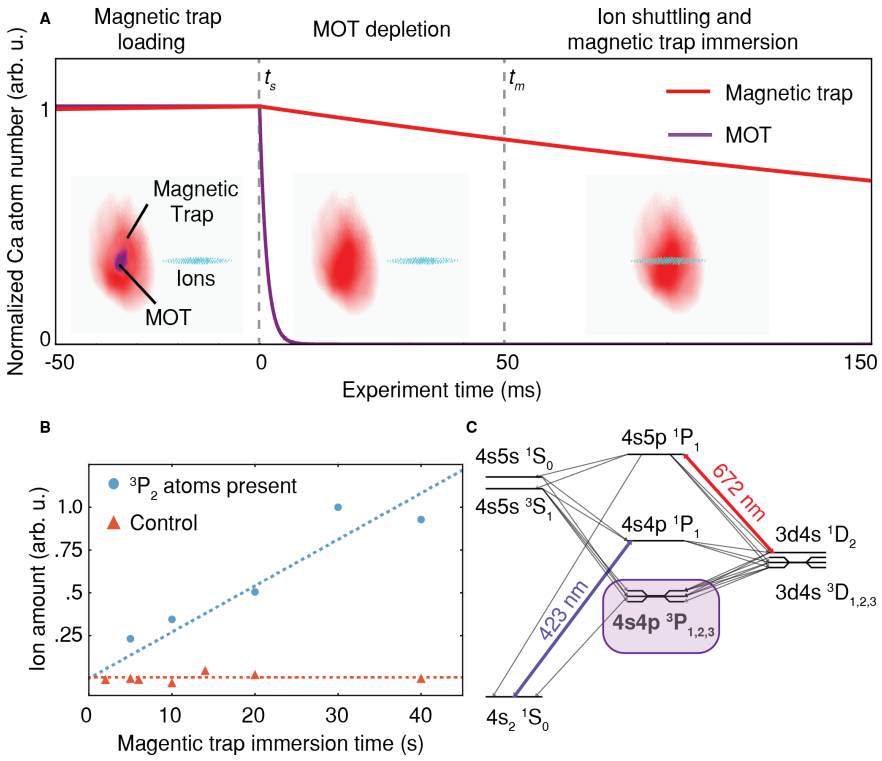

Figure 9.3: Experimental schematic of the hybrid system and ToF apparatus

(A) The number of atoms (normalized by the initial atom amount in each trap) in both the magnetic trap and the MOT probed as a function of experiment time by monitoring the amount of fluorescence produced from each when illuminated with a near-resonant laser. A typical experimental time sequence is also presented, along with scaled false-color fluorescence images of both the atoms and ions for illustration. Approximate spatial scales, provided separately for the atom and ion images, are also displayed for reference. Ions are initially displaced from the MOT as the magnetic trap is loaded. At t_s, the atom cooling beams are extinguished to deplete MOT atoms from the magnetic trap region, and the LQT endcaps are subsequently adjusted at t_m to overlap the ions with the center of the magnetic trap for roughly 500 ms, enabling $BaOCH_3^+$ reactions with Ca ($^3P_2$) atoms. (B) $BaOCa^+$ accumulation, expressed as a fraction of initial Ba+ amount, plotted as a function of interaction time with the magnetic trap. A control case where a laser is used to depopulate the $^3P_2$ Ca level during magnetic trap loading is also presented. Fitted solutions to differential equations, obtained in the same manner as those in Fig. 9.3C, are presented alongside the data, and, after estimating the magnetic trap density, they yield reaction rate constants of $8(3) \times 10^{-9}$ cm^3/s and $0(3) \times 10^{-9}$ cm^3/s for the experimental case and the control, respectively. (C) A level scheme for Ca including the relevant electronic states involved in the laser cooling process, with the reactive $^3P_{0,1,2}$, states highlighted.

Ca, whereas the triplet exit channel minimum may be characterized as a van der Waals type interaction between a planar methyl radical and the incipient $BaOCa^+$ molecule. This

reaction shows very different dynamics on the singlet and triplet surfaces, but in contrast to the commonly seen case of a singlet atom inserting into a covalent bond [GLS03], here the triplet is more reactive as the singlet-triplet splitting is significant in the calcium atom but small at the transition state and in the product.

Given that calculations suggest the reaction is barrierless, we expect that the observed reaction rate can be estimated from long-range capture theory. As the ion approaches the Ca atom, the quadrupole moment of the Ca ^3P_J state leads to a long-range R^{-3} interaction, in addition to the usual R^{-4} polarization potential. We assume that both interactions take place at large separations between reactants, and treat $BaOCH_3^+$ as a point charge. Using treatment developed in other work [Mie73], we evaluate the potential curves for Ca (^3P_J) in states (J, $|m_J|$), using the ^3P_J quadrupole moment Q and the static polarizabilities α_{xx} and α_{zz} calculated elsewhere [MZ08]. Accounting for the spin-orbit coupling [Mie73] and using the fine structure intervals from NIST [SC85], we obtain the potential curves shown in Fig. 9.4B. The curves for $\pm m_J$ are identical, resulting in three distinct curves for J=2, two for J=1, and a single curve for J=0. The effect of the quadrupole is non-trivial, leading to barriers that reduce reaction rates for some channels or more attractive curves that increase the reaction rates for others. We assume a conservative estimated variation of 10% of the adopted values (in atomic units) of Q = 12.9, α_{xx} = 295.3, and α_{zz} = -28.37 from [MZ08] to account for the range of published values for these quantities [Der01, SCG04, MTR01].

After the curves were obtained, to compute theoretical energy-dependent reaction rates, we employed a simple Langevin capture model [Lan05, DMW58]. Fig. 9.4B shows the results for each (J, $|m_J|$) state as a function of the collision energy. An energy-dependent rate constant for each fine structure component J (Fig. 9.4C) was calculated by summing over the m_J components. Whereas at collision energies greater than ~10 K the rate constants decrease with J, this trend shifts drastically at lower temperatures and even reverses for collision energies below ~1 K.

Finally, to directly probe for the existence of a barrier on the triplet surface, we monitored the collision energy evolution of the reaction rate constant. Since the micromotion energy in an ion trap scales with the spatial radial width of the ion crystal, average collision energies

can be controlled by simply changing the size of ion crystals initially loaded into the LQT . Using this method, we probed reaction rates at average collision energies ranging from 0.1 K to 30 K and compared the results (Fig. 9.4E) to the capture theory prediction weighted by the spatially-dependent energy distribution of the ions. As seen here, the measured reaction rate constant does not have a strong collision energy dependence over these temperatures and agrees with the capture theory calculation, indicating a barrierless reaction. Here, the theoretical uncertainty band is based on a 10% range in published theoretical values for the quadrupole moments and polarizabilities used in the molecular potential calculations is also included [Der01, SCG04, MTR01].

Further, in experiments with linear ion chains, $BaOCa^+$ formation was still observed at the lowest collision energies reached of $\sim$0.005 K, confirming the absence of potential barriers to the reaction at temperatures near the ultracold regime. However, at these temperatures, the ion crystals used in the LQT are extremely small, and due to the large accumulation time needed for $BaOCH_3^+$ buildup and ToF measurement shot noise, accurate reaction rate data were experimentally inaccessible. Consequently, such temperatures were excluded from the kinetics data shown in Fig. 9.4E.

9.7 Outlook

Through precise control of entrance channels and fine-tuning of reaction energetics, from high temperature to the ultracold regime, techniques used here and elsewhere offer promising platforms for extending the tools of ultracold physics to the study of high precision quantum chemical dynamics. Therefore, they are expected to enable a next generation of chemical studies in the quantum regime, providing opportunities to look more deeply into chemical bonding and to anticipate and predict new chemical species and structures that may have exotic or useful properties.

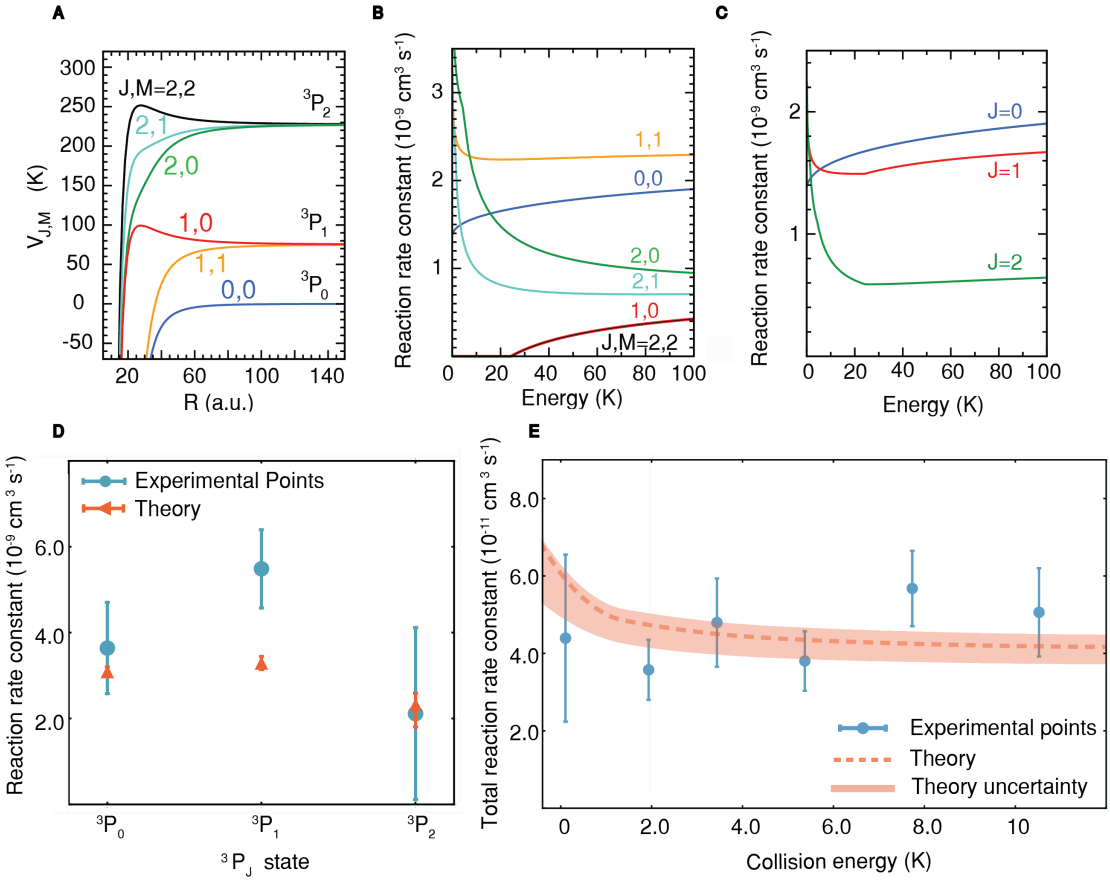

Figure 9.4: Experimental schematic of the hybrid system and ToF apparatus

(A) The molecular potential for each triplet sublevel. **(B)** The subsequent energy dependent rate constants obtained from capture theory. **(C)** The m_J averaged rate constants assuming equal population of each m_J level for each J level. **(D)** The rate constant of each individual triplet state, measured by depopulating the other triplet states through optical pumping and acquiring reaction kinetics data. Solutions of differential equations were fitted to approximately 250 kinetic data points to obtain reaction rate constants at each triplet setting, with experimental uncertainties expressed at the one-sigma level. Theoretical estimates, along with uncertainty bands associated with the polarizability and quadrupole moment values used to construct the molecular potentials in (A), are presented alongside the data. **(E)** The temperature dependence of the total reaction rate compared to theory by varying the micromotion energy of ions in the LQT and recording reaction kinetics data at each temperature, with the theoretical uncertainty denoted by the thickness of the theory band. Roughly 250 data points were collected at each collision energy, and experimental uncertainties are presented at the one-sigma level.

9.8 Corollary measurements and calculations

This section presents ancillary measurements and theoretical calculations that were performed to augment the work presented in the previous sections.

9.8.1 Exclusion of other reactive pathways

Before the ^3P_J reaction pathway for $BaOCa^+$ was identified, it was unclear which electronic state was participating in the reaction, and statistical methods were employed to exclude alternative reaction pathways involving other states populated during Ca laser cooling, i.e. the $4s^2\ ^1S_0$, 4s4p $^1P_1$, 4s5p $^1P_1$ and 3d4s $^1D_2$ states.

First, laser parameters were manipulated in order to vary each electronic state's population over a suitable range, as described earlier. Reaction rates were then extracted for the different population settings and plotted as a function of individual state population. Since the proposed reaction involves a single Ca atom, if a particular electronic state is involved in the reaction, a linear relationship between state population and production rate is expected, and consequently, a linear fit is applied to each data set (Fig. 9.5, A-E).

In order to assess how well the observed reaction rate data matched the expected linear dependency on state population, the reduced chi-squared statistic, $\chi^2_{red}=\frac{1}{n-f}\sum_i \frac{(M_i-C_i)^2}{\sigma_i^2}$, was calculated for each model, where n is the number of observations, f is the number of fit parameters, M_i is the model's prediction for the i^{th} data point, C_i is the average value for the i^{th} data point, and σ_i is the standard error for the i^{th} data point.

According to standard χ^2_{red} analysis, the model that best represents the data is the ^3P_J production pathway, yielding a χ^2_{red}=0.22 (Fig. 9.5E). The 4s5p $^1P_1$ pathway offers the next lowest χ^2_{red} value; however, $BaOCa^+$ production is still observed when the 672 nm repump is shuttered and the 4s5p $^1P_1$ state is unpopulated (Fig. 9.3C), thus invalidating this pathway as the sole means of $BaOCa^+$ production.

Further, the vertical intercept of the ^3P_J fit is consistent with zero, which suggests that there are no other competing reaction entrance channels. For example, if non-adiabatic

coupling from excited singlet surfaces to other electronic states were occurring and resulting in reaction, and the populations of such sates were not correlated with triplet population, we should observe a background reaction rate that would exist even with a 0% triplet population, which is what the y-intercept of the fit of Fig. 9.5E signifies. While we cannot rule out the possibility of such effects occurring, we can experimentally restrict the total reaction rate constant of such events to be $\lesssim 10^{-11}$ cm^3/s, which is derived from the 2σ error in the y-intercept fit and is an order of magnitude smaller than the rates typically accessed in this work.

However, since the population of certain electronic states are coupled to others through spontaneous emission and resonant laser fields, the population of certain singlet channels, such as the 3d4s ^{1}D$_2$ state, are correlated with the population of the triplet state. While no other state beside the ^{3}P$_J$ levels demonstrated a linear correlation with BaOCa$^+$ production, this does not necessarily imply no other states are reactive. For example, if an excited singlet state were indeed reactive through non-adiabatic processes, it is possible that enhanced BaOCa$^+$ production due to increasing population in this state could be masked by a corresponding reduction in the population of the triplet state. While we cannot rule out such multi-component reaction pathways from taking place, the above χ^2_{red} analysis clearly identifies the ^{3}P$_J$ surface as the dominant reaction entrance channel. Moreover, the results of magnetic trap experiment, where the reaction rate between a sample of pure triplet atoms and BaOCH$_3^+$ ions was measured and shown to be consistent with all other observed reaction rates in the study, further suggests that BaOCa$^+$ formation initiates predominantly along the ^{3}P$_J$ Ca potential surface, with all other entrance channels likely negligible on experimental timescales.

9.9 Photofragmentation detection

Although ToF spectra indicated the product of the observed reaction possessed a mass-to-charge ratio consistent with that of BaOCa$^+$, photofragmentation analysis was conducted to further verify the identity of the species. Photodissociation of BaOCa$^+$ was first measured

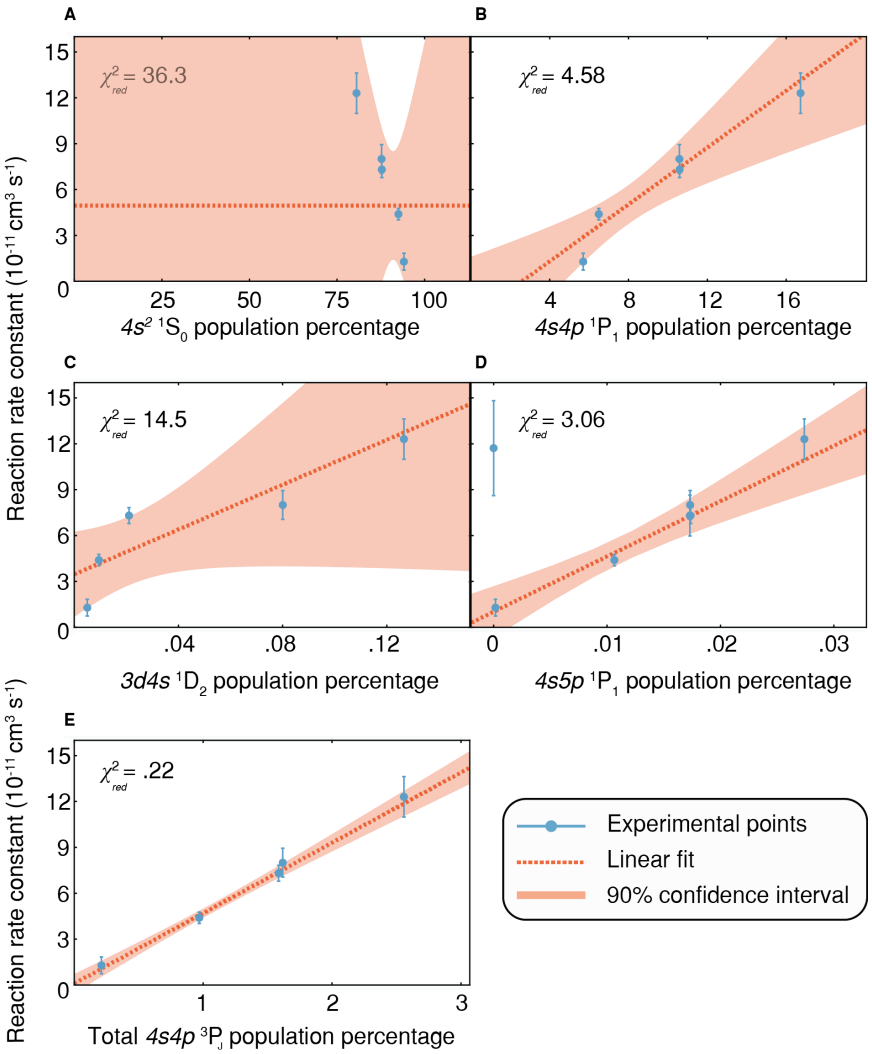

Figure 9.5: BaOCa$^+$ production rate dependency on Ca electronic state populations

Experimentally observed reaction rates are plotted against the (A) 4s^2 ^{1}S$_0$, (B) 4s4p ^{1}P$_1$, (C) 3d4s ^{1}D$_2$, (D) 4s5p ^{1}P$_1$, (E) 4s4p ^{3}P$_J$ electronic state populations, which are the only states populated significantly during the Ca laser cooling process. For each plot, experimental points, along with their associated one-sigma uncertainties, are presented alongside linear fits (dashed) and their 90% confidence interval bands. Further, the χ^2_{red} statistic for each fit is also displayed in the upper left hand corner of the plot. As can be seen from the χ^2_{red} statistics, the ^{3}P$_J$ model best represents the data, supporting the theoretical and experimental findings detailed throughout this report.

as a function of laser intensity at both ∼493 nm and ∼422 nm wavelengths (Fig. 9.6, A and B), which were conveniently accessible with our titanium-sapphire laser system. During data acquisition, $BaOCH_3^+$ ions were first immersed in the MOT for a fixed amount of time to initialize a sample of $BaOCa^+$. Subsequently, photodissociating lasers were introduced into the LQT for varying amounts of time before ejecting the ion trap species into the ToF. A simple exponential decay model $N(t) = N_0 e^{-\Gamma_{PD} t}$, where N is the amount of $BaOCa^+$ present in the LQT, t is the amount of dissociation time, and Γ_{PD} is the decay rate of $BaOCa^+$ due to photodissociation, was fit to the data, allowing a dissociation rate to be extracted. This process was repeated over a wide range of laser intensities at each laser wavelength.

While *ab initio* calculations of the molecular structure of $BaOCa^+$ indicate the energy of the various dissociation asymptotes, estimating the wavelength dependency of the photodissociation cross section is difficult due to lack of information on the excited state potential surfaces of the molecule and their Franck-Condon factors with levels in the electronic ground state potential. While neither a 493 nm photon nor a 422 nm photon possesses enough energy to drive to the lowest energy $Ca^+ + BaO$ dissociation asymptote, a two-photon process at either of these wavelengths would have enough energy to surpass the $Ca^+ + BaOCH_3$, $BaO^+ + BaOCH_3$, and the $Ba^+ + CaO$ asymptotes (Fig. 9.6C), indicating that two-photon photodissociation may be possible at these wavelengths. However, the linear dependency of the photofragmentation rate on intensity (Fig. 9.6, A and B) is suggestive of a one-photon process, perhaps indicating the first step in the two-photon process was saturated by either the ion laser cooling beams or the dissociating beam itself. Regardless of the specifics of the dissociation pathway, identification of any of the Ca^+, BaO^+, or Ba^+ photodissociation fragments would provide further evidence confirming the elemental composition of the molecule, and thus, such a search was conducted. While detection of Ba^+ fragments is precluded by the unavoidable background of Ba^+ from the initial trapped ion crystal, observation of the Ca^+ and BaO^+ dissociation products is possible, although difficult due to competing introduction of these species from other processes in the LQT. Namely, Ca^+ ion production also occurs through ionization of MOT atoms by the laser cooling beams, and BaO^+, whose isotopic

signatures may overlap with $BaOH^+$ in the mass spectra, is produced through reactions of the Ba^+ crystal with the introduced methanol vapor. In order to separate the background ions from the photofragmentation ions, we employed the well-known LQT mass filtering techniques of secular excitation introduction and stability region manipulation to selectively remove the unwanted background species.

For Ca^+ detection, during MOT immersion, the Mathieu q-parameter was modified such that Ca^+ ions were unstable in the ion trap during $BaOCa^+$ production, ensuring no MOT-produced Ca^+ ions would remain trapped. After the MOT beams were shuttered, the q-parameter was modified to allow stable trapping of Ca^+ ions, at which point the 423 nm photofragmentation laser was introduced into the LQT before the ions were ejected into the ToF. Substantial Ca^+ is observed when the photodissociating laser is present (Fig. 9.1D). When compared to a control case in which the above process is repeated while the photofragmentation laser remained shuttered, the difference in Ca^+ production, averaged across $\sim$50 data points, was significant at the 3σ level, with any background Ca^+ in the control case attributable to $BaOCa^+$ dissociation from the ion laser cooling beams.

In order to detect the BaO^+ photodissociation fragments, a mass-specific secular excitation frequency was applied during MOT immersion to purge the LQT of $BaOH^+$ molecules formed from methanol reactions with the Ba^+ crystal, preventing potential ToF spectrum overlap with BaO^+ ions produced from photodissociation. After shuttering the MOT beams, the secular excitation was removed and a 493 nm dissociation beam was introduced into the chamber before ejecting the ions into the ToF to obtain a mass spectrum (Fig. 9.1D). After averaging across $\sim$50 data points, the difference in BaO^+ production compared to the control case was found to be significant at the 3σ level. The detection of both Ca^+ and BaO^+ photodissociation fragments, along with the identification of a mass-to-charge ratio m/z consistent with 193.9 amu for the product molecule through ToF analysis, provides strong evidence that the product of the observed reaction is in fact $BaOCa^+$.

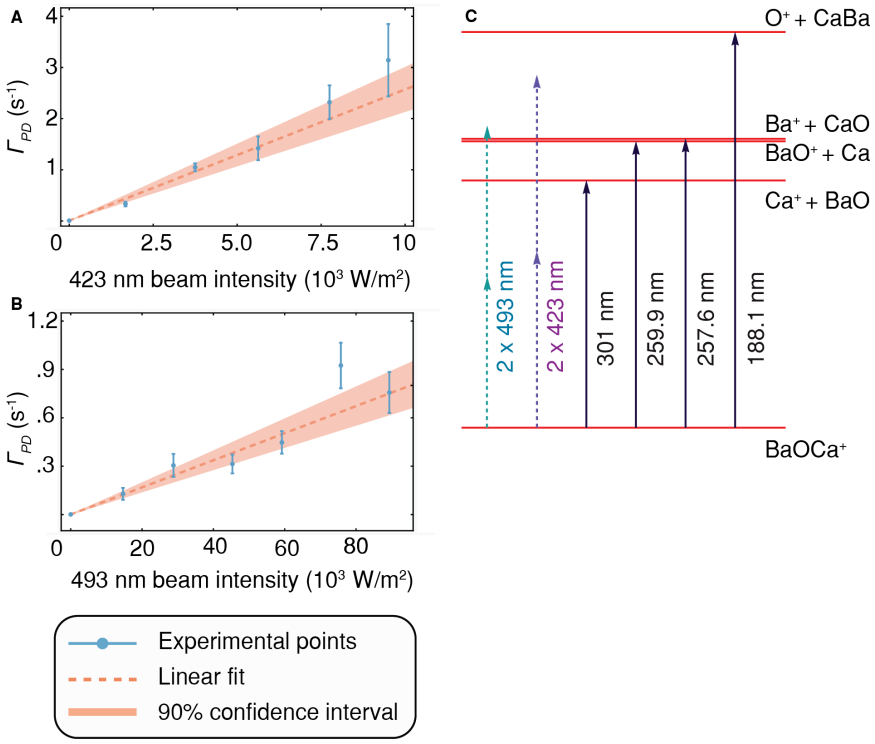

Figure 9.6: $BaOCa^+$ photofragmentation analysis

Experimentally observed photodissociation rates are presented as a function of dissociation beam intensity for both **(A)** 423 nm and **(B)** 493 nm lasers. Roughly 30 data points were acquired at each intensity setting and experimental uncertainties are expressed at the one-sigma level. **(C)** A graphical representation of the various dissociation limits of the molecule, with the asymptotic energy of each represented by arrows labeled in units of photon energy. For comparison, the energy of a two photon process at both 423 nm and 493 nm wavelengths (dashed) is also presented, with both processes possessing an energy above several dissociation limits of the molecule.

CHAPTER 10

Low temperature reactions between $BaCl^+$ and Ca^*

Recent advances have enabled studies of atom-ion chemistry at unprecedentedly low temperatures, allowing precision observation of chemical reactions and novel chemical dynamics. To date, these studies have primarily concerned reactions between atoms and atomic ions or non-polar molecular ions, often in their electronic ground state. Here, we extend this work by studying an excited atom-polar molecular ion chemical reaction ($Ca^* + BaCl^+$) at low temperature in a hybrid atom-ion trapping system. The reaction rate and product branching fractions are measured and compared to model calculations as a function of both atomic quantum state and collision energy. At the lowest collision energy we find that the chemical dynamics dramatically differ from capture theory predictions and are primarily dictated by the radiative lifetime of the atomic quantum state instead of the underlying excited-state interaction potential. This reaction blockading effect, which greatly suppresses the reactivity of short-lived excited states, provides a means for directly probing reaction range and also naturally suppresses unwanted chemical reactions in hybrid trapping experiments.

10.1 Background motivation

Over the last decade, techniques from ultracold physics have been adapted to the study of chemical systems, bringing unique capabilities including precise control of the reagent quantum states and energy [KSS16, CDK09, DBE, TSC13]. While early work focused on all-neutral chemistry, more recently there has been a shift to the study of charged-neutral reactions [HAR13, RSK11, ZW18, RZS12, SMB18], as available techniques allow probing a wider range of energy [BM18] and species, as well as trapping and study of reaction prod-

ucts [SSY16, SCR12, SGM17]. Already, these so-called hybrid systems have been used to study reactions of several atom-ion combinations [TJG17, YLC18a, HW12, ZPS10, ZPR10], showing a dependence of reactivity on molecular conformation [CDK13] and the production of novel molecules [PMS17]. Despite this work, there has yet to be a study of atom-polar molecular ion chemistry in these systems. Given that such reactions play a central role in chemistry of the interstellar medium [SZ96,Smi92,RGM10], which provides the raw materials from which stars, planets, and potentially even life developed, understanding these reactions at low temperature is a fundamental goal for chemistry and physics. Moreover, these same reactions could severely limit experiments aiming to produce quantum-state-selected polar molecular ions [CB18, SHD13, WWH16] via sympathetic cooling [RSS12, Hud16, HLC15] for quantum logic applications [HC18].

Here, we advance these fronts by using a hybrid trap to study the reaction between electronically-excited Ca atoms and $BaCl^+$ molecules. Using the capabilities of the hybrid trap, we measure the reaction rates and product branching fractions of these reactions at collision energies from 15 K down to 0.2 K (all temperatures in this work refer to collision energies in units of $J/k_B = K$, where k_B is the Boltzmann constant). At the lowest energies in our study, which are amongst the lowest ever studied in a molecular ion-atom system [MRJ15, HLC15, ADS, HS91], we find a chemical regime where the chemical dynamics are primarily dictated by the radiative lifetime of the reagent quantum state instead of the underlying excited-state interaction potential. Additionally, we provide a simple rule for calculating at what temperature this regime, where the collision time is longer than the radiative lifetime of the quantum state, is reached.

This result parallels previous work in excited-state ultracold neutral-neutral systems where reduced reaction rate constants have been observed and explained as a consequence of spontaneous emission suppressing short-range excited-state population [JM89a, GP89]. Subsequent studies also demonstrated that external optical fields could be used to modify radiative dynamics and directly control reaction outcome [WBZ99, GG98].

The work presented here extends these techniques to the rapidly developing field of cold molecular-ion chemistry. Specifically, the phenomenon observed here should be universal to

atom-ion chemical systems and, through its dependence on the reactive trajectory, provides a means to probe the range of a chemical reaction. It also greatly suppresses the reactivity of short-lived excited states. Therefore, this work implies that care must be taken when interpreting low temperature atom-ion reaction data and that certain unwanted chemical reactions in hybrid trapping experiments can be mitigated by simply going to low temperature and thereby allowing longer molecular ion coherence and interrogation times.

In the remainder of this work, we first describe the experimental system and technique for energy control and then present the observed total reaction rates and branching fractions of the Ca $^1P_1$ and $^3P_2$ states, which show very different behavior. We then describe a qualitative model for the observed effect that provides a simple means to calculate at what temperature this radiative regime is reached. Finally, we compare our experimental results to a more rigorous model of the observed effect that is integrated into a modified long-range capture theory.

10.2 Results

10.2.1 Experimental system

To tune reactant collision energy, we employ both a recently developed ion-shuttling technique [PMW18] as well as the traditional method of micromotion energy tuning through crystal sample size modulation [GCc09,HHF13]. Additionally, while not measured directly, we expect that the internal degrees of freedom of the reactant $BaCl^+$ molecules are cooled via sympathetic cooling collisions [RSS12] with the Ca MOT.

10.2.2 Observation of reaction blockading

The reaction is energetically forbidden in the ground state; however, by using previously established methods involving optical pumping and magnetic trapping, the reaction is shown to proceed via the Ca $^1P_1$ and Ca $^3P_2$ electronic states (Fig. 10.2).

After identifying the reaction pathways of the system, the dependence of reaction rate

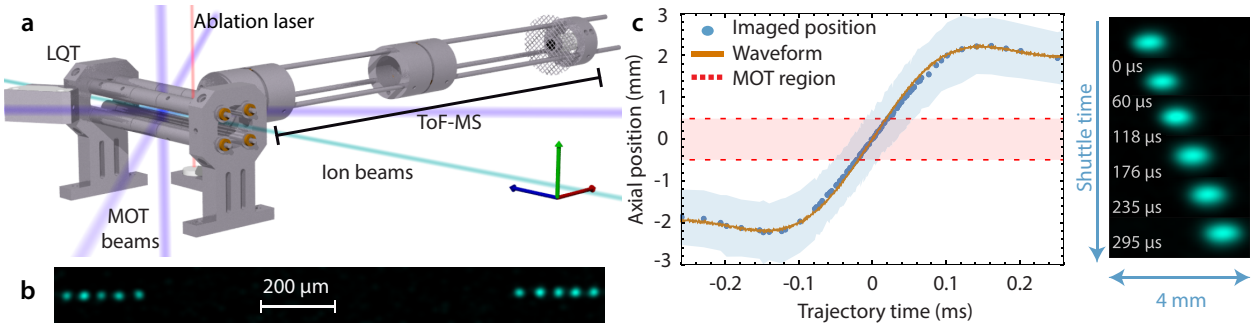

Figure 10.1: Experimental apparatus and techniques

(a) The MOTion trap atom-hybrid trap apparatus **(b)** Image of an ion chain being shuttled over a distance of $\approx$ 1 mm at a collision energy of $\approx$ 750 mK. To reduce secular heating, the ions spend over 90% of the time at the trajectory endpoints, and thus ion fluorescence is only visible at these locations. **(c)** The trajectory of a shuttled ion sample, as determined by fluorescence images acquired by triggering on the phase of the shuttling waveform. Also presented is the location of the potential minimum of the axial potential as predicted from the endcap waveform voltages at particular instances of time. For reference, the blue shaded region represents the $1/e$ spatial density width of the three-dimensional Coulomb crystal used in the measurement. Additionally the horizontal red shaded region represents the $1/e$ spatial distance of the MOT cloud. To the right of the plot, an inset displays experimental false-color fluorescence images of the shuttled ions at various times along the shuttling trajectory.

on the collision energy was explored. Atom-ion chemical reaction cross-sections are typically estimated through a Langevin capture model [DMW58, Lan05] as $\sigma(E_{col}) = \pi b(E_{col})^2$, where the impact parameter $b(E_{col}) = (\ell+1/2)/(\mu v)$ is determined by the maximum angular momentum ℓ that allows the reaction pair to reach short-range at a given collision energy, E_{col}, where μ is the reduced mass of the system and v is the collision velocity. The energy-dependent rate constant, $k(E_{col})$, is subsequently calculated by integrating $\sigma(E_{col})$ over the relative velocity probability distribution of the reaction pair, as $k(E_{col}) = \langle\sigma(E_{col})v\rangle$. Ultimately the long-range form of the studied molecular potential determines how the chemical reaction rate scales with E_{col}. For the excited-state systems studied in this work, standard capture theory predicts a reaction rate that *increases* with *decreasing* collision energy due to the quadrupole-ion interaction.

To asses this trend in the $^3P_2$ state, a $BaCl^+$ sample was overlapped with a magnetic trap of pure triplet atoms while micromotion energy tuning was used to change the reactant collision energy from $\approx 1 - 20$ K. The measured reaction rate appears to increase at low energy as expected for an ion-quadrupole reaction, as shown in Fig. 10.3a.

Two methods, excess micromotion energy tuning through crystal size manipulation and ion shuttling, were used to measure the collision energy dependence of the Ca ($^1P_1$) + $BaCl^+$ reaction. Over their common range (4 K - 20 K), the two methods agree and reveal an essentially energy-independent reaction rate constant. However, interestingly, unlike the Ca ($^3P_2$) state, the measured rate constant *decreases* at low temperature instead of increasing as predicted by standard quadrupole-ion capture theory (Fig. 10.3a). All presented theory curves are averaged over the energy distribution of the ions before comparison with the data, and the theory error bands are determined by uncertainties in the polarizability and quadrupole moment values used to construct the molecular potentials utilized in the calculation (see Section 10.2.6e for a description of the modified capture theory presented in Fig. 10.3a).

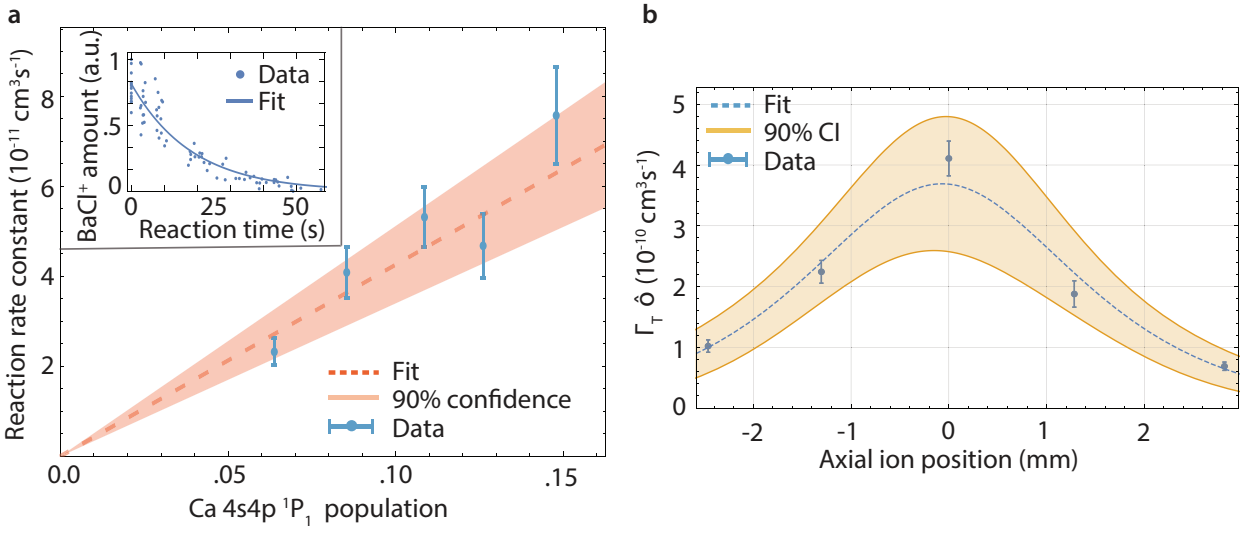

Figure 10.2: Reaction rate characterization

(a) Observed reaction rate constant dependence on Ca 4s4p ^{1}P$_1$ population. The inset displays a typical reactant decay curve used to extract the rates, with the reactant amount determined by integrating over ToF-MS spectra. **(b)** The measured Ca 4s4p ^{3}P$_2$ reaction rate constant, Γ_T, multiplied by the geometric atom-ion overlap factor, $\hat{O}$, obtained at different spatial offsets between the ion sample and the center of a magnetic trap of pure triplet atoms. The corresponding fit curve (dashed line) along with its 90% confidence interval (CI) (yellow band) are displayed as well. The functional form of the fit curve (Eqn. (6.30)) allows for approximate estimation of the magnetic trap density profile. For both plots, each data point consists of approximately 100 measurements, where error bars represent one standard error.

10.2.3 Branching fraction analysis

Given this departure from standard capture theory, we then measured the product branching fractions to gain a fuller understanding of the chemical dynamics. For experimental convenience, reactions between Ca and non-shuttled $BaCl^+$ ions were studied at an average energy of ≈ 5 K. For reactions with the Ca $^1P_1$ and Ca $^3P_2$ states, there are three energetically allowed pathways:

$$BaCl^+ + Ca \longrightarrow CaCl^+ + Ba \tag{10.1}$$

$$\longrightarrow Ba^+ + CaCl \tag{10.2}$$

$$\longrightarrow Ca^+ + BaCl \tag{10.3}$$

Products from the first two reactions are experimentally identified by the appearance of reaction products in ToF-MS spectra (see Fig. 10.3b). While the reaction products are created with $\lesssim 1$ eV of energy, the radial (axial) trap depth of the LQT is $\approx 4(0.5)$ eV, and thus, $\geq$ 95% of charged products are expected to be recaptured in the LQT, assuming isotropic scattering of ions after reaction. Products from the direct charge exchange reaction (Eqn. 10.3) cannot be inferred directly due to a background Ca^+ influx from MOT atom photoionization; thus, these products are inferred indirectly through the presence of the other two products. Additionally, Ba^+ products are distinguished via mass from the isotopically-pure $^{138}Ba^+$ coolant ions since the initial $BaCl^+$ reactant sample is present in natural abundance.

By monitoring the appearance of Ba^+ and $CaCl^+$ ions in the ToF-MS spectra, branching fractions, γ_i, defined as the number of product ions in the i^{th} exit channel formed per $BaCl^+$ loss event, are measured. For the 4s4p $^1P_1$ entrance channel, $[\gamma_{CaCl^+}, \gamma_{Ba^+}, \gamma_{Ca^+}] = [0.014(4), 0.43(6), 0.57(6)]$, while $[\gamma_{CaCl^+}, \gamma_{Ba^+}, \gamma_{Ca^+}] = [0.0001(8), 0.5(2), 0.5(2)]$ is measured for the 4s4p $^3P_2$ state. Notably, the $CaCl^+$ molecule is only definitively detected in $^1P_1$ reactions, providing a means for quantum state control of reaction products.

Also shown in Fig. 10.3c are the branching fractions predicted by a phase space theory

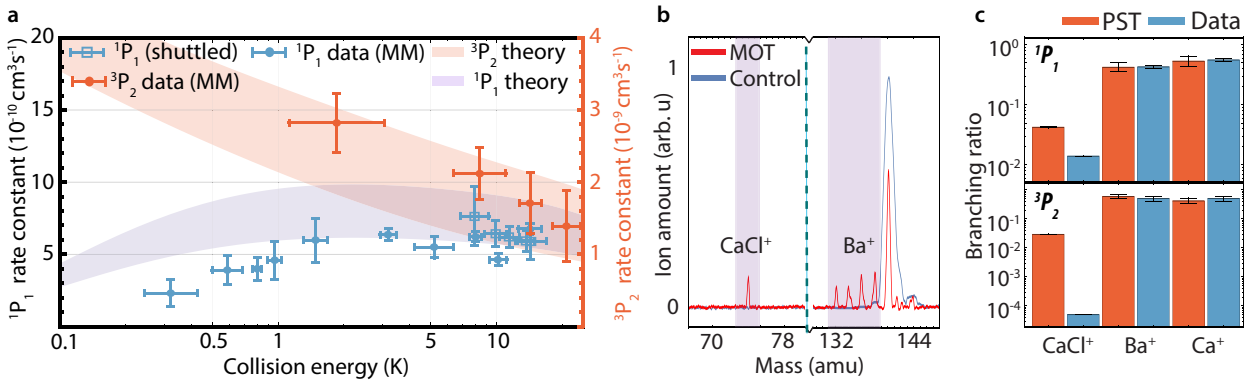

Figure 10.3: Reaction blockading in excited neutral-ion systems

(a) The experimental dependence of reaction rate constant on collision energy, as measured through both micromotion (MM) tuning (circles) and shuttling (squares) for both the singlet and triplet reaction surfaces. Note that the y-axis scale is different for the two reactions. Both data sets are in reasonable agreement with a modified capture theory incorporating reaction blockading, with the reaction rate of the short-lived Ca $^1P_1$ state significantly suppressed at low temperatures as compared to its standard capture theory prediction. For the triplet data, an absolute rate constant is measured at 10 K and all subsequent data points are normalized with respect to this value due to technical difficulties associated with frequent magnetic trap density measurements. Each data point consists of approximately 100 measurements, and standard errors are expressed at the 1σ level. **(b)** Mass spectra, obtained from the ToF-MS, of the identified product ions of the reaction. The shaded portions identify the masses corresponding to the product ions, and a control spectrum is included where the ions were ejected into the ToF-MS without MOT exposure. **(c)** A comparison of the measured branching fractions and the predictions of the statistical phase space theory (PST) for both Ca singlet (top) and triplet (bottom) reactions. Experimental standard errors are expressed at the 1σ level and, in the case of the $CaCl^+$ values, may be smaller than the plot-marker size.

calculation [PLR66]. This calculation assumes all product states that are accessible via energy and angular momentum conservation are equally probable. Thus, product branching fractions are calculated by counting the total number of states available to each reaction product (Sec. 10.2.4). The model predicts branching fractions of $[\gamma_{CaCl^+},\ \gamma_{Ba^+},\ \gamma_{Ca^+}] = [0.04(2), 0.42(17), 0.53(19)]$ for the singlet and $[\gamma_{CaCl^+}, \gamma_{Ba^+}, \gamma_{Ca^+}] = [0.018(14), 0.56(21), 0.41(23)]$ for the triplet, which are in reasonable agreement with the experimental values (Fig. 10.3c). The error bars are primarily determined by energetic uncertainties in the exothermicity of each reaction channel. The relative ordering of the branching fractions can be attributed to two main factors. First, the $CaCl^+$ exit channel has the lowest product exothermicity and therefore the fewest accessible rovibronic states. Second, the ground state of the $CaCl^+$ + Ba asymptote is composed of two singlets, whereas the other asymptotes are composed of two doublets, reducing the number of states accessible to $CaCl^+$ by approximately a factor of four.

The relatively good agreement of this model with the data suggests that the reaction proceeds via a long-lived collision complex, which facilitates the realization of ergodicity and therefore the statistical assumption of the model.

10.2.4 Phase space theory calculation of branching fractions

The phase space model used in the previous section will now be discussed in detail.

Under the assumption of strong coupling, all electronic, orbital, and angular momenta are expected to mix. Thus, while each individual angular momentum is not a conserved quantity throughout the reaction, the total angular momentum, K, along with its cylindrical axis projection, K_z, are conserved [WT72], with K being the magnitude of the vector sum

$$\mathbf{K} = \boldsymbol{\ell} + \mathbf{N} + \mathbf{L} + \mathbf{S} \tag{10.4}$$

where $\boldsymbol{\ell}$, $\mathbf{N}$, $\mathbf{L}$, and $\mathbf{S}$ are the vectors for the orbital, rotational, electronic orbital, and electronic spin angular momenta of the reaction complex. For the reactions studied in this work, $|\mathbf{L}|$ and $|\mathbf{S}|$ are ≤ 1, while generally $|\boldsymbol{\ell}|$ and $|\mathbf{N}|$ can often exceed ≈ 10, meaning the former can be neglected in the following calculation for simplicity.

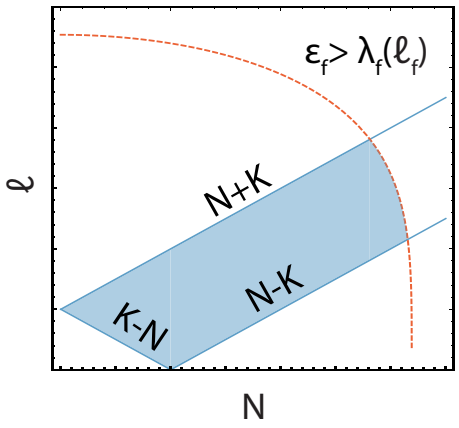

Figure 10.4: Phase space diagram for branching fraction calculation

A phase space diagram showing the range of rotational (N) and orbital (ℓ) angular momentum product states accessible at a given reactant total angular momentum (K). The shaded region of the curve denotes the final states that both obey angular momentum conservation and possess enough product kinetic energy, ϵ_f, to clear the product state centrifugal energy barrier, $\lambda_f(\ell_f)$, and dissociate from the three body reaction complex into the final product atom and diatomic molecule.

In both the reactant (i) and product (f) states, K is bounded as

$$|\ell_{i(f)} - N_{i(f)}| \leq K \leq |\ell_{i(f)} + N_{i(f)}| \tag{10.5}$$

Additionally the final product must possess enough kinetic energy to escape the angular momentum barrier of the exit channel, permitting the three-body complex to dissociate into its molecular and atomic constituents. The later restriction is satisfied by enforcing

$$\epsilon_f \geq \lambda_f(\ell) \tag{10.6}$$

where ϵ_f is the final kinetic energy of a given product state and $\lambda_f(\ell_f)$ is the height of the centrifugal barrier in each product exit channel at orbital angular momentum ℓ_f. ϵ_f can be calculated as

$$\begin{aligned} \epsilon_f(\epsilon_i, v_i, N_i, v_f, N_f, Q_{i,f}) = \\ \epsilon_i + E_{int}(v_i, N_i) - E_{int}(v_f, N_f) + Q_{i,f} \end{aligned} \tag{10.7}$$

where ϵ_i is the initial collision energy of the reaction complex, $Q_{i,f}$ is the exothermicity of

reaction for exit channel f, and

$$\begin{aligned} E_{int}(v_{i(f)}, N_{i(f)}) &= \omega_{i(f)}(v_{i(f)} + 1/2) \\ &+ 2\beta_{i(f)} N_{i(f)}(N_{i(f)} + 1) \\ &- \omega_{i(f)}\chi_{i(f)}(v_{i(f)} + 1/2)^2 \end{aligned} \tag{10.8}$$

is the internal energy in the reactant (product) state associated with the $v_{i(f)}$ and $N_{i(f)}$ vibrational and rotational level, respectively, which is characterized by the spectroscopic constants $\omega_{i(f)}$, $\beta_{i(f)}$, and $\omega_{i(f)}\chi_{i(f)}$.

Equations (10.5) and (10.6) restrict the number of ℓ_f and N_f states accessible to each exit channel (see Fig. 10.4) at a given total angular momentum, K, and exit-channel kinetic energy, ϵ_f. By counting the number of states accessible to each possible exit channel at given K and ϵ_f, one can define the probability of accessing each exit channel as

$$\begin{aligned} &P_f(K, \epsilon_f(\epsilon_i, v_i, N_i, v_f, N_f, Q_{i,f})) \\ &= \frac{\sum_{v_f, N_f} d_f \overline{n_f}(K, \epsilon_f(\epsilon_i, v_i, N_i, v_f, N_f, Q_{i,f}))}{\sum_b \sum_{v_b, N_b} d_b \overline{n_b}(K, \epsilon_b(\epsilon_i, v_i, N_i, v_b, N_b, Q_{i,b}))} \end{aligned} \tag{10.9}$$

where $\overline{n_b}(K, \epsilon_b(\epsilon_i, v_i, N_i, v_b, N_b, Q_{i,b}))$ is the the total number of states accessible for exit channel b at a given K and ϵ_b, and d_b is a degeneracy factor that accounts for the spin multiplicity of each product state. We note that $\overline{n_b}(K, \epsilon_b(\epsilon_i, v_i, N_i, v_b, N_b, Q_{i,b}))$ is proportional to the area bounded by curves presented in Fig. 10.4.

Therefore, again following Ref. [PL65], the total reaction cross-section for a given exit channel, f, given an initial reactant rotational quantum number, N_i (assuming the reactant is in the ground vibrational state), and summed over all accessible product rotational and vibrational states is given as

$$\begin{aligned} \sigma_f(N_i, \epsilon_i) &= \sum_{\ell_i=0}^{\ell_{\max}(\epsilon_i)} \frac{2(\ell_i + 1)\pi\hbar^2}{2\mu_f \epsilon_i} P_f(\ell_i) \\ &= \sum_{\ell_i=0}^{\ell_{\max}(\epsilon_i)} \frac{\pi\hbar^2}{2\mu_f \epsilon_i (2N_i + 1)} \sum_{\substack{|\ell_i - N_i| \le \\ K \le |\ell_i + N_i|}} (2K + 1) \\ &\times P_f(K, \epsilon_f(\epsilon_i, v_i, N_i, v_f, N_f, Q_{i,f})) \end{aligned} \tag{10.10}$$

where μ_f is the reduced mass of the product complex.

Lastly, to calculate the final branching fractions, we must average each cross-section across the rotational temperature of the sample as

$$\begin{aligned}\overline{\sigma_f} = \sum_{N_i} \frac{1}{Z}(2N_i+1) \\ \times e^{-2\beta_i N_i(N_i+1)/(k_B T)}\sigma_f(N_i,\epsilon_i)\end{aligned} \tag{10.11}$$

where $T \approx 2\epsilon_i/k_B$ is the effective rotational temperature of the initial reactant molecular ion and Z is the rotational partition function.

Finally, after the relevant cross-sections have been computed, the branching fraction into each exit channel, γ_f, is given by

$$\gamma_f = \frac{\overline{\sigma_f}}{\sum_f \overline{\sigma_f}} \tag{10.12}$$

Eqn. 10.12 is applied to the Ca^*+$BaCl^+$ system, and the results are compared directly to experimental branching fractions in Fig. 10.3c. In addition to the product branching fractions, Eqn. 10.12 is also applied to estimate the percentage of collisions that occur and result in excited states of [$BaCl^+$ + Ca] that ultimately radiatively decay back into the [$BaCl^+$ + Ca] ground state. This factor will be included as χ_S in Eqn. 10.18 and adjusts our rate constant calculation to account for experimentally indistinguishable events where inelastic collisions occur but no new molecular products are formed (see Section 10.2.6). Errors in the calculated branching ratios can be primarily attributed to uncertainties in the exit channel exothermicities, nonergodicity in the system, and uncertainties in the molecular constants used in the state counting process.

10.2.5 Modeling of reaction blockading

Given the evidence for a long-lived collision complex from the product branching data and the dramatic difference in reactivity as a function of temperature for quantum states with a long ($^3P_2$, $\tau \approx 118$ min) and short ($^1P_1$, $\tau \approx 4$ ns) radiative lifetime, the observations suggest that that spontaneous emission modifies the chemical dynamics. Because any reaction on an excited surface starts in the separated atom limit, the reagents must propagate inward to

short-range separation ($\sim 10\ a_0$) before a chemical reaction can occur. If the time it takes to propagate inward to form a collision complex and pass through the transition state to products is similar to the radiative lifetime of the excited reagent, it is likely that spontaneous emission will occur during the chemical event. In this limit, which is more likely at extremely low temperatures, the reactivity of excited reagents will be given by the reactivity of the surface reached through spontaneous emission, which in the present case is the endoergic ground-state surface.

To estimate the temperature at which this effect becomes important, it is necessary to calculate the dependence of the total collision time on temperature. Normally, this would be estimated by calculating the lifetime of the three-body collision complex from Rice-Ramsperger-Kassel-Marcus theory [RR27,Dag77]; however, this lifetime, which is typically a few vibrational periods, severely underestimates the total collision time at low temperature as it neglects the time it takes for the reagents to fall into the collision complex.

Following similar approaches in neutral-neutral systems [WBZ99], to account for this effect we consider the collision trajectory of the reactants as they spiral inward along their ground-state and excited-state surfaces. Since these surfaces have different long-range forms, due to their differing polarizabilities and quadrupole moments, they diverge from one another as the atom-ion separation distance decreases. This causes any lasers resonant with the system in the dissociation limit to become far-detuned in the region where chemical dynamics occur. At cold temperatures, this effect, dubbed reaction blockading, makes it unlikely that the Ca atom will remain in the excited state long enough to react before spontaneously emitting; however, at higher collision velocities, such events are less likely to occur before the atom reaches short-range.

This effect is particularly sensitive to the atomic lifetime of the reactive state, as longer excited-state lifetimes allow the reaction complex to reach short-range more easily before being interrupted by a spontaneous emission event. As a result, once reaction blockading is integrated into the capture theory predictions, we observe good agreement with the Ca $^1P_1$ data; whereas, for the long-lived triplet state, the effect of reaction blockading is negligible, as expected (Fig. 10.3a).

While a more quantitatively rigorous model of the blockading effect is presented in the next section, we first develop a simple model to estimate when radiative effects become significant. The collision energy, E_B, at which the blockading effect reduces the total reaction rate by 1/2 can be approximated by considering the amount of time, $t_B = \tau \ln(2)$, it takes to deplete the excited state population by the same amount, where τ is the excited-state lifetime.

From conservation of energy, $E_{tot} = E_{col}(r) + V_{ex}(r)$, where E_{tot} is the total energy of the system and $V_{ex}(r)$ is the excited-state potential of the system, and thus, t_B can be expressed in terms of the collision energy as

$$\tau \ln(2) = \int_{r_c}^{r_s} \left(\frac{\mu}{2[E_{tot} - V_{ex}(r)]} \right)^{1/2} dr \tag{10.13}$$

where r_s is the short-range distance at which the chemical event occurs ($\approx$ 50 a_0 in our system) and r_c is the critical internuclear separation distance where the addressing laser becomes detuned from its associated atomic transition ($\approx$ 1200 a_0 in our system). We obtain r_c by solving $V_{ex}(r_c) = V_{gs}(r_c) + \Delta E - \hbar\Gamma$ where $V_{ex}(r)$ and $V_{gs}(r)$ are the excited-state and ground-state molecular potentials of the system, ΔE is the separation-limit energetic difference between the ground and excited states, and Γ is the linewidth of the neutral cooling transition.

Further, if we approximate the velocity, and thus the kinetic energy, of the system as being constant during the latter portion of the trajectory, then $E_{tot} - V_{ex}(r) \approx E_B$ and Eqn. 10.13 can be inverted to yield the final result

$$\begin{aligned} E_B &= \frac{1}{\ln(2)^2} \frac{(r_c - r_s)^2}{\tau^2} \frac{\mu}{2} \\ &\approx \frac{1}{\ln(2)^2} \frac{r_c^2}{\tau^2} \frac{\mu}{2} \end{aligned} \tag{10.14}$$

where $r_s \ll r_c$ in the latter approximation. Applying Eqn. 10.14 to the Ca^*+$BaCl^+$ system, we calculate E_B to be 560 mK for the $^1P_1$ state and $\ll$ 1 μK for the $^3P_2$ state.

10.2.6 Modified capture theory

For quantitative comparison to the measured rate constant, we require a more rigorous model of the blockading effect than the one presented in the previous section. To this end, a semi-classical model for the reaction blockading effect was constructed that considers the effect of each participating partial wave on the total reaction cross-section by solving an Einstein rate equation model for the Ca atom in the presence of a laser field. As the atom approaches the ion along its reactive trajectory, the energy spacing between the ground and excited state changes from its separation limit value due to the differing long-range forms of the respective potentials. Thus, any laser fields that are resonant with the atoms in the separation limit become detuned as the reaction trajectory proceeds, resulting in a reduced excited-state population at short-range as compared the steady-state value.

To account for this effect and to calculate the proper population fractions at short-range, the model assigns the optical field a time-dependent laser detuning, $\Delta(t) = [V_{ex}(r(t), \ell) - V_{gs}(r(t), \ell)]/\hbar$, where $V_{ex}(r(t), \ell)$ is the excited-state molecular potential, $V_{gs}(r(t), \ell)$ is the ground-state molecular potential, $r(t)$ is the time-dependent internuclear-separation distance, and $\hbar$ is the reduced Planck's constant.

Two levels are considered in the rate equation model, the ground Ca ^{1}S$_0$ state (N$_{0,0}$) and the excited Ca ^{1}P$_1(m_J = 0)$ state (N$_{1,0}$). The system of equations is constructed as follows

$$\begin{aligned} \frac{dN_{0,0}}{dt} &= B_{10}(t)(N_{1,0} - N_{0,0}) \\ \frac{dN_{1,0}}{dt} &= A_{10}N_{1,0} + B_{10}(t)(N_{0,0} - N_{1,0}) \end{aligned} \tag{10.15}$$

where N_{J,m_J} refers to population in the (J, m_J) state and A_{10} is the Einstein-A coefficient between the two levels. $B_{10}(t)$ is the time-dependent Einstein-B coefficient between the two levels that incorporates $\Delta(t)$ and is given as

$$B_{10}(t) = \Gamma_{10}\frac{\pi^2 c^3}{\hbar\omega_{10}^3}\frac{I}{2\pi c}\frac{\Gamma_{10}}{(\delta - \Delta(t))^2 + (\Gamma_{10}/2)^2} \tag{10.16}$$

where Γ_{10} is the transition linewidth, ω_{10} is the transition energy, and δ is the separation-limit laser frequency detuning from the atomic transition.

$r(t)$ is determined by solving Newton's classical law of motion in the collision frame, $\mu\ddot{r} = \frac{d}{dr}V_{av}(r)$. To estimate the force the system experiences as it transitions between the ground and excited state potentials, we use an averaged potential, $V_{av}(r)$, that is weighted by the ground-state and excited-state populations as

$$V_{av}(r) = \begin{cases} \rho_{pp}V_{ex}(r,\ell) + (1-\rho_{pp})V_{gs}(r,\ell) & r > r_c \\ \\ V_{gs}(r,\ell) & r \leq r_c \end{cases} \tag{10.17}$$

where ρ_{pp} is the steady-state excited-state fraction of the Ca MOT [MPY17] and r_c is defined in Eqn. 10.13 ($\rho_{pp} \approx 0.2$ under standard laser-cooling conditions). In the model, the averaged potential is approximated as transitioning to a fully ground-state potential at r_c. This approximation is made since at r_c, the addressing laser field is detuned by one linewidth from resonance, meaning the atoms primarily reside in their ground state potential. An abrupt shift in potential was chosen over continuous updating of the weightings of the averaged potential for computational convenience.

The initial conditions for the equation of motion are chosen as follows: $r(0) = 3000$ nm and $\dot{r}(t) = (2E_{col}/\mu)^{1/2}$. The computation was repeated with $r(0)$ being varied across 1000 nm, confirming that choice of initial condition did not affect the trajectory result within a $< 1\%$ level. Both $V_{ex}(r(t),\ell)$ and $V_{gs}(r(t),\ell)$ contain the orbital-angular-momentum-dependent centrifugal barrier term, $\hbar^2\ell(\ell+1)/(2\mu r^2)$, where ℓ is the orbital angular momentum of the system, ensuring that each partial wave has a unique collision trajectory.

The reaction blockade factor for each partial wave, $P_\ell(E_{col}, m_J)$, can be determined by dividing the excited-state fraction predicted by the rate equation model at short-range by its long-range value, ρ_{pp}. The separation distance at which the chemical event occurs is r_s, and therefore the excited-state fraction for the $m_J = 0$ projection state at short-range is given as $N_{1,0}(t_c)$ where t_c is defined as $r(t_c) = r_c$. Consequently, $P_\ell(E_{col}, m_J) = N_{1,m_J}(t_c)/\rho_{pp}$, and

the total cross-section, including the blockading effect, can be calculated as

$$\sigma(E_{col}) \approx \frac{\pi\hbar^2}{2\mu E_{col}} \sum_{m_J} \frac{\eta_{m_J}\chi_S}{2J+1} \sum_{\ell=0}^{\ell_{\max}(E_{col},m_J)} (2\ell+1)P_\ell(E_{col},m_J) \tag{10.18}$$

where η_{m_J} is the probability that the m_J Zeeman level reacts if it reaches short-range, χ_S is the probability that the reaction does not produce an excited $BaCl^+$ molecule, and $\ell_{\max}(E_{col},m_J)$ is the maximum orbital angular momentum that the entrance system can possess at energy E_{col} while still being able to reach short-range. The collision energy of the system sets the initial velocity of the collision complex and has a significant effect on how likely the Ca atom is to reach short-range before spontaneously decaying. We note that exclusion of dark states, such as the Ca 3d4s $^1D_2$ state, in the model is warranted since over the collision energy range studied, the atom-ion complex accelerates to short-range in < 10 atomic lifetimes, and the branching fraction into dark levels from the excited Ca singlet state is $1:10^5$.

The sum over all ℓ and m_J states in Eqn. 10.18 is carried out for both the triplet and singlet manifold, with the results plotted alongside the data in Fig. 10.3a. We also note for all molecular potentials with repulsive long-range forms, such as the $(J,m_J)=(1,\pm1)$ projection states, the reactants repel one another and thus do not reach short-range, resulting in $P_\ell(E_{col},\pm1)=0$. Lastly, for further explanation of the η_{m_J} factors in the above equation as well as a more thorough discussion of cases where $P_\ell(E_{col},m_J)=0$, refer to the proceeding section.

10.2.7 Long range curve and short range potentials

The long-range potentials, assuming the ion to be a positive point charge, are dominated by the ion-dipole polarizability and ion-quadrupole terms. As depicted in Fig. 10.5a,e, the effect of the quadrupole moment on the long-range curves is non-trivial, leading to barriers that reduce reaction rates for some channels or more attractive curves that increase the reaction rates for others.

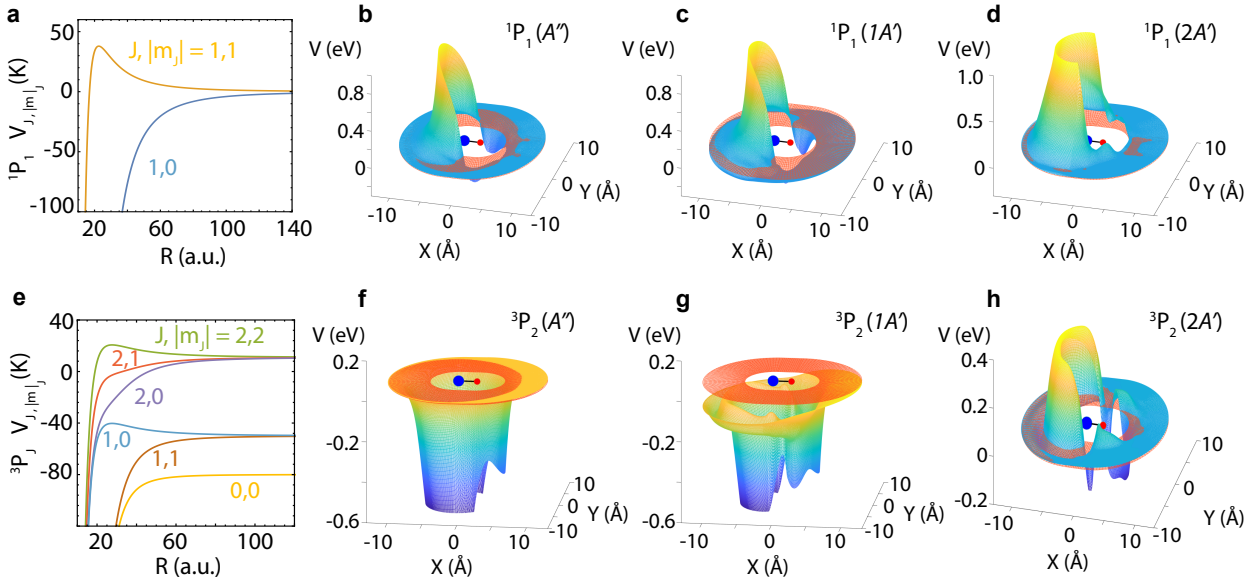

Figure 10.5: Potential energy curves and surfaces.

(a) Potential energy curves for each (J,$|m_J|$) level expressed as a function of internuclear separation coordinates for $BaCl^+$ + Ca ($^1P_1$), where the molecular ion is considered as a point charge placed at the origin (Ba^+ in blue, Cl in red) . **(b-d)** Potential energy surfaces corresponding to **(b)** the A$''$ symmetry and (**c** and **d**) the two A' symmetries for the $BaCl^+$ + Ca ($^1P_1$) complex. The x and y axes are in Å and the z axis in eV. The orange plane is the asymptotic value 3.08 eV above the global ground state of $BaCl^+$ + Ca, computed with the same level of theory at R = 50 Å. Short-range energetic barriers along the A'' (b) and $2A'$ (d) surfaces prevent the reactants in these surfaces from reaching the reaction region at short-range, resulting in a reduction of the overall Ca $^1P_1$ reaction rate by a factor of 1/3 (see Eqn. 10.18). **(e-h)** Similarly for the $BaCl^+$ + Ca($^3P_2$) complex, potential energy curves **(e)** and surfaces are displayed corresponding to the A'' (**f**) and the two A' symmetries (**g** and **h**), with axes consistent with those of the singlet. The orange plane is the asymptotic value 1.88 eV above the global ground state of $BaCl^+$ + Ca (singlet) computed with the same level of theory at R = 30 Å. Unlike the Ca $^1P_1$ surfaces, no short-range energetic barriers prevent reaching the reaction region for the triplet surfaces and thus there is no additional reduction in triplet reaction rate.

Consequently, the long-range curves have a strong effect on the modified capture theory presented in Section 10.2.6. The theoretical cross-sections are dependent on the factor $P_\ell(E_{col}, m_J)$ (see Eqn. 10.18), which is only non-zero if the long-range potential for a particular m_J projection-state is attractive. Therefore, if a J manifold has repulsive m_J projection states, its average cross-section, and also its reaction rate, will be reduced accordingly.

The long-range curves plotted in Fig. 10.5a,e can be used to determine these reduction factors for both the singlet and triplet manifolds. Let $\sigma^{S/T}_{J,|m_J|}(E)$ correspond to the energy-dependent cross-section for the $(J, |m_J|)$ projection state within either the singlet (S) or triplet (T) manifold. For the singlet manifold corresponding to $BaCl^+ + Ca\ (^1P_1)$, we find that both $m_J = \pm 1$ projection states corresponding to the $(J, |m_J|) = (1, 1)$ curve are repulsive (Fig. 10.5a). Therefore, at low energy, both $P_\ell(E_{col}, |m_J|)$ and $\sigma^S_{J,|m_J|}(E_{col})$ are approximately zero for these states. The total cross-section for the singlet manifold is given by the sum over all projection states, as described in Eqn. 10.18, leading to a total singlet cross-section of

$$\begin{aligned}\sigma^S(E_{col}) &= \sum_{m_J} \sigma^S_{J,|m_J|}(E_{col}) \\ &= \frac{2}{3}\sigma^S_{1,1}(E_{col}) + \frac{1}{3}\sigma^S_{1,0}(E_{col}) \\ &\approx \frac{1}{3}\sigma^S_{1,0}(E_{col})\end{aligned} \tag{10.19}$$

Similarly, in the triplet case, since only the $J = 2$ of Ca (^3P_J) was excited when reaction rate data was experimentally acquired, we find that

$$\begin{aligned}\sigma^T(E_{col}) &= \sum_{m_J} \sigma^T_{J,|m_J|}(E_{col}) \\ &= \frac{2}{5}\sigma^T_{2,2}(E_{col}) + \frac{2}{5}\sigma^T_{2,1}(E_{col}) + \frac{1}{5}\sigma^T_{2,0}(E_{col}) \\ &\approx \frac{2}{5}\sigma^T_{2,1}(E_{col}) + \frac{1}{5}\sigma^T_{2,0}(E_{col})\end{aligned} \tag{10.20}$$

again due to the energetic barrier for $(J, |m_J|)$=(2,2) projection states (Fig. 10.5e). Note that for all cases studied in this work, the potentials for both $(J, \pm m_J)$ are degenerate.

For a complete reaction rate calculation, the results from the long-range potential energy surfaces (PESs) must be matched the shorter-range PESs; consequently, electronic structure

calculations are performed to calculate the latter. The reaction surface for each excited-state reagent is computed using coupled cluster theory including single and double excitations (CCSD). For the electronically excited states that correlate to Ca* + $BaCl^+$, with Ca (4s4p $^1P_1$) and Ca (4s4p $^3P_2$), reaction surfaces are computed using equation-of-motion coupled cluster theory including single and double excitations (EOM-CCSD). The reaction surface calculations are performed on a grid of 133 points at various angles and distances of approach using the triple-zeta correlation consistent basis sets (cc-pwCVTZ-PP on calcium and barium and cc-pVTZ on chlorine). The core electrons in calcium and barium are replaced by effective core potentials. The electronic structure calculations are performed using the Gaussian 09 [FTS09] and Molpro 2012 [WKK12a] program packages.

The resulting potential surfaces for separation between $BaCl^+$ and Ca ranging from 4 and 10 are shown in Fig. 10.5 for the three excited singlet and triplet symmetries, $1A'$, $2A'$, and A''. The orange mesh in each panel indicates the asymptotic energy of $BaCl^+$ + Ca – 3.08 eV for the singlet and 1.88 eV for the triplet, neglecting spin-orbit couplings. The potential energy surfaces (PESs) for the three excited singlet and triplet symmetries, $1A'$, $2A'$ and A'', are produced by interpolating the 133 points computed on a grid ranging from 4 to 10 and angles between 0 and 180° (i.e. from Ca approaching $BaCl^+$ from Cl to Ca approaching $BaCl^+$ from Ba, and angles between these two linear approaches corresponding to 0 and 180°, respectively). The dark plane in each panel indicates the asymptotic energy of $BaCl^+$ + Ca*, 3.08 eV for singlet and 1.88 eV for triplet.

For the singlet case, each of the three long-range curves obtained by considering $BaCl^+$ as a point charge will be mapped roughly equally onto the three shorter-range PESs, as the $BaCl^+$ molecular axis is randomly oriented along the x, y, or z axis in the laboratory frame defining the m_J long-range projections. We account for this by assigning a probability of 1/3 to each of the (J, m_J) curves to correspond to the $1A'$, A'', or $2A'$ PES at shorter-range, and write the total probability of reaching the short-range reaction region, η_S, as

$$\eta_S = \frac{1}{3}\eta_{1A'} + \frac{1}{3}\eta_{A''} + \frac{1}{3}\eta_{2A'} \,, \tag{10.21}$$

where η_S is the probability of reaching the short-range reaction region for the singlet PES.

As shown in Fig. 10.5, there is a barrier preventing Ca* to reach that region for both PES corresponding to A'' and $2A'$, while no such barrier exists for $1A'$, i.e. $\eta_{A''} = \eta_{2A'} = 0$ and $\eta_{1A'} = 1$, leading to $\eta_S = 1/3$.

In the case of the triplet manifold, all three short-range PESs corresponding to $1A'$, A'' and $2A'$ allow Ca* to reach the reaction region, *i.e.* $\eta_{1A'} = P_{A''} = \eta_{2A'} = 1$. In this case, any long-range curve allowing Ca* to reach short-range will also permit the system to evolve in the reaction region, resulting in

$$\eta_T = 1 \tag{10.22}$$

where η_T is the probability of reaching the short-range reaction region for the triplet PES.

Finally, for the present system, there are many inelastic channels that lead to a loss of the initial reagent population, but result in excited states of [$BaCl^+$ + Ca] that ultimately radiatively decay back into the [$BaCl^+$ + Ca] ground state, making such reactions indistinguishable from non-reaction events. To estimate the probability of such events, we apply the phase space theory model described earlier (Sec. 10.2.4) to the exit channel product [$BaCl^+$ + Ca]. After including all energetically accessible excited states, we obtain χ_S = 0.76(13) and 0.72(17) for the singlet and triplet channels, respectively, with the errors again determined by uncertainties in exit channel exothermicities (Section 10.2.4).

The results of this modified long-range capture model, after thermal averaging, are shown in Fig. 10.3a and are in reasonable agreement with the data. Our model, while capturing the key features of the blockading effect, does not consider non-adiabatic processes that could also play a role in the system. For example, relaxation of the excited-state complex during the collision through internal conversion processes could lead to ground-state reactions and thus a global increase in reaction rate at all studied collision energies. Additionally, the radiative lifetime of the collision complex may change as the system transitions to short-range; however, in our model, we assume this lifetime to be constant, fixed by its value in the separated-atom limit.

10.3 Discussion

The observed reaction blockading is expected to be a general effect in low temperature ion-neutral chemistry, as the monopole field of the ion significantly alters the electronic structure of the neutral at relatively long-range. While the modified capture theory developed here can quantitatively treat the suppression effect, the simple expression presented in Eqn. 10.14 can be used to estimate if reaction blockading will be important for a given system. For example, in the ($Rb + N_2^+$) [HW12] and ($Rb + Ba^+$) [HAR13] systems studied by the Basel group, Eqn. 10.14 predicts that reaction blockading is important at $E \lesssim 10$ mK, significantly below the temperatures of their studies.

In addition to the role reaction blockading may play in the interpretation of low-temperature excited-state reactions, it has an important consequence for the field of quantum-state-selected molecular ions. The reactions studied here represent the dominant loss mechanism for preparing cold molecular ions with laser-cooled neutral atoms [Hud16], and the described suppression effect may be critical for enhancing sample overlap times in next-generation hybrid trapping experiments [SHS10, HC18].

In summary, we have presented an investigation of polar molecular ion-neutral chemistry at cold temperature. A recently developed ion-shuttling technique, along with micromotion-energy tuning, was employed to measure the dependence of the reaction rate on collision energy. Branching fractions for the reaction were measured and advanced electronic structure calculations, complemented by a long-range capture theory analysis, were performed to understand the collision dynamics of the system, revealing a strong dependence of the reaction on approach angle of the incoming Ca atom. Further, we have demonstrated that spontaneous emission during the collision strongly affects the reaction rate of the system, resulting in a reaction blockading phenomenon. This effect is incorporated into a modified-capture theory model and compared to the experimental data, demonstrating reasonable agreement. Further, a rule of thumb is developed to estimate at what temperature the reaction blockading effect becomes important for a given chemical system. This work builds on previous studies exploring radiative effects in neutral-neutral reactions [WBZ99,GG98,GP89]

and represents an important step towards understanding quantum chemical dynamics in hybrid systems and well as controlling such dynamics with optical and electromagnetic fields.

This work was supported by National Science Foundation (PHY-1205311, PHY-1806653, and DGE-1650604) and Army Research Office (W911NF-15-1-0121, W911NF-14-1-0378, and W911NF-13-1-0213) grants.

CHAPTER 11

Optical control of radiatively suppressed charge exchange collisions

The reaction blockading effect detailed in the previous chapter may have a profound impact on future atom-ion trapping experiments. This current chapter describes an experiment where this effect was studied in greater detail and even controlled optically, providing another tool for engineering excited state atom-ion chemistry.

Using a recently developed method for precisely controlling collision energy, we observe a dramatic suppression of inelastic collisions between an atom and ion (Ca + Yb^+) at low collision energy. This suppression, as detailed previously in Ch. 10, is expected to be a universal phenomenon and arises when the spontaneous emission lifetime of the excited state is comparable to or shorter than the collision complex lifetime. We develop a technique to remove this suppression and engineer excited-state interactions. By dressing the system with a strong catalyst laser, a significant fraction of the collision complexes can be excited at a specified atom-ion separation. This technique allows excited-state collisions to be studied, even at ultracold temperature, and provides a general method for engineering ultracold excited-state interactions.

11.1 Background motivation

In the last quarter century, the development of techniques for producing ultracold matter led to the ability to observe few and even single partial wave collision events, enabling the observation of quantum threshold behavior and unitarity limited processes [TKJ04, ONW10, NOW10]. It also revealed the impact chemical binding forces, quantum statistics, internal

structure, and dimensionality have on collisions, as well as provided the potential for control of chemical reactions [DBB99, JTL06, LWS08, HTS06, RZS12, YLC18b, CXY19].

The overwhelming majority of these studies were performed with collision partners in their ground electronic state. This is at least partially due to the fact that interactions at ultracold temperatures tend to naturally suppress electronically excited collisions, as pointed out in [JM89b] and demonstrated in [WSD95, PMS18]. This suppression arises as the long-range interactions between collision partners tend to shift any laser that would electronically excite one of the collision partners out of resonance at very long range. This effect, known as reaction blockading [PMS18], is especially strong in systems with long-range interactions such as atom-ion or molecule-molecule pairs.

Collisions involving electronically excited atoms and molecules play an important role in processes such as combustion [SSF08], explosives, atmospheric chemistry [Wie82], stellar evolution [MBH06], interactions in the interstellar medium [AGC10], and the formation of new molecules [PMS17], yet many studies of these reactions have been limited to high temperature, where quantum effects are often obscured. Here, we demonstrate a general technique to enable the study of such collisions at ultracold temperatures in a prototypical atom-ion system. Building from work on hyperfine-changing collisions in laser-cooled systems [SWM89, WSD95, SGT95], we apply a strong laser field that dresses the system and promotes the molecular collision complex to a specified excited state at a specified range. In this way, we engineer the electronic excitation of collision partners at short range and extract the excited channel rate constants. Additionally, by controlling the range at which this laser addresses the reactants, this technique is sensitive to the features of molecular potentials, enabling a new class of experiments to probe molecular potentials at controlled atom-ion separations. Excitingly, the technique appears to be completely general and can be applied at higher temperatures.

In what follows, we use a recently developed method [PMW18] for precisely controlling collision energy to study the charge-exchange collision between $\mathrm{Ca}(4s4p\ {}^1\mathrm{P}_1) + \mathrm{Yb}^+(6s\ {}^2\mathrm{S}_{1/2})$ as a function of collision energy from 0.05 K to 0.65 K. From this data, we observe reaction blockading of the charge-exchange rate and measure the dependence of this suppression on

collision energy. Finally, we introduce a strong laser to dress the system and observe an increased charge-exchange rate for the Ca(4s4p ^{1}P$_1$) + Yb$^+$(6s ^{2}S$_{1/2}$) channel, effectively eliminating the suppression. A quantum coupled-channels calculation based on ground- and excited-state diabatic potentials, their couplings, and the infinite-order sudden approximation is presented and shows good agreement with the data. The technique is qualitatively explained using a simple semi-classical model based on dressed molecular potentials and a Landau-Zener type transition.

11.2 Experimental technique

Using this shuttling method, we measure the charge-exchange rate of Ca(4s4p ^{1}P$_1$) + Yb$^+$(6s ^{2}S$_{1/2}$) as a function of collision energy and observe reaction blockading of the rate, shown in Fig. 11.1(d). By extinguishing the 369 nm Yb$^+$ cooling laser when the Yb$^+$ ions are shuttled through the Ca MOT, the ions are prepared in the ground 6s ^{2}S$_{1/2}$ state. Specifically, for an ion chain with 50 mK collision energy (defined as $\langle E_{col}\rangle/k_B$, where $\langle E_{col}\rangle$ is the average kinetic energy in the center of mass frame and k_B is the Boltzmann constant), we measure a rate constant of $k_p = (4.6 \pm 0.6) \times 10^{-10}$ cm^3/s, compared to the no-suppression theoretical prediction of $k_p = 23 \times 10^{-10}$ cm^3/s, an observed suppression factor of ~ 5.

This reaction blockading can be understood by considering the long-range atom-ion interaction [JM89b, PMS18]. At long range the atom and ion interact primarily through the charge-induced dipole and charge-quadrupole potentials of the forms $-\frac{\alpha}{2}R^{-4}$ and $-\frac{Q}{2}(3\cos^2(\theta)-1)R^{-3}$, respectively, where R is the atom-ion separation, α is the neutral atom polarizability, Q is the neutral atom quadrupole moment, and θ is the angle between the quadrupole moment and the internuclear axis. Thus, a laser resonant with two atomic states at long range, which have different polarizabilities and quadrupole moments, is no longer resonant when the atom and ion are in close proximity. For the Ca ^{1}P$_1 \leftarrow {}^1$S$_0$ transition with linewidth Γ and a laser detuning $\delta = -\Gamma = 2\pi\times(-34.6$ MHz), the laser becomes resonant at $R \approx 1300$ a_0 and becomes detuned by 10Γ at ~ 600 a_0. Therefore, for a charge-exchange event to occur, the atom-ion pair must propagate inward without the Ca atom decaying from this

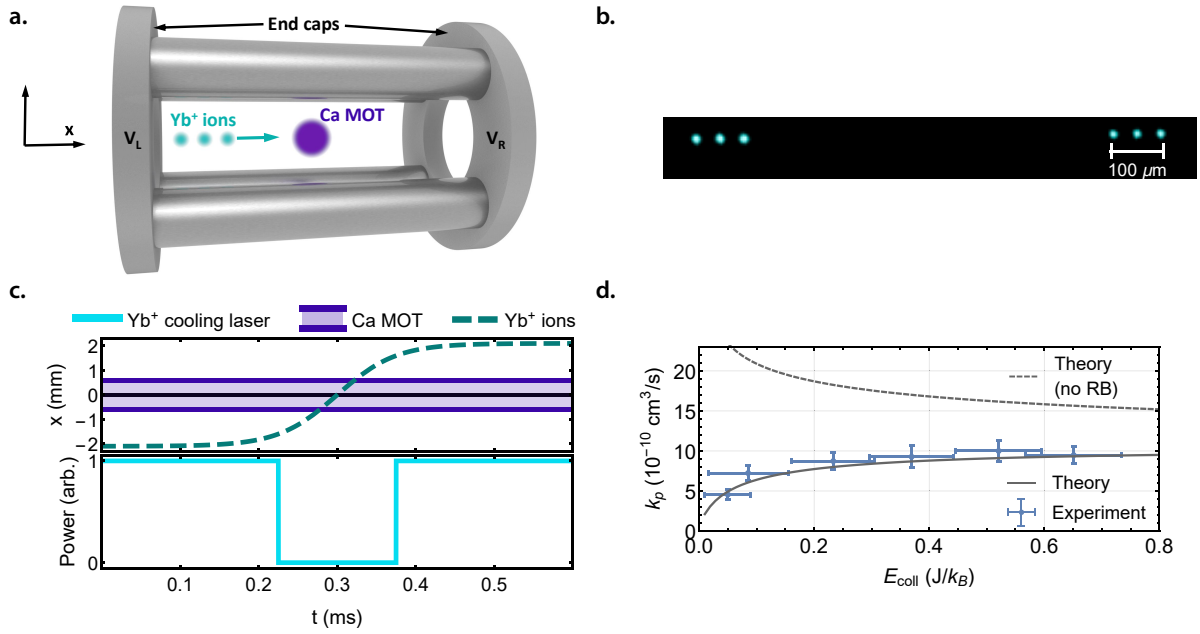

Figure 11.1: Shuttling in the hybrid atom-ion MOTion trap. **(a)** Schematic of the MOTion trap. **(b)** False-color fluorescence image of 3 shuttled Yb^+ ions. As the exposure time is greater than the shuttling period, fluorescence from the 3 ions is concentrated at the positions of the two end points, where the ions spend the most time. **(c)** Experimental sequence illustrating the shuttling technique. As the Yb^+ ions are shuttled through the Ca MOT, the 369 nm Yb^+ cooling beams are extinguished to prepare the ions in the 6s $^2S_{1/2}$ state. **(d)** Measured charge-exchange rate coefficient (with standard errors) for $Ca(^1P_1) + Yb^+(^2S_{1/2})$ as a function of collision energy using the shuttling technique. Also shown are rate coefficients from coupled-channels calculations, one with (solid line) and one without (dashed line) the effect of reaction blockading (RB).

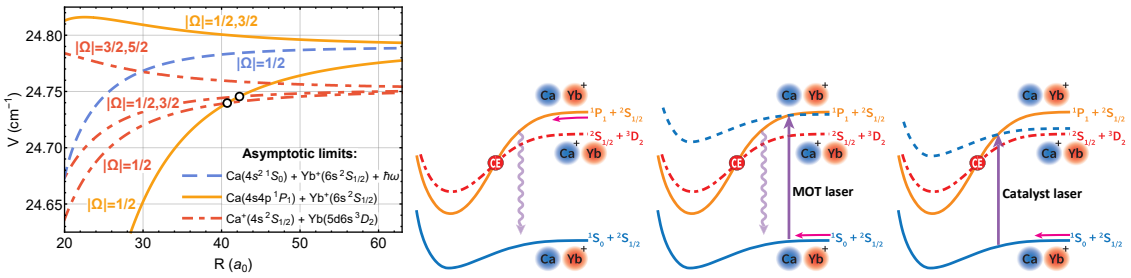

Figure 11.2: Long-range diabatic potential energy curves. **(a)** Relevant long-range molecular potentials. The two crossings between potentials relevant for charge exchange are indicated with black circular markers. The potential energy zero is located at the $Ca(4s^2\ ^1S_0) + Yb^+(6s\ ^2S_{1/2})$ dissociation limit. **(b)** The first pathway corresponds to a collision between an excited $4s4p\ ^1P_1$ Ca atom with a ground-state $6s\ ^2S_{1/2}$ Yb^+ ion. The charge-exchange (CE) crossing is shown by a red circle. The vertical wavy line represents spontaneous emission to the ground $Ca(4s^2\ ^1S_0) + Yb^+(6s\ ^2S_{1/2})$ channel. **(c)** The second pathway corresponds to a collision between a ground-state $4s^2\ ^1S_0$ Ca atom with a $6s\ ^2S_{1/2}$ Yb^+ ion in the presence of a photon of the MOT laser. The dashed blue curve corresponds to the dressed-state potential for this entrance channel. It has an avoided crossing with the excited $Ca(4s4p\ ^1P_1) + Yb^+(6s\ ^2S_{1/2})$ potential. **(d)** In the presence of a catalyst laser, the incoming $Ca(4s^2\ ^1S_0) + Yb^+(6s\ ^2S_{1/2})$ state is coupled to the reactive $Ca(4s4p\ ^1P_1) + Yb^+(6s\ ^2S_{1/2})$ state at short range, where spontaneous emission is unlikely before reaction.

distance to distances of $\sim 40\ a_0$, where couplings to other states become significant. For collision temperatures greater than $\gtrsim 10$ K, the atom-ion pair approaches quickly enough such that the Ca $^1P_1$ state is unlikely to decay before reaching short range, affecting the rate coefficient by $\lesssim 1\%$. For a collision temperature of 1 mK, however, this effect leads to a suppression by a factor of $\sim$100.

11.3 Theoretical underpinnings

To understand this behavior, we first consider charge exchange at low temperatures with no measures taken to overcome reaction blockading. Fig. 11.2 shows the relevant $CaYb^+$ long-range diabatic potentials, labeled by the projection Ω of the total angular momentum onto the intermolecular axis, as a function of atom-ion separation R. These potentials are

the diagonal matrix elements in our diabatic electronic basis, which changes only slowly with R. Asymptotically, these basis states correspond to atomic eigenstates so that non-adiabatic coupling among the potentials are negligible. The variable R describes the separation between the center of mass of the atom and ion. Moreover, the center of mass changes in charge transfer. The couplings originating from these changes are negligibly small for our purposes, justifying our definition for R. The entrance channel to the studied charge-exchange process, Ca(4s4p $^1P_1$) + Yb$^+$(6s $^2S_{1/2}$), has both a four-fold-degenerate ($|\Omega| = 1/2, 3/2$) repulsive potential and two-fold-degenerate ($|\Omega| = 1/2$) attractive potential. Substantial non-radiative charge transfer only occurs to the Ca$^+$(4s $^2S_{1/2}$) + Yb(5d6s $^3D_2$) exit channel. The Ca$^+$(4s $^2S_{1/2}$) + Yb(5d6s $^3D_3$) channel is energetically inaccessible to this entrance channel, and the Ca$^+$(4s $^2S_{1/2}$) + Yb(5d6s $^3D_1$) channel is only crossed at short range $R \approx 25\ a_0$, where the the estimated couplings between these diabatic potentials, using the Heitler-London method [TTY98], are too large to significantly contribute to the rate coefficient. More details about the potentials, the diabatic couplings, and the calculation are given in our accompanying paper of Ref. [LMP19].

Therefore, the non-radiative charge transfer is primarily driven by coupling of the $|\Omega| = 1/2$ entrance channel diabats at their crossings with the exit channels. In the diabatic representation, this coupling arises from the molecular electrostatic interaction and therefore conserves Ω, implying that only charge transfer to the $|\Omega| = 1/2$ exit channel diabats, at crossing points $R_c = 40.7\ a_0$ and $42.3\ a_0$, is relevant. Since the electronic basis functions are very different for the two channels, the non-adiabatic coupling is localized and approximated by identical Lorentzians centered at each R_c. The half width of this Lorentzian, R_0, is chosen to match the experimentally determined charge transfer rates. In the absence of any additional means to overcome reaction blockading, the atom-ion pair can reach these crossing points and undergo a charge-exchange reaction via two pathways. The first pathway is directly on the Ca(4s4p $^1P_1$) + Yb$^+$(6s $^2S_{1/2}$) entrance channel, where we determine the population of Ca atoms in the $^1P_1$ state by solving a rate equation derived from the optical Bloch equations, which includes the distance-dependent detuning of the MOT beams [MPY17]. The second pathway describes a collision on the photon-dressed Ca(4s^2 $^1S_0$) +

$Yb^+(6s\ ^2S_{1/2})$ state, which is coupled to the $Ca(4s4p\ ^1P_1) + Yb^+(6s\ ^2S_{1/2})$ state via the MOT laser. Because the MOT laser is tuned $2\pi \times 34.6$ MHz below the asymptotic transition energy, as the atom and ion collide the laser is shifted into resonance. At this point, there is a resonant amplification of the coupling to the $Ca(4s4p\ ^1P_1) + Yb^+(6s\ ^2S_{1/2})$ state by the molecular interaction due to the large density of states near the threshold.

Using the infinite-order sudden approximation (IOSA) [Pac74, Sec75, Hun75, Kou79], a coupled-channels calculation is performed on these potentials to determine the charge transfer cross-section, $\sigma(E, \ell)$. The effect of spontaneous emission is included by classically computing the collision time on the entrance channel and determining the probability, $p(E, \ell)$, for a colliding pair to survive to R_c without spontaneously emitting. The charge transfer rate constant is then determined as

$$k = \sum_{\ell=0}^{\infty} (2\ell + 1) p(E, \ell) \sigma(E, \ell) \tag{11.1}$$

where ℓ is the average orbital angular momentum quantum number used in the IOSA and E is the collision energy. The resulting rate constant is displayed alongside the data in Fig. 11.1(d) for $R_0 = 0.39\ a_0$, with and without the inclusion of $p(E, \ell)$. A detailed description of the excited-state potentials and charge transfer can be found in [LMP19].

11.4 Optical control of reaction blockading

Given that this reaction blockading is expected to occur in all low-temperature excited-state collisions, it is desirable to develop a method to remove it. Here, we demonstrate one such means. Building on ideas developed for control of hyperfine-changing collisions [WSD95, SGT95,ZMM96], we apply a strong laser, dubbed the catalyst laser, that couples the ground-state with an excited state at short range. This allows selection of the excited-state reaction channel and may, in principle, be used to select a desired reaction product in polyatomic systems.

The operation of the technique is sketched in Fig. 11.2(d), where the $CaYb^+$ molecular potentials dressed by the photon energy of the applied laser are shown. Near the

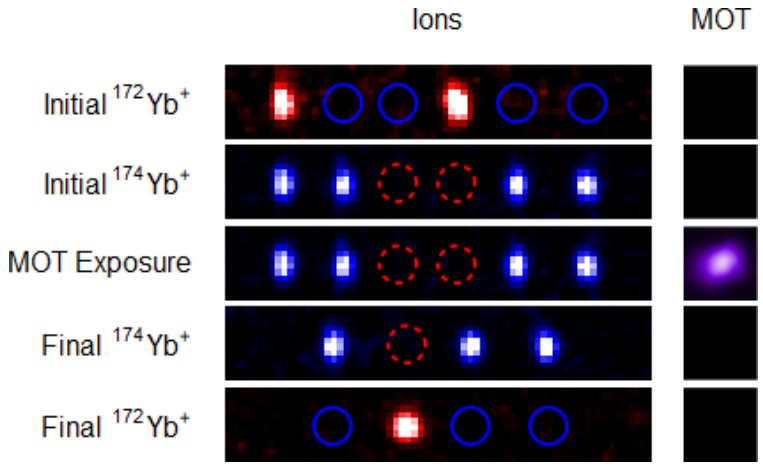

Figure 11.3: Dual-isotope technique. False-color fluorescence images of the Yb^+ ions and the Ca MOT (not to scale) illustrating the dual-isotope method used to measure the low decay rate of $^{172}Yb^+(^2S_{1/2})$. We first trap $^{172}Yb^+$ and $^{174}Yb^+$, while laser-cooling only $^{172}Yb^+$ ions (shown in red), while $^{174}Yb^+$ ions (shown as blue circles) remain dark. We then switch the 369 nm cooling laser frequency to cool $^{174}Yb^+$ ions (shown in blue), while the $^{172}Yb^+$ ions (shown as red dashed circles) remain dark. We then overlap the MOT with the laser-cooled $^{174}Yb^+$ ions as well as the ground-state $^{172}Yb^+(^2S_{1/2})$ ions for a variable amount of time. Finally, we cool and measure the final number of $^{172}Yb^+$ ions.

catalyst laser avoided crossing distance R_{CL}, the catalyst beam couples the upper and lower states, promoting the complex to the $Ca(^1P_1)$ + $Yb^+(^2S_{1/2})$ state at short range. The probability of promotion can be estimated from Landau-Zener transition theory as $P(\Omega_R) = 1 - \mathrm{Exp}\left[-\pi(\hbar\Omega_R)^2/\left(2\hbar v\frac{\partial}{\partial R}\Delta E\right)\right]$, where Ω_R is the Rabi frequency of the catalyst beam, v is the radial velocity, and ΔE is the energy difference between the diabatic potentials [Wit05]. Thus, for a scattering event with rate constant, k, this technique yields an experimentally observable rate $k_o = kP(\Omega_R)e^{-\Delta t(R_{CL})/\tau_P}$, where $\Delta t(R_{CL})$ is the time required for the atom-ion pair to propagate from R_{CL} to short range and τ_P is the lifetime of the excited state.

In order to test the catalyst laser technique at the lowest possible collision energy, where the suppression is strongest, the ions cannot be shuttled but must be arranged in a stationary linear ion chain overlapped with the MOT. Due to collisional heating ef-

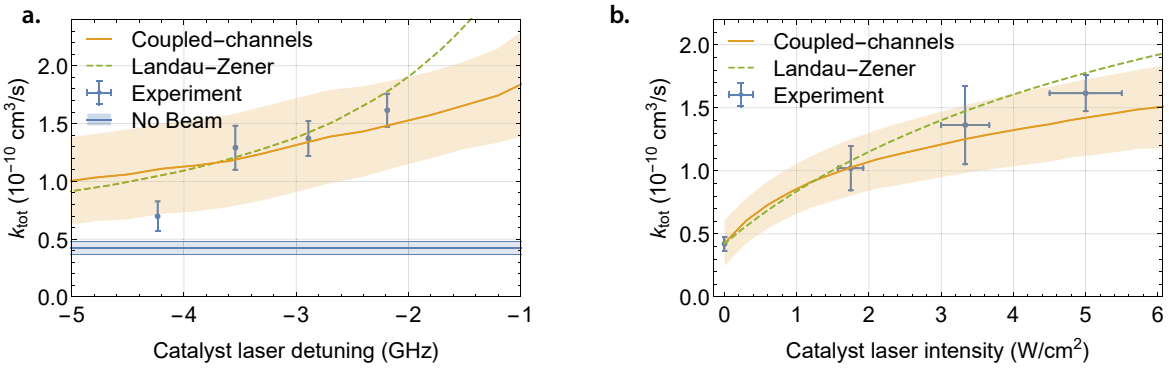

Figure 11.4: Removing suppression with addition of a catalyst laser. Total charge-exchange rate coefficient as a function of catalyst laser **(a)** frequency and **(b)** intensity. Plotted alongside experimental data are the results of a coupled-channels calculation and an estimate using the Landau-Zener approximation. For reference, the experimental rate with no catalyst beam is shown. Error bars correspond to the standard error in experimental measurements and error bands include uncertainties from the theoretical simulations and experimental parameters. Horizontal error bars in (a) are smaller than the plot marker.

fects [CSR13, CSH14, SDC16], the linear ion chain cannot be maintained during MOT exposure without active laser cooling. However, if the ions are laser cooled, the charge-exchange rates include collisions originating in the $Yb^+(^2P_{1/2})$ and $Yb^+(^2D_{3/2})$ states [RSK11]. Therefore, in order to isolate the $Ca(^1P_1) + Yb^+(^2S_{1/2})$ charge-exchange rate without the shuttling method, we develop and implement a dual-isotope technique (see Fig. 11.3) for collision rate measurement. Specifically, we simultaneously trap both $^{172}Yb^+$ and $^{174}Yb^+$ ions, while laser-cooling only the $^{174}Yb^+$ ions, which, in turn, sympathetically cool the $^{172}Yb^+$ ions. As the $^{172}Yb^+$ ions are only sympathetically cooled, they remain in the 6s $^2S_{1/2}$ state. Due to off-resonant scattering of the cooling laser for the $^{174}Yb^+$ ions, it is necessary to apply a repumping laser for the $^{172}Yb^+$ ions to prevent population from accumulating in the 5d $^2D_{3/2}$ state. Therefore, by monitoring the number of $^{172}Yb^+$ ions with time, we isolate and measure the charge exchange of $Ca(^1P_1) + Yb^+(^2S_{1/2})$.

Figs. 11.4(a) and (b) show the results of using this dual-isotope technique to monitor $Ca(^1P_1) + Yb^+(^2S_{1/2})$ charge-exchange reactions as a function of the detuning and intensity of the catalyst laser, respectively, at a collision temperature of $\sim$50 mK. For large detunings,

although the atom-ion pair is promoted at a small value of R_{CL}, increasing the likelihood of reaching short range before spontaneous emission, the large value of $\frac{\partial}{\partial R}\Delta E$ and the high velocity of the reactants leads to a lower probability of promotion to the reactive state from Landau-Zener transition theory. For the given experimental intensity of 5 W/cm^2, the catalyst beam cannot be closer to resonance than ~ -2 GHz due to adverse effects on the MOT.

11.5 Theoretical treatment of catalyst laser effect

The dependence of the measured rate on the catalyst laser intensity can be understood by the increased probability of promotion to the reactive state given by Landau-Zener transition theory for increasing Rabi frequencies Ω_R. Also shown are the results of a coupled-channels calculation. Here, the rates are calculated by allowing for, in addition to the two previously discussed pathways from the MOT laser, a catalyst-laser-enhanced charge-exchange pathway, coupling the Ca(^{1}S$_0$) + Yb$^+$(^{2}S$_{1/2}$) entrance channel to the Ca$^+$(^{2}S$_{1/2}$) + Yb(^{3}D$_2$) exit channel via the intermediate Ca(^{1}P$_1$) + Yb$^+$(^{2}S$_{1/2}$) channel. The experimental data shows good agreement with both the coupled-channels calculations and the simple Landau-Zener model, supporting this interpretation of the results.

In summary, we have investigated and engineered electronically excited-state collisions of Ca with Yb$^+$ at low collision energy. Using a method for precise control of collision energy, we find that the interaction of the atom with the ion leads to a strong shift between the ground and excited atomic states, causing any laser addressing the bare atomic transition frequency to be shifted from resonance, even at long range. Thus, at low collision energy, an atomic excited state is likely to undergo spontaneous emission before reaching short range. This leads to a strong suppression of scattering events that occur via molecular states corresponding to an atomic excited state. These features are expected to be universal at low temperature for systems with short-lived electronic excitations and long-ranged interactions. To overcome this suppression, we demonstrate a technique using a catalyst laser, which selectively excites colliding molecular complexes at short range. This technique removes the observed reaction

blockading, allowing excited-state collisions to be studied even at ultracold temperatures. As low-temperature techniques provide precise information about the underlying dynamics, this technique should find use as a general tool for studying excited-state collisions. Further, because the technique selectively excites the colliding pair to a chosen state it may be used as a means to select a desired product outcome in polyatomic chemical reactions.

Finally, the reaction blockading effect observed and controlled here is extremely important for the growing field of hybrid atom-ion trapping, where sympathetic cooling of ions with laser-cooled atoms is being pursued [RSS12, Hud16, HC18]. The existence of this reaction blockading effect means that detrimental chemical reactions from excited atomic states, which are energetically unavoidable, will not occur during the sympathetic cooling process. Thus, a large variety of molecular ions can be cooled by laser-cooled atoms without loss to unwanted chemical reactions.

We thank Wesley Campbell for helpful discussions. This work was supported in part by the National Science Foundation and the Army Research Office. Work at the Temple University is supported by the Army Research Office, the U.S. Air Force Office of Scientific Research, and the National Science Foundation.

11.6 Corollary calculations and measurements

The following section summarizes ancillary measurements and calculations that were performed to complement the above study.

11.6.1 Determination of state-specific rate constants

Experimental data is recorded by initializing an ion chain and loading the Ca MOT, which is overlapped with the Yb^+ ions. After a variable amount of exposure time, some ions undergo charge exchange (CEX), leading to a loss of ion fluorescence, shown in Fig. 11.5. Also apparent from Fig. 11.5, the presence of Ca does result in the blurring of the Yb^+ ions, due to collisional heating effects [SDC16], but does not result in a statistically significant

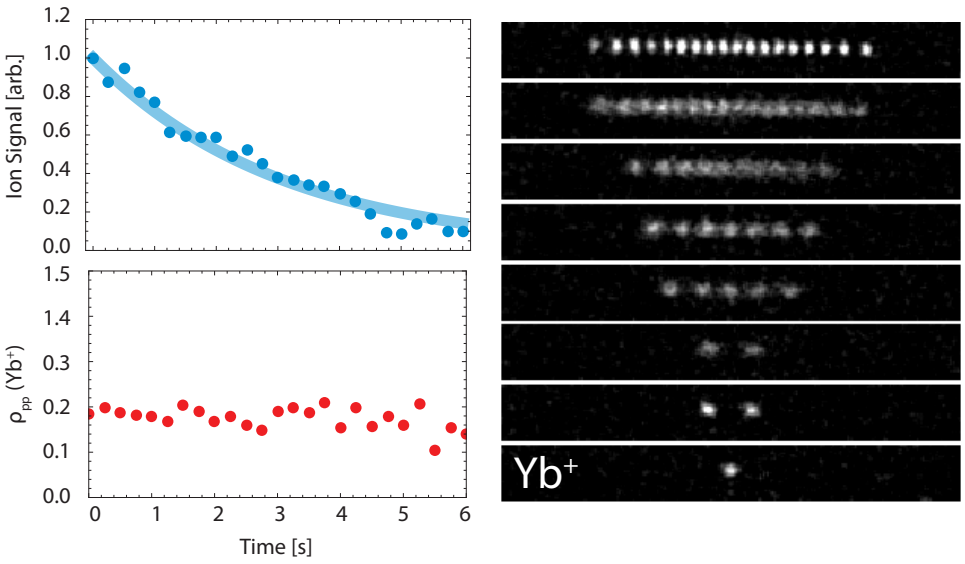

Figure 11.5: Charge Exchange Reaction Exponential decay (upper left) of $^{174}Yb^+$ fluorescence during immersion in the Ca MOT due to CEX as indicated by the CCD images (right). The excited state fraction ρ_{pp} (bottom left), as determined by fluorescence per ion, is shown to be constant.

change in the fraction of time the Yb^+ ion spends in the 6p $^2P_{1/2}$ state, ρ_{pp}. By fitting the fluorescence decay to an exponential loss, we can determine the reaction rate and calculate the rate coefficient using the density of the Ca atom cloud, measured by absorption imaging.

Repeating this measurement for a variety of Yb^+ laser cooling parameters with constant MOT parameters, the rate constant is measured with various sets of Yb^+ excitation values, $\vec{\rho}_i = \{\rho^i_{ss}, \rho^i_{pp}, \rho^i_{dd}\}$. These values are inferred from the fluorescence measurement of ρ^i_{pp} along with a rate equation model using known experimental parameters. The experimental results using this method of fluorescence detection are shown by blue data points in Fig. 11.6 as a function of $\vec{\rho}_i$. Vertical error bars represent standard errors in the reaction rate, and horizontal error bars are estimated uncertainties in parameters for the rate equation model.

The positive correlation between rate constant and the populations in the 6p $^2P_{1/2}$ and 5d $^2D_{3/2}$ states suggests that theses channels exhibit a larger charge exchange rate with Ca than the 6s $^2S_{1/2}$ state. However, because $|\vec{\rho}_i| \equiv 1$, it is necessary to perform a multidimensional fit of the experimental rate constant, k_{tot}, as a function of $^{174}Yb^+$ excited fraction to the model: $k_{tot} = \rho_{ss}k_s + \rho_{pp}k_p + \rho_{dd}k_d$. Here the k_i are the channel specific rate constants

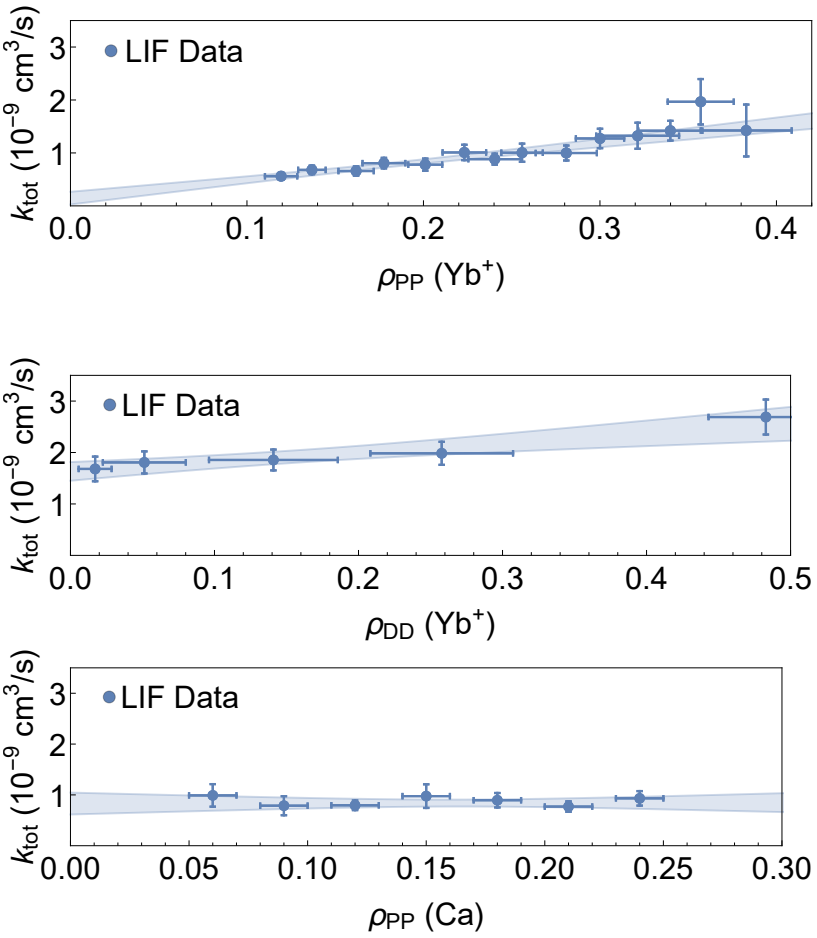

Figure 11.6: Measured Charge Exchange Rate Constants CEX rate constants as a function of excited state fractions of $^{174}Yb^+(^2P_{1/2})$ (top) and $^{174}Yb^+(^2D_{3/2})$ (middle). The CEX rate constant appears to be independent of the excited state fraction of $Ca(^1P_1)$ (bottom). This, however, *actually* reflects the experimental inability of measuring the reactivity of the $Ca(^1P_1)$ state due to its short life time and the shifting of the transition energy in close proximity to the Yb^+ ion.

for the three Yb^+ states occupied in the system. From this fit, we find the state-specific reaction rate constants given in Table 11.1. The reaction rate constant k_s cannot be resolved with this method, due to the inability of the system to maintain a resolved ion chain at low cooling power, *i.e.* low ρ^i_{pp}.

Similarly, we also measure the charge exchange rate constant as a function of the state populations, $\vec{\rho}_a = \{\rho^a_{ss}, \rho^a_{pp}, \rho^a_{dd}\}$, of the Ca atoms in MOT, while holding the ion cooling parameters constant. This is accomplished by modulating the presence of the MOT lasers with an acousto-optic switch, which effectively reduces their intensity and changes the values of $\vec{\rho}_a$. The measured rate constant along one of the populations, ρ^a_{pp} is shown in Fig. 11.6(c).

Naively, the lack of dependence on ρ^a_{pp} might be interpreted to suggest that the internal state of the Ca atom does not affect the charge exchange rate. However, as discussed in [RSK11, JM89b] the relatively short lifetime of the Ca 4p $^1P_1$-state ($\tau_p \approx 4.5$ ns) and the energy shift of the $^1P_1 \leftarrow {}^1S_0$ transition as the Yb^+ ion approaches the atom combine to create a dramatic suppression of any collisions on the excited neutral atom channel. Thus, the reactions we observe here are dominated by the reactive excited states of Yb^+ with the ground state of Ca. To observe the suppressed reactions with the Ca($^1P_1$) state, we use the dual isotope technique to isolate Yb^+ in its $^2S_{1/2}$ ground state, removing the large charge exchange rate from the excited Yb^+ states and allowing greater sensitivity to reactions from excited states of Ca.

Table 11.1: Measured state-resolved charge exchange rate coefficients for the Yb^+ + Ca system.

Yb^+ state	Ca state	k_i (cm^3/s)
6p $^2P_{1/2}$	4s^2 $^1S_0$	$3.3(3) \times 10^{-9}$
5d $^2D_{3/2}$	4s^2 $^1S_0$	$4.2(2) \times 10^{-9}$
6s $^2S_{1/2}$	4s^2 $^1S_0$	$< 3 \times 10^{-11}$
6s $^2S_{1/2}$	4s4p $^1P_1$	$7.5(1.5) \times 10^{-10}$

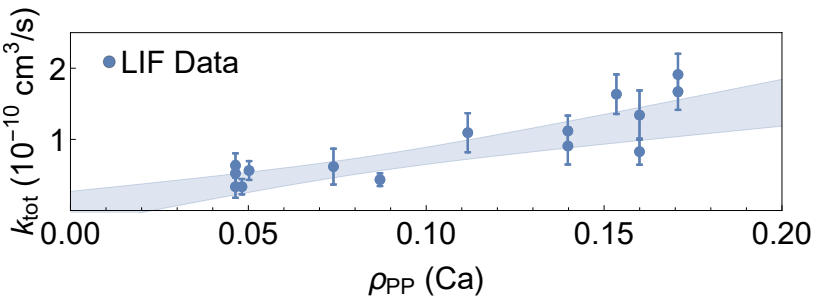

Figure 11.7: Measured CEX rate constant for $^{172}Yb^+(^2S_{1/2})$ as a function of $Ca(^1P_1)$ state population fraction ρ_{pp}. Using the dual isotope method, we are able to detect the $Ca(^1P_1)$ + $Yb^+(^2S_{1/2})$ rate constant which was previously overshadowed by CEX involving the $Yb^+(^2P_{1/2})$ state.

11.6.2 CEX rate coefficient uncertainty bands

We estimate uncertainties in the CEX rate coefficients that are caused by uncertainties in both experimental measurements and theoretical calculations. The vertical error bars in Fig. 11.1 and 11.4 show the standard error of the rate coefficient measurements. The horizontal error bars in Fig. 11.1 come from the uncertainty in the experimental determination of the ion temperature.

In Fig. 11.4, other uncertainties in the experiment, including the ion temperature and the intensity of the catalyst laser, are incorporated in the uncertainty bands of the coupled-channels calculations along with theoretical uncertainties as described in more detail in the following.

We account for the uncertainty in the relative temperature of the data, which is measured to lie between 20 mK and 100 mK. As the rate coefficient is not linear over this temperature range we compute it every 10 mK within this entire range.

The experimental uncertainty of the intensity of the catalyst laser is due to the uncertainty of its spatial alignment relative to the location of atom and ion clouds. In Fig. 11.4(a), the intensity is estimated to be $I = 5(1)$ W/cm^2. We compute rate coefficients for $I = 4$ W/cm^2 and 6 W/cm^2 and rely on its monotonic dependence on I in this range for other values. The intensity of the experimental data in Fig. 11.4(b) is assumed to be 5/6 of the

peak intensity of the given laser power and beam waist with a 20% uncertainty.

A major theoretical uncertainty is due to the uncertainty of the scattering length of the ground state potential and the bound state structure in the excited attractive $|\Omega| = 1/2$ $Ca(4s4p\ ^1P_1) + Yb^+(6s\ ^2S_{1/2})$ potential. There is no spectroscopic data available from literature about these potentials. We account for such uncertainty by varying the scattering length of the ground-state $Ca(4s^2\ ^1S_0) + Yb^+(6s\ ^2S_{1/2})$ potential. We slightly modify the depth of this potential and create three potentials with vastly different scattering lengths, $a \approx 0$, β_4, and ∞, but with the same number of $l = 0$ bound states, where $\beta_4 = \sqrt{2\mu|C_4|/\hbar^2} = 3.05\times10^3\ a_0$ is the characteristic length scale for the C_4/R^4 potential. The range of scattering lengths modifies the thermalized rate coefficients of the catalyst pathway and increase the width of the uncertainty band to up to 15%.

Another theoretical uncertainty is related to the width of the non-adiabatic coupling between the excited potentials at their crossings that lead to charge exchange. The area of the crossings is schematically marked by "CE" in a circle in Fig. 11.2(b), (c), and (d). Assuming to be a Lorentzian function, the non-adiabatic coupling matrix element has a half width $R_0 = 0.37\ a_0$ with an uncertainty $\sim 0.02\ a_0$. The values are determined by fitting the coupled-channel calculations to the experimentally measured CEX rate coefficients without the catalyst laser. Details can be found in [LMP19]. To incorporate this uncertainty, we compute rate coefficients for $R_0 = 0.35\ a_0$ and $0.39\ a_0$ and rely on its monotonic behavior with R_0 for other values.

All these uncertainties are added in quadrature to find the final uncertainty bands in both Figs. 11.4(a) and (b).

CHAPTER 12

Rotational-state readout and future outlook

The following chapter will describe the future of the MOTion project. Primarily, we are interested in developing a means for ro-vibrational control of our polar molecular ion of interest, $BaCl^+$. Before this control can be established, a method for initializing the molecule to its internal ground state must be developed. However, as these molecules are initially produced at room temperature, they occupy hundreds of rotational and vibrational states and therefore must be cooled to their ro-vibrational ground state. While vibrational cooling of $BaCl^+$ has previously been demonstrated [RSS12], rotational cooling has not yet been confirmed, primarily because a method for rotational state readout has not yet been developed in our system. Once internal state readout and initialization have been enabled, a new host of exciting experiments will be accessible with applications to state-to-state chemistry and quantum information.

For example, one application of internal state control is developing a qubit based on the rotational levels of $BaCl^+$. Indeed, such a system has been suggested recently [HC18] to provide an excellent platform for high fidelity quantum logic.

There are two main reasons why polar molecular ions are advantageous for quantum information. Firstly, the two lowest rotational levels in such molecules typically have energy splittings on the order of $\sim$GHz, meaning spontaneous emission operates on extremely long timescales, leaving plenty of time to perform coherent manipulations. Secondly, the dipole moments of molecules can be quite strong in comparison to atoms, and thus two adjacent molecules can be entangled solely using the dipole-dipole interaction. On the other hand, atomic ions, currently one of the most competitive qubit platforms, have comparatively weaker dipole moments and thus must be entangled using the motional modes of their

LQT potential. However, as these LQT systems are scaled to the chip-size level, yet-to-be-fully-understood effects of anomalous heating [BKW18] have provided a serious challenge to maintaining motional state stability, thus making dipole-dipole based entanglement a potentially attractive alternative.

Before qubit manipulations can be performed on the molecules, we must first develop a method for both initializing and reading out the internal state of these species. In most laser-coolable atomic ions, the energy structure is fairly hydrogen-like, and thus laser manipulations can easily be used for both of these purposes. However, molecules have a comparatively more complex structure. Specifically, due to the absence of vibrational selection rules in heteronuclear diatomics, excited states can often decay to wide range of lower energy states, for the moment preventing optical cooling cycles from being identified in a wide majority of molecules, with notable exceptions [BMN14, KBM17].

As previously demonstrated in $BaCl^+$ and other systems [SHS10, RSS12], sympathetic cooling offers another means for internal state cooling. In $BaCl^+$, collisions with an ultracold Ca bath have been shown to effectively cool molecular vibrational degrees of freedom; however, rotational cooling has not yet been confirmed since a method for rotational state readout has not yet been developed for this system. Essentially, before we can tell how cold these things are, we need a thermometer. The remainder of this section will detail recent efforts to develop a method of rotational state readout for $BaCl^+$ that will allow the sample's rotational temperature to be estimated and future qubit manipulations to be performed.

12.1 Photodissociative thermometry

Many different methods for internal state readout have been proposed and implemented. For example, quantum logic spectroscopy [WWH16] has been impressively implemented for state detection in MgH^+ and promises to be a general, albeit complex, method for non-destructive state readout in molecules. Similarly, other creative methods involving detection of state specific heating rates for ro-vibrational readout in polyatomic systems have also been proposed [Pat18].

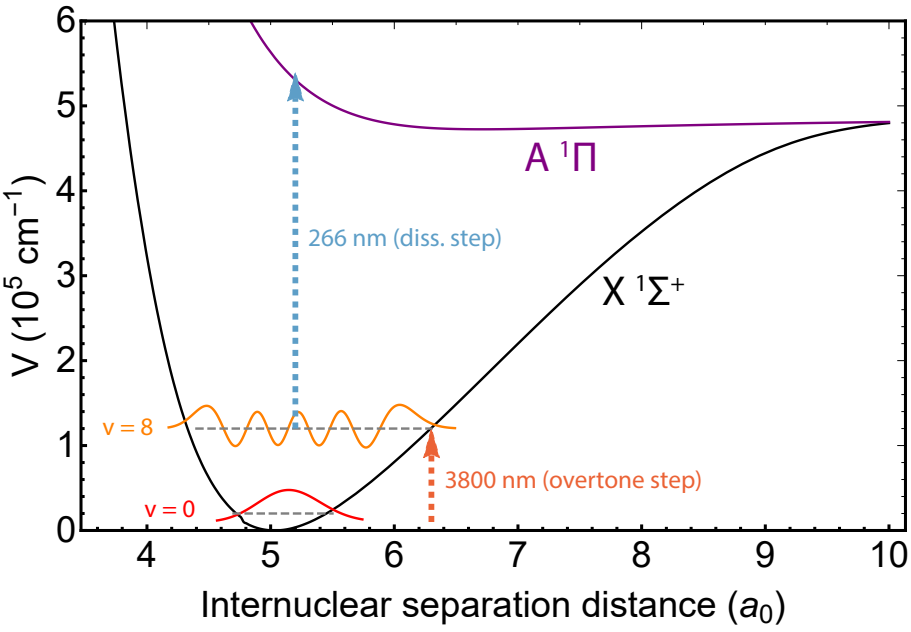

Figure 12.1: Two photon photodissociaton rotational state readout scheme

Rotational readout scheme whereby population from a single rotational level is first transferred to the v=8 state through a midIR photon. At this point, a 266 nm photon dissociates the molecule into Ba^+, which can be detected through laser fluorescence.

However, here we chose to follow a photodissociative thermometry method similar to that implemented in Ref. [RSS12], where we measure the $BaCl^+$ rotational populations by driving rotational-state-selective dissociation transitions. This scheme, while destructive by nature due to the dissociation step, offers a balance of performance and ease of implementation.

The photodissociation scheme, illustrated in Fig. 12.1, works in two steps. Firstly, in order to probe the molecular population in a particular rotational level, population in that level is first driven to a higher vibrational level in the electronic ground state through an overtone transition ($\sim$ 3800 nm). Once the population has been transferred, a second photodissociating laser can be introduced that selectively dissociates the higher vibrational level while leaving population in the other states intact. $BaCl^+$ is dissociated into Ba^+, which can subsequently be laser-cooled and imaged; thus, after this process has been performed, the increase in observed Ba^+ number can be used as a one-to-one mapping of the amount of $BaCl^+$ that was initially present in the rotational state that was probed. This process can

be repeated with the first step being resonant with different rotational levels in the ground state manifold, allowing the populations, and thus rotational temperature, of these states to be measured.

12.1.1 Selection of overtone transition

So which overtone transition should be used? Essentially, there are three main considerations. Firstly, we want to be able to exclusively dissociate the intermediate level in our scheme. Therefore, if the v=0 state, or any other level feasibly populated by our molecular sample during the experiment, were to have a significant photodissociation cross-section at the second-step dissociation laser wavelength, our signal would be comprised since we would also be dissociating molecules not driven along the overtone transition.

Essentially this precludes using dissociation laser wavelengths bluer than ∼260 nm [RSS12] as the v=0-3 levels that are populated substantially via the 300 K chamber blackbody can be dissociated here. Of course, during MOT operation, primarily only the v=0 manifold will be populated, but for reasons to become evident later, being able to use this rotational-state-readout scheme with a room temperature sample is desirable. This constraint essentially rules out the v=0-5 levels from being used.

Secondly, we would like the overtone transitions to have as high of a Franck-Condon factor as possible so we can deplete the population in a particular rotational level with high efficiency. The Franck-Condon factors (FCF's) have not been experimentally probed and thus can only be roughly estimated from theoretical molecular potentials.

Lastly, we would ideally like to use a 266 nm photodissociating laser since it is convenient to produce from the FHG of our ND:YAG laser and thus does not require handling carcinogenic dyes.

In Fig. 12.2, the Eistein A coefficient for the R-branch $(0,0) \rightarrow (v,1)$ transition is plotted against the photodissociation rate for the upper vibrational state, $\lambda_{PD} = \frac{\sigma(266\,\mathrm{nm}) I_{PD}}{\hbar \omega_{PD}}$, where $\sigma(266\,\mathrm{nm})$ is the photodissociation cross section for the upper vibrational level at 266 nm, I_{PD} is the intensity of the photodissociation beam at typical operating parameters, and ω_{PD}

is the angular frequency of the photodissociation laser.

Ideally we would like to choose a vibrational level with large values in both coordinates; however, a few caveats need to be considered. Firstly, the Einstein-A coefficient is dependent on the square of the transition dipole matrix and thus is highly susceptible to theory noise. Thus, the theory values should be taken as being within error of one another if they reside within a factor of $\sim$5. Further, as a general rule of thumb, experimentally, overtone transition rates decrease will increasing vibrational number, meaning given two roughly equivalent theoretical Einstein-A coefficeints, the lower vibrational level should be preferred. Lastly, an additional consideration is the ease of which the overtone laser can be obtained.

Keeping these three considerations in mind (see Fig. 12.2), the $v = 8$ level was the intermediate level that was chosen. It has a $\sim$ 3800 transition wavelength that can be procured from commercial midIR laser manufacturers. Further, it has the largest anticipated photodissociation cross section of the levels explored. While higher vibrational states potentially offered larger FCF's, according to theory, ultimately the likelihood that this enhancement was legitimate and not merely theory-dependent did not outweigh the risk of potentially smaller dissociation cross-sections and the added difficulty of procuring the necessary laser system. However, in actuality, due to the reliance on theoretical predictions in the selection process, which are incredibly difficult to perform accurately in this many-body system, ultimately it is difficult to say with confidence which choice of intermediate level is most optimal. Thus our choice of the v=8 is more of an educated guess than anything firm.

12.2 Experimental scheme

The energy difference between the of the $v = 8$ and $v = 0$ state (sans any rotational energy differences) can be determined from the spectroscopic constants given in Sec. 6.3.3 as

$$E[(v = 0) \rightarrow (v = 8)] = \omega_e(8 + 1/2) - \omega_e\chi_e(8 + 1/2)^2 - [\omega_e(1/2) - \omega_e\chi_e(1/2)^2] \quad (12.1)$$

where we have taken into account the zero-point energy of the system.

Considering the experimental errors in the utilized spectroscopic constants, this energy

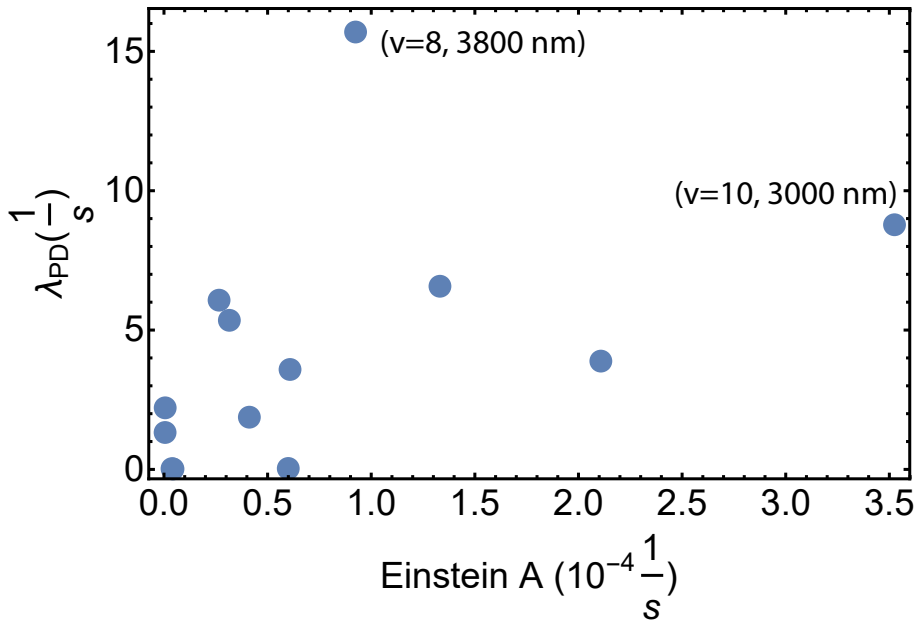

Figure 12.2: Overtone transition properties

The Einstein A coefficient for the R-branch $(0,0) \rightarrow (v,1)$ transition plotted against, $\lambda_{PD} == \frac{\sigma(266\text{ nm})I_{PD}}{\hbar\omega_{PD}}$, the photodissociation rate for the v=5-20 levels. Only select vibrational levels are labeled along with their overtone transition wavelengths. For our scheme, the v=8 band was chosen as the intermediate state in our two-photon process due to its combination of high λ_{PD}, relatively high Einstein-A coefficient, and ease of experimental implementation at 3800 nm.

difference is 3800(25) nm. Therefore, we need an overtone laser capable of scanning this range continuously. A laser capable of mod-hop-free tuning in the midIR is a challenge to construct from scratch, and thus, for this purpose we purchased a Daylight Solutions laser system (M1038-PC-QCL-J0162, 200 mW output, ∼1 MHz linewidth, 3650-3850 nm tuning range), whose tuning curve is shown in Fig. 12.3.

Once the laser system has been integrated into our system, finer spectroscopy of the overtone transition must first be performed so we can identify the overtone transitions more accurately. We can perform this spectroscopy in-house, but we must first choose whether to do this initial search with an internally cold (through introduction of the MOT) or internally room-temperature sample (not MOT introduced).

If internally cold, the rotational population would ideally compress to the J=0 level. This

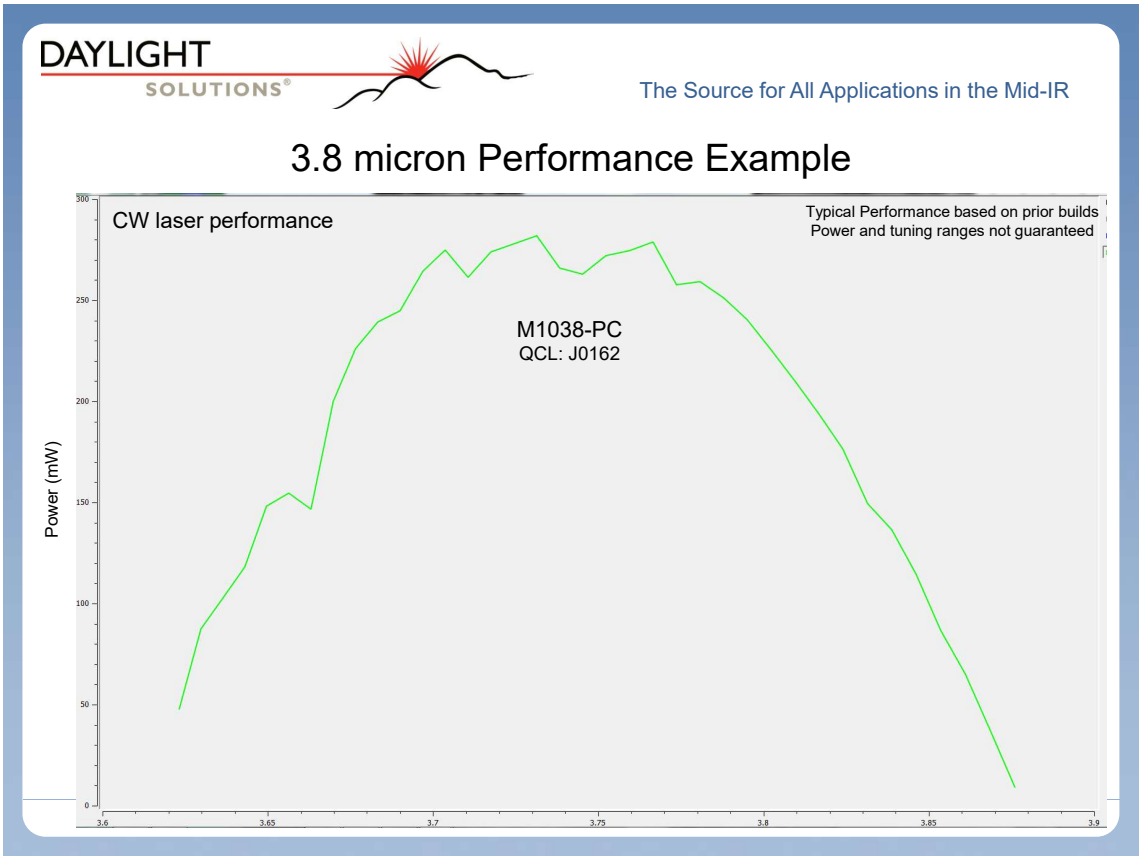

Figure 12.3: Overtone transition properties

Tuning curve for the Daylight solutions M1038-PC-QCL-J0162 midIR laser system used to drive the overtone transition in the rotational readout photodissociation scheme

would mean we would be looking for a single transition amidst a 40 nm search region. As our laser is tunable, the next question in this approach is what step size to use. If we use a step size too small ($\sim$1 MHz), we may need to acquire tens of thousands of data points before identifying the transition. On the other hand, if we choose to sweep in $\sim$100 GHz increments, we also risk not having enough spectral density to drive the transition of interest. To the latter point, if the MOT is present, due to reactions between $BaCl^+$ and Ca, our molecule lifetimes could be on the order of $\sim$10 s, meaning we would need enough spectral density to drive the transition significantly within this timeframe. The last restriction, as determined by a computational model to be discussed below, limits the size of frequency sweeps that

can be used to the ∼GHz level, which would in turn still likely necessitate thousands of data points being collected before the transition is identified. Further, proper sympathetic cooling requires constant optimization of the atomic density and the atom-ion overlap factors, adding additional layers of complexity to the experiment. These two restrictions make it difficult, but certainly not impossible, to perform the initial spectroscopy with the Ca MOT present.

Alternatively, for a room temperature sample, ∼70 rotational levels will be significantly populated under equilibrium conditions. Since the rotational splitting is of order ∼4 GHz, this means a band of rotational transitions would be spread across a ∼300 GHz spectral region. Thus, with a room temperature sample, we could scan our laser across a convenient ∼300 GHz range to address the entire rotational manifold. Further, our molecular ion lifetimes without a MOT present are of order ∼ 1 hr, meaning we can accrue signal for much longer timescales than with a MOT present and thus can detect smaller transition rates. Due to these advantages, once the Daylight system has arrived, we will likely choose to perform the experiment with a room-temperature sample first.

12.3 Experimental implementation

For the 266 nm light in our scheme, we utilize the FHG output of our QuantaRay ND:YAG laser system (∼5 mJ/pulse). In order achieve greater beam intensity, we focus our beam using a Galilean telescope (∼ 1 mm waist). However, one must be careful not to overfocus the beam and thus risk damaging the viewports on the vacuum system.

In a typical experimental sequence, we load a large sample of Ba^+ ions into the LQT. We then react approximately 30% of the sample into $BaCl^+$ using our leak valve apparatus. Ideally we want as large of a $BaCl^+$ sample as possible, but we also want to maintain translational sympathetic cooling, which is why the 30% value is chosen.

Once the bi-sample has been initialized, both the midIR and the 266 nm laser are introduced into the system. The 266 nm light actually dissociates the $BaOCH_3^+$ molecules also present in the LQT due to background gas reactions, a feature convenient for helping optimize beam alignment. The midIR laser can be aligned by overlapping the beam with one

of the Ba^+ cooling lasers, as verified through Thorlabs midIR viewing cards (VRC6S). One may also verify the overlap of the beams using two well-stabilized irises and a power-meter to ensure both lasers are approximately aligned to the same beam path.

Both lasers can now be left in for approximately 1 hr as the frequency of the midIR beam is swept and the camera records ion-fluorescence images at fixed time intervals. At the end of this cycle, the entire sample is ejected into the ToF-MS. Utilizing these detection methods, both an increase in overall ion-fluorescence and a decay in $BaCl^+$ amount can be searched for as evidence of driving the dissociation transitions.

While both measurements can be made concurrently, for this application, ToF-MS detection is preferable to fluorescence detection as the latter is subject to slow timescale frequency and intensity laser drifts in the lab; however, both may be used to corroborate any possible detection signals that are encountered.

While the Dayligtht Solutions laser system has not yet been integrated into our experimental system, we have performed this experiment with no midIR laser present as a control. Fig. 12.4 displays the Ba^+ fluorescence as a function of time for a sample control point; here, there are a few features to take note of.

Firstly, the amount of Ba^+ fluorescence is affected by background methanol reactions that reduce the amount of Ba^+ in the LQT as a function of time. While the effect of these reactions is partially limited since the 266 nm laser dissociates $BaOCH_3^+$ back into Ba^+, $BaOH^+$ is not significantly dissociated by any lasers in our system and thus represents an avenue of Ba^+ loss. Despite this loss channel, the Ba^+ amount still appears to increase in time as there appears to be a background $BaCl^+$ photodissociation rate. This is likely due to the molecules undergoing micromotion interruption collisions with background gas particles in our chamber that promote the sample to excited internal states. These states, if possessing a significant dissociation cross section at 266 nm, can then be dissociated by our FHG output, resulting in the observed background. Typically we operate our dissociation energy at < 2 mJ/pulse to limit these events.

When these two effects are taken into account the fluorescence curve in Fig. 12.4 is

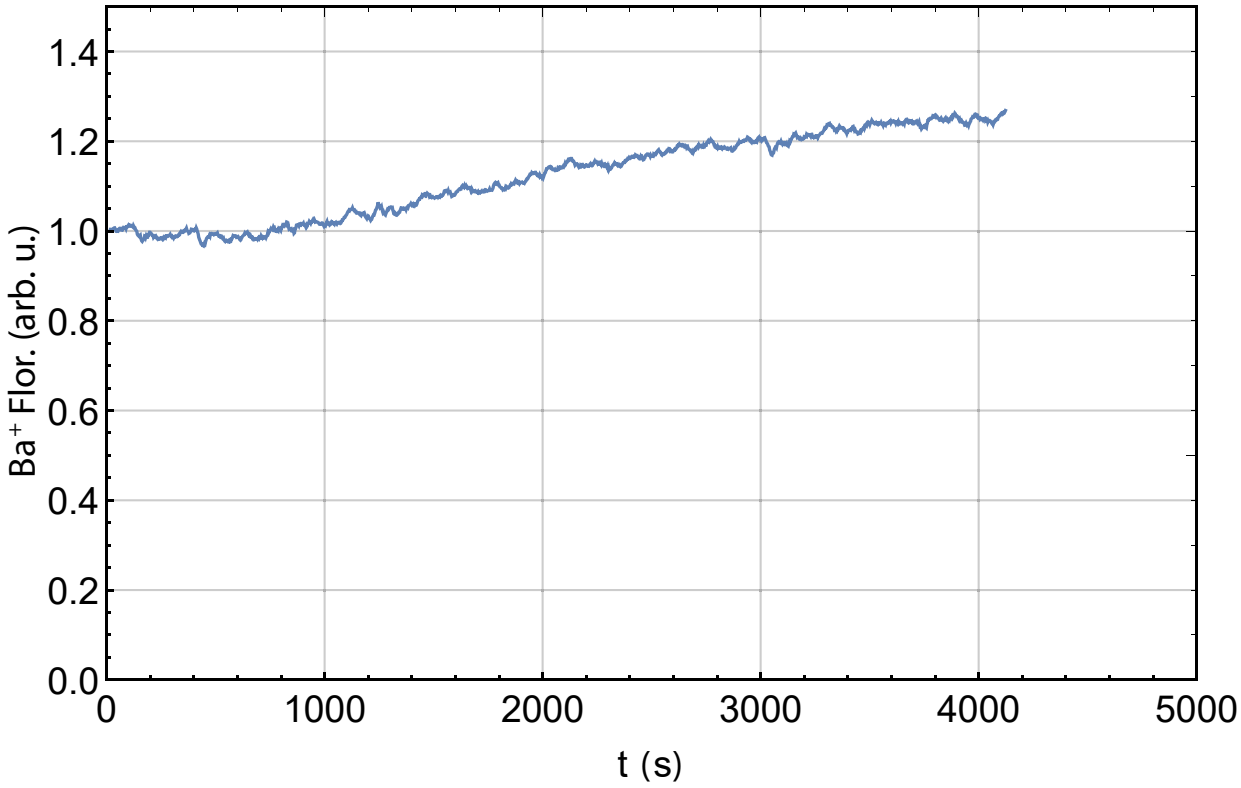

Figure 12.4: Overtone transition properties

Ba^+ fluorescence as a function of experiment time when no midIR laser is present. The combined effect of background reactions with methanol and background $BaCl^+$ photodissociation combine to cause a slight increase in Ba^+ fluorescence as a function of time.

observed. Once again, here the combined effects of Ba^+ reactions and $BaCl^+$ background dissociation combine to create a slight increase in Ba^+ over the timescale studied.

12.4 Computational modeling

In order to estimate the anticipated difference between our experimental dissociation rates and that of our controls, we constructed a computational rate equation model of the system using molecular potentials and dipole moment functions provided by Professor Hua Guo's group at the University of New Mexico. All photodissociation cross-section values, energy splittings, and matrix elements were obtained by feeding the potentials and dipole moment functions into the LEVEL and BCONT program packages.

The model considers state decay/promotion events due to both blackbody radiation and laser stimulated emission/absorption, as well as spontaneous emission. The model also considers photodissociation processes for each level. Further, the temperature of the sample is set to be 350 K instead of the 300 K of our chamber to allow our model to crudely mimic the micromotion interruption events discussed above, with the 350 K temperature chosen mainly to fit the observed background $BaCl^+$ decay rate observed in the control.

Given these effects, the rate equation for a general (v, j) level is given as

$$\begin{aligned}\frac{dN_{v,j}}{dt} = &-\frac{\sigma_{v,j}(\lambda_{266})}{h\nu} I_{PD} N_{v,j} + \sum_{E(v',j')>E(v,j)}^{v_{max},j_{max}} A_{(v',j')\leftrightarrow(v,j)} \\ &- \sum_{v'=0,j'=0}^{E(v',j')<E(v,j)} A_{(v,j)\leftrightarrow(v',j')} + \sum_{v'=0,j'=0,(v',j')\neq(v,j)}^{v_{max},j_{max}} \rho_{IR}(\Delta_{(v,j)}^{(v',j')}) B_{(v',j')\leftrightarrow(v,j)} (N_{v',j'} - N_{v,j}) \\ &+ \sum_{v'=0,j'=0,(v',j')\neq(v,j)}^{v_{max},j_{max}} \rho_{BBR}(\Delta_{(v,j)}^{(v',j')}) B_{(v',j')\leftrightarrow(v,j)} (N_{v',j'} - N_{v,j})\end{aligned} \tag{12.2}$$

where $N_{v,j}$ is the population in the (v, j) level, $\sigma_{v,j}(\lambda_{266})$ is the photodissociation cross-section at $\lambda = 266$ nm, I_{PD} is the time-averaged intensity of the photodissociating beam, $A_{(v',j')\leftrightarrow(v,j)}$ is the Einstein A-coefficient between the (v', j') and (v, j) states, $\rho_{BBR}(\Delta_{(v,j)}^{(v',j')})$ is the spectral energy density of the blackbody spectrum at the energy of the $(v, j) \rightarrow (v', j')$ transition ($\Delta_{(v,j)}^{(v',j')}$), and $\rho_{IR}(\Delta_{(v,j)}^{(v',j')})$ is defined similarly for the midIR laser. Further we note if the amount of Ba^+ is also desired to be tracked as a function of time, the model can be extended by tracking how many particles are dissociated and also by including the effects of methanol reactions on this species.

For computational convenience, we include the first 15 vibrational levels ($v_{max} = 15$) and the first 100 rotational levels ($j_{max} = 100$) of $BaCl^+$, which allows us to explore if higher order overtone transitions ($v = 1 \rightarrow v = 9$, $v = 2 \rightarrow v = 10$, etc.) are also being driven by our broadband laser source while not bogging down our computation time with an unnecessarily high v_{max}. Secondly, we consider the time averaged intensity of the photodissociation beam when in reality it is supplied through a train of 10 Hz laser pulses with 10 ns pulse widths.

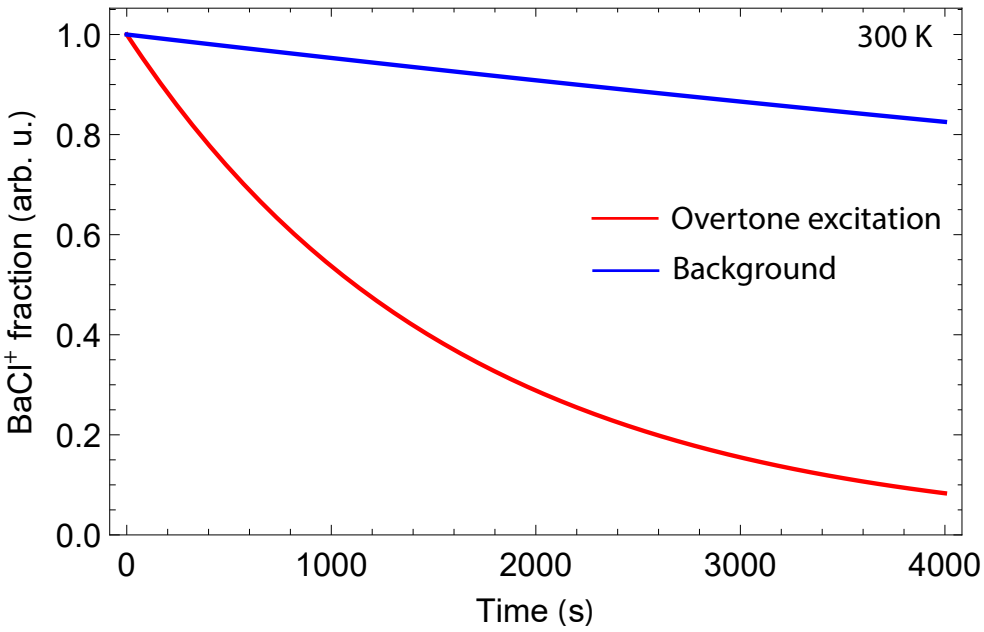

Figure 12.5: Overtone transition properties

Model predictions of $BaCl^+$ amount both when the midIR laser is present and when it is not. In the simulation, the photodissociating laser is given a pulse energy of 2 mJ and has a wavelength of 266 nm, while the midIR laser is given 200 mW of power and has a 250 GHz sweep range. As can be seen in the figure, the overtone laser is expected to produce a dissociation rate than should be easily differentiable from that of our control.

The functional form of the blackbody spectral energy density is given in standard textbooks; however, the spectral density of the laser is derived assuming a flat-top intensity profile of the laser as it is swept over a particular spectral region. The optimal sweep range for the laser can be estimated from the model after inputting the parameters of our system, such as photodissociaiton pulse energy and midIR beam intensity. In general, we find over most operating parameters, a sweep range of $\sim$250 GHz offers a decent combination of both spectral coverage and spectral density at each rotational transition.

In the model, the internal states of the molecules are initialized according to a Boltzmann distribution. After solving the differential equations numerically, the number of dissociated $BaCl^+$ molecules can be tracked in the simulation, both when the midIR laser is included and when it is not, and the corresponding expected change in $BaCl^+$ amount is plotted in

Fig. 12.5. As can be seen in the plot, over the course of an hour the signal is expected to be significant when compared to the control.

12.5 Experimental equipment

The midIR laser can be profiled by both a Miriad S3 midIR spectrometer (1-5 μm range) and a Bristol 671A-MIR wavemeter. The spectrometer allows for quick ($\sim$1 ms) spectral profiling of the beam and further can be used to ensure even frequency sweeps are being performed, while the wavemeter ($\sim$500 ms duty cycle, $\sim$10 MHz resolution) can eventually be used for locking to rotational transitions.

Once the bandhead for the $(v = 0) \rightarrow (v = 8)$ transition has been identified, finer spectroscopy can be performed to resolve individual rotational lines. Then, the next step will be to introduce the MOT and see how the rotational population differs from that of a room temperature sample. If the cooling is efficient enough, we can then attempt to follow the procedure outlined in Ref. [HC18] and perform high fidelity quantum logic on cotrapped molecular ions. Further once internal state control of $BaCl^+$ has been achieved, a host of other experiments will become possible, including those involving atom-ion state-to-state chemistry.

12.6 Wrapping up

Despite how much we've seemingly diverged from this goal in recent years, in some ways the MOTion project has always been an experiment geared towards obtaining full internal state control over polar molecular ions. However, as our internal cooling scheme involves pairing cold samples of molecules and atoms together, along with optical and electromagnetic fields, chemistry and energy exchange between the two species are inevitable. While some of these processes were anticipated and welcomed as avenues of research, it was always an open question how much unanticipated, yet-to-be-identified processes would hamper our dream of full internal state control.

In large part, much of the chemistry [CSK11, RSK11, SRK12, al11, PMS17] research conducted by this lab, as well as much of the previous research into atom-ion thermodynamics [CSH14, CSR13, SDC16], was performed to answer these questions by helping understand the limitations and challenges that atomic sympathetic cooling poses. While perhaps initially seen as excursions, these side-projects spawned some of the most interesting work the lab has produced, demonstrating that as much as you try to plan science, often times you are led down paths you never anticipated but are glad to have followed.

At this point, we understand how to navigate the chemistry, and we understand how to make the thermodynamics work in our favor. Now, the path to achieving full internal control of polar molecular ions appears clear, and the lab may finally be on the cusp of doing so. Once a method for reliable rotational readout has been developed, a new host of quantum information and quantum chemistry experiments will be available, with plenty of room for side excursions that I'm sure will inspire several more theses-worth of impromptu science.

References

[AAB18] Loïc Anderegg, Benjamin L. Augenbraun, Yicheng Bao, Sean Burchesky, Lawrence W. Cheuk, Wolfgang Ketterle, and John M. Doyle. "Laser cooling of optically trapped molecules." *Nature Physics*, **14**(9):890–893, 2018.

[Abe13] Manabu Abe. "Diradicals." *Chemical Reviews*, **113**(9):7011–7088, 2013. PMID: 23883325.

[ABH11] Ivan O. Antonov, Beau J. Barker, and Michael C. Heaven. "Pulsed-field ionization zero electron kinetic energy spectrum of the ground electronic state of BeOBe+." *The Journal of Chemical Physics*, **134**(4):044306, 2011.

[ADS] Pitt Allmendinger, Johannes Deiglmayr, Otto Schullian, Katharina Höveler, Josef A. Agner, Hansjürg Schmutz, and Frédéric Merkt. "New Method to Study Ion–Molecule Reactions at Low Temperatures and Application to the Reaction." *ChemPhysChem*, **17**(22):3596–3608.

[AF11] P.W. Atkins and R.S. Friedman. *Molecular Quantum Mechanics*. OUP Oxford, 2011.

[AGC10] M. Agúndez, J. R. Goicoechea, J. Cernicharo, A. Faure, and E. Roueff. "The chemistry of vibrationally excited H_2 in the interstellar medium." *Astrophys. J.*, **713**(1):662, 2010.

[AJB91] Jamie S. Andrews, Dylan Jayatilaka, Richard G.A. Bone, Nicholas C. Handy, and Roger D. Amos. "Spin contamination in single–determinant wavefunctions." *Chemical Physics Letters*, **183**(5):423 – 431, 1991.

[al87] E.L. Raab et al. "Trapping of neutral sodium atoms with radiation pressure." *Phys. Rev. Lett.*, **59**:2631, 1987.

[al11] S.T. Sullivan et al. "Trapping molecular ions formed via photo-associative ionization of ultracold atoms." *Phys. Chem. Chem. Phys.*, **13**:18859, 2011.

[al15] P. Hamilton et al. "Atom-interferometry constraints on dark energy." *Science*, **349**:849, 2015.

[al16] A.M. Kaufman et al. "Quantum thermalization through entanglement in an isolated many-body system." *Science*, **353**:794, 2016.

[ALB09] Aldenius, M., Lundberg, H., and Blackwell–Whitehead, R. "Experimental Calcium oscillator strengths for the 4p–5s triplet." *Astron. Astrophys.*, **502**(3):989–994, 2009.

[AP10] P. Atkins and J. de Paula. *Atkins' Physical Chemistry*. OUP Oxford, 2010.

[Arm04] P. B. Armentrout. "Fundamentals of ion-molecule chemistry." *J. Anal. At. Spectrom.*, **19**(5):571–580, 2004.

[AS17] Chandika Amarasinghe and Arthur G. Suits. "Intrabeam Scattering for Ultracold Collisions." *The Journal of Physical Chemistry Letters*, **8**(20):5153–5159, 2017.

[PMID: 28976761.]

[BBM00] P. Bouyer, V. Boyer, S. G. Murdoch, G. Delannoy, Y. Le Coq, A. Aspect, and M. Lecrivain. "RF-induced evaporative cooling and BEC in a high magnetic field." March 2000. Preprint at arXiv:physics/0003050.

[BC03] John M. Brown and Alan Carrington. *Rotational Spectroscopy of Diatomic Molecules*. Cambridge Molecular Science. Cambridge University Press, 2003.

[BD80] S. E. Butler and A. Dalgarno. "Charge transfer of multiply charged ions with hydrogen and helium Landau Zener calculations." *The Astrophysics Journal*, **241**:838–843, October 1980.

[BF94] T. Brage and C. F. Fischer. "Spline-Ggerkin methods ayylxed to Rydberg series between the 4S 'S and 3d 'D limits of calcium." *Phys. Rev. A*, **50**:2937, 1994.

[BJP03] B.H. Bransden, C.J. Joachain, and T.J. Plivier. *Physics of Atoms and Molecules*. Pearson Education. Prentice Hall, 2003.

[BKW18] Ivan A. Boldin, Alexander Kraft, and Christof Wunderlich. "Measuring Anomalous Heating in a Planar Ion Trap with Variable Ion-Surface Separation." *Phys. Rev. Lett.*, **120**:023201, Jan 2018.

[BM07] Rodney J. Bartlett and Monika Musiał. "Coupled-cluster theory in quantum chemistry." *Rev. Mod. Phys.*, **79**:291–352, Feb 2007.

[BM18] Maximilian Beyer and Frédéric Merkt. "Half–Collision Approach to Cold Chemistry: Shape Resonances, Elastic Scattering, and Radiative Association in the $H^+ + H$ and $D^+ + D$ Collision Systems." *Phys. Rev. X*, **8**:031085, Sep 2018.

[BMB98] D. J. Berkeland, J. D. Miller, J. C. Bergquist, W. M. Itano, and D. J. Wineland. "Minimization of ion micromotion in a Paul trap." *Journal of Applied Physics*, **83**(10):5025–5033, 1998.

[BMN14] J. F. Barry, D. J. McCarron, E. B. Norrgard, M. H. Steinecker, and D. DeMille. "Magneto-optical trapping of a diatomic molecule." *Nature*, **512**:286, aug 2014.

[BO27] Max Born and Robert Oppenheimer. "Zur Quantentheorie der Molekeln." *Annalen der Physik*, **84**:457–484, 1927.

[BON15] Astrid Bergeat, Jolijn Onvlee, Christian Naulin, Ad van der Avoird, and Michel Costes. "Quantum dynamical resonances in low–energy CO (j=0) + He inelastic collisions." *Nature Chemistry*, **7**:349, March 2015.

[BOV09] R. B. Blakestad, C. Ospelkaus, A. P. VanDevender, J. M. Amini, J. Britton, D. Leibfried, and D. J. Wineland. "High-Fidelity Transport of Trapped-Ion Qubits through an **X**-Junction Trap Array." *Phys. Rev. Lett.*, **102**:153002, Apr 2009.

[BOV11] R. B Blakestad, C. Ospelkaus, A. P VanDevender, J. H Wesenberg, M. J Biercuk, D. Leibfried, and D. J Wineland. "Near-ground-state transport of trapped-ion qubits through a multidimensional array." *Phys. Rev. A*, **84**:032314, Sep 2011.

[BP03] Heinz-Peter Breuer and Francesco Petruccione. *Concepts and Methods in the Theory of Open Quantum Systems*, pp. 65–79. Springer Berlin Heidelberg, Berlin, Heidelberg, 2003.

[BSG12] B. Ostojićand P.R. Bunker, P. Schwerdtfeger, Artur Gertych, and Per Jensen. "The predicted infrared spectrum of the hypermetallic molecule CaOCa in its lowest two electronic states $\tilde{X}\,^1\Sigma_g^+$ and $\tilde{a}\,^3\Sigma_u^+$." *Journal of Molecular Structure*, **1023**:101 – 107, 2012.

[BV12] Mark Brouard and Claire Vallance, editors. *Tutorials in Molecular Reaction Dynamics*. The Royal Society of Chemistry, 2012.

[BVH15] Joshua H. Bartlett, Robert A. VanGundy, and Michael C. Heaven. "Characterization of the $BaCl^+(X^1\Sigma^+)$ cation by photoelectron spectroscopy." *Journal of Molecular Spectroscopy*, **316**:119 – 121, 2015.

[CB18] Aaron T. Calvin and Kenneth R. Brown. "Spectroscopy of Molecular Ions in Coulomb Crystals." *J. Phys. Chem. Lett.*, **9**(19):5797–5804, 2018.

[CCJ17] Theo Cremers, Simon Chefdeville, Niek Janssen, Edwin Sweers, Sven Koot, Peter Claus, and Sebastiaan Y. T. van de Meerakker. "Multistage Zeeman decelerator for molecular-scattering studies." *Phys. Rev. A*, **95**(4):43415, apr 2017.

[CD00] R. Côté and A. Dalgarno. "Ultracold atom-ion collisions." *Phys. Rev. A*, **62**:012709, Jun 2000.

[CDK09] Lincoln Carr, David DeMille, Roman Krems, and Jun Ye. "Cold and ultracold molecules: science, technology and applications." *N. J. Phys.*, **11**(5):055049, 2009.

[CDK13] Yuan-Pin Chang, Karol Długołkecki, Jochen Küpper, Daniel Rösch, Dieter Wild, and Stefan Willitsch. "Specific Chemical Reactivities of Spatially Separated 3-Aminophenol Conformers with Cold Ca^+ Ions." *Science*, **342**(6154):98–101, 2013.

[CGc12] Marko Cetina, Andrew T. Grier, and Vladan Vuletić. "Micromotion-Induced Limit to Atom-Ion Sympathetic Cooling in Paul Traps." *Phys. Rev. Lett.*, **109**:253201, Dec 2012.

[CGG77] M. L. Citron, H. R. Gray, C. W. Gabel, and C. R. Stroud. "Experimental study of power broadening in a two-level atom." *Phys. Rev. A*, **16**:1507–1512, Oct 1977.

[CLC13] Boon Leng Chuah, Nicholas C. Lewty, Radu Cazan, and Murray D. Barrett. "Detection of ion micromotion in a linear Paul trap with a high finesse cavity." *Opt. Express*, **21**(9):10632–10641, May 2013.

[CLM16] Ludwig E. de Clercq, Hsiang-Yu Lo, Matteo Marinelli, David Nadlinger, Robin Oswald, Vlad Negnevitsky, Daniel Kienzler, Ben Keitch, and Jonathan P. Home. "Parallel Transport Quantum Logic Gates with Trapped Ions." *Phys. Rev. Lett.*, **116**:080502, Feb 2016.

[CMY12] Aron J. Cohen, Paula Mori-Sánchez, and Weitao Yang. "Challenges for Density Functional Theory." *Chemical Reviews*, **112**(1):289–320, 2012. PMID: 22191548.

[Cre11] Dieter Cremer. "Møller–Plesset perturbation theory: from small molecule methods to methods for thousands of atoms." *Wiley Interdisciplinary Reviews: Computational Molecular Science*, **1**(4):509–530, 2011.

[Cre13] Dieter Cremer. "From configuration interaction to coupled cluster theory: The quadratic configuration interaction approach." *Wiley Interdisciplinary Reviews: Computational Molecular Science*, **3**(5):482–503, 2013.

[CSH14] Kuang Chen, Scott T. Sullivan, and Eric R. Hudson. "Neutral Gas Sympathetic Cooling of an Ion in a Paul Trap." *Phys. Rev. Lett.*, **112**:143009, Apr 2014.

[CSK11] Kuang Chen, Steven J. Schowalter, Svetlana Kotochigova, Alexander Petrov, Wade G. Rellergert, Scott T. Sullivan, and Eric R. Hudson. "Molecular-ion trap-depletion spectroscopy of $BaCl^+$." *Phys. Rev. A*, **83**:030501, Mar 2011.

[CSR13] Kuang Chen, Scott T. Sullivan, Wade G. Rellergert, and Eric R. Hudson. "Measurement of the Coulomb Logarithm in a Radio–Frequency Paul Trap." *Phys. Rev. Lett.*, **110**:173003, Apr 2013.

[cTR06] Boris Brkić, Stephen Taylor, Jason F. Ralph, and Neil France. "High-fidelity simulations of ion trajectories in miniature ion traps using the boundary-element method." *Phys. Rev. A*, **73**:012326, Jan 2006.

[CXY19] Gary K. Chen, Changjian Xie, Tiangang Yang, Anyang Li, Arthur G. Suits, Eric R. Hudson, Wesley C. Campbell, and Hua Guo. "Isotope–selective chemistry in the $Be^+(^2S_{1/2})$ + HOD $\rightarrow$ $BeOD^+/BeOH^+$ + H/D reaction." *Phys. Chem. Chem. Phys.*, p. Advance Article, 2019.

[Dag77] Paul J. Dagdigian. "Dependence of collision complex lifetime on product internal state: Laser fluorescence detection of the Ca + NaCl crossed beam reaction." *Chem. Phys.*, **21**(3):453 – 466, 1977.

[Dah00] D. A. Dahl. "SIMION for the personal computer in reflection." *Int. J. Mass Spectrom.*, **200**(3), 2000.

[DBB99] B. DeMarco, J. L. Bohn, J. P. Burke, M. Holland, and D. S. Jin. "Measurement of p-Wave Threshold Law Using Evaporatively Cooled Fermionic Atoms." *Phys. Rev. Lett.*, **82**:4208–4211, May 1999.

[DBE] John M. Doyle, Friedrich Bretislav, and Narevicius Edvardas. "Physics and Chemistry with Cold Molecules." *ChemPhysChem*, **17**(22):3581–3582.

[DeM02] D. DeMille. "Quantum Computation with Trapped Polar Molecules." *Phys. Rev. Lett.*, **88**:067901, Jan 2002.

[Dem06] W. Demtröder. *Atoms, Molecules and Photons: An Introduction to Atomic-, Molecular- and Quantum-physics.* Advanced texts in physics. Springer, 2006.

[Der01] Andrei Derevianko. "Feasibility of Cooling and Trapping Metastable Alkaline-Earth Atoms." *Phys. Rev. Lett.*, **87**:023002, Jun 2001.

[DFK96] V. A. Dzuba, V. V. Flambaum, and M. G. Kozlov. "Combination of the many-body perturbation theory with the configuration-interaction method." *Phys. Rev. A*, **54**(5):3948–3959, nov 1996.

[DK11] Andrei Derevianko and Hidetoshi Katori. "Colloquium: Physics of optical lattice clocks." *Rev. Mod. Phys.*, **83**(2):331–348, may 2011.

[DKW11] Olivier Dulieu, Roman Krems, Matthias Weidem´uller, and Stefan Willitsch. "Physics and Chemistry of Cold Molecules." *Phys. Chem. Chem. Phys.*, **13**:18703–18704, 2011.

[DMW58] A. Dalgarno, M. McDowell, and A. Williams. "The mobilities of ions in unlike gases." *Phil. Trans. R. Soc.*, **250**:411–425, 1958.

[DP11] Andrei Derevianko and Sergey G. Porsev. "Accurate evaluation of parameters of optical lattice clocks." In Ennio Arimondo, Paul R Berman, and Chun C Lin, editors, *Advances in Atomic, Molecular, and Optical Physics*, volume 60, pp. 415–459. Academic Press, 2011.

[DS09] Irina Dumitriu and Alejandro Saenz. "Photodissociation of the HeH^+ molecular ion." *Journal of Physics B: Atomic, Molecular and Optical Physics*, **42**(16):165101, jul 2009.

[DSL93] H. Floyd Davis, Arthur G. Suits, Yuan T. Lee, Christian Alcaraz, and Jean-Michel Mestdagh. "State specific reactions of $Ba(^1S_0)$ and $Ba(^1D_2)$ with water and methanol." *The Journal of Chemical Physics*, **98**(12):9595–9609, 1993.

[DSL05] Carsten Degenhardt, Hardo Stoehr, Christian Lisdat, Guido Wilpers, Harald Schnatz, Burghard Lipphardt, Tatiana Nazarova, Paul-Eric Pottie, Uwe Sterr, Jürgen Helmcke, and Fritz Riehle. "Calcium optical frequency standard

with ultracold atoms: Approaching 10^{-15} relative uncertainty." *Phys. Rev. A*, **72**:062111, Dec 2005.

[DTS15] Katrin Dulitz, Atreju Tauschinsky, and Timothy P. Softley. "Zeeman deceleration of electron-impact-excited metastable helium atoms." *New Journal of Physics*, **17**(3):035005, 2015.

[DW69] P.H. Dawson and N.R. Whetten. "Non-linear resonances in quadrupole mass spectrometers due to imperfect fields I. The quadrupole ion trap." *International Journal of Mass Spectrometry and Ion Physics*, **2**(1):45 – 59, 1969.

[DXW10] Wenrui Dong, Chunlei Xiao, Tao Wang, Dongxu Dai, Xueming Yang, and Dong H. Zhang. "Transition-State Spectroscopy of Partial Wave Resonances in the F + HD Reaction." *Science*, **327**(5972):1501–1502, 2010.

[EA07] Pablo Echenique and J. L. Alonso. "A mathematical and computational review of Hartree Fock SCF methods in quantum chemistry." *Molecular Physics*, **105**(23-24):3057–3098, 2007.

[Ear48] S. Earnshaw. "On the Nature of the Molecular Forces which Regulate the Constitution of the Luminiferous Ether." *Transactions of the Cambridge Philosophical Society*, **7**:97, 1848.

[Ebe16] P. Eberle. "A Dynamic Ion-Atom Hybrid Trap for High-Resolution Cold-Collision Studies." *ChemPhysChem*, **17**(22):3769, 2016.

[EBH85] W. Ertmer, R. Blatt, J. L. Hall, and M. Zhu. "Laser Manipulation of Atomic Beam Velocities: Demonstration of Stopped Atoms and Velocity Reversal." *Phys. Rev. Lett.*, **54**:996–999, Mar 1985.

[EDP15] Pascal Eberle, Alexander D Dørfler, Claudio von Planta, Krishnamurthy Ravi, Dominik Haas, Dong Zhang, Sebastiaan Y. T. van de Meerakker, and Stefan Willitsch. "Ion-Atom and Ion-Molecule Hybrid Systems: Ion-Neutral Chemistry at Ultralow Energies." *Journal of Physics: Conference Series*, **635**(1):012012, sep 2015.

[Ein16] Albert Einstein. "Zur Quantentheorie der Strahlung. (German) [On the Quantum Theory of Radiation]." *Mitt. phys. Ges. Zürich*, **16**:47–62, 1916.

[FGP14] H. A. Fürst, M. H. Goerz, U. G. Poschinger, M. Murphy, S. Montangero, T. Calarco, F. Schmidt-Kaler, K. Singer, and C. P. Koch. "Controlling the transport of an ion: classical and quantum mechanical solutions." *New Journal of Physics*, **16**(7):075007, 2014.

[Foo05] C.J. Foot. *Atomic physics*. Oxford master series in physics. Oxford University Press, 2005.

[FSL91] W. Fritsch, R. Shingal, and C.-D. Lin. "Close–coupling study of electron excitation in 1–300-keV/u He^{2+}–H collisions." *Phys. Rev. A*, **44**:5686–5692, Nov 1991.

[FT03] C. F. Fischer and G. Tachiev. "Allowed and spin-forbidden electric dipole transitions in Ca I." *Phys. Rev. A*, **68**:012507, 2003.

[FTS09] M. J. Frisch, G. W. Trucks, H. B. Schlegel, G. E. Scuseria, M. A. Robb, J. R. Cheeseman, G. Scalmani, V. Barone, B. Mennucci, G. A. Petersson, H. Nakatsuji, M. Caricato, X. Li, H. P. Hratchian, A. F. Izmaylov, J. Bloino, G. Zheng, J. L. Sonnenberg, M. Hada, M. Ehara, K. Toyota, R. Fukuda, J. Hasegawa, M. Ishida, T. Nakajima, Y. Honda, O. Kitao, H. Nakai, T. Vreven, J. A. Montgomery, J. E. Peralta, F. Ogliaro, M. Bearpark, J. J. Heyd, E. Brothers, K. N. Kudin, V. N. Staroverov, R. Kobayashi, J. Normand, K. Raghavachari, A. Rendell, J. C. Burant, S. S. Iyengar, J. Tomasi, M. Cossi, N. Rega, J. M. Millam, M. Klene, J. E. Knox, J. B. Cross, V. Bakken, C. Adamo, J. Jaramillo, R. Gomperts, R. E. Stratmann, O. Yazyev, A. J. Austin, R. Cammi, C. Pomelli, J. W. Ochterski, R. L. Martin, K. Morokuma, V. G. Zakrzewski, G. A. Voth, P. Salvador, J. J. Dannenberg, S. Dapprich, A. D. Daniels, Farkas, J. B. Foresman, J. V. Ortiz, J. Cioslowski, and D. J. Fox. "Gaussian 09, Revision B.01.", 2009.

[GCc09] Andrew T. Grier, Marko Cetina, Fedja Oručević, and Vladan Vuletić. "Observation of Cold Collisions between Trapped Ions and Trapped Atoms." *Phys. Rev. Lett.*, **102**:223201, Jun 2009.

[GG98] S. D. Gensemer and P. L. Gould. "Ultracold Collisions Observed in Real Time." *Phys. Rev. Lett.*, **80**:936–939, Feb 1998.

[GH01] J. Grünert and A. Hemmerich. "Optimizing the production of metastable calcium atoms in a magneto-optical trap." *Applied Physics B*, **73**(8):815–818, 2001.

[GJS07] Shaun P. Green, Cameron Jones, and Andreas Stasch. "Stable Magnesium(I) Compounds with Mg-Mg Bonds." *Science*, **318**(5857):1754–1757, 2007.

[GLS03] Richard L. Gross, Xianghong Liu, and Arthur G. Suits. "O(3P) versus O(1D) reaction dynamics with n-pentane: a crossed-beam imaging study." *Chemical Physics Letters*, **376**(5):710 – 716, 2003.

[GMG12] Koos B. Gubbels, Sebastiaan Y. T. van de Meerakker, Gerrit C. Groenenboom, Gerard Meijer, and Ad van der Avoird. "Scattering resonances in slow NH_3–He collisions." *The Journal of Chemical Physics*, **136**(7):074301, 2012.

[GP89] Alan Gallagher and David E. Pritchard. "Exoergic collisions of cold Na^*-Na." *Phys. Rev. Lett.*, **63**:957–960, Aug 1989.

[Gri05] D.J. Griffiths. *Introduction to Quantum Mechanics*. Pearson international edition. Pearson Prentice Hall, 2005.

[Gro00] J. Grotendorst. *Modern Methods and Algorithms of Quantum Chemistry: Winterschool, 21 - 25 February 2000, Forschungszentrum, Julich, Germany – Proceedings*. NIC series. John von Neumann Institute for Computing (NIC), 2000.

[Hal13] Felix Hall. *Cold ion-neutral reactions.* PhD thesis, The University of Basel, 2013.

[Ham10] Paul Hamilton. *Preliminary results in the search for the electron electric dipole moment in PbO.* PhD thesis, Yale University, 2010.

[HAR13] Felix H.J. Hall, Mireille Aymar, Maurice Raoult, Olivier Dulieu, and Stefan Willitsch. "Light-assisted cold chemical reactions of barium ions with rubidium atoms." *Mol. Phys.*, **111**(12-13):1683–1690, 2013.

[HB76] D. P. Hodgkinson and J. S. Briggs. "Resonant charge exchange at low velocities." *Journal of Physics B: Atomic and Molecular Physics*, **9**(2):255–267, 1976.

[HC18] Eric R. Hudson and Wesley C. Campbell. "Dipolar quantum logic for freely rotating trapped molecular ions." *Phys. Rev. A*, **98**:040302, Oct 2018.

[HD14] A. Härter and J. Hecker Denschlag. "Cold atom–ion experiments in hybrid traps." *Contemporary Physics*, **55**(1):33–45, 2014.

[HG11] Joshua W. Hollett and Peter M. W. Gill. "The two faces of static correlation." *The Journal of Chemical Physics*, **134**(11):114111, 2011.

[HGS12] A. B. Henson, S. Gersten, Y. Shagam, J. Narevicius, and E. Narevicius. "Observation of Resonances in Penning Ionization Reactions at Sub-Kelvin Temperatures in Merged Beams." *Science*, **338**(6104):234–238, 2012.

[HH79] G. Herzberg and K.P. Huber. *Molecular Spectra and Molecular Structure: Constants of diatomic molecules.* Molecular Spectra and Molecular Structure. Van Nostrand Reinhold, 1979.

[HHF13] Shinsuke Haze, Sousuke Hata, Munekazu Fujinaga, and Takashi Mukaiyama. "Observation of elastic collisions between lithium atoms and calcium ions." *Phys. Rev. A*, **87**, 05 2013.

[Hil82] Robert C. Hilborn. "Einstein coefficients, cross sections, f values, dipole moments, and all that." *American Journal of Physics*, **50**(11):982–986, 1982.

[HLC15] Daniel Hauser, Seunghyun Lee, Fabio Carelli, Steffen Spieler, Olga Lakhmanskaya, Eric S Endres, Sunil S Kumar, Franco Gianturco, and Roland Wester. "Rotational state-changing cold collisions of hydroxyl ions with helium." *Nat. Phys.*, **11**:467, may 2015.

[HLH99] J. E. Hansen, C. Laughlin, H. W van der Hart, and G. Verbockhaven. "Energy levels, wavefunction compositions and electric dipole transitions in neutral Ca." *J. Phys. B: At. Mol. Opt. Phys.*, **32**:2099, 1999.

[HP86] L. R. Hunter and S. K. Peck. "Precision atomic lifetime measurements using collisionally induced coherence transfer." *Phys. Rev. A*, **33**:4452–4455, Jun 1986.

[HPO96] T. Helgaker, Jørgensen P., and J. Olsen. *Molecular Electronic Structure Theory.* Wiley, 1996.

[HR86] David Husain and Gareth Roberts. "Energy pooling from Ca[4s4p(3P)] and Ca[4s3d(1D2)] studied by time-resolved atomic emission following pulsed dye-laser excitation." *J. Chem. Soc., Faraday Trans. 2*, **82**:1921–1933, 1986.

[HS91] M. Hawley and M. A. Smith. "Gas phase collisional quenching of NO^+ (v=1) ions below 5 K." *The Journal of Chemical Physics*, **95**(11):8662–8664, 1991.

[HTS06] Eric R. Hudson, Christopher Ticknor, Brian C. Sawyer, Craig A. Taatjes, Heather J. Lewandowski, Jason R. Bochinski, John L. Bohn, and Jun Ye. "Production of cold formaldehyde molecules for study and control of chemical reaction dynamics with hydroxyl radicals." *Phys. Rev. A*, **73**(6):063404, 2006.

[Hud09] Eric R. Hudson. "Method for producing ultracold molecular ions." *Phys. Rev. A*, **79**:032716, Mar 2009.

[Hud16] E. R. Hudson. "Sympathetic cooling of molecular ions with ultracold atoms." *EPJ Tech. Instrum.*, **3**(1):8, Dec 2016.

[Hun75] L. W. Hunter. "On infinite order sudden approximations for an arbitrary potential energy." *J. Chem. Phys.*, **62**(7):2855–2859, 1975.

[HW10] S. Hooker and C. Webb. *Laser Physics.* Oxford Master Series in Physics. OUP Oxford, 2010.

[HW12] Felix H. J. Hall and Stefan Willitsch. "Millikelvin Reactive Collisions between Sympathetically Cooled Molecular Ions and Laser-Cooled Atoms in an Ion-Atom Hybrid Trap." *Phys. Rev. Lett.*, **109**:233202, Dec 2012.

[HWW85] L. R. Hunter, G. M. Watson, D. S. Weiss, and A. G. Zajonc. "High-precision measurement of lifetimes and collisional decay parameters in Ca ^{1}D states using the two-photon Hanle effect." *Phys. Rev. A*, **31**:2268–2278, Apr 1985.

[HYO08] D. Hucul, M. Yeo, S. Olmschenk, C. Monroe, W. K. Hensinger, and J. Rabchuk. "On the Transport of Atomic Ions in Linear and Multidimensional Ion Trap Arrays." *Quantum Info. Comput.*, **8**(6):501–578, July 2008.

[IOG10] Nick Indriolo, Takeshi Oka, T. R. Geballe, and Benjamin J. McCall. "Constraining the Environment of CH^+ Formation with CH_3^+ Observations." *The Astrophysical Journal*, **711**(2):1338, 2010.

[Jam98] D.F.V. James. "Quantum dynamics of cold trapped ions with application to quantum computation." *Applied Physics B*, **66**(2):181–190, Feb 1998.

[JC63] E. T. Jaynes and F. W. Cummings. "Comparison of quantum and semiclassical radiation theories with application to the beam maser." *Proceedings of the IEEE*, **51**(1):89–109, Jan 1963.

[Jec14] Thierry Jecko. "On the mathematical treatment of the Born–Oppenheimer approximation." *Journal of Mathematical Physics*, **55**(5):053504, 2014.

[JM89a] Paul S. Julienne and Frederick H. Mies. "Collisions of ultracold trapped atoms." *J. Opt. Soc. Am. B*, **6**(11):2257–2269, Nov 1989.

[JM89b] Paul S. Julienne and Frederick H. Mies. "Collisions of ultracold trapped atoms." *J. Opt. Soc. Am. B*, **6**(11):2257–2269, Nov 1989.

[JTL06] Kevin M. Jones, Eite Tiesinga, Paul D. Lett, and Paul S. Julienne. "Ultracold photoassociation spectroscopy: Long-range molecules and atomic scattering." *Rev. Mod. Phys.*, **78**:483–535, May 2006.

[KBM17] Ivan Kozyryev, Louis Baum, Kyle Matsuda, Benjamin L. Augenbraun, Loic Anderegg, Alexander P. Sedlack, and John M. Doyle. "Sisyphus Laser Cooling of a Polyatomic Molecule." *Phys. Rev. Lett.*, **118**:173201, Apr 2017.

[Kos64] H. Köstlin. "Evidence for sympathetic vibrational cooling of translationally cold molecules." *Z. Phys.*, **178**:200, 1964.

[Kou79] Donald Jack Kouri. *Rotational Excitation II: Approximation Methods*, pp. 301–358. Springer US, Boston, MA, 1979.

[KPB15] J. Keller, H. L. Partner, T. Burgermeister, and T. E. Mehlst'aubler. "Precise determination of micromotion for trapped-ion optical clocks." *Journal of Applied Physics*, **118**(10):104501, 2015.

[KPS15] M. G. Kozlov, S. G. Porsev, M. S. Safronova, and I. I. Tupitsyn. "CI-MBPT: A package of programs for relativistic atomic calculations based on a method combining configuration interaction and many-body perturbation theory." *Comput. Phys. Commun.*, **195**:199–213, 2015.

[KRR16] A. Kramida, Yu. Ralchenko, J. Reader, and NIST ASD Team. "NIST Atomic Spectra Database (version 5.4).", 2016.

[KS92] T. Kurosu and F. Shimizu. "Laser cooling and trapping of alkaline earth atoms." *Jpn. J. Appl. Phys.*, **31**:908, 1992.

[KSS16] Ayelet Klein, Yuval Shagam, Wojciech Skomorowski, Piotr S. Żuchowski, Mariusz Pawlak, Liesbeth M. C. Janssen, Nimrod Moiseyev, Sebastiaan Y. T. van de Meerakker, Ad van der Avoird, Christiane P. Koch, and Edvardas Narevicius. "Directly probing anisotropy in atom–molecule collisions through quantum scattering resonances." *Nature Physics*, **13**:35, oct 2016.

[KWS12] Moritz Kirste, Xingan Wang, H. Christian Schewe, Gerard Meijer, Kopin Liu, Ad van der Avoird, Liesbeth M. C. Janssen, Koos B. Gubbels, Gerrit C. Groenenboom, and Sebastiaan Y. T. van de Meerakker. "Quantum-State Resolved Bimolecular Collisions of Velocity-Controlled OH with NO Radicals." *Science*, **338**(6110):1060–1063, 2012.

[KWS15] Jongjin B. Kim, Marissa L. Weichman, Tobias F. Sjolander, Daniel M. Neumark, Jacek Kłos, Millard H. Alexander, and David E. Manolopoulos. "Spectroscopic observation of resonances in the F + H_2 reaction." *Science*, **349**(6247):510–513, 2015.

[Lan05] P. Langevin. "A fundamental formula of kinetic theory." *Ann. Chim. Phys*, **5**:245–288, 1905.

[LBM03] D. Leibfried, R. Blatt, C. Monroe, and D. Wineland. "Quantum dynamics of single trapped ions." *Rev. Mod. Phys.*, **75**:281–324, Mar 2003.

[LBY15] Andrew D. Ludlow, Martin M. Boyd, Jun Ye, E. Peik, and P. O. Schmidt. "Optical atomic clocks." *Rev. Mod. Phys.*, **87**:637–701, Jun 2015.

[LH87] L. P. Lellouch and L. R. Hunter. "Measurement of the 4s4p 'P-4s3d 'D spontaneous emission rate in calcium by use of a Stark-electric-quadrupole interference." *Phys. Rev. A*, **36**:3490, 1987.

[LH96] C. Laughlin and J. E. Hansen. "An accurate model-potential description of the valence spectrum of Ca." *J. Phys. B: At. Mol. Opt. Phys.*, **29**:L441, 1996.

[LL82] L.D. Landau and E.M. Lifshitz. *Mechanics*. Number v. 1. Elsevier Science, 1982.

[LML69] Y. T. Lee, J. D. McDonald, P. R. LeBreton, and D. R. Herschbach. "Molecular Beam Reactive Scattering Apparatus with Electron Bombardment Detector." *Review of Scientific Instruments*, **40**(11):1402–1408, 1969.

[LMP19] Ming Li, Michael Mills, Prateek Puri, Alexander Petrov, Eric R. Hudson, and Svetlana Kotochigova. "Excitation-assisted nonadiabatic charge-exchange reaction in a mixed atom-ion system." *to be published*, 2019.

[LWS08] F. Lang, K. Winkler, C. Strauss, R. Grimm, and J. Hecker Denschlag. "Ultracold Triplet Molecules in the Rovibrational Ground State." *Phys. Rev. Lett.*, **101**:133005, Sep 2008.

[LXC99] Jiabo Li, Jianhua Xing, Christopher J. Cramer, and Donald G. Truhlar. "Accurate dipole moments from Hartree–Fock calculations by means of class IV charges." *The Journal of Chemical Physics*, **111**(3):885–892, 1999.

[LY98] Wenyun Lu and Shihe Yang. "Reactions of Alkaline Earth Metal Ions with Methanol Clusters." *The Journal of Physical Chemistry A*, **102**:825–840, 01 1998.

[Maj32] Ettore Majorana. "Atomi orientati in campo magnetico variabile." *Il Nuovo Cimento (1924-1942)*, **9**(2):43–50, Feb 1932.

[Mar05] Andreas Markmann. "Adibatic and Diabatic Representations.", November 2005.

[MBH06] C. Matei, L. Buchmann, W. R. Hannes, D. A. Hutcheon, C. Ruiz, C. R. Brune, J. Caggiano, A. A. Chen, J. DÁuria, A. Laird, and et al. "Measurement of the Cascade Transition via the First Excited State of O 16 in the C 12 (α, γ) O 16 Reaction, and Its S Factor in Stellar Helium Burning." *Phys. Rev. Lett.*, **97**(24):242503, 2006.

[MBH09] Jeremy M. Merritt, Vladimir E. Bondybey, and Michael C. Heaven. "Spectroscopy, Structure, and Ionization Energy of BeOBe." *The Journal of Physical Chemistry A*, **113**(47):13300–13309, 2009. PMID: 19921943.

[McQ08] Donald A McQuarrie. *Quantum chemistry*. University Science Books, Sausalito, Calif., 2008.

[Mie73] F. H. Mies. "Molecular Theory of Atomic Collisions: Fine-Structure Transitions." *Phys. Rev. A*, **7**:942–957, Mar 1973.

[Mit93] J. Mitroy. "Energy levels and oscillator strengths for neutral calcium." *J. Phys. B: At. Mol. Opt. Phys. 361*, **26**:3703, 1993.

[Mor04] Donald C. Morton. "Erratum: "Atomic Data for Resonance Absorption Lines. III. Wavelengths Longward of the Lyman Limit for the Elements Hydrogen to Gallium" (ApJS, 149, 205 [2003])." *Astrophys. J. Suppl. Ser.*, **151**(2):403, 2004.

[MPY17] Michael Mills, Prateek Puri, Yanmei Yu, Andrei Derevianko, Christian Schneider, and Eric R. Hudson. "Efficient repumping of a Ca magneto-optical trap." *Phys. Rev. A*, **96**:033402, Sep 2017.

[MRJ15] Dmytro Mulin, Štěpá'n Roučka, Pavol Jusko, Illia Zymak, Radek Plašil, Dieter Gerlich, Roland Wester, and Juraj Glosík. "H/D exchange in reactions of OH^- with D_2 and of OD^- with H_2 at low temperatures." *Phys. Chem. Chem. Phys.*, **17**:8732–8739, 2015.

[MS03] H. J. Metcalf and P. van der Straten. "Laser cooling and trapping of atoms." *J. Opt. Soc. Am. B*, **20**(5):887–908, May 2003.

[MS17] Ricardo A. Mata and Martin A. Suhm. "Benchmarking Quantum Chemical Methods: Are We Heading in the Right Direction?" *Angewandte Chemie International Edition*, **56**(37):11011–11018, 2017.

[MSA99] Murray J. McEwan, Graham B. I. Scott, Nigel G. Adams, Lucia M. Babcock, R. Terzieva, and Eric Herbst. "New H and H2 Reactions with Small Hydrocarbon Ions and Their Roles in Benzene Synthesis in Dense Interstellar Clouds." *The Astrophysical Journal*, **513**(1):287, 1999.

[MTR01] Mohammadou Mérawa, Claire Tendero, and Michel Rérat. "Excited states dipole polarizabilities of calcium atom and long-range dispersion coefficients for the low-lying electronic states of Ca2 and CaMg." *Chemical Physics Letters*, **343**(3):397 – 403, 2001.

[MZ08] J. Mitroy and J.-Y. Zhang. "Properties and long range interactions of the calcium atom." *J. Chem. Phys.*, **128**(13):134305, 2008.

[NC15] Masayoshi Nakano and Benoît Champagne. "Theoretical Design of Open-Shell Singlet Molecular Systems for Nonlinear Optics." *The Journal of Physical Chemistry Letters*, **6**(16):3236–3256, 2015.

[NOW10] K-K Ni, S. Ospelkaus, D. Wang, G. Quéméner, B. Neyenhuis, M. H. G. De Miranda, J. L. Bohn, J. Ye, and D. S. Jin. "Dipolar collisions of polar molecules in the quantum regime." *Nature*, **464**(7293):1324, 2010.

[NSG02] Stéphane Noury, Bernard Silvi, and Ronald J. Gillespie. "Chemical Bonding in Hypervalent Molecules : Is the Octet Rule Relevant?" *Inorganic Chemistry*, **41**(8):2164–2172, 2002. PMID: 11952370.

[OBF99] C.W. Oates, F. Bondu, R.W. Fox, and L. Hollberg. "A diode-laser optical frequency standard based on laser-cooled Ca atoms: Sub-kilohertz spectroscopy by optical shelving detection." *The European Physical Journal D - Atomic, Molecular, Optical and Plasma Physics*, **7**(3):449–460, 1999.

[OBH12] J. M. Oldham, M. T. Bell, L. D. Harper, and T. P. Softley. "Cold Ion-Molecule Chemistry with a Stark Decelerator Beamline." In *67th International Symposium on Molecular Spectroscopy*, June 2012.

[OBS11] B. Ostojić, P. R. Bunker, P. Schwerdtfeger, B. Assadollahzadeh, and Per Jensen. "The predicted spectrum of the hypermetallic molecule MgOMg." *Phys. Chem. Chem. Phys.*, **13**:7546–7553, 2011.

[OJS13] B. Ostojić, Per Jensen, P. Schwerdtfeger, and P. R. Bunker. "The Predicted Spectrum and Singlet–Triplet Interaction of the Hypermetallic Molecule SrOSr." *The Journal of Physical Chemistry A*, **117**(39):9370–9379, 2013. PMID: 23506078.

[ONW10] S. Ospelkaus, K.-K. Ni, D. Wang, M. H. G. de Miranda, B. Neyenhuis, G. Quéméner, P. S. Julienne, J. L. Bohn, D. S. Jin, and J. Ye. "Quantum-State Controlled Chemical Reactions of Ultracold Potassium-Rubidium Molecules." *Science*, **327**(5967):853–857, 2010.

[Osw15] R. Oswald. *"Velocity Control of Trapped Ions for Transport Quantum Logic Gates."*. Master's thesis, Swiss Federal Institute of Technology Zurich, 2015.

[Pac74] Russell T. Pack. "Space–fixed vs body–fixed axes in atom–diatomic molecule scattering. Sudden approximations." *J. Chem. Phys.*, **60**(2):633–639, 1974.

[Pat14] G.P. Patil. *Weighted Distributions*. American Cancer Society, 2014.

[Pat18] David Patterson. "Method for preparation and readout of polyatomic molecules in single quantum states." *Phys. Rev. A*, **97**:033403, Mar 2018.

[PFL09] L. P. Parazzoli, N. Fitch, D. S. Lobser, and H. J. Lewandowski. "High-energy-resolution molecular beams for cold collision studies." *New Journal of Physics*, **11**(5):055031, 2009.

[PKR01] S. G. Porsev, M. G. Kozlov, Yu. G. Rakhlina, and A. Derevianko. "Many-body calculations of electric-dipole amplitudes for transitions between low-lying levels of Mg, Ca, and Sr." *Phys. Rev. A*, **64**:012508, 2001.

[PL65] Philip Pechukas and John C. Light. "On Detailed Balancing and Statistical Theories of Chemical Kinetics." *J. Chem. Phys.*, **42**(9):3281–3291, 1965.

[PLR66] Philip Pechukas, John C. Light, and Charles Rankin. "Statistical Theory of Chemical Kinetics : Application to Neutral Atom–Molecule Reactions." *J. Chem. Phys.*, **44**(2):794–805, 1966.

[PMS17] Prateek Puri, Michael Mills, Christian Schneider, Ionel Simbotin, John A. Montgomery, Robin Côté, Arthur G. Suits, and Eric R. Hudson. "Synthesis of mixed hypermetallic oxide $BaOCa^+$ from laser-cooled reagents in an atom-ion hybrid trap." *Science*, **357**(6358):1370–1375, 2017.

[PMS18] Prateek Puri, Michael Mills, Ionel Simbotin, John A. Montgomery, Robin Côté, Elizabeth P. West, Christian R. Schneider, Arthur G. Suits, and Eric R. Hudson. "Radiative suppression of charged-neutral photochemistry at low collision energy." *to be published*, 2018.

[PMW18] Prateek Puri, Michael Mills, Elizabeth P. West, Christian Schneider, and Eric R. Hudson. "High-resolution collision energy control through ion position modulation in atom-ion hybrid systems." *Rev. Sci. Instrum.*, **89**(8):083112, 2018.

[PRT76] W. H. Parkinson, E. M. Reeves, and F. S. Tomkinst. "Neutral calcium. strontium and barium : determination of f values of the principal series by the hook method." *J. Phys. B: Atom. Molec. Phys.*, **9**:157, 1976.

[PST07] Gianluca Panati, Herbert Spohn, and Stefan Teufel. "The time-dependent Born–Oppenheimer approximation." *ESAIM: Mathematical Modelling and Numerical Analysis - Modélisation Mathématique et Analyse Numérique*, **41**(2):297–314, 2007.

[PT05] Jingzhi Pu and Donald G. Truhlar. "Benchmark Calculations of Reaction Energies, Barrier Heights, and Transition–State Geometries for Hydrogen Abstraction from Methanol by a Hydrogen Atom." *The Journal of Physical Chemistry A*, **109**(5):773–778, 2005. PMID: 16838946.

[RGM10] V. Sivaranjana Reddy, S. Ghanta, and S. Mahapatra. "First Principles Quantum Dynamical Investigation Provides Evidence for the Role of Polycyclic Aromatic Hydrocarbon Radical Cations in Interstellar Physics." *Phys. Rev. Lett.*, **104**:111102, Mar 2010.

[RLB06] R. Reichle, D. Leibfried, R.B. Blakestad, J. Britton, J.D. Jost, E. Knill, C. Langer, R. Ozeri, S. Seidelin, and D.J. Wineland. "Transport dynamics of single ions in segmented microstructured Paul trap arrays." *Fortschritte der Physik*, **54**(8-10):666–685, 2006.

[RM87] B. R. Rowe and J. B. Marquette. "CRESU studies of ion/molecule reactions." *International Journal of Mass Spectrometry and Ion Processes*, **80**:239–254, 1987.

[RMV16] R. Roos, B. O. an Lindh, R. Malmqvist, V. Veryazov, and P. Widmark. *Hartree Fock Theory*, chapter 4, pp. 43–58. John Wiley & Sons, Ltd, 2016.

[RP95] B. R. Rowe and D. C. Parent. "Techniques for the study of reaction kinetics at low temperatures: application to the atmospheric chemistry of Titan." *Planetary and Space Science*, **43**(1):105–114, 1995.

[Exobiology.]

[RR27] Oscar Knefler Rice and Herman C. Ramsperger. "Theories of unimolecular gas reactions at low pressures." *J. Am. Chem. Soc.*, **49**(7):1617–1629, 1927.

[RSK11] Wade G. Rellergert, Scott T. Sullivan, Svetlana Kotochigova, Alexander Petrov, Kuang Chen, Steven J. Schowalter, and Eric R. Hudson. "Measurement of a Large Chemical Reaction Rate between Ultracold Closed-Shell ^{40}Ca Atoms and Open-Shell $^{174}Yb^{+}$ Ions Held in a Hybrid Atom-Ion Trap." *Phys. Rev. Lett.*, **107**:243201, Dec 2011.

[RSS12] W. G. Rellergert, S. T. Sullivan, S. J. Schowalter, S. Kotochigova, K. Chen, and E. R. Hudson. "Evidence for sympathetic vibrational cooling of translationally cold molecules." *Nature*, **495**(7442):490–494, 2012.

[RW17] I. Rouse and S. Willitsch. "Superstatistical Energy Distributions of an Ion in an Ultracold Buffer Gas." *Phys. Rev. Lett.*, **118**:143401, Apr 2017.

[RZS12] Lothar Ratschbacher, Christoph Zipkes, Carlo Sias, and Michael Köhl. "Controlling chemical reactions of a single particle." *Nat. Phys.*, **8**:649, jul 2012.

[Saa11] Y. Saad. *Numerical Methods for Large Eigenvalue Problems*. Society for Industrial and Applied Mathematics, 2011.

[SB08] Theodore P. Snow and Veronica M. Bierbaum. "Ion Chemistry in the Interstellar Medium." *Annual Review of Analytical Chemistry*, **1**(1):229–259, 2008. PMID: 20636080.

[SC85] J. Sugar and C. Corliss. "Atomic energy levels of the iron period elements: Potassium through nickel." **14**, 01 1985.

[SCG04] Robin Santra, Kevin V. Christ, and Chris H. Greene. "Properties of metastable alkaline-earth-metal atoms calculated using an accurate effective core potential." *Phys. Rev. A*, **69**:042510, Apr 2004.

[Sch16] Steven Schowalter. *Action Spectroscopy of Molecular Ions and Studies of Cold Collisions in a Hybrid Atom-Ion Trap.* PhD thesis, University of California, Los Angeles, 2016.

[SCR12] Steven J. Schowalter, Kuang Chen, Wade G. Rellergert, Scott T. Sullivan, and Eric R. Hudson. "An integrated ion trap and time-of-flight mass spectrometer for chemical and photo- reaction dynamics studies." *Rev. Sci. Instrum.*, **83**(4):043103, 2012.

[SDC16] S. J. Schowalter, A. J. Dunning, K. Chen, P. Puri, C. Schneider, and E. R. Hudson. "Blue-sky bifurcation of ion energies and the limits of neutral-gas sympathetic cooling of trapped ions." *Nat. Comm.*, **7**:12448, 2016.

[SDS04] U. Sterr, C. Degenhardt, H. Stoehr, Ch. Lisdat, H. Schnatz, J. Helmcke, F. Riehle, G. Wilpers, Ch. Oates, and L. Hollberg. "The optical calcium frequency standards of PTB and NIST." *Comptes Rendus Physique*, **5**(8):845 – 855, 2004.

[Sec75] Don Secrest. "Theory of angular momentum decoupling approximations for rotational transitions in scattering." *J. Chem. Phys.*, **62**(2):710–719, 1975.

[SGM17] P. C. Schmid, J. Greenberg, M. I. Miller, K. Loeffler, and H. J. Lewandowski. "An ion trap time-of-flight mass spectrometer with high mass resolution for cold trapped ion experiments." *Rev. Sci. Instrum.*, **88**(12):123107, 2017.

[SGT95] V. Sanchez-Villicana, S. D. Gensemer, K. Y. N. Tan, A. Kumarakrishnan, T. P. Dinneen, W. Süptitz, and P. L. Gould. "Suppression of Ultracold Ground-State Hyperfine-Changing Collisions with Laser Light." *Phys. Rev. Lett.*, **74**:4619–4622, Jun 1995.

[SHD13] M. Shi, P. F. Herskind, M. Drewsen, and I. L. Chuang. "Microwave quantum logic spectroscopy and control of molecular ions." *N. J. Phys.*, **15**(11):113019, 2013.

[She95] David Sherrill. "An Introduction to Configuration Interaction Theory.", June 1995.

[She00] David Sherrill. "An Introduction to Hartree–Fock Molecular Orbital Theory.", June 2000.

[She04] David Sherrill. "The Multiconfigurational Self–Consistent-Field Method.", March 2004.

[She14] David Sherrill. "Basis sets in Quantum Chemistry.", March 2014.

[SHS10] P. F. Staanum, K. Højbjerre, P. S. Skyt, A. K. Hansen, and M. Drewsen. "Rotational laser cooling of vibrationally and translationally cold molecular ions." *Nat. Phys.*, **6**, 2010.

[Sin07] Oktay Sinanğlu. *Many-Electron Theory of Atoms, Molecules and Their Interactions*, pp. 315–412. John Wiley & Sons, Ltd, 2007.

[SJ02] I. M. Savukov and W. R. Johnson. "Combined configuration-interaction and many-body-perturbation-theory calculations of energy levels and transition amplitudes in Be, Mg, Ca, and Sr." *Phys. Rev. A*, **65**:042503, 2002.

[SKD00] M. Sudakov, N. Konenkov, D.J. Douglas, and T. Glebova. "Excitation frequencies of ions confined in a quadrupole field with quadrupole excitation." *Journal of the American Society for Mass Spectrometry*, **11**(1):10 – 18, 2000.

[SKS15] Yuval Shagam, Ayelet Klein, Wojciech Skomorowski, Renjie Yun, Vitali Averbukh, Christiane P. Koch, and Edvardas Narevicius. "Molecular hydrogen interacts more strongly when rotationally excited at low temperatures leading to faster reactions." *Nature Chemistry*, **7**:921, oct 2015.

[SL90] Gustavo E. Scuseria and Timothy J. Lee. "Comparison of coupled cluster methods which include the effects of connected triple excitations." *The Journal of Chemical Physics*, **93**(8):5851–5855, 1990.

[SLG16] Hongwei Song, Anyang Li, and Hua Guo. "Rotational and Isotopic Effects in the $H_2 + OH^+ \rightarrow H + H_2O^+$ Reaction." *The Journal of Physical Chemistry A*, **120**(27):4742–4748, 2016. PMID: 26731677.

[SMA17] Tomas Sikorsky, Ziv Meir, Nitzan Akerman, Ruti Ben-shlomi, and Roee Ozeri. "Doppler cooling thermometry of a multilevel ion in the presence of micromotion." *Phys. Rev. A*, **96**:012519, Jul 2017.

[SMB18] Tomas Sikorsky, Ziv Meir, Ruti Ben-shlomi, Nitzan Akerman, and Roee Ozeri. "Spin-controlled atom–ion chemistry." *Nat. Comm.*, **9**(1):920, 2018.

[SMD11] E. J. Salumbides, V. Maslinskas, I. M. Dildar, A. L. Wolf, E.-J. van Duijn, K. S. E. Eikema, and W. Ubachs. "High-precision frequency measurement of the 423-nm Ca i line." *Phys. Rev. A*, **83**:012502, Jan 2011.

[Smi88] G. Smith. "Oscillator strengths for neutral calcium lines of 2.9 eV excitation." *J. Phys. B: At. Mol. Opt. Phys.*, **21**:2827, 1988.

[Smi92] David Smith. "The ion chemistry of interstellar clouds." *Chem. Rev.*, **92**(7):1473–1485, nov 1992.

[doi: 10.1021/cr00015a001.]

[SN11] J.J. Sakurai and J. Napolitano. *Modern Quantum Mechanics*. Addison-Wesley, 2011.

[SO75] G. Smith and J. A. O'Neill. "Absolute transition probabilities for some lines of neutral calcium." *Astron. Astrophys.*, **38**:1–4, Jan 1975.

[SO96] A. Szabo and N. S. Ostlund. *Modern Quantum Chemistry: Introduction to Advanced Electron Structure Theory.* Dover, 1996.

[SR81] G. Smith and D. J. Raggett. "Oscillator strengths and collisional damping parameters for lines of neutral calcium." *J. Phys. B: At. Mol. Phys.*, **14**:4015, 1981.

[SR00] Ian W. M. Smith and Bertrand R. Rowe. "Reaction Kinetics at Very Low Temperatures – Laboratory Studies and Interstellar Chemistry." *Accounts of Chemical Research*, **33**(5):261–268, 2000. PMID: 10813870.

[SRA15] Humberto da Silva Jr., Maurice Raoult, Mireille Aymar, and Olivier Dulieu. "Formation of molecular ions by radiative association of cold trapped atoms and ions." *New Journal of Physics*, **17**(4):045015, 2015.

[SRK12] Scott T. Sullivan, Wade G. Rellergert, Svetlana Kotochigova, and Eric R. Hudson. "Role of Electronic Excitations in Ground-State-Forbidden Inelastic Collisions Between Ultracold Atoms and Ions." *Phys. Rev. Lett.*, **109**:223002, Nov 2012.

[SS96] David Smith and Patrik Španěl. "Application of ion chemistry and the SIFT technique to the quantitative analysis of trace gases in air and on breath." *International Reviews in Physical Chemistry*, **15**(1):231–271, 1996.

[SSC14] Christian Schneider, Steven J. Schowalter, Kuang Chen, Scott T. Sullivan, and Eric R. Hudson. "Laser-Cooling-Assisted Mass Spectrometry." *Phys. Rev. Applied*, **2**:034013, Sep 2014.

[SSF08] V. V. Smirnov, O. M. Stelmakh, V. I. Fabelinsky, D. N. Kozlov, A. M. Starik, and N. S. Titova. "On the influence of electronically excited oxygen molecules on combustion of hydrogen–oxygen mixture." *J. Phys. D: Appl. Phys.*, **41**(19):192001, 2008.

[SSY16] Christian Schneider, Steven J. Schowalter, Peter Yu, and Eric R. Hudson. "Electronics of an ion trap with integrated time-of-flight mass spectrometer." *Int. J. Mass Spectrom.*, **394**:1 – 8, 2016.

[Sul13] Scott Sullivan. *The MOTion trap: a hybrid atom-ion trap system for experiments in cold-chemistry and the production of cold polar molecular ions.* PhD thesis, University of California, Los Angeles, 2013.

[Sur89] Péter R. Surján. *The Brillouin Theorem*, pp. 87–92. Springer Berlin Heidelberg, Berlin, Heidelberg, 1989.

[Swi62] D. F. Swinehart. "The Beer–Lambert Law." *Journal of Chemical Education*, **39**(7):333, 1962.

[SWM89] D. Sesko, T. Walker, C. Monroe, A. Gallagher, and C. Wieman. "Collisional losses from a light-force atom trap." *Phys. Rev. Lett.*, **63**(9):961, 1989.

[SZ96] P. C. Stancil and B. Zygelman. "Radiative Charge Transfer in Collisions of Li With H^+." *Astrophys. J.*, **472**(1):102, 1996.

[Sza05] P. G. Szalay. chapter Configuration Interaction: Corrections for Size Consistency. American Cancer Society, 2005.

[Tar15] M. R. Tarbutt. "Magneto-optical trapping forces for atoms and molecules with complex level structures." *New Journal of Physics*, **17**(1):015007, jan 2015.

[TJG17] M. Tomza, K. Jachymski, R. Gerritsma, A. Negretti, T. Calarco, Z. Idziaszek, and P. S. Julienne. "Cold ion-atom systems." August 2017. Preprint at https://arxiv.org/abs/1708.07832.

[TKJ04] Nicholas R. Thomas, Niels Kjærgaard, Paul S. Julienne, and Andrew C. Wilson. "Imaging of s and d Partial-Wave Interference in Quantum Scattering of Identical Bosonic Atoms." *Phys. Rev. Lett.*, **93**:173201, Oct 2004.

[TRL12] D. A. Tabor, V. Rajagopal, Y.-W. Lin, and B. Odom. "Suitability of linear quadrupole ion traps for large Coulomb crystals." *Applied Physics B: Lasers and Optics*, **107**:1097–1104, June 2012.

[TSC13] S. Trippel, M. Stei, J. A. Cox, and R. Wester. "Differential Scattering Cross-Sections for the Different Product Vibrational States in the Ion-Molecule Reaction $Ar^+ + N_2$." *Phys. Rev. Lett.*, **110**:163201, Apr 2013.

[TTY98] K.T. Tang, J. P. Toennies, and C. L. Yiu. "The generalized Heitler-London theory for interatomic interaction and surface integral method for exchange energy." *Int. Rev. Phys. Chem.*, **17**(3):363–406, 1998.

[UHF82] Kiyoshi Ueda, Yoshihiro Hamaguchi, and Kuniya Fukuda. "Measurements of Oscillator Strengths for the Transitions from the Metastable 3P Levels of Alkaline–Earth Atoms. III. Calcium–Low–n Members." *J. Phys. Soc. Jpn.*, **51**(9):2973–2976, 1982.

[UHF83] Kiyoshi Ueda, Yoshihiro Hamaguchi, and Kuniya Fukuda. "Measurements of Oscillator Strengths for the Transitions from the Metastable 3P Levels of Alkaline–Earth Atoms. IV. Calcium–High–n Members." *J. Phys. Soc. Jpn.*, **52**(8):2666–2672, 1983.

[UOY10] Muhammet Uyanik, Hiroaki Okamoto, Takeshi Yasui, and Kazuaki Ishihara. "Quaternary Ammonium (Hypo)iodite Catalysis for Enantioselective Oxidative Cycloetherification." *Science*, **328**(5984):1376–1379, 2010.

[VOC15] Sjoerd N. Vogels, Jolijn Onvlee, Simon Chefdeville, Ad van der Avoird, Gerrit C. Groenenboom, and Sebastiaan Y. T. van de Meerakker. "Imaging resonances in low-energy NO-He inelastic collisions." *Science*, **350**(6262):787–790, 2015.

[Voo15] Troy Van Voorhis. "The Born–Oppenheimer Approximation.", October 2015.

[Vut15] Amar Vutha. "Optical frequency standards for gravitational wave detection using satellite Doppler velocimetry." *New Journal of Physics*, **17**(6):063030, 2015.

[WBZ99] John Weiner, Vanderlei S. Bagnato, Sergio Zilio, and Paul S. Julienne. "Experiments and theory in cold and ultracold collisions." *Rev. Mod. Phys.*, **71**:1–85, Jan 1999.

[Wei35] Viktor Weisskopf. "Probleme der neueren Quantentheorie des Elektrons." *Naturwissenschaften*, **23**(37):631–637, Sep 1935.

[Wie82] John R. Wiesenfeld. "Atmospheric chemistry involving electronically excited oxygen atoms." *Accounts Chem. Res.*, **15**(4):110–116, 1982.

[Wit05] Curt Wittig. "The Landau–Zener Formula." *J. Phys. Chem. B*, **109**(17):8428–8430, 2005. PMID: 16851989.

[WKK12a] Hans-Joachim Werner, Peter J. Knowles, Gerald Knizia, Frederick R. Manby, and Martin Schütz. "Molpro: a general-purpose quantum chemistry program package." *WIREs Comput. Mol. Sci.*, **2**(2):242–253, Feb 2012.

[WKK12b] Matthias Wolke, Julian Klinner, Hans Keßler, and Andreas Hemmerich. "Cavity Cooling Below the Recoil Limit." *Science*, **337**(6090):75–78, 2012.

[WKK18] H.-J. Werner, P. J. Knowles, G. Knizia, F. R. Manby, M. Schütz, et al. "MOLPRO, version 2018.2, a package of ab initio programs.", 2018.

[WM55] W. C. Wiley and I. H. McLaren. "Time-of-Flight Mass Spectrometer with Improved Resolution." *Review of Scientific Instruments*, **26**(12):1150–1157, 1955.

[WOH06] G. Wilpers, C.W. Oates, and L. Hollberg. "Improved uncertainty budget for optical frequency measurements with microkelvin neutral atoms: Results for a high-stability ^{40}Ca optical frequency standard." *Applied Physics B*, **85**(1):31–44, 2006.

[WSD95] C. D. Wallace, V. Sanchez-Villicana, T. P. Dinneen, and P. L. Gould. "Suppression of Trap Loss Collisions at Low Temperature." *Phys. Rev. Lett.*, **74**:1087–1090, Feb 1995.

[WT72] Albert F. Wagner and Donald G. Truhlar. "Comment on Enhancement of the Reaction Cross Section of $He + H_2^+ \rightarrow HeH^+ + H$ by Vibrational Excitation of H_2^+ and the Treatment of Nuclear Spin by the Statistical Phase–Space Theory." *J. Chem. Phys.*, **57**(9):4063–4064, 1972.

[WWH16] Fabian Wolf, Yong Wan, Jan C. Heip, Florian Gebert, Chunyan Shi, and Piet O. Schmidt. "Non-destructive state detection for quantum logic spectroscopy of molecular ions." *Nature*, **530**:457, feb 2016.

[Wys11] G. M. Wysin. "Quantization of the Free Electromagnetic Field: Photons and Operators.", August 2011.

[YLC18a] Tiangang Yang, Anyang Li, Gary K. Chen, Changjian Xie, Arthur G. Suits, Wesley C. Campbell, Hua Guo, and Eric R. Hudson. "Optical control of reactions between water and laser-cooled Be^+ ions." *J. Phys. Chem. Lett.*, **9**(13):3555–3560, jul 2018.

[doi: 10.1021/acs.jpclett.8b01437.]

[YLC18b] Tiangang Yang, Anyang Li, Gary K. Chen, Changjian Xie, Arthur G. Suits, Wesley C. Campbell, Hua Guo, and Eric R. Hudson. "Optical Control of Reactions between Water and Laser-Cooled Be^+ Ions." *J. Phys. Chem. Lett.*, **9**(13):3555–3560, 2018. PMID: 29893569.

[ZBR00] Götz Zinner, Tomas Binnewies, and Fritz Riehle. "Atom-interferometry constraints on dark energy." *Phys. Rev. Lett.*, **85**:2292, 2000.

[ZD88] B. Zygelman and A. Dalgarno. "Radiative quenching of He(2 ^1S) induced by collisions with ground-state helium atoms." *Phys. Rev. A*, **38**:1877–1884, Aug 1988.

[ZFT09] Zhanchun Zuo, Miho Fukusen, Yoshihito Tamaki, Tomoki Watanabe, Yusuke Nakagawa, and Keníchi Nakagawa. "Single atom Rydberg excitation in a small dipole trap." *Opt. Express*, **17**(25):22898–22905, Dec 2009.

[ZMM96] S. C. Zilio, L. Marcassa, S. Muniz, R. Horowicz, V. Bagnato, R. Napolitano, J. Weiner, and P. S. Julienne. "Polarization Dependence of Optical Suppression in Photoassociative Ionization Collisions in a Sodium Magneto-optic Trap." *Phys. Rev. Lett.*, **76**:2033–2036, Mar 1996.

[ZOH91] M. Zhu, C. W. Oates, and J. L. Hall. "Continuous high-flux monovelocity atomic beam based on a broadband laser-cooling technique." *Phys. Rev. Lett.*, **67**:46–49, Jul 1991.

[ZPR10] Christoph Zipkes, Stefan Palzer, Lothar Ratschbacher, Carlo Sias, and Michael Köhl. "Cold Heteronuclear Atom-Ion Collisions." *Phys. Rev. Lett.*, **105**:133201, Sep 2010.

[ZPS10] Christoph Zipkes, Stefan Palzer, Carlo Sias, and Michael Köhl. "A trapped single ion inside a Bose–Einstein condensate." *Nature*, **464**:388, mar 2010.

[ZRP11] Christoph Zipkes, Lothar Ratschbacher, Stefan Palzer, Carlo Sias, and Michael Köhl. "Hybrid quantum systems of atoms and ions." **264**:012019, 01 2011.

[ZW18] Dongdong Zhang and Stefan Willitsch. In *Cold Chemistry: Molecular Scattering and Reactivity Near Absolute Zero Ch.10*. The Royal Society of Chemistry, London, 2018.